On Aspects of Cardiac and Artificial Muscle Modelling
–
Insights into Orthotropic Tissue Structure and Dielectric Elastomer Actuators

Aspekte der Modellierung von kardialen und künstlichen Muskeln
–
Einblicke in die orthotrope Gewebestruktur und dielektrische Elastomeraktoren

Der Technischen Fakultät
der Friedrich-Alexander-Universität
Erlangen-Nürnberg

zur

Erlangung des Doktorgrades Dr.-Ing.
vorgelegt von

David Holz

aus Würzburg

Als Dissertation genehmigt
von der Technischen Fakultät
der Friedrich-Alexander-Universität Erlangen-Nürnberg

Tag der mündlichen Prüfung: 19. Dezember 2023

Gutachter/in: Prof. Dr.-Ing. habil. Sigrid Leyendecker
Prof. Oliver Röhrle, PhD

Impressum

Prof. Dr.-Ing. habil. Sigrid Leyendecker
Lehrstuhl für Technische Dynamik
Friedrich-Alexander-Universität Erlangen-Nürnberg
Immerwahrstraße 1
91058 Erlangen

On Aspects of Cardiac and Artificial Muscle Modelling
–
Insights Into Orthotropic Tissue Structure and Dielectric Elastomer Actuators

Aspekte der Modellierung von kardialen und künstlichen Muskeln
–
Einblicke in die orthotrope Gewebestruktur und dielektrische Elastomeraktoren

David Holz

Schriftenreihe Technische Dynamik
Band 10 2024
Herausgeber: Prof. Dr.-Ing. habil. Sigrid Leyendecker

Vorwort

Diese Arbeit entstand während meiner Tätigkeit als wissenschaftlicher Mitarbeiter bei Frau Prof. Dr.-Ing. habil. Sigrid Leyendecker am Lehrstuhl für Technische Dynamik an der Friedrich-Alexander-Universität Erlangen-Nürnberg. Die Projektidee entwickelte sich im Rahmen des durch die Klaus Tschira Stiftung geförderten Projekts "Etablierung eines Herzunterstützungssystems basierend auf einer dem Herzbeutel nachgebildeten kontraktilen Membran".

Mein besonderer Dank gilt Frau Prof. Dr.-Ing. habil. Sigrid Leyendecker. Ihr entgegengebrachtes Vertrauen bezüglich Lehre und Forschung hat mir stets Mut und Motivation geschenkt. Ihre fachliche und persönliche Unterstützung haben meine akademische Reise bereichert. Besonders das Ermöglichen einer Vielzahl an Konferenzbesuchen mit wertvollen Kontakten zu anderen internationalen Wissenschaftlern habe ich stets sehr geschätzt.

Mein Dank gilt zudem Herrn Prof. Oliver Röhrle Ph.D. für die Begutachtung meiner Arbeit, Frau Prof. Dr.-Ing. Silvia Budday für die Übernahme des Prüfungsvorsitzes und Prof. Dr. med. habil. Dr. rer. nat. Dipl.-Phys. Oliver Friedrich für das Mitwirken in der Prüfungskommission.

Bedanken möchte ich mich auch bei allen Kooperationspartnern, allen voran bei Dr. rer. nat Muhannad Alkassar, der das Klaus Tschira Projekt initiiert hat und in unzähligen Besprechungen mit seiner medizinischen Expertise zur Verfügung stand. Bedanken möchte ich mich außerdem bei den Kollegen vom Lehrstuhl für Technische Mechanik, insbesondere bei Dr.-Ing. Gunnar Possart für die Unterstützung und Zusammenarbeit bei einer Vielzahl von Lehrtätigkeiten.

Ein großes Dankschön geht an alle Studierenden (Anika Kreipp, Ludwig Herrnböck, Theresa Ach, Kevin Lösch, Dorothee Lippold, Thomas Hufnagel, Daria Frolova, Kim Myoungsic, Emely Schaller, Dorothea Brackenhammer) und Kollegen (Dr.-Ing. Denisa Martonová, Dr.-Ing. Minh Tuan Duong, Dr.-Ing. Dengpeng Huang), die im Herzprojekt am Lehrstuhl für Technische Dynamik mitgewirkt haben. Hervorheben möchte ich dabei die hilfreichen und konstruktiven Diskussionen mit meiner Kollegin Dr.-Ing. Denisa Martonová, die grundlegende Entwicklung des Herzmodells am Lehrstuhl durch Dr.-Ing. Minh Tuan Duong sowie die fachliche Unterstützung von Dr.-Ing. Dengpeng Huang bei der Modellentwicklung dielektrischer Schalen. Weiter danke ich allen ak-

tuellen und ehemaligen Kollegen am Lehrstuhl für Technische Dynamik für die angenehme Atmosphäre, Unterstützung und gemeinsamen unvergesslichen Erinnerungen. Insbesondere möchte ich mich bei meinen Zimmerkollegen und -nachbarn Uday Phutane, Martina Stavole und Dhananjay Phansalkar für die vielen gemeinsamen Abende mit gutem Essen, zu viel Alkohol und Karaoke bedanken. Ein außergewöhnliches Dankeschön geht an Beate Hegen, die immer ein offenes Ohr für mich hatte und mit Rat und Tat zur Seite stand, selbst am Feiertag, weil die Konferenzgebühr bezahlt werden musste. Auch bedanken möchte ich mich bei Elisa Fleischmann, die unterstützte, wann immer es notwendig war.

Ein unendlich großer Dank gilt abschließend meiner gesamten Familie und meinen Freunden, insbesondere meinen Eltern, meinem Bruder und meiner Freundin Johanna. Sie haben mich bedingungslos unterstützt und immer an mich geglaubt.

Erlangen, Mai 2024 David Holz

Abstract

The heart is a fascinating organ whose seemingly simple function of mechanically pumping blood throughout the body is ensured by a complex interaction of mechanical, electrical, chemical and biological mechanisms. However, complex systems inherently bear the risk of disruptions, causing a variety of cardiovascular diseases (CVD) such as myocardial infarction, heart failure, arrhythmia, and hypertension. The field of biomechanics is playing a key role in the fundamental research concerning CVDs. In this context, computational modelling and simulation of the cardiovascular system are crucial in furthering the understanding of CVDs, enhancing diagnostic capabilities, and developing patient-specific therapeutic interventions. Moreover, computer models can facilitate the development of novel medical devices, such as cardiac assist devices (CaAD) comprised of dielectric materials. In this thesis, the focus is on the development of two types of computational muscle models, specifically a cardiac muscle model based on biological tissue and an artificial muscle model based on dielectric materials. The work on the cardiac muscle model primarily focuses on the modelling of the orthotropic cardiac tissue structure. The developed tissue structure model (TSM) is based on a discontinuous Galerkin framework to accurately assess the transmural path and thickness in the myocardial wall. The framework enables more accurate modelling of the orthotropic tissue structure compared to established methods. Moreover, due to the modularity, the framework can be easily integrated into other TSMs. In this regard, transmural fibre and sheet angle rules are proposed for the left ventricle based on diffusion tensor magnetic resonance imaging (DT-MRI) data and demonstrate enhanced fidelity in representing the measurement data compared to existing rules. A study about the influence of different TSMs on important characteristics of cardiac function, based on an electromechanical model of the cardiac tissue, underscores the significant influence of the TSM. The artificial muscle model is inspired by the idea of an innovative concept for cardiac assist devices (CaAD) based on dielectric elastomers. However, there is a dearth of computational models that are able to simulate the complex electromechanical, dynamic, and viscoelastic behaviour of such a dielectric elastomer actuator-based CaAD. In this thesis, the computational model of the artificial muscle is based on an electromechanical shell formulation, including dynamics and viscoelasticity. The variational formulation of the dynamic, viscoelastic, and electromechanical shell is derived from the Lagrange-d'Alembert principle. A variational time integration ensures a good long-term energy behaviour. To demonstrate the potential of the model, numerical examples,

including different geometries as well as deformation states, are presented. Overall, the proposed TSM, in conjunction with the improved transmural fibre and sheet angle rules, is a robust, efficient and accurate method by which to compute the orthotropic tissue structure for finite element models of the cardiac tissue. Furthermore, the significant influence of different TSMs on important characteristics of cardiac function is demonstrated. The electromechanical shell model proves to be a promising approach towards the development of patient-specific CaADs based on dielectric elastomer actuators (DEA).

Kurzfassung

Das Herz ist ein faszinierendes Organ, dessen scheinbar einfache Funktion, das mechanische Pumpen von Blut durch den Körper, durch eine komplexe Interaktion zwischen mechanischen, elektrischen, chemischen und biologischen Vorgängen gewährleistet wird. Allerdings bergen komplexe Systeme inhärent das Risiko von Störungen, die verschiedene Herz-Kreislauf-Erkrankungen wie Myokardinfarkt, Herzinsuffizienz, Arrhythmie und Hypertonie verursachen können. Einen wichtigen Baustein in der grundlegenden Forschung zu Herz-Kreislauf-Erkrankungen stellt das Gebiet der Biomechanik dar. Computergestützte Modellierung und Simulation des Herz-Kreislauf-Systems im Bereich der Biomechanik sind von entscheidender Bedeutung für ein weitreichenderes Verständnis von Herz-Kreislauf-Erkrankungen, die Verbesserung der diagnostischen Möglichkeiten und die Entwicklung patientenspezifischer therapeutischer Maßnahmen. Darüber hinaus können Computermodelle genutzt werden, um die Entwicklung neuartiger medizinischer Geräte, wie z. B. Herzunterstützungsgeräte aus dielektrischen Materialien, zu unterstützen. In dieser Arbeit liegt der Fokus auf der Entwicklung zweier Muskelmodelle: einem kardialen Muskelmodell basierend auf biologischem Gewebe und einem künstlichen Muskelmodell basierend auf dielektrischen Materialien. Beim kardialen Muskelmodell steht die Modellierung der komplexen orthotropen Struktur des Herzgewebes im Vordergrund. Das entwickelte Gewebestrukturmodell basiert auf einem Discontinuous-Galerkin-Ansatz, um den transmuralen Pfad und die Dicke der Myokardwand präzise zu bestimmen. Die Methode ermöglicht eine genauere Modellierung der orthotropen Gewebestruktur im Vergleich zu etablierten Methoden. Aufgrund der Modularität kann die Methode problemlos in bestehende Gewebestrukturmodelle integriert werden. Zusätzlich werden transmurale „fibre“- und „sheet“-Winkelfunktionen für die linke Herzkammer auf Basis von Diffusionstensor-Magnetresonanztomographie-Daten entwickelt, welche die Messdaten deutlich besser abbilden können als bisher verwendete Funktionen. Eine Studie über den Einfluss der orthotropen Gewebestruktur auf wichtige Charakteristika der Herzfunktion, basierend auf einem elektromechanischen Modell des Herzgewebes, unterstreicht den signifikanten Einfluss verschiedener Gewebestrukturmodelle. Das künstliche Muskelmodell basiert auf der Idee eines innovativen Konzepts für kardiale Unterstützungssysteme durch dielektrische Elastomere. Allerdings mangelt es bisher an computergestützten Modellen, um das komplexe elektromechanische, dynamische und viskoelastische Verhalten solcher Unterstützungssysteme zu simulieren. In dieser Arbeit beruht das Modell des künstlichen Muskels auf einer elektromech-

anischen Schalenformulierung, die Dynamik und Viskoelastizität berücksichtigt. Die variationsbasierte Formulierung der dynamischen, viskoelastischen und elektromechanischen Schale wird ausgehend vom Lagrange-d'Alembert-Prinzip hergeleitet. Eine variationsbasierte Zeitintegration gewährleistet ein gutes Langzeit-Energieverhalten. Um das Potential des Schalenmodells zu demonstrieren, werden diverse numerische Beispiele mit unterschiedlichen Geometrien und Deformationszuständen präsentiert.
Insgesamt stellt das entwickelte Gewebestrukturmodell in Verbindung mit den verbesserten transmuralen „fibre"- und „sheet"-Winkelfunktionen eine robuste, effiziente und genaue Methode zur Berechnung der orthotropen Gewebestruktur für Finite-Elemente-Modelle des Herzmuskels dar. Es konnte zudem der signifikante Einfluss verschiedener Gewebestrukturmodelle auf wichtige Charakteristika der Herzfunktion gezeigt werden. Das elektromechanische Schalenmodell zeigt sich als ein vielversprechender Ansatz auf dem Weg zur Entwicklung von patientenspezifischen kardialen Unterstützungssystemen auf Basis von dielektrischen Elastomeren.

Contents

Nomenclature

A	assembly operator
α_{endo}	fibre angle endocardium
α_{epi}	fibre angle epicardium
$\alpha(\boldsymbol{X})$	fibre angle rule
$\Delta\alpha_i^j$	local difference in fibre angle
α_e	oscillation threshold control
$\alpha(\xi^1, \xi^2)$	incremental parameter of the electric potential
a	apicobasal depth
a_s	apical shortening during systole
a_r	outer to inner radius ratio
$\partial\mathcal{B}_{0,en}$	boundary surface endocardium
$\partial\mathcal{B}_{0,ep}$	boundary surface epicardium
$\partial\mathcal{B}_T$	boundary surface mechanical Neumann boundary condition
$\partial\mathcal{B}_Q$	boundary surface electrical Neumann boundary condition
$\mathcal{B}_0$	undeformed configuration
$\mathcal{B}_t$	deformed configuration
$\mathcal{B}^h$	discretised domain
$\mathcal{B}^h_{0,e}$	element of discretised domain $\mathcal{B}^h_0$
$\beta(\boldsymbol{X})$	sheet angle function
$\boldsymbol{b}_0$	body force – deformed configuration

$\boldsymbol{B}_0$	body force – undeformed configuration
β_{endo}	sheet angle endocardium
β_{epi}	sheet angle epicardium
$\boldsymbol{c}(\boldsymbol{X})$	circumferential direction
$C_{mat}(\boldsymbol{X})$	local orthonormal material coordinate system
$C_{ref}(\boldsymbol{X})$	local orthonormal reference coordinate system
$\mathbf{D}$	anisotropic conductivity tensor
d_{ani}	anisotropic conductivity parameter
da	area element
$\Delta\boldsymbol{\varphi}$	increment displacement
$\Delta\bar{\boldsymbol{\Phi}}$	increment potential
$\boldsymbol{D}$	electric displacement
δ_1, δ_2	isoparametric coordinates
Δ_a^j	deviation of local characteristics
$\boldsymbol{d}(\xi^1, \xi^2, t)$	director of the shell
d_{iso}	isotropic conductivity parameter
$d\boldsymbol{x}$	line element
$d_{DG}(\boldsymbol{X})$	normalised discontinuous Galerkin-based transmural depth
$d(\boldsymbol{X})$	transmural depth
dv	volume element
$\boldsymbol{E}_1, \boldsymbol{E}_2, \boldsymbol{E}_3$	inertial basis
$\mathbf{E}$	Green-Lagrange strain
$\boldsymbol{E}^e$	electric field
$\epsilon_{\alpha\beta}$	membrane strains

$\epsilon_{1,1}$	fibre strain
$e_{\alpha,\beta}$	error function fibre and sheet rules
$\mathbf{E}^x$	Green-Lagrangian strain based on the displacement field $\boldsymbol{u}$
F^{Φ}	nonlinear current source term
F_e^{Φ}	electrically induced source term
F_m^{Φ}	mechanically induced source term
$\mathbf{F}(\boldsymbol{X}, t)$	deformation gradient
$\mathbf{F}^{\mathrm{a}}$	active part of deformation gradient
$\mathbf{F}^{\mathrm{iso}}$	isochoric part of deformation gradient
$\mathbf{F}^{\mathrm{e}}$	elastic part of deformation gradient
$\boldsymbol{f}$	fibre direction
$\boldsymbol{f}_0$	fibre orientation – undeformed configuration
f_{int}	interior facet
$\mathcal{F}_h^{int}$	set of interior facets f_{int}
$\boldsymbol{f}^k$	forces in the dielectric shell
$\boldsymbol{f}^{\mathrm{ext}}$	non-conservative generalised forces
γ_α	transverse shear strains
$\boldsymbol{g}(\boldsymbol{q})$	holonomic constraints
G_s	maximum conductance
H^1	Sobolev space
$\mathbf{I}$	3×3 identity matrix
I	external stimulus
$I_1, I_{4f}, I_{4s}, I_{8fs}$	isochoric invariants
J	Jacobian of the deformation

$\kappa_{\alpha\beta}$	bending strains
κ	bulk modulus
k_ϕ	conversion parameter
k_t	conversion parameter
$\boldsymbol{K}$	stiffness matrix
λ	active fibre stretch
L_d	discrete Lagrangian
$\mathcal{L}$	Lagrangian density
$\boldsymbol{\lambda}_n$	time discrete Lagrange multiplier
$L_0(\boldsymbol{X})$	arc length of transmural path to endocardium
$L_1(\boldsymbol{X})$	arc length of transmural path to epicardium
L_2	space of square-integrable functions
$\boldsymbol{l}(\boldsymbol{X})$	longitudinal direction
$\mathbf{M}^{ij}$	mass matrix
$\boldsymbol{m}^k$	torques in the dielectric shell
ν	active modulus
$\boldsymbol{N}$	unit surface normal - undeformed configuration
$\boldsymbol{n}$	unit surface normal - deformed configuration
$\boldsymbol{n}$	sheet normal direction
N	shape functions
$\Omega(\mathbf{F}, \boldsymbol{E}^e)$	potential energy density functional
$\boldsymbol{\varpi}(\boldsymbol{x}, t)$	deformation map - current to initial configuration
ϕ_e	dimensionless electric potential
$\phi_m(\xi^1, \xi^2)$	electric potential on the mid-surface of the dielectric shell

$\phi(\xi^1, \xi^2, \xi^3)$	electric potential dielectric shell
$\delta\boldsymbol{\varphi}$	vector-valued test function
$\delta\Phi$	scalar-valued test function
$\mathbf{P}$	first Piola-Kirchhoff stress tensor
$\mathbf{P}^{\mathrm{m,e}}$	mechanical and electrical part of the first Piola-Kirchhoff stress tensor
$\mathbf{P}^{\mathrm{v}}(\mathbf{F}, \dot{\mathbf{F}})$	viscous part of the first Piola-Kirchhoff stress tensor
$\mathbf{P}^{\mathrm{m,e,v}}$	first Piola-Kirchhoff stress tensor consisting of a mechanical, electrical and viscous part
Π	potential energy
$\boldsymbol{p}_0$	initial momentum
P_k	space of polynomials of degree k
$p_{lv}(t)$	pressure in left ventricle
$p_a(t)$	pressure in aorta
p_{max}	peak pressure in left ventricle
Ψ_{act}	active part of the strain energy function
Ψ_{HO}	orthotropic Holzapfel-Ogden strain energy density function
Ψ_{pas}	passive part of the strain energy function
$\Psi_{\mathrm{V}}(J)$	volumetric part of the strain energy function
$\dot{\Phi}$	time derivative of the transmembrane potential
$\hat{q}$	surface charge – current configuration
$\boldsymbol{q}(t)$	configuration vector
$\boldsymbol{Q}$	electrical flux
$\boldsymbol{q}_i^{DG}$	discontinuous Galerkin based orientation
$\boldsymbol{q}_i^{DT-MRI}$	measured local material orientation

$\hat{Q}$	surface charge – undeformed configuration
$\boldsymbol{r}(\boldsymbol{X})$	transmural direction
$\mathbb{R}^3$	three-dimensional real coordinate space
$\triangle r$	linearisation of weighted residuals
r^{Φ}	residual of the electrical balance equation
r^{φ}	residual of the balance of linear momentum
ρ	mass density
R_p	resistance periphery
R_{v1}	resistance aorta
R_{v2}	resistance atrioventricular valve
S	action
S_d	discrete action
s_c^j	sensitivity marker
$\boldsymbol{s}$	sheet direction
$\boldsymbol{\sigma}$	Cauchy stress
$\sigma_{1,1}^{act}$	active fibre stress
$\mathbf{S}$	second Piola-Kirchhoff stress tensor
$\mathbf{S}^{\mathrm{act}}$	active part of the second Piola-Kirchhoff stress tensor
$\mathbf{S}^{\mathrm{pas}}$	passive part of the second Piola-Kirchhoff stress tensor
$\boldsymbol{T}_a(\boldsymbol{X})$	normalised apicobasal/longitudinal direction
$\hat{\boldsymbol{t}}$	surface traction – current configuration
Δt	time step
t	current time
t_0	initial time

$\dot{(\bullet)}$	first time derivative
$\ddot{(\bullet)}$	second time derivative
$\mathcal{T}(\dot{\boldsymbol{x}})$	kinetic energy density
T	kinetic energy
$\hat{\boldsymbol{T}}$	surface traction – undeformed configuration
$\boldsymbol{T}(\boldsymbol{X}, t, \boldsymbol{N})$	traction vector
$\boldsymbol{T}_f(\boldsymbol{X})$	transmural path direction
t_f	fractional wall thickening
$\boldsymbol{u}$	displacement field
V_{red}	myocardial volume reduction during systole
$V_h^{\mathrm{CG},k}$	test function space - continuous
$V_h^{\mathrm{DG},k}$	test function space - discontinuous
W^{v}	viscoelastic contribution external work
W^{ext}	work of the external non-conservative forces
$\boldsymbol{w}_h$	test function
$W(\boldsymbol{X})$	thickness of myocardium
ξ^1, ξ^2, ξ^3	curvilinear coordinates
$\boldsymbol{\varphi}(\boldsymbol{X}, t)$	deformation map - initial to current configuration
$\boldsymbol{X}$	material point - initial configuration

Acronyms and abbreviations

B-RBM	Bayer-Rule-Based-Method
BC	boundary condition
BP	base point
CaAD	cardiac assist device
CAD	computer-aided design
CFD	computational fluid dynamics
CVD	cardiovascular disease
DEA	dielectric elastomer actuator
DGM	discontinuous Galerkin method
DoF	degree of freedom
DT-MRI	diffusion tensor magnetic resonance imaging
EAP	electroactive polymers
ECG	electrocardiogram
ED	end-diastolic
EDP	end-diastolic pressure
EDV	end-diastolic volume
EF	ejection fraction
ES	end-systolic
ESC	European Society of Cardiology
EU	European Union
FEM	finite element method
FSI	fluid-structure interaction
FVM	finite volume method
H-RBM	Holz-Rule-Based-Method
LDRBM	Laplace-Dirichlet-Rule-Based-Method
LV	left ventricle
MEF	mechano-electrical feedback
MI	myocardial infarction
MRI	magnetic resonance imaging

MV	myocardial volume
PDE	partial differential equation
RAM	Random-Access Memory
RBM	Rule-Based-Method
RP	reference point
SFEM	smoothed finite element method
SP	section point
TP	transmembrane potential
TSM	tissue structure model
VAD	ventricular assist device
W-RBM	Wong-Rule-Based-Method

List of Figures

List of Tables

1 Introduction

According to the 2021 report of the European Society of Cardiology (ESC), cardiovascular diseases (CVDs) remain the leading cause of mortality in Europe. The number of 12.7 million new cases of CVDs across Europe (ESC member countries) has been estimated for 2019 (latest available data) with a prevalence of 113 million people living with CVDs. The healthcare costs for the European Union's (EU) economy associated with CVDs were estimated to be approximately 200 billion Euros per annum. These health and economic statistics underscore the prevailing interest in reducing the mortality and morbidity associated with CVDs so as to lower the cost burden on the relevant healthcare systems. Ongoing fundamental research and development have already led to a better understanding and means of prevention as well as to a continuous improvement in clinical diagnoses and treatments for CVDs [1]. A key role in the fundamental research concerning CVDs falls to the field of biomedical engineering, bridging the gap between engineering and medicine. The field of biomedical engineering applies engineering principles to medicine and biology with a view to developing innovative solutions to medical challenges. The field of biomedical engineering encompasses various subfields, including imaging technologies, medical devices, tissue engineering, and biomechanics, etc. This thesis focuses on two specific aspects, namely the biomechanical modelling of the cardiac muscle as well as an artificial muscle for cardiac devices.

Cardiac muscle models In the context of biomedical engineering in cardiac research, biomechanics and computational biomechanics are powerful tools through which to investigate and better understand CVDs, improve diagnoses and develop patient-specific treatments [2, 3, 4, 5, 6, 7, 8, 9]. Traditionally, computational biomechanics has applied numerical methods established in engineering, such as the finite element method (FEM) to study, *inter alia*, the mechanics of the cardiac muscle or vascular system. Nowadays, these computational models go beyond the realm of pure mechanics and encompass multi-physics models that incorporate various disciplines, including electromechanics or electrochemistry [10] and are especially useful in cases of risk minimisation (e.g., drug testing), circumvention of challenging experimental setups and costs or ethical restrictions, surgical simulation and development of patient-specific devices.

Artificial muscle models in cardiac application A particularly promising approach, and one that has gained increasing attention, especially during the last decade, is the use of artificial muscles (e.g., pneumatic, electromechan-

ical, and electrochemical) to serve as cardiac assist devices (CaADs), see [11, 12, 13, 14, 15, 16, 17, 18, 19, 20]. The concept of artificial muscles serving as CaADs is grounded in the fundamental idea of applying external mechanical pressure to the heart and its associated vessels, thereby providing support to cardiac function without having direct blood contact. This concept has a long history, see [21] for mechanical biventricular assistance via glass cup and [22] for a review on direct mechanical ventricular actuation. Notably, the application of artificial muscles based on dielectric elastomer actuators (DEAs) as CaADs is of great interest. In [12, 14], thin and curved DEAs serve as an augmentation of the ascending or descending aorta [12, 14]. In [13], the use of dielectric elastomers for all-soft artificial hearts is discussed. DEAs offer a unique combination of softness, flexibility, and the ability to undergo large deformations in response to electrical stimulation, making them ideal candidates for replicating the mechanical properties of soft biological tissue. Incorporating DEAs into cardiac research has presented exciting new opportunities for the development of innovative and more effective treatments for cardiac diseases.

The current stage of research of both, the modelling of cardiac as well as artificial muscles based on DEAs, motivates this thesis. Further advancements in cardiac and artificial muscle models are of significant interest to better understand CVDs, improve diagnoses and develop patient-specific treatments and devices. In Section 1.1, a brief introduction to cardiac physiology is given. To define the objectives of this work, a review of existing cardiac muscle models, as well as artificial muscle models based on DEAs, is given in Section 1.2 and Section 1.3, respectively. Chapter 1 concludes with the definition of the main objectives of this work in Section 1.4.

1.1 Cardiac physiology

The heart, an efficacious and pulsatile organ, operates as the principal driving force of the circulatory system. It weighs roughly 150-320 grams in a healthy adult [23, 24, 25] but the weight differs depending on various factors such as age, sex and physical activity. The cardiac anatomy comprises four chambers, namely the right and left atria and the right and left ventricles, see Fig. 1.1 (a). The atrioventricular valves – known as the mitral and tricuspid valves – are situated between the atria and ventricles. The semilunar valves, which include the aortic and pulmonary valves, are located between the ventricles and the arteries. The heart's walls are composed of three layers, namely the epicardium (thin outer layer), myocardium (thick middle, muscular layer), and endocardium (thin inner layer). The main function of the heart is to pump blood through the body, supplying the organism with oxygen and nutrients while transporting metabolic waste products to the kidneys and liver. The pumping

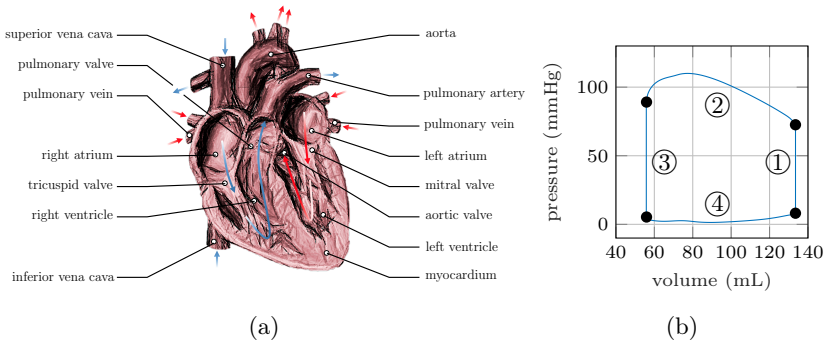

(a) (b)

Figure 1.1: (a) anatomy human heart. (b) pressure-volume-loop left ventricle.

function of the heart involves a cyclic sequence of four phases, see Fig. 1.1 (b): isovolumetric contraction ①, ejection ②, isovolumetric relaxation ③ and a refilling phase ④. In the isovolumetric contraction phase, the atrioventricular valves and semilunar valves remain closed. The oxygenated blood (red arrow) in the left ventricle and deoxygenated blood (blue arrow) in the right ventricle are compressed by the active contraction of the myocardial muscle cells. Due to the nearly incompressible nature of blood, a sudden blood pressure increase occurs while the volume of the left and right ventricle cavities is approximately conserved. As soon as the pressure in the cavities surpasses the pressure in the aorta and pulmonary artery, the semilunar valves open and the ejection phase takes place. Blood is ejected under high pressure and the ejection remains active until a certain volume of blood is ejected (stroke volume) and the ventricular pressure falls below the pressure of the aorta and pulmonary artery, causing the closure of the semilunar valves. This event marks the start of the isovolumetric relaxation state in which the muscle starts to repolarise leading to a further decrease in pressure, while the volume of ventricle cavities are approximately preserved. The filling phase starts when the pressure in the cavities drops below the pressure in the right and left atria, causing the opening of the atrioventricular valves and, subsequently, an inflow of blood from the circulatory system (superior and inferior vena cava and pulmonary veins).

1.2 Computational models – cardiac muscle

The modelling of cardiac tissue has a long history and dates back to the middle of the last century. The first model describing the action and pacemaker potential of the cardiac muscle was developed by Noble in 1960 [26, 27]. This model is based on the Hodgkin and Huxley equations proposed by [28].

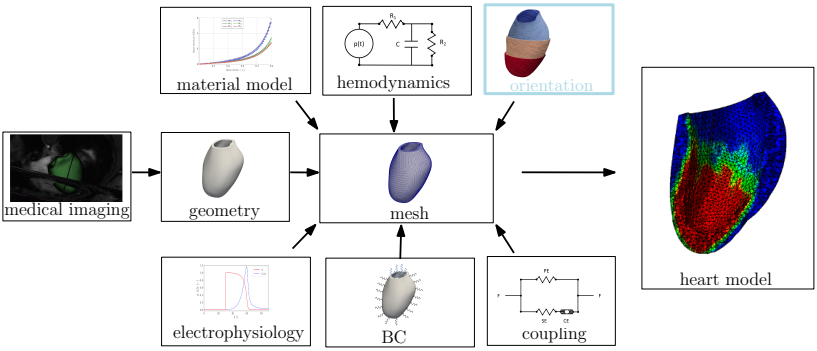

Figure 1.2: Basic workflow of FEM-based cardiac muscle models. The particular focus of this work is on the myocardial tissue structure model and its influence on cardiac function (box with blue frame).

Mechanical models of the cardiac muscle tissue have been initially described based on simplified geometries, e.g. spherical [29, 30], ellipsoidal [31, 32, 33] and cylindrical [34] geometries. First approaches to include the anisotropy of the myocardial tissue with transmurally changing fibre orientation can be found in models by [35, 34]. Earliest FEM-based models have been developed by [36, 37]. In the late 1980s and early 1990s, FEM has gained increasing attention in cardiac modelling [38, 39, 40, 41, 42, 43]. Models advanced through more complex geometries (e.g. biventricular models with detailed fibre orientation and a physical contraction model [44]). Nowadays, FEM models have become the gold standard for patient-specific cardiac modelling. Various FEM models exist, e.g., four chamber heart models including atrial structures [45, 46, 47, 48, 49, 50], patient-specific models of heart valves [51, 52], arrhythmia risk stratification [6, 53], ablation therapy [54], electromechanics [55, 56], model order reduction techniques to reduce the computational costs [57] or models representing atrial mechanics and closed-loop circulation [58, 59, 60]. However, other approaches such as mesh-free methods [61, 62] or smoothed finite element methods (SFEM) [63, 64, 65] have been proposed as alternatives. Reviews on patient-specific cardiovascular computational modelling and computational models in cardiology can be found in [66, 67].
In this thesis, the focus is on a FEM-based model of the cardiac muscle. Therefore, the schematic structure of a FEM-based cardiac muscle model is depicted in Fig. 1.2, exemplified through a patient-specific left ventricular (LV) geometrical model. In the following section, a brief review of the relevant literature concerning the main model blocks from Fig. 1.2 is provided. It is worth noting that the review provided is a condensed summary of significant references pertaining to this work and does not aim to be complete.

Medical imaging, geometry and mesh Over the last decades, the complexity of geometrical models of the heart has increased considerably. Starting with simple geometrical shapes of single cavities, typically the left ventricle *(which generates the primary pumping force)*, researchers have developed anatomically more accurate models based on histoanatomical slices (e.g., for rabbit and canine models see [43, 68]). Moreover, the field of computer-aided design (CAD) has been advancing rapidly, allowing for geometrical models of almost arbitrary complexity. The emergence of image-based models has facilitated the acquisition of complex patient-specific geometrical models, both via in-vivo and ex-vivo measurements. Nowadays, magnetic resonance imaging (MRI) [69, 70, 71, 72, 73], echocardiography [74] and computer tomography [75, 76, 77, 78] are commonly used to obtain patient-specific information about the geometrical properties. Based on the medical imaging data, via manual or automatic segmentation and surface reconstruction, a detailed geometrical model can be derived. Subsequently, the geometrical model is discretised with finite elements by using various types of algorithms, such as Delaunay triangulation [79] or Advancing Front Techniques [80].

Passive material models To characterise the passive material properties of cardiac tissue, various mechanical tests have been performed to develop appropriate passive material models. Biaxial mechanical properties of the passive myocardial tissue (canine/human myocardium) are described for instance in [81, 82, 83, 84]. Nowadays, there is consensus within the biomechanical community that the passive myocardial tissue can be interpreted as an orthotropic material [85, 86, 87, 88]. This assumption is supported by various experimental studies, including the results for the shear properties of passive ventricular myocardium of pig hearts in [89] and biaxial tension/triaxial shear tests of humans in [88]. Over the past few decades, various types of passive material models have been proposed. These are comprised of isotropic [90], transversely isotropic [91, 92, 93, 94] and orthotropic [95, 96, 97, 87] material assumptions.

Electrophysiology Since the pioneering work of Hodgkin and Huxley in 1952 [28], numerous mathematical models have been developed to describe the electrophysiology of the heart. These models can be divided into physiological and phenomenological models. In 1962, a first physiological model of cardiac tissue was developed [26, 27]. Subsequently, various physiologically motivated ionic models have emerged to describe the membrane currents of cardiac cells [98, 99, 100, 101, 102, 103, 104, 105, 106]. Ionic models have numerous applications, including drug testing on a cell drum consisting of three distinct cardiac stem cells [107], as well as drug investigations pertaining to biventricular geometry [53]. However, physiological models are computationally expensive and not well suited, e.g. where phenomena arise across larger spatial

dimensions, such as re-entrant cardiac arrhythmias. Therefore, phenomenological models were developed aiming to capture main characteristics of the cardiac electrophysiology such as the transmembrane potential (TP) evolution, (see [108, 109, 110, 111, 112, 113]), having a significantly fewer equations and unknowns than physiological models. Thus, phenomenological models are less complex, easier to implement and reduce computational costs [114].

Electromechanical coupling A coupling between the TP evolution and passive material response is of fundamental importance to translate a change in TP into an excitation-induced active contraction or relaxation of cardiomyocytes, respectively. Two coupling approaches are commonly used, specifically active stress and active strain approach. The active stress approach, which involves adding an active contribution to the mechanical stress, is the most commonly used method, see [115, 116, 117]. The active strain approach is based on a multiplicative decomposition of the deformation gradient into a passive elastic and an active part, see [118, 119, 120, 114]. A combination of these approaches is proposed, e.g., in [121]. Apart from the excitation-induced contraction of cardiac cells, the depolarisation and, subsequently, the contraction of cardiomyocytes can also be triggered by the opening of ion channels in response to stretching, which is commonly known as mechanoelectrical feedback (MEF) [122, 123]. The MEF can shorten TP duration or the time course of repolarisation [124], break up spiral waves [125] and cause premature ventricular excitation [126, 127]. This phenomenon assumes a crucial role in elucidating the intricate interrelationship between the electrophysiological and mechanical mechanisms of cardiomyocytes [128, 129]. Often, electromechanical simulations are solved in a decoupled manner [130, 46] or staggered approach for one-way coupling formulations [131, 132, 128, 133]. To study the effect of the MEF, strongly coupled models are required [115, 134, 135, 136].

Haemodynamics The most common approaches to modelling haemodynamics for FEM-based cardiac models can be divided into computational fluid dynamics (CFD) [137], fluid-structure interaction (FSI) [138] or lumped parameter [139] models. With the advancement of medical imaging technologies and therewith accurate geometrical models, CFD and FSI have gained increasing attention. CFD models, which are based on the Navier-Stokes equations, can be used to determine detailed information about blood pressure, pressure gradients, velocities, wall shear stresses, the effects of arterial geometry etc. FSI models, on the other hand, couple fluid dynamics with structural mechanics to simulate the interactions arising between blood flow and the surrounding tissues to gain insight into mechanical properties such as deformation and stress distribution in the tissue or to study the effects of haemodynamic factors on the development and rupture of cerebral or aortic aneurysms [140]. However, for certain research

questions, it may not be necessary to employ highly detailed CFD or FSI models. Rather, simplified lumped parameter models that accurately capture the pressure-flow relationship of the circulatory system may be adequate. These models can be especially useful in substituting computationally costly FSI/CFD models if detailed information about the blood flow/fluid-tissue interaction is not required. Windkessel models are a well-known class of lumped parameter models. These describe the cardiovascular system as being analogous to an electrical circuit with resistors and capacitors. The most commonly used Windkessel models are the two-element and the three-element models [139]. These models are often used to study the dynamics of arterial pressure and blood flow, estimate cardiac output in patients with heart failure or analyse the effects of arterial stiffness on blood pressure and cardiac function.

Mechanical boundary conditions The definition of physiologically accurate mechanical and electrical boundary conditions (BCs) in a FEM-based cardiac model is essential to obtain meaningful simulation results. Mechanical BCs basically comprise two physiological mechanisms, namely blood flow within the chambers (blood pressure and shear stresses acting on the endocardium) and external support of the cardiac muscle (elastic properties of the surrounding structures including pericardium acting on the epicardium as well as the connection to the great vessels such as the aorta, pulmonary arteries and veins, superior and inferior vena cava). However, for computational models of single ventricles, often simplified BCs are defined. For the simulation of the left ventricle (represented by truncated ellipsoidal geometry), the outer baseline is spatially fixed so only in-plane movement of the base surface is assumed [141]. Multiple BCs exist for the pericardium, e.g. a no penetration condition [142, 143], constraining movement in the normal direction of the epicardial surface [135] or spring-dashpot systems on the epicardial and base surfaces [130] for truncated geometries (see [144, 60]). Commonly used BCs for four-chamber geometries involve a combination of Dirichlet BCs applied at the cut-off region of the vessels, an elastic apical boundary condition [142, 145] or springs attached to the great vessels [146]. In [46], connector elements are applied on the epicardial surface, thereby constraining the movement along the pericardial–epicardial surface. In [147], the pericardial–myocardial interaction is modelled via frictionless sliding.

Electrical boundary conditions The heart's electric activation begins in the sinoatrial node in the right atrium and spreads through the atria before reaching the atrioventricular node. The atrioventricular node connects to the Purkinje network through the bundle of His (after the cardiologist Wilhelm His) which branches throughout the ventricles. In computational models, the electrical activation is modelled with different levels of complexity, for instance, models

of the Purkinje network via a fractal tree algorithm [148, 149] or cardiac activation mapping (e.g., via neural networks [150]). Furthermore, surrogate models of the Purkinje network exist, e.g. via faster electrical conduction on endocardial structures [59] or the detection of Purkinje network junctions locations from electrical measurements [151, 152].

Orthotropic tissue structure In a FEM-based cardiac model, the specific tissue structure of the myocardium, atria, vessels, etc. needs to be taken into account. The orthotropic myocardial tissue comprises a distinct fibre direction $\boldsymbol{f}$, sheet normal direction $\boldsymbol{n}$ and sheet direction $\boldsymbol{s}$, which constitute a right-handed orthonormal coordinate system, see Fig. 1.3 (c) and [87]. The fibre and sheet direction vary transmurally from the endocardium to the epicardium. This variation can be observed via histological studies [153, 154, 33, 85, 155], diffusion tensor magnetic resonance imaging (DT-MRI) [86, 156, 69, 157, 158], elastography [159], ultrasound [160], micro computed tomography or X-ray phase contrast [161, 162]. Numerous tissue structure models (TSMs) have been developed to compute the characteristic orthotropic tissue structure in computational heart models. Nowadays, the most widely used methods for assigning an orthotropic structure to a finite element model of the myocardium, atria or whole organ, are either image-based [158, 71, 163, 72, 164] or rule-based [165, 166, 85, 167, 166, 168, 169, 170, 171]. Rule-based methods (RBMs) have to be used, wherever no direct mapping from the measurement onto the finite element model is possible or else available (this depends on noise effects, the complexity of the geometry, measurement technique, etc.). These methods/algorithms are denoted "rule-based" as they describe the orthotropic tissue structure with mathematically formulated rules which are, in turn, based on experimental observations. However, RBMs lead to a certain method-specific orthotropic tissue structure, which subsequently influences the heart simulation. Various studies show the decisive influence of the orthotropic tissue orientation on the mechanical and electrical function of the heart (see [172, 173, 174, 175, 176, 177]). Moreover, the tissue structure can be altered during cardiac failure or disease [71, 178, 179]. Therefore, a precise definition of the orthotropic tissue structure in FEM-based cardiac models is indispensable. As shown in Fig. 1.3 (b) and (c), the rules in RBMs are often describing the change in fibre angle α and/or sheet angle β along the transmural path (i.e., the path through the wall from the endocardial to epicardial surface). The arc length of this path is commonly normalised and termed the so-called normalised transmural depth $d \in [0, 1]$, see Fig. 1.3 (b). The normalised transmural depth assigns to each material point in the myocardium a scalar value between 0 and 1 (0 on endocardium, 1 on epicardium). The transmural evolutions in fibre angle α and sheet angle β are defined with respect to an orthonormal reference coordinate system, e.g. $\boldsymbol{c}, \boldsymbol{l}, \boldsymbol{r}$ corresponding to the circumferential,

longitudinal and radial directions, respectively. In summary, the following ingredients are required to compute the rule-based local orthotropic tissue orientation $\boldsymbol{f}$, $\boldsymbol{n}$ and $\boldsymbol{s}$:

- a local reference coordinate system $\boldsymbol{c}$, $\boldsymbol{l}$, $\boldsymbol{r}$
- normalised transmural depth d
- rules for the fibre angle α and sheet angle β over d

Various approaches to defining the longitudinal direction $\boldsymbol{l}$ exist, for instance, a globally constant [168] or local [167, 169, 171] longitudinal direction. This simplification of a globally constant longitudinal direction can lead to inaccuracies or singularities in geometrically complex regions of the heart (e.g., owing to endocardial structures), as also described in [167]. The local transmural direction $\boldsymbol{r}$ can be determined based on various approaches (e.g., the most proximal distance to the endo- and epicardium), 3-D distance transform algorithm [165, 163] or by using the Laplace equation [167, 169, 171]. Finally, the circumferential direction $\boldsymbol{c}$ follows as $\boldsymbol{c} = \boldsymbol{l} \times \boldsymbol{r}$.
In the last decade, a subgroup of RBMs, namely Laplace-Dirichlet-Rule-Based-Methods (LDRBMs), has been developed (e.g., by [167, 168, 169, 171]), which provide a smoothly varying local material coordinate system, even for complex geometries, see also Fig. 1.3 (a). Laplace's equation is utilised to directly compute the transmural depth d [167, 169, 171] or to interpolate vector coordinates of $\boldsymbol{f}$, $\boldsymbol{n}$ or $\boldsymbol{s}$ [168]. However, for complex geometries, Laplace's equation neither accurately determines the transmural depth d, nor ensures a geometrically appropriate interpolation of vector coordinates.
The development of a new robust, efficient and accurate LDRBMs motivates the first objective of this thesis, see objective I.I.A.-D. in Section 1.4. The LDRBM is based on a computational model to accurately assess the transmural depth d on unstructured 3D finite element meshes (objective I.I.A.). The transmural depth model is founded on a novel computational framework to accurately determine the arc length of the transmural path (i.e., the wall thickness of the myocardium) (objective I.I.B.). The proposed framework can be used to efficiently and accurately determine the wall thickness for arbitrary 3D geometries of ventricles, atria, vessels, which can be beneficial for clinicians, as wall thickness serves as a crucial risk indicator for a variety of cardiac diseases. Further, the proposed LDRBM includes novel regional transmural fibre/sheet angle rules for the left ventricle based on DT-MRI data (objective I.I.C.). Finally, the developed LDRBM is compared with established LDRBMs (objective I.I.D.). Objective I.I.A.-D. is mainly covered by Chapter 3 in this thesis.
Besides a methodological comparison of different LDRBMs (objective I.I. D.), there is, so far, a lack of comparison among these methods in the context of electromechanical simulation. Only in [171], three different LDRBMs are compared based on a biventricular electromechanical model. To further explore

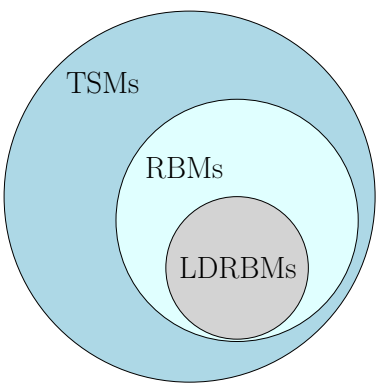

(a) groups of tissue structure models (TSMs).

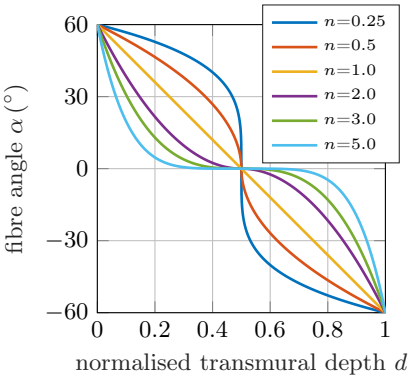

(b) fibre function α.

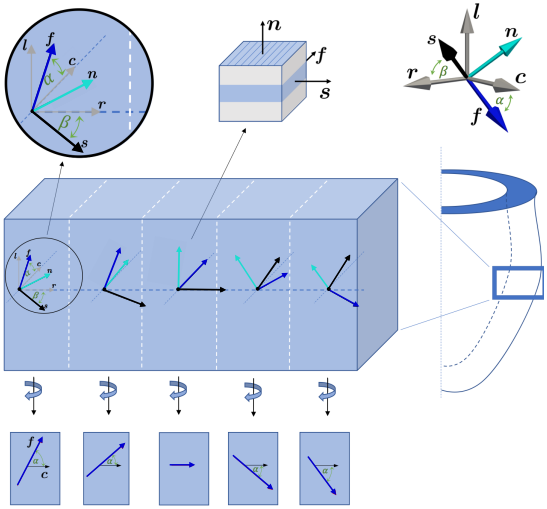

(c) local tissue structure.

Figure 1.3: (a) rule-based methods (RBMs) and Laplace-Dirichlet-Rule-Based-Method (LDRBM) as subgroups of tissue structure models (TSMs) for cardiac simulation. (b) transmural fibre angle based on rule given in e.g. [166]. (c) The cardiac tissue structure with a distinct fibre direction $\boldsymbol{f}$, sheet normal direction $\boldsymbol{n}$ and sheet direction $\boldsymbol{s}$. The fibre angle α and sheet angle β vary along the transmural path. The fibre and sheet angles are defined with respect to a local orthonormal reference coordinate system $\boldsymbol{c}, \boldsymbol{l}, \boldsymbol{r}$.

the extent, to which LDRBM-based orthotropic tissue structures influence the electromechanical characteristics of the cardiac model, motivates objective I.II. In detail, this study investigates the influence of different LDRBMs on important characteristics of cardiac function, based on an electromechanical model of the cardiac tissue. The electromechanical model is equipped with three different LDRBMs ([167], [168] and the developed LDRBM in this work). The quantitative comparison is based on the distinct characteristic orthotropic tissue structure of the three LDRBMs, global (ejection fraction, peak pressure, apex shortening, myocardial volume reduction, and pressure-volume loops) and local (active fibre stress, fibre strain) characteristics. Objective I.II. is mainly covered by Chapter 4 and 5 in this thesis. It is worth noting that Chapter 3, 4 and 5 are to a great extent based on [170, 180].

1.3 Computational models – DEA artificial muscles in cardiac application

If conservative therapies are insufficient to treat the pathology of the heart, dysfunctions that can be caused by a variety of diseases (e.g., myocardial infarction (MI), congenital heart failure or cardiomyopathy), there are usually only two options to counter such a life-threatening condition – specifically the use of a CaAD or heart transplantation. However, there is a systemically chronic shortage of donors. In Germany, only 329 patients received a donor heart in 2021 although 727 patients were waiting on the transplant list[1]. While heart transplantation is still superior in terms of survival and functional capacity, significant improvements in the field of CaADs present a promising solution by which to close the gap between availability and demand for donor hearts [181, 182]. Over the last decades, various types of mechanical pumping systems (ventricular assist devices (VADs)) have been developed [183]. These are used as an invasive form of therapy to directly support blood circulation. In principle, these systems mostly work as a bypass in cases of cardiac insufficiency. The usage of such VADs can relieve the load on the heart and allows a short to medium-term alleviation of cardiac insufficiency until transplantation (bridge-to-transplantation) and may even be used as a permanent solution (destination therapy) [184].
Despite the fact that the development of new devices is rapid and post-surgery survival and functional capacity now approaches that of heart transplantation, there are still many complications to solve including bleeding, coagulation *(anti-coagulants are used to avoid blood clots and thus strokes)*, infection *(especially caused by the driveline connecting the control unit with the pump)* and electrolyte disorders [185, 186, 187, 188]. However, wireless energy transfer technology in conjunction with rapidly evolving battery technologies can reduce

[1] https://www.organspende-info.de

the risk of infections (as they employ no driveline) [189, 190, 191]. Additionally, the existing devices are already developed further by miniaturisation to place the whole system inside the thorax. By addressing the aforementioned issues, future CaADs may outperform heart transplantations and thereby solve the systemically-related chronic shortage of donors. As previously mentioned, one promising approach which has gained increasing attention, especially over the past decade, is the use of artificial muscles based on DEAs which serve as cardiac assist devices (CaADs).

The modelling of dielectric elastomer actuators has a long history. Initial theoretical discussions on various electromechanically coupled field theories are to be found in [192, 193, 194, 195, 196]. More recently, [197, 198, 199, 200] dealt with coupling effects concerning magnetoelasticity and electroelasticity. First, finite element implementations can be found in [201, 202, 203, 204]. As dielectric materials exhibit viscoelastic characteristics, [205, 206, 207, 208] introduced viscoelastic terms to account for the dynamic behaviour of dielectric elastomers. In [209], the electromechanical finite element model from [204] is extended by inertia terms and a variational time integration scheme is derived in the Lagrangian setting. The stretch-dependent permittivity of acrylic dielectric elastomers and the associated consequences for a reduced lumped parameter model are discussed in [210], and in [211] optimal control problems for dielectric elastomer actuated multibody systems are solved based on a reduced lumped parameter model for stacked actuators. The incompressibility of dielectric elastomers and associated numerical difficulties are discussed in [212, 213, 214]. The mentioned FEM serve as a highly effective toolset for solving problems that involve electromechanical coupling phenomena, however, the numerical solving is computationally costly [211].

To support the heart during the course of the cardiac cycle in real-time, the active control of the CaAD based on DEAs occurs on a short timescale, necessitating the use of computationally efficient methods (e.g., lumped parameter models [210, 211]). Today, a very limited number of artificial muscle models based on DEAs for cardiac application exist. In [14, 215], an analytical model of a tubular DEA has been proposed for the ascending and descending aorta. In [216, 184], the cardiac function of a diseased heart suffering from restrictive cardiomyopathy was investigated by imitating the diseased tissue through a reduced contraction/stiffer tissue response and supporting the heart via epicardial pressure during diastole and systole. However, the pressure-generating system has not yet been modelled.

In Fig. 1.4, potential applications of DEA-based CaADs are depicted. The general idea is based on thin and curved structures (e.g., to augment the ventricular or aortic functions). From a mechanical point of view, this motivates to model DEA-based CaADs as structural elements such as shells, which are well suited since they capture complex geometries for patient-specific device design, save computational time as compared to 3D FEM, allow for simpli-

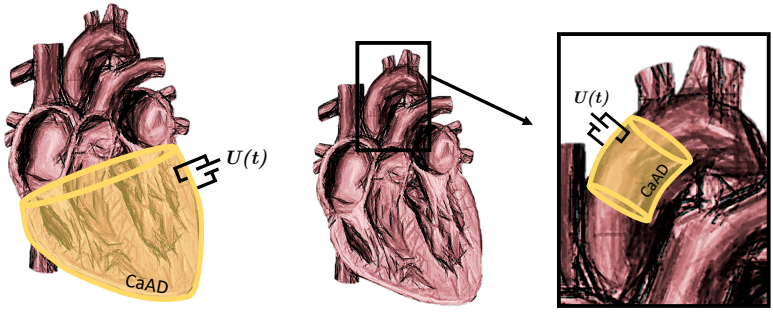

(a) ventricular support. (b) aortic support.

Figure 1.4: (a) DEA-based CaAD – ventricles. (b) DEA-based CaAD – aorta.

fied meshing algorithms compared to volume meshes, are easy to integrate into multibody systems and optimal control problems, and are less prone to negative Jacobian errors.
Various types of shell formulations exist, including kinematics (Mindlin-Reissner, Kirchhoff-Love), fields (mechanical, electrical, electromechanical), variational principles (virtual work, Hellinger-Reissner, Hu-Washizu), and static and dynamic formulations. In [217], a solid shell finite element formulation for dielectric elastomers is proposed. A review on Cosserat-type theories for plates and shells is given in [218]. In [219], thermodynamic effects in Cosserat shells are discussed. The incorporation of a geometrically exact shell model into multibody dynamics is described ([220, 221]. A promising approach for a structural element formulation of dielectric materials can be found in [222], where a dynamic, viscoelastic, electromechanically coupled beam model is developed including variational time integration and null space projection. Additionally, in [223], the beam model is used in optimal control simulation of dielectric elastomer actuated multibody systems.
However, to the best of our knowledge, a dynamic, viscoelastic, electromechanically coupled shell formulation based on a variational time integration scheme has yet to be developed. Therefore, the development of a dynamic, viscoelastic, electromechanically coupled shell formulation based on a variational time integration scheme motivates the second part of this thesis (objective II.I.A.-D.). Further, to demonstrate the potential of the model, numerical examples including different geometries as well as deformation states are presented (objective II.II.).

1.4 Objectives and outline of this work

This section provides an overview of the defined objectives of this thesis. More details about the definition of the objectives can be found in the previous Sections 1.2 and 1.3. Note that objectives I.I. and I.II. are, to a great extent, based on [170, 180]. In [170, 180], the doctoral candidate contributed by conceptualisation, methodology, software, formal analysis, writing - original draft, and visualisation of the studies.

Cardiac muscle model

I.I. Development of a robust, efficient and accurate Laplace-Dirichlet-Rule-Based-Method (LDRBM) – [170].

- A. Computational model to accurately assess the transmural depth on unstructured 3D finite element meshes.
- B. Integration of wall thickness assessment.
- C. Development of regional transmural fibre and sheet angle rules for the left ventricle based on DT-MRI measurements.
- D. Comparison of the proposed method with established LDRBMs.

I.II. Electromechanical model of the cardiac tissue and study about the influence of orthotropic tissue orientation on overall cardiac function based on defined cardiac characteristics – [180].

Artificial muscle model

II.I. Development of a shell model for dielectric elastomer actuators (DEAs) as CaAD including:

- A. dynamics;
- B. viscoelasticity;
- C. electromechanical coupling; and,
- D. structure-preserving time integration.

II.II. Implementation and numerical examples of the derived shell formulation.

This thesis is structured as follows: In Chapter 2, a short introduction into continuum mechanics and the finite element method is given. The novel LDRBM is presented in Chapter 3, see (I.I.A.-D.). In Chapter 4 and 5, the electromechanical model of the cardiac tissue is introduced and the influence of the orthotropic tissue on cardiac function is studied, see (I.II.). In Chapters 6 and 7, the shell formulation is derived (II.I.), implemented and numerical examples are presented (II.II.). The work concludes with Chapter 8, which discusses the findings, relevance, and future prospects for this work.

2 Background – cardiac muscle model

In the following chapter, the basic concepts of continuum mechanics as well as the continuous and discontinuous Galerkin FEM are briefly introduced. These concepts are important in the subsequent Chapters 3, 4 and 5. Since this Chapter presents a concise overview, please refer to the standard literature for a detailed description of continuum mechanics [224, 225, 226] and FEM [227, 228, 229, 230, 231, 232, 233, 234, 235].

In Section 2.1, the fundamental equations and relevant quantities of continuum mechanics are introduced. Additionally, in Section 2.2, a brief discussion of the basic concept of FEM is provided and the difference between the continuous and discontinuous Galerkin FEM is highlighted.

2.1 Continuum mechanics and electromechanics

The basic assumption in continuum mechanics is that materials can be described as a continuous mass. Therefore, the concept neglects the fact that every matter consists of atoms (discrete particles) and is obviously not continuous. However, on a significantly larger scale than the atomistic level, continuum mechanics is able to accurately describe the mechanical behaviour of matter. The basic equations in continuum mechanics can be subdivided into the kinematic description (Section 2.1.1), balance equations (Section 2.1.2) and constitutive laws (Section 2.1.3).

2.1.1 Kinematics

The kinematics in continuum mechanics geometrically describes the motion and deformation of a body by taking into account the time, space, velocity and acceleration without considering the cause of the motion (i.e., forces, mass, etc). In the following, the important quantities, namely the deformation map and deformation gradient are introduced, followed by the definition of some fundamental strain measures.

Deformation map Figure 2.1 represents the basic finite deformation map between the initial configuration (also known as material or undeformed configuration) and current configuration (also known as spatial or deformed configuration). The deformation map describes the relation between the initial configuration $\mathcal{B}_0$ and the current configuration $\mathcal{B}_t$. At the initial time t_0, the

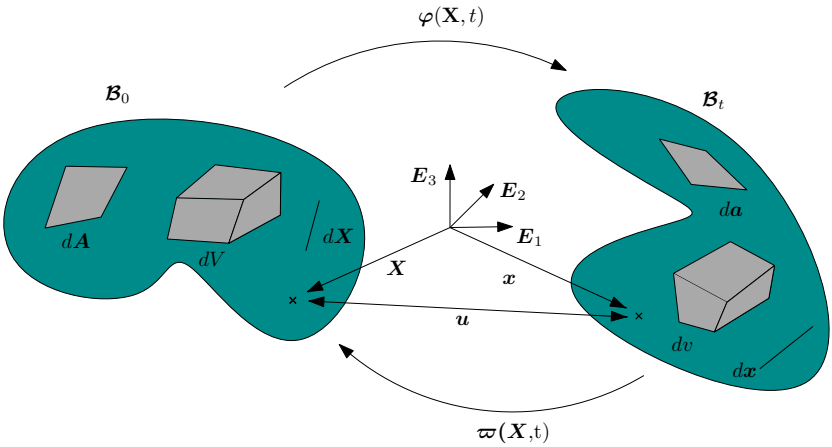

Figure 2.1: Deformation maps $\boldsymbol{\varphi}(\boldsymbol{X},t)$ and $\boldsymbol{\varpi}(\boldsymbol{x},t)$ between initial and current configuration.

position of a considered material point in the undeformed configuration $\mathcal{B}_0$ is described by the position vector $\boldsymbol{X} \in \mathbb{R}^3$. At the current time t, the position of the material point in the deformed configuration $\mathcal{B}_t$ is described by the position vector $\boldsymbol{x} \in \mathbb{R}^3$. To map the material point from the undeformed configuration $\mathcal{B}_0$ to the deformed configuration $\mathcal{B}_t$, a nonlinear deformation map $\boldsymbol{\varphi}(\boldsymbol{X},t)$ is defined. The Lagrangian description of the motion reads

$$\boldsymbol{x} = \boldsymbol{\varphi}(\boldsymbol{X},t) \quad \text{with} \quad \boldsymbol{\varphi} : \mathcal{B}_0 \to \mathcal{B}_\mathrm{t}, \tag{2.1}$$

where $\mathcal{B}_0, \mathcal{B}_\mathrm{t} \subseteq \mathbb{R}^3$. Similarly, the inverse nonlinear deformation map $\boldsymbol{\varpi}$ from the deformed to the undeformed configuration, called the Eulerian description of motion, is defined as

$$\boldsymbol{X} = \boldsymbol{\varpi}(\boldsymbol{x},t) \quad \text{with} \quad \boldsymbol{\varpi} : \mathcal{B}_\mathrm{t} \to \mathcal{B}_0. \tag{2.2}$$

Based on the Lagrangian description, the displacement field $\boldsymbol{u}$ is determined by the difference between the current position vector $\boldsymbol{x}$ and the initial position vector $\boldsymbol{X}$

$$\boldsymbol{u}(\boldsymbol{X},t) = \boldsymbol{\varphi}(\boldsymbol{X},t) - \boldsymbol{X}. \tag{2.3}$$

Deformation gradient The deformation gradient $\mathbf{F}(\boldsymbol{X},t)$, which characterises the local deformation at a material point $\boldsymbol{X}$, is given as

$$\mathbf{F}(\boldsymbol{X},t) = \nabla_\mathrm{X} \boldsymbol{\varphi}(\boldsymbol{X},t) \tag{2.4}$$

$$= \mathbf{I} + \nabla_\mathrm{X} \boldsymbol{u}(\boldsymbol{X},t) \quad \text{with} \quad \mathbf{F} : T\mathcal{B}_0 \to T\mathcal{B}_\mathrm{t}, \tag{2.5}$$

where $T\mathcal{B}_0, T\mathcal{B}_t$ are the initial and current tangent spaces, respectively. With the deformation gradient $\mathbf{F}(\boldsymbol{X}, t)$, the Jacobian $J = \det(\mathbf{F}) > 0$, the initial and current outward unit surface normals $\boldsymbol{N} \in \mathbb{R}^3$ and $\boldsymbol{n} \in \mathbb{R}^3$ on the boundaries $\partial\mathcal{B}_0$ and $\partial\mathcal{B}_t$ and the Nanson's formula at hand, the transformation of an arbitrary line element $d\boldsymbol{X}$, area element dA and volume element dV from the initial configuration $\mathcal{B}_0$ to the current configuration $\mathcal{B}_t$ can be written as

$$(line\ element) \qquad d\boldsymbol{x} = \mathbf{F} \cdot d\boldsymbol{X}, \tag{2.6}$$

$$(area\ element,\ Nanson's\ formula) \qquad da\ \boldsymbol{n} = J\ dA\ \mathbf{F}^{-t} \cdot \boldsymbol{N}, \tag{2.7}$$

$$(volume\ element) \qquad dv = J\ dV, \tag{2.8}$$

see also Fig. 2.1.

Strain measures In case of large deformation (nonlinear theory), deformation measures such as the Green-Lagrange strain $\mathbf{E}$ are defined. The Green-Lagrange strain reads

$$\mathbf{E} = \frac{1}{2}[\mathbf{F}^T \cdot \mathbf{F} - \mathbf{I}] = \frac{1}{2}[\mathbf{C} - \mathbf{I}], \tag{2.9}$$

where the right Cauchy-Green tensor $\mathbf{C} = \mathbf{F}^T \cdot \mathbf{F}$ and $\mathbf{I}$ is the unit tensor. A multiplicative decomposition of the deformation gradient into a volumetric $(\bullet)^\circ$ and isochoric $(\bullet)^\diamond$ part is introduced for incompressible or nearly incompressible materials

$$\boldsymbol{F} = \mathbf{F}^\circ \cdot \mathbf{F}^\diamond, \tag{2.10}$$

with $\boldsymbol{F}^\circ = J^{1/3}\mathbf{I}$, $\boldsymbol{F}^\diamond = J^{-1/3}\boldsymbol{F}$ and $\mathbf{C}^\diamond = \boldsymbol{F}^{\diamond T} \cdot \boldsymbol{F}^\diamond$.

Time derivatives In order to describe dynamic effects (e.g. viscous material behaviour), velocities and accelerations have to be taken into account. The velocity and acceleration of a material point $\boldsymbol{X}$ are defined as

$$\dot{\boldsymbol{x}} = \dot{\boldsymbol{\varphi}}(\boldsymbol{X}, t) = \frac{d\,\boldsymbol{\varphi}}{dt}, \tag{2.11}$$

$$\ddot{\boldsymbol{x}} = \ddot{\boldsymbol{\varphi}}(\boldsymbol{X}, t) = \frac{d\,\dot{\boldsymbol{\varphi}}}{dt}. \tag{2.12}$$

The time derivative of the deformation gradient $\mathbf{F}$ is given as

$$\dot{\mathbf{F}}(\boldsymbol{X}, t) = \nabla_{\mathrm{X}} \dot{\boldsymbol{\varphi}}(\boldsymbol{X}, t). \tag{2.13}$$

2.1.2 Balance equations

The fundamental balance equation states that for an arbitrary domain $\mathcal{B}_0$, the temporal change of a balance quantity $(\triangle)_0$ in $\mathcal{B}_0$ is equal to the sum of all source terms $(\odot)_0$ in $\mathcal{B}_0$ and flux terms $(\blacksquare)_0 \cdot \boldsymbol{N}$ on the boundary $\partial\mathcal{B}_0$. In the reference configuration, the fundamental balance equation can be written as

$$\dot{\overline{\int_{\mathcal{B}_0} (\triangle)_0 \, dV}} = \int_{\mathcal{B}_0} (\odot)_0 \, dV + \int_{\partial\mathcal{B}_0} (\blacksquare)_0 \cdot \boldsymbol{N} \, dA. \tag{2.14}$$

By applying the divergence theorem and assuming that Eq. (2.14) has to hold for any arbitrary region $\mathcal{B}_0$, the local form is defined as

$$(\dot{\triangle})_0 - (\odot)_0 - \nabla_{\boldsymbol{X}} \cdot ((\blacksquare)_0) = 0 \quad \forall \boldsymbol{X} \in \mathcal{B}_0. \tag{2.15}$$

Based on Eq. (2.14), the mechanical balance equations (conservation of mass, balance of linear momentum, balance of angular momentum) and electrical balance equation are briefly discussed in the following.

Conservation of mass In this work, the total mass m in the system is conserved. Thus, the source and flux terms in Eq. (2.14) vanish and the local balance of mass reads

$$\dot{\rho}_0 = 0 \quad \forall \boldsymbol{X} \in \mathcal{B}_0, \tag{2.16}$$

where ρ_0 is the material density in the domain.

Balance of linear momentum The balance of linear momentum in material form reads

$$\nabla_{\boldsymbol{X}} \cdot \mathbf{P} + \boldsymbol{B}_0 = \rho_0 \ddot{\boldsymbol{x}} \quad \forall \boldsymbol{X} \in \mathcal{B}_0, \tag{2.17}$$

where $\mathbf{P} \in \mathbb{R}^{3\times3}$ is the first Piola-Kirchhoff stress tensor and $\boldsymbol{B}_0$ is the body force vector. The first Piola-Kirchhoff stress tensor $\mathbf{P}$ is defined such that the traction vector $\boldsymbol{T}(\boldsymbol{X}, t, \boldsymbol{N}) = \mathbf{P}(\boldsymbol{X}, t) \cdot \boldsymbol{N}$. The first Piola-Kirchhoff stress tensor $\mathbf{P}$ is related to the well-known stress measure in the current configuration $\boldsymbol{\sigma}$ (Cauchy stress tensor) by the transformation $\mathbf{P} = J\,\boldsymbol{\sigma} \cdot \mathbf{F}^{-T}$. Another important stress measure is the second Piola-Kirchhoff stress tensor $\mathbf{S} = J\mathbf{F}^{-1} \cdot \sigma \cdot \mathbf{F}^{-T} = \mathbf{F}^{-1}\mathbf{P}$.

Balance of angular momentum The local balance of angular momentum yields

$$\mathbf{F} \cdot \mathbf{P}^T = \mathbf{P} \cdot \mathbf{F}^T \quad \forall \boldsymbol{X} \in \mathcal{B}_0, \tag{2.18}$$

which implies that the spatial Cauchy stress tensor $\boldsymbol{\sigma} = J^{-1}\mathbf{P} \cdot \mathbf{F}^T$ is symmetric, while the first Piola-Kirchhoff stress tensor $\mathbf{P}$ is not in general (Cauchy's stress theorem). It is worth noting that the second Piola-Kirchhoff stress tensor $\mathbf{S}$ is symmetric.

Electrical balance equation The electrical field is described by the spatiotemporal evolution of the transmembrane potential Φ and reads

$$\nabla_{\boldsymbol{X}} \cdot \boldsymbol{Q} + F^{\Phi} = \dot{\Phi} \quad \forall \boldsymbol{X} \in \mathcal{B}_0, \tag{2.19}$$

where $\dot{\Phi}$ denotes the material time derivative of the transmembrane potential, $\boldsymbol{Q}$ is the electrical flux and F^{Φ} is the nonlinear current source term. The electrical flux $\boldsymbol{Q}$ is defined as $\boldsymbol{Q} = \mathbf{D} \cdot \nabla \Phi$, where the anisotropic conductivity tensor is given as $\mathbf{D} = d_{iso}\mathbf{I} + d_{ani}\boldsymbol{f}_0 \otimes \boldsymbol{f}_0$, with $\boldsymbol{f}_0$ being the fibre orientation in the reference configuration.

2.1.3 Constitutive laws

In the following, the constitutive equations for the active mechanics, as well as the electrophysiology and mechano-electrical feedback (MEF), are introduced. A more detailed description can be found in the corresponding Chapter 4.

Active and passive mechanics In the material configuration, the second Piola-Kirchhoff stress tensor $\mathbf{S}$ is additively decomposed into a passive part $\mathbf{S}^{\text{pas}}$ and an active part $\mathbf{S}^{\text{act}}$, see e.g. [121],

$$\mathbf{S} = \mathbf{S}^{\text{pas}} + \mathbf{S}^{\text{act}}. \tag{2.20}$$

In this work, a hyperelastic material model is used to capture the mechanical behaviour of the cardiac muscle tissue. The strain energy density function Ψ is subdivided into a passive and an active part, namely Ψ_{pas} and Ψ_{act}, respectively. The passive and active part of the second Piola-Kirchhoff stress tensor $\mathbf{S}$ are defined as the derivative of the strain energy density function w.r.t. the right Cauchy-Green tensor $\mathbf{C}$

$$\mathbf{S}^{\text{pas}} = 2\frac{\partial \Psi_{\text{pas}}}{\partial \mathbf{C}}, \qquad \mathbf{S}^{\text{act}} = 2\frac{\partial \Psi_{\text{act}}}{\partial \mathbf{C}}. \tag{2.21}$$

Electrophysiology and mechano-electrical feedback (MEF) The term F^{Φ} in Eq. (2.19) is additively decomposed into an electrically induced source term F_e^{Φ} and a mechanically induced source term F_m^{Φ}. The source term F_m^{Φ} accounts for the electric potential generation due to mechanical deformation (MEF). Consequently, the nonlinear source term F^{Φ} reads

$$F^{\Phi} = F_e^{\Phi} + F_m^{\Phi}. \tag{2.22}$$

In general, the electromechanical problem consisting of the balance of linear momentum in Eq. (2.17), the electrical balance equation in Eq. (2.19), constitutive laws in Eq. (2.20)–(2.22) cannot be solved analytically and require spatial and temporal discretisation. In this work, the FEM is utilised for the spatial discretisation and its basic concept will be introduced in the following.

2.2 Finite element method

For the spatial finite element discretisation of the electromechanical problem, the strong forms in Eq. (2.17) and Eq. (2.19) have to be transformed into an integral form (weak form).

Weak formulation The integral form is obtained by multiplying the considered strong forms in Eq. (2.17) and Eq. (2.19) with a test function, integrating over the computational domain, integration by parts, applying the divergence theorem, satisfying the essential boundary conditions ($\delta\boldsymbol{\varphi} = \mathbf{0}$ on $\partial_u\mathcal{B}_0$, $\delta\Phi = 0$ on $\partial_\Phi\mathcal{B}_0$) and applying the Neumann boundary conditions ($\hat{\boldsymbol{T}} = \mathbf{P}\cdot\boldsymbol{N} = \boldsymbol{T}$ on $\partial_T\mathcal{B}_0$, $\hat{Q} = \boldsymbol{Q}\cdot\boldsymbol{N} = Q$ on $\partial_Q\mathcal{B}_0$). The corresponding weak forms for the mechanical and electrical field are given as

$$\int_{\mathcal{B}_0} \delta\boldsymbol{\varphi}\cdot\rho_0\ddot{\boldsymbol{\varphi}}\;dV + \int_{\mathcal{B}_0} \nabla_{\boldsymbol{X}}(\delta\boldsymbol{\varphi}) : \mathbf{P}\;dV - \int_{\mathcal{B}_0} \delta\boldsymbol{\varphi}\cdot\boldsymbol{B}_0\;dV - \int_{\partial_T\mathcal{B}_0} \delta\boldsymbol{\varphi}\cdot\hat{\boldsymbol{T}}\;dA = 0, \tag{2.23}$$

$$\int_{\mathcal{B}_0} \delta\Phi\,\dot{\Phi}\;dV + \int_{\mathcal{B}_0} \nabla_{\boldsymbol{X}}(\delta\Phi)\cdot\boldsymbol{Q}\;dV - \int_{\mathcal{B}_0} \delta\Phi F^{\Phi}\;dV - \int_{\partial_Q\mathcal{B}_0} \delta\Phi\hat{Q}\;dA = 0, \tag{2.24}$$

where $\delta\boldsymbol{\varphi}$ and $\delta\Phi$ represent the vector- and scalar-valued test functions for the mechanical and electrical weak forms, respectively. Subsequently, the nonlinear weak forms in Eq. (2.23) and Eq. (2.24) need to be linearised and discretised.

Linearisation Rewriting Eq. (2.23) and Eq. (2.24) in terms of residuals

$$r^{\varphi} = 0, \tag{2.25}$$

$$r^{\Phi} = 0, \tag{2.26}$$

the linearisation of Eq. (2.25) is given by the derivative with respect to $\boldsymbol{\varphi}$ and Φ

$$\triangle r^{\varphi\varphi} = \frac{\partial r^{\varphi}(\boldsymbol{\varphi},\Phi)}{\partial\boldsymbol{\varphi}}\cdot\triangle\boldsymbol{\varphi} = \boldsymbol{K}^{\varphi\varphi}\cdot\triangle\boldsymbol{\varphi}, \tag{2.27}$$

$$\triangle r^{\varphi\Phi} = \frac{\partial r^{\varphi}(\boldsymbol{\varphi},\Phi)}{\partial\Phi}\cdot\triangle\Phi = K^{\varphi\Phi}\cdot\triangle\Phi. \tag{2.28}$$

The linearisation of Eq. (2.26) follows analogously and reads

$$\triangle r^{\Phi\varphi} = \frac{\partial r^{\Phi}(\boldsymbol{\varphi},\Phi)}{\partial\boldsymbol{\varphi}}\cdot\triangle\boldsymbol{\varphi} = \boldsymbol{K}^{\Phi\varphi}\cdot\triangle\boldsymbol{\varphi}, \tag{2.29}$$

$$\triangle r^{\Phi\Phi} = \frac{\partial r^{\Phi}(\boldsymbol{\varphi},\Phi)}{\partial\Phi}\cdot\triangle\Phi = K^{\Phi\Phi}\cdot\triangle\Phi. \tag{2.30}$$

Spatial and temporal discretisation The continuous weak forms in Eq. (2.25) and Eq. (2.26) are approximated by the conventional isoparametric Galerkin concept. The spatial discretisation of the initial domain $\mathcal{B}_0$ leads to the discretised domain $\mathcal{B}_0^h$ ($\mathcal{B}_0 \approx \mathcal{B}_0^h = \bigcup_{e=1}^{n_{el}} \mathcal{B}_{0,e}^h$), where the assembly operator A is introduced to assemble all elements in the domain

$$\int_{\mathcal{B}_0} (...)\, dV \approx \int_{\mathcal{B}_0^h} (...)\, dV = \mathop{\mathsf{A}}_{e=1}^{n_{el}} \int_{\mathcal{B}_{0,e}^h} (...)\, dV. \tag{2.31}$$

The total number of discretised elements in the domain is denoted by n_{el}. For further details regarding the discretisation, please refer to Section 4.6. In the following work, we neglect the dynamic term in the balance of linear momentum. Thus, only the evolution of the transmembrane potential $\dot{\Phi}$ needs to be discretised in time. The implicit Euler integration scheme is used for Eq. (2.19) with the time derivative of the transmembrane potential approximated as finite difference

$$\dot{\Phi} \approx \frac{\Phi(\boldsymbol{X}, t_{n+1}) - \Phi(\boldsymbol{X}, t_n)}{\Delta t}, \tag{2.32}$$

where $\Delta t = t_{n+1} - t_n$ and t_{n+1}, t_n represent the current and previous time step, respectively. Finally, with the discretised linearised weak form, the globally assembled system of equations reads

$$\begin{bmatrix} \mathbf{K}^{\varphi\varphi} & \mathbf{K}^{\varphi\Phi} \\ \mathbf{K}^{\Phi\varphi} & \mathbf{K}^{\Phi\Phi} \end{bmatrix} \cdot \begin{bmatrix} \Delta\boldsymbol{\varphi} \\ \Delta\boldsymbol{\Phi} \end{bmatrix} = \begin{bmatrix} -\boldsymbol{r}^{\varphi} \\ -\boldsymbol{r}^{\Phi} \end{bmatrix}. \tag{2.33}$$

This system of equations can be solved via e.g. the Newton-Raphson method. An incremental update of the Newton-Raphson method for an arbitrary time step $n+1$ in the k-th iteration is defined as

$$\boldsymbol{r}_k^{\varphi,n+1} + \mathbf{K}_k^{\varphi\varphi,n+1} \cdot \triangle\boldsymbol{\varphi} + \mathbf{K}_k^{\varphi\Phi,n+1} \cdot \triangle\boldsymbol{\Phi} = \mathbf{0}, \tag{2.34}$$

$$\boldsymbol{r}_k^{\Phi,n+1} + \mathbf{K}_k^{\Phi\varphi,n+1} \cdot \triangle\boldsymbol{\varphi} + \mathbf{K}_k^{\Phi\Phi,n+1} \cdot \triangle\boldsymbol{\Phi} = \mathbf{0}. \tag{2.35}$$

The incremental update of the solution variables for the mechanical and electrical field are defined as $\boldsymbol{\varphi}_{k+1}^{n+1} = \boldsymbol{\varphi}_k^{n+1} + \Delta\boldsymbol{\varphi}$ and $\boldsymbol{\Phi}_{k+1}^{n+1} = \boldsymbol{\Phi}_k^{n+1} + \Delta\boldsymbol{\Phi}$. After computing the residua $\boldsymbol{r}_{k+1}^{\varphi,n+1}$ and $\boldsymbol{r}_{k+1}^{\Phi,n+1}$, the next time step will take place for $\left|\boldsymbol{r}_{k+1}^{\varphi,n+1}\right| \leq \text{tol}$ and $\left|\boldsymbol{r}_{k+1}^{\Phi,n+1}\right| \leq \text{tol}$ or the next iteration for $\left|\boldsymbol{r}_{k+1}^{\varphi,n+1}\right| \geq \text{tol}$ and $\left|\boldsymbol{r}_{k+1}^{\Phi,n+1}\right| \geq \text{tol}$, where tol is a predefined tolerance value.

2.2.1 Continuous Galerkin approximation

Within the continuous Galerkin approximation (classical FEM), a test function space $V_h^{\mathrm{CG},k}$ is defined as

$$V_h^{\mathrm{CG},k} = \{\boldsymbol{w}_h \in \mathrm{H}^1(\mathcal{B}_0) : \ \boldsymbol{w}_h|_{\mathcal{B}_{0,e}^h} \in \mathrm{P}_k(\mathcal{B}_{0,e}^h) \quad \forall \mathcal{B}_{0,e}^h \in \mathcal{B}_0^h\}, \tag{2.36}$$

where $\boldsymbol{w}_h$ is the test function, H^1 is a Sobolev space, and P_k is the space of polynomials of degree k. The solution (e.g. the displacement $\boldsymbol{u}$ in case of the balance of linear momentum) is sought in the same finite dimensional subspace $V_h^{\mathrm{CG},k}$ (otherwise Petrov-Galerkin). The solution in the domain is continuous ($\mathcal{C}^0$).

2.2.2 Discontinuous Galerkin approximation

In contrast, for the discontinuous Galerkin approximation, only L_2 regularity of the solution is required (the solution must be sought in the space of square-integrable functions) and no continuity over element boundaries is enforced. Due to the missing intra-element continuity, the discontinuous Galerkin approximation leads to a different derivation of the weak form. The test function space $V_h^{\mathrm{DG},k}$ is defined as

$$V_h^{\mathrm{DG},k} = \{\boldsymbol{w}_h \in \mathrm{L}^2(\mathcal{B}_0) : \ \boldsymbol{w}_h|_{\mathcal{B}_{0,e}^h} \in \mathrm{P}_k(\mathcal{B}_{0,e}^h) \quad \forall \mathcal{B}_{0,e}^h \in \mathcal{B}_0^h\}, \tag{2.37}$$

where $\boldsymbol{w}_h$ is the test function, L_2 is the space of square-integrable functions, and P_k is the space of polynomials of degree k.

3 Orthotropic tissue structure model

In this chapter, we present a novel Laplace-Dirichlet-Rule-Based-Method (LDRBM) to compute the orthotropic tissue structure on unstructured finite element grids. Instead of directly using the solution of the classical Laplace problem as the transmural depth, see e.g. [167, 169, 171], we make use of a well-established model for the assessment of the transmural thickness/depth [236, 237]. The model consists of two first-order partial differential equations (PDEs) for the definition of a transmural path, whereby the transmural thickness is defined as the arc length of this path. Subsequently, the transmural depth is determined based on the position on the transmural path. Originally, the PDEs were solved via finite differences on structured grids. In order to circumvent the need for two grids and mapping between the structured (to determine the transmural depth) and unstructured (electromechanical heart simulation) grid, we solve the equations directly on the same unstructured tetrahedral mesh. We propose a discontinuous Galerkin method-based (DGM) approach. DGMs are an important class of methods for solving differential equations and are utilised in a wide field of application including chemical transport [238], viscoelasticity [239, 240], elasticity [241, 242], elliptic problems [243, 244], hyperbolic problems [245, 246], parabolic problems [247, 248], gas dynamics [249, 250], see also [251]. The basic concept of the DGMs was first introduced in 1973 by Reed and Hill [233] for solving the steady-state first-order neutron transport equation. DGMs are especially attractive e.g. for advection/convection-dominated problems as they are more stable when compared to the classical continuous Galerkin FEM. Moreover, DGMs are readily usable for parallel computing, well suited for higher-order accurate models and advantageous due to a simplified assembly of the stiffness matrix and mesh refinement. Based on the accurate transmural depth, we assign the local material orientation of the orthotropic tissue structure in the usual fashion. We show that this approach leads to a more accurate definition of the transmural depth compared to existing LDRBMs. We compare the results for different LDRBMs based on a simplified geometry of a hollow cylinder. Furthermore, for the left ventricle (LV), we propose rules for the transmural fibre and sheet orientation and fit them to DT-MRI literature data. The proposed functions provide a distinct improvement compared to existing rules from the literature and can be readily integrated into established methods e.g. [167, 169]. Note that this chapter is to a great extent based on [170].

3.1 Comparison of Laplace-Dirichlet-Rule-Based-Methods

In the following, the well-established reference LDRBMs – B-RBM ([167]) and W-RBM ([168]) – are introduced as they serve as a benchmark for the novel H-RBM method. The H-RBM method will be introduced in detail in the subsequent Section 3.2. In Tab. 3.1, a brief overview of the basic workflow for the methods B-RBM, W-RBM and H-RBM is given.

Table 3.1: Basic workflow for methods B-RBM, H-RBM, W-RBM.

B-RBM	W-RBM	H-RBM
• geometry & mesh 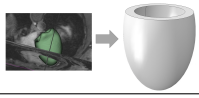	• geometry & mesh 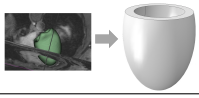	• geometry & mesh 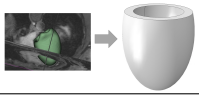
• trans. rule $\alpha_w(d(\boldsymbol{x}))$ in Eq. (3.12) $\beta_w(d(\boldsymbol{x}))$ in Eq. (3.13)	• $\boldsymbol{f}/\boldsymbol{s}$ on $\partial\mathcal{B}_{0,en}/\partial\mathcal{B}_{0,ep}$ 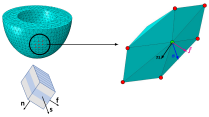	• trans. rule $\alpha(d(\boldsymbol{x}))$ in Eq. (3.47) $\beta(d(\boldsymbol{x}))$ in Eq. (3.48)
• Laplace (2x) $\Delta d(\boldsymbol{x}) = 0$ in Eq. (3.1) b.c. Eq. (3.2)/(3.3) 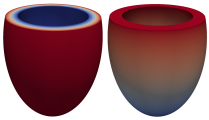	• Laplace (6x) $\Delta d(\boldsymbol{x}) = 0$ in Eq. (3.1) b.c. Eq. (3.20)/(3.21) 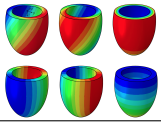	• Laplace (2x) $\Delta d(\boldsymbol{x}) = 0$ in Eq. (3.1) b.c. Eq. (3.2)/(3.3) 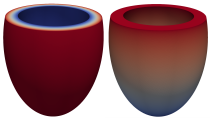
-	-	• find trans. path $L_{0/1}$ in Eq. (3.23)/(3.24) b.c. Eq. (3.25)/(3.26) 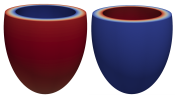
• Eq. (3.4)-(3.14) 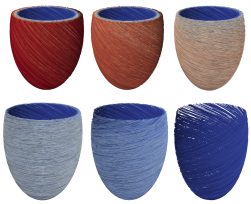	• via Laplace (6x) 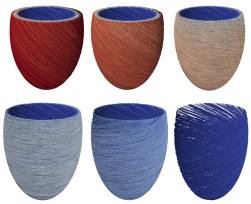	• Eq. (3.43)-(3.48) 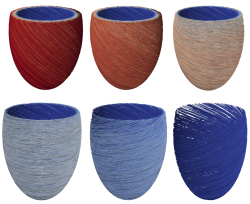

B-RBM

The approach by [167] is based on the definition of a transmural depth $d(\boldsymbol{x})$ in the computational domain $\mathcal{B}_0$. The transmural depth is obtained by solving the Laplace equation

$$\Delta d(\boldsymbol{X}) = 0 \qquad \text{in } \mathcal{B}_0 \quad \forall \boldsymbol{X} \in \mathcal{B}_0, \tag{3.1}$$

where Δ denotes the Laplacian, $d(\boldsymbol{X})$ represents the transmural depth of the ventricular wall with $d : \mathcal{B}_0 \to [0, 1]$, $\boldsymbol{x} \in \mathcal{B}_0$ and $\mathcal{B}_0$ is a bounded domain in $\mathbb{R}^3$. The Dirichlet boundary conditions for the Laplace problem are given as

$$d(\boldsymbol{X}) = 0 \quad \text{on} \quad \partial\mathcal{B}_{0,en} \quad \forall \boldsymbol{X} \in \partial\mathcal{B}_{0,en}, \tag{3.2}$$
$$d(\boldsymbol{X}) = 1 \quad \text{on} \quad \partial\mathcal{B}_{0,ep} \quad \forall \boldsymbol{X} \in \partial\mathcal{B}_{0,en}, \tag{3.3}$$

where $\partial\mathcal{B}_{0,en}$ and $\partial\mathcal{B}_{0,ep}$ represent the endocardial and epicardial surfaces, respectively. Furthermore, a locally defined orthonormal reference coordinate system $C_{ref}(\boldsymbol{X}) = [\boldsymbol{c}(\boldsymbol{X}), \boldsymbol{l}(\boldsymbol{X}), \boldsymbol{r}(\boldsymbol{X})]$ consisting of a local circumferential, longitudinal and radial direction is defined as

$$\boldsymbol{l}(\boldsymbol{x}) = \boldsymbol{T}_a(\boldsymbol{x}), \tag{3.4}$$
$$\boldsymbol{r}(\boldsymbol{x}) = \frac{\boldsymbol{T}_f(\boldsymbol{x}) - (\boldsymbol{l}(\boldsymbol{x}) \cdot \boldsymbol{T}_f(\boldsymbol{x}))\boldsymbol{l}(\boldsymbol{x})}{\|\boldsymbol{T}_f(\boldsymbol{x}) - (\boldsymbol{l}(\boldsymbol{x}) \cdot \boldsymbol{T}_f(\boldsymbol{x}))\boldsymbol{l}(\boldsymbol{x})\|}, \tag{3.5}$$
$$\boldsymbol{c}(\boldsymbol{x}) = \boldsymbol{l}(\boldsymbol{x}) \times \boldsymbol{r}(\boldsymbol{x}), \tag{3.6}$$

with the normalised transmural direction $\boldsymbol{T}_f(\boldsymbol{X})$ defined as

$$\boldsymbol{T}_f(\boldsymbol{X}) = \frac{\nabla d(\boldsymbol{X})}{\|\nabla d(\boldsymbol{X})\|}, \tag{3.7}$$

and $\boldsymbol{T}_a(\boldsymbol{X})$ being the normalised apicobasal direction. The local normalised apicobasal direction $\boldsymbol{T}_a(\boldsymbol{X})$ is defined by solving a second Laplace problem (analogous to Eq. 3.1) to determine the local longitudinal axis of the LV

$$\Delta a(\boldsymbol{X}) = 0 \qquad \text{in } \mathcal{B}_0 \quad \forall \boldsymbol{X} \in \mathcal{B}_0, \tag{3.8}$$

see also [167]. We define Dirichlet boundary conditions

$$a(\boldsymbol{X}) = 0 \quad \text{on} \quad \partial\mathcal{B}_{0,ap} \quad \forall \boldsymbol{X} \in \partial\mathcal{B}_{0,ap}, \tag{3.9}$$
$$a(\boldsymbol{X}) = 1 \quad \text{on} \quad \partial\mathcal{B}_{0,ba} \quad \forall \boldsymbol{X} \in \partial\mathcal{B}_{0,ba}, \tag{3.10}$$

where $\partial\mathcal{B}_{0,ap}$ represents a small apical, epicardial subregion and $\partial\mathcal{B}_{0,ba}$ is the basal plane. We obtain the normalised gradient vector field $\boldsymbol{T}_a(\boldsymbol{X})$ by

$$\boldsymbol{T}_a(\boldsymbol{X}) = \frac{\nabla a(\boldsymbol{X})}{\|\nabla a(\boldsymbol{X})\|}. \tag{3.11}$$

The procedure to construct the local orthonormal reference coordinate system $C_{ref}(\boldsymbol{X})$ is based on the assumption that the longitudinal direction $\boldsymbol{l}(\boldsymbol{X})$ and $\boldsymbol{T}_a(\boldsymbol{X})$ coincide, see Eq. (3.4). In case that $\boldsymbol{T}_a(\boldsymbol{X})$ and $\boldsymbol{T}_f(\boldsymbol{X})$ are not orthogonal, Eq. (3.5) assigns that part of $\boldsymbol{T}_f(\boldsymbol{X})$ to the transmural direction $\boldsymbol{r}(\boldsymbol{X})$ which is orthogonal to $\boldsymbol{T}_a(\boldsymbol{X})$. In the special case that $\boldsymbol{T}_a(\boldsymbol{X})$ and $\boldsymbol{T}_f(\boldsymbol{X})$ are orthogonal, $\boldsymbol{r}(\boldsymbol{X})$ is simply $\boldsymbol{T}_f(\boldsymbol{X})$. Additionally, based on the transmural depth $d(\boldsymbol{X})$, the local fibre angle $\alpha_w(d(\boldsymbol{X}))$ and sheet angle $\beta_w(d(\boldsymbol{X}))$ are defined as (notation from [167])

$$\alpha_w(d(\boldsymbol{X})) = \alpha_{endo} \cdot (1 - d(\boldsymbol{X})) + \alpha_{epi} \cdot d(\boldsymbol{X}), \tag{3.12}$$

$$\beta_w(d(\boldsymbol{X})) = \beta_{endo} \cdot (1 - d(\boldsymbol{X})) + \beta_{epi} \cdot d(\boldsymbol{X}), \tag{3.13}$$

where α_{endo}, α_{epi}, β_{endo}, β_{epi} represent the given fibre and sheet angles on the endocardium and epicardium, respectively. With the known local fibre angle $\alpha_w(d(\boldsymbol{X}))$ and sheet angle $\beta_w(d(\boldsymbol{X}))$, a local material coordinate system $C_{mat}(\boldsymbol{X}) = [\boldsymbol{f}(\boldsymbol{X}), \boldsymbol{n}(\boldsymbol{X}), \boldsymbol{s}(\boldsymbol{X})]$, representing the local myofibre orientation (fibre direction $\boldsymbol{f}$, sheet normal direction $\boldsymbol{n}$, sheet direction $\boldsymbol{s}$) is obtained by

$$C_{mat} = \begin{pmatrix} 1 & 0 & 0 \\ 0 & \cos(\beta_w) & \sin(\beta_w) \\ 0 & -\sin(\beta_w) & \cos(\beta_w) \end{pmatrix} \begin{pmatrix} \cos(\alpha_w) & -\sin(\alpha_w) & 0 \\ \sin(\alpha_w) & \cos(\alpha_w) & 0 \\ 0 & 0 & 1 \end{pmatrix} C_{ref}. \tag{3.14}$$

The charm of the method lies in the straightforward implementation, robust computation, smoothly varying material orientation throughout the domain and the arbitrarily selectable functions for the fibre angle $\alpha_w(d(\boldsymbol{X}))$ as well as the sheet angle $\beta_w(d(\boldsymbol{X}))$. However, it is trivial to see that the definition of the local material coordinate system $C_{mat}(\boldsymbol{X})$ depends on the solution $d(\boldsymbol{X})$ of the Laplace problem. In Fig. 3.1, we consider a cylindrical geometry (representing a short axis ventricular slice) with an inner-to-outer radius ratio $a_r = 0.62$. The reference solution in Fig. 3.1 (a) shows the desired linear change of the normalised transmural depth d along the path A_0–B_1, where $C_{0.5}$ lies exactly in the middle of the ventricular slice. In contrast, the Laplace solution in Fig. 3.1 (b) from Eq. (3.1) shows a nonlinear change of d along the same path A_0–B_1. This can be also seen in Fig. 3.2, where one can compare the linear change (blue curve) with the yellow curve obtained by Eq. (3.1) with $a_r = 0.62$. E.g. at an ordinate value of $d_{true} = 0.5$ of the blue curve (linear), the horizontal distance to the yellow curve shows the deviation of the centre point $C_{0.5}$ in Fig. 3.1 (b). The point $C_{0.5}$ of the yellow curve is shifted by 0.06 (0.44 instead of 0.5) to the endocardial point A_0. Consequently, this imprecise transmural depth $d(\boldsymbol{X})$ leads to a nonlinear transmural fibre and sheet angle distribution in Eq. (3.12) and (3.13). This can be also seen in Fig. 3.4 (c, ●), where the maximum deviation of the fibre angle α from the desired linear rule is up to 7° for the method in [167].

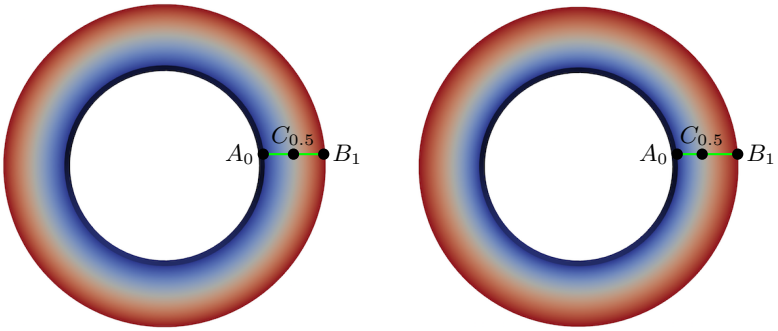

(a) Linear change - reference. (b) Laplace approach – $d(\boldsymbol{X})$.

Figure 3.1: (a) linear change of d_{true} along the green line ($C_{0.5}$ centred). (b) nonlinear change of $d(\boldsymbol{X})$ in Eq. (3.1) ($C_{0.5}$ shifted towards A_0). The colourmap is in the range of 0 (blue ●) to 1 (red ●). Reprinted with permission from [170]. Copyright © 2022 by ASME.

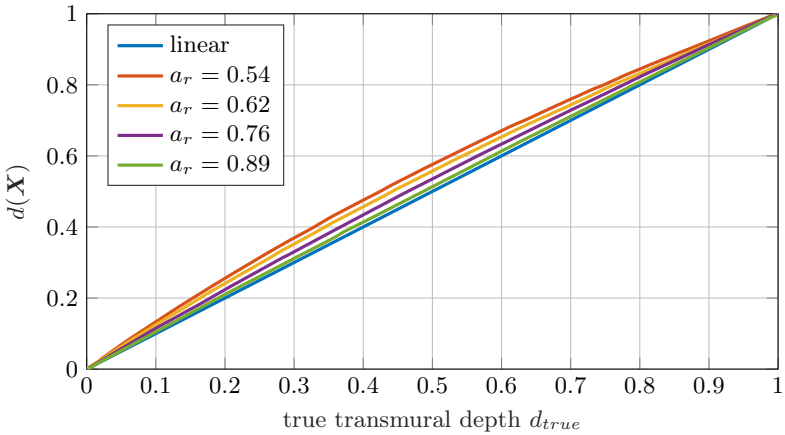

Figure 3.2: The transmural depth $d(\boldsymbol{X})$ based on Eq. (3.1) is plotted over the true transmural depth d_{true} for different values of a_r. The true transmural depth d_{true} is defined as the normalised radial distance (inner to outer radius) for the cylindrical geometry from Fig. 3.1. The transmural depth $d(\boldsymbol{X})$ from Eq. (3.1) only coincides with the assumed true transmural depth d_{true} if the ratio a_r is close to 1, which is not the case in the human heart. Reprinted with permission from [170]. Copyright © 2022 ASME.

W-RBM

In [168], no rules based on the transmural depth d are defined, but on the diffusion coefficients in the Poisson problem itself. A special case of the Poisson equation – the homogeneous Laplacian – is utilised by choosing isotropic constant diffusion coefficients. The local myofibre orientation is initially defined on the endocardium and epicardium. The definition of the local myofibre orientation is based on a globally constant longitudinal axis of the heart $\boldsymbol{z} = \boldsymbol{p}_1 - \boldsymbol{p}_2$, where $\boldsymbol{p}_1$ and $\boldsymbol{p}_2$ represent an apex and basal point, respectively. Subsequently, the circumferential direction $\boldsymbol{c}$ is calculated by the following cross product

$$\boldsymbol{c} = \delta[\boldsymbol{z} \times \boldsymbol{n}], \tag{3.15}$$

where $\boldsymbol{n}$ is the normal vector of a particular node on the endocardium and epicardium obtained by averaging the connected facet normals and

$$\delta = \begin{cases} +1 & \text{on} \quad \partial\mathcal{B}_{0,ep} \\ -1 & \text{on} \quad \partial\mathcal{B}_{0,en} \end{cases} . \tag{3.16}$$

Based on the definitions of $\boldsymbol{z}$, $\boldsymbol{n}$ and $\boldsymbol{c}$, the fibre and sheet direction $\boldsymbol{f}$ and $\boldsymbol{s}$ are computed by

$$\boldsymbol{s} = \text{sign}(\boldsymbol{n}_{cz} \cdot \boldsymbol{n})\boldsymbol{n}, \tag{3.17}$$

$$\mathbf{f} = [-\boldsymbol{p} \cdot \boldsymbol{s}]\boldsymbol{n}_{cz} + [\boldsymbol{n}_{cz} \cdot \boldsymbol{s}]\boldsymbol{p}, \tag{3.18}$$

where $\boldsymbol{n}_{cz} = \boldsymbol{c} \times \boldsymbol{z}$, $\boldsymbol{p} = \text{proj}(\boldsymbol{f}) = \cos(\alpha)\boldsymbol{c} + \sin(\alpha)\boldsymbol{z}$ and

$$\alpha = \begin{cases} \alpha_{endo} & \text{on} \quad \partial\mathcal{B}_{0,en} \\ \alpha_{epi} & \text{on} \quad \partial\mathcal{B}_{0,ep} \end{cases} , \tag{3.19}$$

where α_{endo} and α_{epi} define the fibre angle on the endocardial and epicardial surface, respectively. Finally, the vector coordinates in fibre and sheet direction $\boldsymbol{f} = [f_1, f_2, f_3]$, $\boldsymbol{s} = [s_1, s_2, s_3]$ are interpolated via the Laplace equation. In detail, each vector coordinate of $\boldsymbol{f}$ and $\boldsymbol{s}$ is interpreted as a scalar-valued feature on the boundaries $\partial\mathcal{B}_{0,en}$ and $\partial\mathcal{B}_{0,ep}$ and six Laplace equations are solved independently with the following Dirichlet boundary conditions

$$d(\boldsymbol{x}) = u_i^j \quad \text{on} \quad \partial\mathcal{B}_{0,en}, \tag{3.20}$$

$$d(\boldsymbol{x}) = u_i^j \quad \text{on} \quad \partial\mathcal{B}_{0,ep}, \tag{3.21}$$

where $i = [f, s]$ and $j = [1, 2, 3]$, see also Fig 3.3. This method is widely established due to its straightforward implementation, smooth material orientation throughout the domain, robust and efficient computation and applicability to sparse and non-uniform data. On the contrary, it is ambitious to define

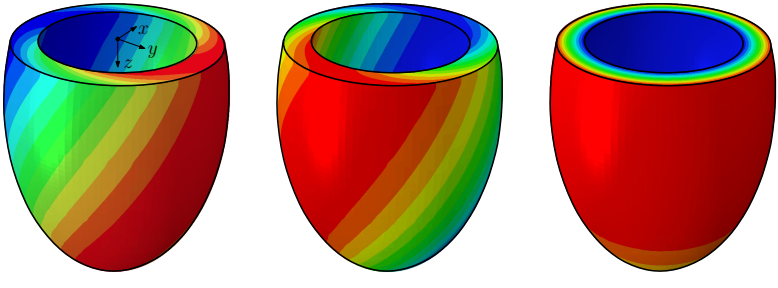

(a) coordinate f_1. (b) coordinate f_2. (c) coordinate f_3.

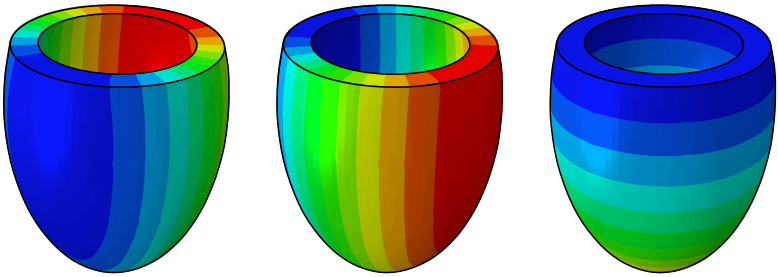

(d) coordinate s_1. (e) coordinate s_2. (f) coordinate s_3.

Figure 3.3: Solution of the Laplace equation for the method W-RBM with the boundary conditions defined in Eq. (3.20) and Eq. (3.21). (a)-(c) solution for the fibre vector coordinates f_1, f_2 and f_3. (d)-(e) solution for the sheet vector coordinates s_1, s_2 and s_3.

an arbitrary rule for the transmural fibre and sheet angle as it requires the element-wise variation of the diffusion tensor. Further, the method does not necessarily enforce the desired interpolation (e.g. linear) through the thickness, see Fig. 3.4. It is important to remark that a linear change of the vector coordinates does not necessarily lead to a linear change in angle. Thus, for the previously described geometry of the hollow cylinder with $a_r = 0.62$ in Fig. 3.1, the deviation from the desired linear change of the fibre angle α shows a maximum of 17°, see Fig. 3.4 (●). The larger deviation compared to B-RBM (7°) can be justified with the accumulation of a) the geometrical inaccuracy of a linear interpolation of vector coordinates in [168] and b) the inaccuracy based on the Laplace problem itself due to the dependence on a_r, see Fig. 3.4. The inaccuracy caused by b) motivates this work. A remedy for a) concerning W-RBM would require the element-wise variation of the diffusion tensor (no longer a Laplace problem.). However, the main focus in this work is on a

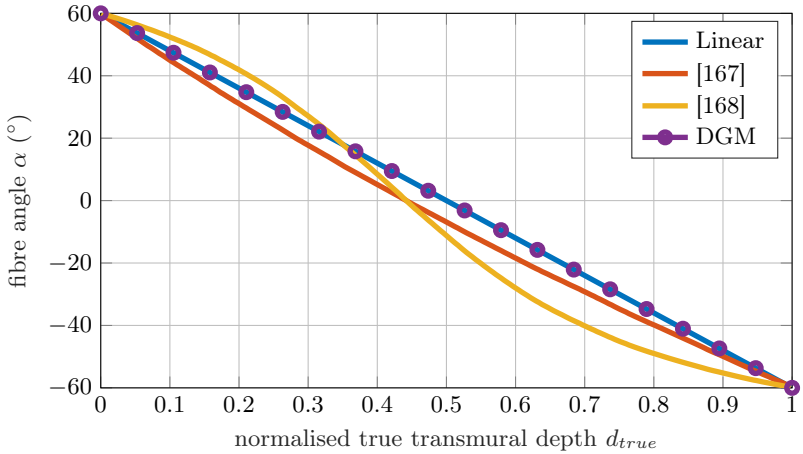

Figure 3.4: The plot shows the different results for the transmural fibre angle α in (°) over the normalised true transmural depth d_{true} based on the methods in [167, 168]. The desired linear change in fibre angle can be achieved by utilisation of the proposed discontinuous Galerkin approach. Reprinted with permission from [170]. Copyright © 2022 ASME.

remedy for b) concerning B-RBM and thus on the accurate representation of the transmural depth d that is independent of a_r, since it is a reasonable model assumption (otherwise, the rules in Eq. (3.12) and Eq. (3.13) would depend on a_r and thus become geometry-dependent rules). In the current form, the solution of Eq. (3.1)-(3.3) only leads to an accurate transmural depth as long as the ratio a_r is close to 1. This is illustrated in Fig. 3.4, where we compute the solution for Eq. (3.1) with boundary conditions specified by Eq. (3.2) and Eq. (3.3) for different values of $a_r \in \{0.54, 0.62, 0.76, 0.89\}$. The true transmural depth d_{true} in such a concentric geometry is simply based on the radial coordinate in a cylindrical coordinate system. We are plotting $d(\boldsymbol{X})$ from Eq. (3.1) over the normalised true transmural depth d_{true}. With an increasing value of a_r, the deviation of $d(\boldsymbol{X})$ compared to the true transmural depth d_{true} increases. Thus, for a realistic value of a_r in a heart or ventricular geometry ($a_r \neq 1$), the use of $d(\boldsymbol{X})$ leads to a – preventable – geometry-dependent inaccuracy.

It is worth noting that the naming of the variables for the sheet and sheet normal direction is not consistent in literature, e.g. in [87] the directions are termed (s,n), while [167] and [168] use (T,S) and (s,m), respectively. There

should be an unambiguous convention in the future to minimise the potential for misinterpretation or confusion.
In summary, the challenge of a precise assessment of the transmural depth in a finite element setting motivates this work. The main purpose is the development of a finite element-based approach to accurately determine the transmural depth. We propose a DGM-based approach for the computation of the wall thickness defined in [236, 237], which is originally approximated via finite differences on a structured grid. It is shown that the method results in an accurate assessment of the transmural depth, which improves and facilitates (no mapping between structured and unstructured grid) the assignment of the rule-based tissue structure. Furthermore, for the left ventricle (LV), we propose novel rules for the transmural fibre and sheet orientation by fitting them to literature-based DT-MRI data. The proposed regional transmural fibre and sheet angle rules based on DT-MRI measurements of the left ventricle show an improved fit to DT-MRI data compared to existing 2-parameter functions (e.g., [166]) and can be readily integrated into established methods (e.g. [167, 169, 171]).

3.2 Methods

The approach of the novel LDRBM is fundamentally inspired by the works of Jones [236] and Yezzi [237]. Based on the solution of Eq. (3.1), the common basic idea is to find the transmural trajectory from the inner surface to the outer surface, such as via the assessment of the cortical and myocardial thickness. While [236] constructs equipotential surfaces (isolines) and sums up the length (straight lines) between all the equipotential surfaces, [237] solves two first-order differential equations to find the transmural trajectory/path from an arbitrary point in the domain to the inner (endocardium) and outer (epicardium) surface, respectively. Yezzi [237] proposed a finite-difference scheme via upwinding to solve the differential equations. This approach is widely used (e.g., for the assessment of regional left ventricular [252] or bi-atrial [253] wall thickness). However, we adapt the method by [237] and develop a finite element-based discontinuous Galerkin framework to solve these equations directly on the unstructured tetrahedral mesh. The finite element-based framework has the crucial merits that the transmural thickness and depth can be computed on the same tetrahedral mesh like the subsequent electromechanical simulation of the cardiac cycle, it is not limited to structured meshes in the finite difference framework and allows, due to the modularity of the framework, a simple integration into existing approaches (e.g., [167, 169]). Further, the method can be readily used to assess the local myocardial thickness during the cardiac cycle on the deformed mesh (local myocardial thickness is an important indicator for the health condition of the heart/myocardium [254]).

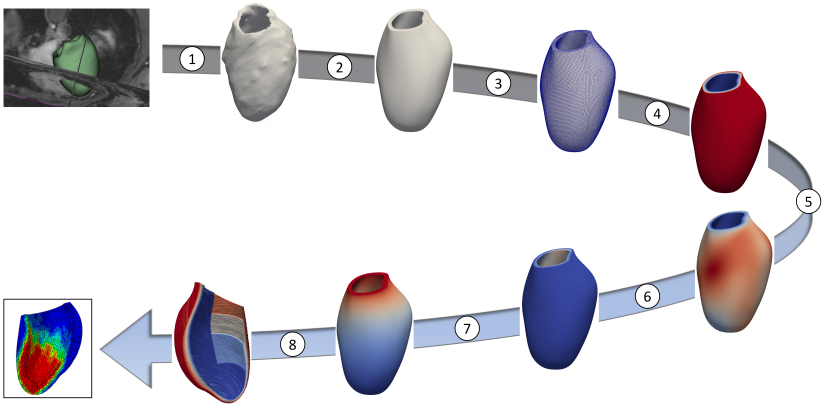

Figure 3.5: Workflow: from medical imaging to the orthotropic tissue structure in the finite element model. Reprinted with permission from [170]. Copyright © 2022 ASME.

In the following, the basic workflow of the proposed LDRBM is described. Fig. 3.5 illustrates the step-by-step workflow (step ① – ⑧) exemplified by a patient-specific LV. While the general workflow from step ④ – ⑧ is based on the method in [167], step ⑤ – ⑥ is the novel modular discontinuous Galerkin framework in order to ensure an accurate transmural depth d. Table 3.2 provides a pseudo-code that summarises the sequential steps of the proposed LDRBM. The entire framework is set up within the open-source finite element software FEniCS [255, 256]. The geometry is obtained via segmentation of the MRI data. From the segmentation, a smooth geometrical model for the finite element simulation is derived and subsequently discretised with tetrahedral finite elements, see Fig. 3.5 – steps ①,② and ③. In step ④, we assess the three-dimensional transmural thickness of the myocardium based on Eq. (3.1), following the approach by [167, 169]. Based on Eq. (3.1), more precisely the normalised gradient field of its solution (Eq. (3.22)), we are going to subsequently solve two first-order PDEs (Eq. (3.23) and Eq. (3.24), see step ⑤,⑥) in order to find the arc length of the path to the endocardium $L_0(\boldsymbol{X})$ and epicardium $L_1(\boldsymbol{X})$. In step ⑦, based on Eq. (3.42), we compute the local longitudinal/apicobasal direction $\boldsymbol{T}_a(\boldsymbol{X})$. Finally, in step ⑧, based on the proposed and fitted rules for the fibre angle α and sheet angle β from Eq. (3.47) and (3.48), the final orthotropic tissue structure is computed.

Table 3.2: Pseudo-code – DG-based orthotropic tissue structure for computational heart models.

① **segmenting myocardium**
② **smoothing geometrical model**
③ **generating mesh for the cardiac simulation**
④ **solving Laplace problem in Eq. (3.1)**
computing $\boldsymbol{T}_f(\boldsymbol{X})$ – Eq. (3.22)
⑤ **solving equations for transmural path to endo**
computing $L_0(\boldsymbol{X})$ – Eq. (3.23)
⑥ **solving equations for transmural path to epi**
computing $L_1(\boldsymbol{X})$ – Eq. (3.24)
computing $d_{DG}(\boldsymbol{X})$ – Eq. (3.38)
⑦ **computing apicobasal direction in Eq. (3.39)**
computing $\boldsymbol{T}_a(\boldsymbol{X})$ – Eq. (3.42)
⑧ **assigning local coordinate systems**
fitting rules for fibre and sheet angle – Eq. (3.50)
computing $C_{ref}(\boldsymbol{X})$ – Eq. (3.43),(3.44),(3.45)
computing $C_{mat}(\boldsymbol{X})$ – Eq. (3.46)

3.2.1 Normalised gradient vector field

The transmural path direction/ tangent of unit length $\boldsymbol{T}_f(\boldsymbol{X})$ is computed by

$$\boldsymbol{T}_f(\boldsymbol{X}) = \frac{\nabla d(\boldsymbol{X})}{\|\nabla d(\boldsymbol{X})\|}, \tag{3.22}$$

where the gradient is based on the solution $d(\boldsymbol{X})$ from Eq. (3.1). The vector field $\boldsymbol{T}_f(\boldsymbol{X})$ is visualised in Fig. 3.6 – path A–A', illustrating a 2D transmural path through the left ventricular wall. It is worth noting that one can construct any kind of vector field, which serves as the transmural path direction. However, we believe that the transmural path based on the gradient field in Eq. (3.22) is a reasonable model assumption.

3.2.2 Transmural path length

Following the approach in [237], the arc length functions of the corresponding transmural path to the endocardium ($L_0(\boldsymbol{X})$ in Eq. (3.23) and Fig. 3.6 – path $A(\boldsymbol{X})$–A) and epicardium ($L_1(\boldsymbol{X})$ in Eq. (3.24) and Fig. 3.6 – path $A(\boldsymbol{X})$–A'), considering an arbitrary point $\boldsymbol{X}$ in the domain $\mathcal{B}_0$, are computed

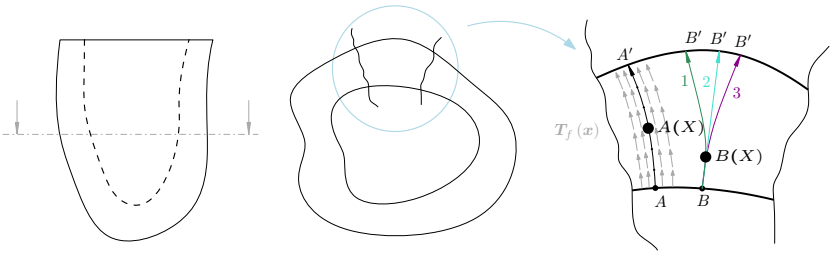

Figure 3.6: Illustration of the possible transmural paths in a 2D slice of the left ventricle to show the non-trivial assessment. All three arbitrary sketched paths (1–3) seem to be plausible as a transmural path through an arbitrary point $B(x)$ in the domain. The path A–A' is obtained by the solution of Eq. (3.1)/(3.22). Reprinted with permission from [170]. Copyright © 2022 ASME.

by the following first-order PDEs

$$\nabla L_0(\boldsymbol{X}) \cdot \boldsymbol{T}_f(\boldsymbol{X}) = 1 \quad \text{in} \quad \mathcal{B}_0 \quad \forall \boldsymbol{X} \in \mathcal{B}_0, \tag{3.23}$$

$$-\nabla L_1(\boldsymbol{X}) \cdot \boldsymbol{T}_f(\boldsymbol{X}) = 1 \quad \text{in} \quad \mathcal{B}_0 \quad \forall \boldsymbol{X} \in \mathcal{B}_0, \tag{3.24}$$

with the corresponding Dirichlet boundary conditions

$$L_0(\boldsymbol{X}) = 0 \quad \text{on} \quad \partial\mathcal{B}_{0,en} \quad \forall \boldsymbol{X} \in \partial\mathcal{B}_{0,en}, \tag{3.25}$$

$$L_1(\boldsymbol{X}) = 0 \quad \text{on} \quad \partial\mathcal{B}_{0,ep} \quad \forall \boldsymbol{X} \in \partial\mathcal{B}_{0,ep}. \tag{3.26}$$

In a physical sense, Eq. (3.23) and Eq. (3.24) can be considered a pure advection problem, one that describes the motion of particles with a prescribed velocity field $\boldsymbol{T}_f(\boldsymbol{X})$. As already mentioned above, these equations are those utilised in, for instance [253], to estimate the wall thickness of a 3D bi-atrial chamber. In [252], they compared the obtained wall thickness between two widely used imaging techniques, namely 2D echocardiography and cardiac cine-magnetic resonance imaging (MRI). Both approaches are based, like [237], on a finite difference approach, which commonly discretises the domain by means of a structured grid. This is feasible for the assessment of the thickness of arbitrary domains (e.g., via segmentation of the cortical thickness or the myocardium based on MRI or echocardiography data). Nevertheless, to utilise the thickness information from the finite difference domain in a finite element cardiac simulation with unstructured tetrahedral meshes requires interpolation/mapping, which can be cumbersome, error-prone and emphasises solving these linear PDEs directly on the finite element mesh.
In the following, we only introduce the weak formulation of Eq. (3.23) since

Eq. (3.24) follows analogously. The formulation is based on a discontinuous Galerkin approximation. More details about the discontinuous Galerkin approximation can be found in [257, 246].
The vector field $\boldsymbol{T}_f(\boldsymbol{X})$ from Eq. (3.22) is a vector-valued function defined on $\mathcal{B}_0$. We define the inflow $\partial\mathcal{B}_{0,en}$ and outflow $\partial\mathcal{B}_{0,ep}$ boundaries as follows

$$\partial\mathcal{B}_{0,en} = \{\boldsymbol{X} \in \partial\mathcal{B}_0 : \boldsymbol{T}_f(\boldsymbol{x}) \cdot \boldsymbol{n}(\boldsymbol{x}) < 0\}, \tag{3.27}$$

$$\partial\mathcal{B}_{0,ep} = \{\boldsymbol{X} \in \partial\mathcal{B}_0 : \boldsymbol{T}_f(\boldsymbol{x}) \cdot \boldsymbol{n}(\boldsymbol{x}) > 0\}, \tag{3.28}$$

where $\boldsymbol{n}(\boldsymbol{X})$ denotes the unit outward normal vector to $\partial\mathcal{B}_0$ at $\boldsymbol{X} \in \partial\mathcal{B}_0$. Let $b \in \mathrm{L}^2(\mathcal{B}_0)$, $g \in \mathrm{L}^2(\partial\mathcal{B}_{0,en})$. We consider the following boundary value problem

$$\nabla L_0(\boldsymbol{X}) \cdot \boldsymbol{T}_f(\boldsymbol{X}) = b \qquad \text{in} \qquad \mathcal{B}_0 \quad \forall \boldsymbol{X} \in \mathcal{B}_0, \tag{3.29}$$

$$L_0(\boldsymbol{X}) = g \qquad \text{on} \qquad \partial\mathcal{B}_{0,en} \quad \forall \boldsymbol{X} \in \partial\mathcal{B}_{0,en}, \tag{3.30}$$

where $b \equiv 1$ and $g \equiv 0$. The geometry is approximated by the following discretised domain $\mathcal{B}_0^h$

$$\mathcal{B}_0^h = \bigcup_{e=1}^{n_e} \mathcal{B}_{0,e}^h, \tag{3.31}$$

where $\mathcal{B}_{0,e}^h$ represents a single finite element in the discretised domain $\mathcal{B}_0^h$. We introduce *average* $\{\cdot\}$ and *jump* $[\![\cdot]\!]$ operators of scalar- and vector-valued functions across the facets of $\mathcal{B}_0^h$

$$\{\psi\} = \frac{1}{2}(\psi^i + \psi^j), \quad [\![\psi]\!] = \psi^i \boldsymbol{n}^i + \psi^j \boldsymbol{n}^j \ \text{ on } \ f_{int} \in \mathcal{F}_h^{int}, \tag{3.32}$$

where $\mathcal{F}_h^{int}$ is the set of interior facets f_{int} and ψ is a scalar function, piecewise smooth on $\mathcal{B}_0^h$, with $\psi^e := \psi\,|_{\mathcal{B}_{0,e}^h}$. The analogous definition holds for a vector-valued function $\boldsymbol{\tau}$, piecewise smooth on $\mathcal{B}_0^h$, see [246]. The unit normal vectors $\boldsymbol{n}^i$ and $\boldsymbol{n}^j$ are defined on f_{int} pointing outwards to $\mathcal{B}_{0,i}^h$ and $\mathcal{B}_{0,j}^h$ with $i \neq j$, respectively.
The finite element space of discontinuous piecewise polynomial functions V_h^k is given as

$$V_h^k = \{v_h \in \mathrm{L}^2(\mathcal{B}_0) : \ v_h|_{\mathcal{B}_{0,e}^h} \in \mathrm{P}_k(\mathcal{B}_{0,e}^h) \quad \forall \mathcal{B}_{0,e}^h \in \mathcal{B}_0^h\}, \tag{3.33}$$

where P_k is the space of polynomials of degree k or less ($k > 0$). By multiplying Eq. (3.29) with the test function $v_h \in V_h^k$, integration by parts, and using the divergence theorem, we obtain

$$\begin{aligned} \sum_{\mathcal{B}_{0,e}^h \in \mathcal{B}_0^h} \Big(\int_{\mathcal{B}_{0,e}^h} -L_0 \ \nabla \cdot (\boldsymbol{T}_f \ v_h) \ \mathrm{d}x + \int_{\partial\mathcal{B}_{0,e}^h} (\boldsymbol{T}_f \cdot \boldsymbol{n}) \ L_0 \ v_h \ \mathrm{d}s \Big) \\ = \sum_{\mathcal{B}_{0,e}^h \in \mathcal{B}_0^h} \int_{\mathcal{B}_{0,e}^h} b \ v_h \ \mathrm{d}x. \end{aligned} \tag{3.34}$$

Following [257, 246], we rewrite as follows

$$\begin{aligned}\sum_{\mathcal{B}_{0,e}^h \in \mathcal{B}_0^h} \int_{\partial \mathcal{B}_{0,e}^h} (\boldsymbol{T}_f \cdot \boldsymbol{n})\ L_0\ v_h\ \mathrm{d}s &= \sum_{f_{int} \in \mathcal{F}_h} \int_{f_{int}} \{\boldsymbol{T}_f L_0\} \cdot [\![v_h]\!]\ \mathrm{d}s \\ &= \sum_{f_{int} \not\subset \partial \mathcal{B}_{0,\mathrm{en}}} \int_{f_{int}} \{\boldsymbol{T}_f L_0\} \cdot [\![v_h]\!]\ \mathrm{d}s + \\ &\quad \sum_{f_{int} \subset \partial \mathcal{B}_{0,\mathrm{en}}} \int_{f_{int}} \boldsymbol{T}_f \cdot \boldsymbol{n}\ g\ v_h\ \mathrm{d}s.\end{aligned} \tag{3.35}$$

For stability, we make use of the common upwinding scheme and substitute on every internal facet the average $\{\boldsymbol{T}_f L_0\}$ from Eq. (3.35) by

$$\{\boldsymbol{T}_f L_0\}_{up} = \begin{cases} \boldsymbol{T}_f L_0^i & \text{if } \boldsymbol{T}_f \cdot \boldsymbol{n}^i > 0 \\ \boldsymbol{T}_f L_0^j & \text{if } \boldsymbol{T}_f \cdot \boldsymbol{n}^i < 0 \\ \boldsymbol{T}_f \{L_0\} & \text{if } \boldsymbol{T}_f \cdot \boldsymbol{n}^i = 0. \end{cases} \tag{3.36}$$

After solving Eq. (3.23) and Eq. (3.24), it follows that the transmural thickness $W(\boldsymbol{X})$ of the myocardium is given by [237]

$$W(\boldsymbol{X}) = L_0(\boldsymbol{X}) + L_1(\boldsymbol{X}), \tag{3.37}$$

which leads to the normalised discontinuous Galerkin-based transmural depth

$$d_{DG}(\boldsymbol{X}) = \frac{L_0(\boldsymbol{X})}{W(\boldsymbol{X})}. \tag{3.38}$$

3.2.3 Longitudinal axis

The basic idea to compute the local material coordinate system based on the transmural thickness can be found [167]. To construct the local reference coordinate system, the transmural direction $\boldsymbol{T}_f(\boldsymbol{X})$, the transmural depth $d_{DG}(\boldsymbol{X})$ as well as the longitudinal or apicobasal direction – we call it $\boldsymbol{T}_a(\boldsymbol{X})$ – need to be known. With the previously determined transmural direction $\boldsymbol{T}_f(\boldsymbol{X})$ and transmural depth $d_{DG}(\boldsymbol{X})$ at hand, we solve a Laplace problem to determine the local longitudinal axis

$$\Delta a(\boldsymbol{X}) = 0 \qquad \text{in } \mathcal{B}_0 \quad \forall \boldsymbol{X} \in \mathcal{B}_0. \tag{3.39}$$

We define Dirichlet boundary conditions

$$a(\boldsymbol{X}) = 0 \quad \text{on} \quad \partial \mathcal{B}_{0,ap} \quad \forall \boldsymbol{X} \in \partial \mathcal{B}_{0,ap}, \tag{3.40}$$

$$a(\boldsymbol{X}) = 1 \quad \text{on} \quad \partial \mathcal{B}_{0,ba} \quad \forall \boldsymbol{X} \in \partial \mathcal{B}_{0,ba}, \tag{3.41}$$

where $\partial\mathcal{B}_{0,ap}$ is a small apical, epicardial subregion and $\partial\mathcal{B}_{0,ba}$ is the basal plane. Subsequently, the normalised gradient vector field $\boldsymbol{T}_a(\boldsymbol{X})$, which serves as the local longitudinal direction, is given by

$$\boldsymbol{T}_a(\boldsymbol{X}) = \frac{\nabla a(\boldsymbol{X})}{\|\nabla a(\boldsymbol{X})\|}. \tag{3.42}$$

3.2.4 Local reference coordinate system

Following [167], with the determined transmural direction $\boldsymbol{T}_f(\boldsymbol{X})$, transmural depth $d_{DG}(\boldsymbol{X})$ and longitudinal or apicobasal direction $\boldsymbol{T}_a(\boldsymbol{X})$, the local orthonormal reference coordinate system $C_{ref}(\boldsymbol{X}) = [\boldsymbol{c}(\boldsymbol{X}), \boldsymbol{l}(\boldsymbol{X}), \boldsymbol{r}(\boldsymbol{X})]$ is defined by

$$\boldsymbol{l}(\boldsymbol{X}) = \boldsymbol{T}_a(\boldsymbol{X}), \tag{3.43}$$

$$\boldsymbol{r}(\boldsymbol{X}) = \frac{\boldsymbol{T}_f(\boldsymbol{X}) - (\boldsymbol{l}(\boldsymbol{X}) \cdot \boldsymbol{T}_f(\boldsymbol{X}))\boldsymbol{l}(\boldsymbol{X})}{\|\boldsymbol{T}_f(\boldsymbol{X}) - (\boldsymbol{l}(\boldsymbol{X}) \cdot \boldsymbol{T}_f(\boldsymbol{X}))\boldsymbol{l}(\boldsymbol{X})\|}, \tag{3.44}$$

$$\boldsymbol{c}(\boldsymbol{X}) = \boldsymbol{l}(\boldsymbol{X}) \times \boldsymbol{r}(\boldsymbol{X}). \tag{3.45}$$

3.2.5 Local material coordinate system

For a given point in the domain $\mathcal{B}_0$, the local orthonormal material coordinate system is obtained by $C_{mat}(\boldsymbol{X})= [\boldsymbol{f}(\boldsymbol{X}), \boldsymbol{n}(\boldsymbol{X}), \boldsymbol{s}(\boldsymbol{X})]$

$$C_{mat} = \begin{pmatrix} 1 & 0 & 0 \\ 0 & \cos(\beta) & \sin(\beta) \\ 0 & -\sin(\beta) & \cos(\beta) \end{pmatrix} \begin{pmatrix} \cos(\alpha) & -\sin(\alpha) & 0 \\ \sin(\alpha) & \cos(\alpha) & 0 \\ 0 & 0 & 1 \end{pmatrix} C_{ref}, \tag{3.46}$$

where α and β are the fibre and sheet angle, respectively.

3.2.6 Transmural fibre and sheet rules

Adapted from the 2-parameter rules in [165, 163, 166], we propose a 3- and 4-parameter rule for the fibre angle α and the sheet angle β, respectively

$$\alpha(\boldsymbol{X}) = R * \mathrm{sgn}(M(\boldsymbol{X}))|M(\boldsymbol{X})|^n + R^*, \tag{3.47}$$

$$\beta(\boldsymbol{X}) = B(2H(\boldsymbol{X}) - 1) + B^*, \tag{3.48}$$

with $H(\boldsymbol{X}) = (1+exp(-K(2(d_{DG}(\boldsymbol{X})+T)-1)))^{-1}$ and $M(\boldsymbol{X}) = 1 - 2d_{DG}(\boldsymbol{X})$. The parameters $R, R^*, n, B, B^*, K, T \in \mathbb{N}$ influence the specific characteristic of the rules. We additionally introduce the parameters R^* and B^* in order to allow an angle shift on the endocardium and epicardium, respectively. In Eq. (3.48), the parameter T allows a shift of the rule along the transmural direction.

To obtain a meaningful parameter set for the rules in Eq. (3.47) and (3.48), we optimise the parameters R, R^*, n, B, B^*, K and T by fitting the rules to DT-MRI derived data [86].
In order to fit DT-MRI one can perform the following optimisation

$$\min_{\boldsymbol{\mu}} \sum_{i=0}^{N^{exp}} \left(\cos^{-1} \left| \frac{\boldsymbol{q}_i^{DG}(\boldsymbol{\mu}) \cdot \boldsymbol{q}_i^{DT-MRI}}{\| \boldsymbol{q}_i^{DG}(\boldsymbol{\mu}) \| \| \boldsymbol{q}_i^{DT-MRI} \|} \right| \right)^2, \tag{3.49}$$

which minimises the sum of squared angles between the measured local material orientation $\boldsymbol{q}_i^{DT-MRI}$ and the discontinuous Galerkin-based orientation $\boldsymbol{q}_i^{DG}$ computed by the rules in Eq. (3.47) and (3.48). Due to a lack of DT-MRI data, we utilise 2D post-processed DT-MRI-based rules for the fibre and sheet angle over the transmural depth [86]. In [86], these rules are provided for different parts of the ventricle, namely the apical-septal, apical-anterior, apical-lateral, apical-posterior, basal-septal, basal-anterior, basal-lateral and basal-posterior subregions. We determine distinct parameter sets for all subregions as well as an additional, simultaneous fit over all subregions, see Section 3.3.3. We perform the following optimisation

$$\min_{\boldsymbol{\mu}} \sum_{j=1}^{S} \sum_{i=1}^{N_{(j)}^{exp}} (\gamma_j^i(\boldsymbol{\mu}) - \bar{\gamma}_j^i)^2, \tag{3.50}$$

where $\bar{\gamma}_j^i$ represents a data point for $i = 1, \dots, N_{(j)}^{exp}$, with $N_{(j)}^{exp}$ being the number of data points throughout the local transmural path in the j-th region. Further, $j = 1, \dots, S$ indicates the number of the subregion in the myocardium and $\gamma_j^i(\boldsymbol{\mu})$ is the angle predicted by the rules in Eq. (3.47) and (3.48). The vector $\boldsymbol{\mu}$ contains the respective parameter set, where $\boldsymbol{\mu} = [R, n, R^*]^T$ for the fibre angle in Eq. (3.47) and $\boldsymbol{\mu} = [B, K, B^*, T]^T$ for the sheet angle in Eq. (3.48).

3.2.7 Mesh generation and definition of boundary surfaces

For the finite element mesh generation, the open source 3D finite element mesh generator Gmsh was utilised [258]. After importing the geometrical model, for instance as an .stp-file, the necessary boundary surfaces (endocardial, epicardial, apical and basal regions) are defined via the graphical user interface under geometry -> physical groups -> add -> surfaces. Subsequently, the geometry is meshed with 172023 tetrahedral elements, stored as an .msh-file and imported into the FEniCS environment. The code snippet to import, read and store the mesh information including the boundary surfaces is given in Listing 3.1.

Listing 3.1: Code snippet - import .msh. file from Gmsh for FEniCS.

```
import meshio
import numpy as np
from dolfin import Mesh, XDMFFile,
                   File, MeshValueCollection, cpp,
                   DirichletBC, FunctionSpace,

# write and read mesh information
msh = meshio.read("AnyMesh.msh")
meshio.write("mesh.xdmf",
         meshio.Mesh(points=msh.points,
                     cells={"tetra": msh.cells["tetra"]}))
meshio.write("physical_boundaries.xdmf",
         meshio.Mesh(points=msh.points,
                     cells={"triangle": msh.cells["triangle"]},
                     cell_data={"triangle": {"name_to_read":
                     msh.cell_data["triangle"]["gmsh:physical"]}}))
mesh = Mesh()
with XDMFFile("mesh.xdmf") as infile:
    infile.read(mesh)
File("mesh.pvd").write(mesh)

mvc = MeshValueCollection("size_t", mesh, 2)
with XDMFFile("physical_boundaries.xdmf") as infile:
    infile.read(mvc, "name_to_read")

# contains the defined boundaries in Gmsh
mf = cpp.mesh.MeshFunctionSizet(mesh, mvc)
File("boundaries.pvd").write(mf)

V = FunctionSpace(mesh, 'CG', 2)

# definition Dirichlet b.c. based on GMSH mesh marks
bc = DirichletBC(V, Constant(0.2), mf, 3)
```

3.3 Results

The results of the derived LDRBM as applied to an idealised geometry (hollow cylinder from Fig. 3.4) and an MRI-based patient-specific geometry of an LV are described below. Further, we present the optimised parameters for Eq. (3.47) and (3.48) for the distinct subregions of the myocardium as well as for the simultaneous fit in Tab. 3.3.

3.3.1 Hollow cylinder

In Fig. 3.1 (a) and (b), the difference in transmural depth $d_{DG}(\boldsymbol{X})$ for Eq. (3.38) and $d(\boldsymbol{X})$ for Eq. (3.1) is depicted. While Eq. (3.38) yields a linear change in transmural depth along the path A_0–B_1 as desired, the Laplace solution in Fig. 3.1 (b) shows a nonlinear change in transmural depth, which is also visualised for different values of a_r in Fig. 3.2. Fig. 3.1 (c,●●●) shows the comparison for an assumed linear fibre angle distribution through the wall. The discontinuous Galerkin-based method improves the accuracy of the transmural depth and therewith the definition of the local material coordinate system C_{mat}. Fig. 3.7 shows the assignment of the local reference coordinate system C_{ref} from Section 3.2.4 for the hollow cylinder. The solution of Eq. (3.43) is depicted in Fig. 3.7 (a) (longitudinal direction $\boldsymbol{l}$ ●), the solution of Eq. (3.44) in Fig. 3.7 (b) (radial direction $\boldsymbol{r}$ ●) and the solution of Eq. (3.45) in Fig. 3.7 (c) (circumferential direction $\boldsymbol{c}$ ●). In Fig. 3.7 (d), the local reference coordinate system at an arbitrary material point $\boldsymbol{X}$ in the computational domain is shown. The final local fibre direction $\boldsymbol{f}$ is visualised in Fig. 3.8 (a).

3.3.2 Left ventricle

Fig. 3.8 (b) and Fig. 3.9 (a) and (b) visualise the fibre direction $\boldsymbol{f}$ for the LV in its layered structure. In Fig. 3.9 (c), the sheet orientation of the LV is shown. The parameters for the visualisation are set to: $R = 45$, $R^* = 0$, $B = 45$, $B^* = 0$, $n = 1$, $K = 10$, $T = 0$. We analysed the computational time by comparing the processor time of the approach in [167] and the novel LDRBM=] (mesh of 172023 tetrahedral elements, 2,8 GHz Intel Core i7, 16 GB RAM). The total processor time slightly increased by 33.00s which corresponds to an increase of 5.96 %.

3.3.3 Fitting rule-based fibre and sheet rules

For the fibre and sheet angle rules, DT-MRI-data published in [86] is utilised. In [86], the fibre and laminar structure in the healthy human heart were investigated ex vivo. The different subregions of the ventricle (basal-apical, basal-anterior etc.) can be found in Tab. 3.3 and [86]. Please note that the definition of the sheet angle β is different compared to [86] ($\beta = \beta_{[86]} - \frac{\pi}{2}$). We solve the optimisation problem in Eq. (3.50) to determine the global (all 8 subregions) best fit for the ventricle as well as the distinct fit for each subregion, see Tab. 3.3. The error $e_{\alpha,\beta}$ is computed as the averaged deviation

$$e_{\alpha,\beta} = \sqrt{\frac{1}{S}\sum_{j=1}^{S}\frac{1}{N_{(j)}^{exp}}\sum_{i=1}^{N_{(j)}^{exp}}(\gamma_j^i(\boldsymbol{\mu}_{min}) - \bar{\gamma}_j^i)^2}. \tag{3.51}$$

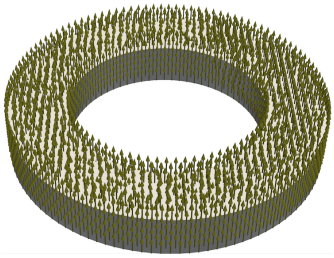

(a) longitudinal direction l.

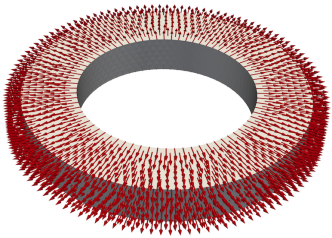

(b) radial direction r.

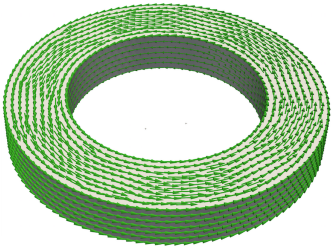

(c) circumferential direction c.

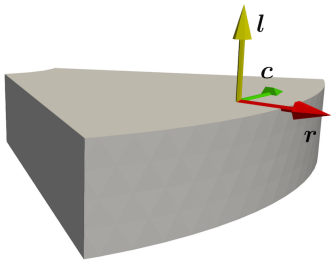

(d) reference coordinate system C_{ref}.

Figure 3.7: (a)-(c) longitudinal direction l (●) from Eq. (3.43), radial direction r (●) from Eq. (3.44) and circumferential direction c (●) from Eq. (3.45). (d) assignment of the local reference coordinate system C_{ref} from Section 3.2.4. Reprinted with permission from [170]. Copyright © 2022 ASME.

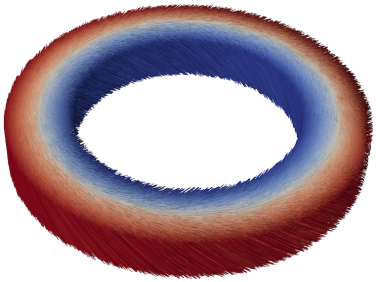

(a) fibre vector $\boldsymbol{f}$ - cylinder.

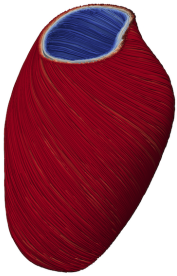

(b) fibre vector $\boldsymbol{f}$ - ventricle.

Figure 3.8: (a) fibre direction $\boldsymbol{f}$ of the hollow cylinder. (b) fibre direction $\boldsymbol{f}$ of the left ventricle. Reprinted with permission from [170]. Copyright © 2022 ASME.

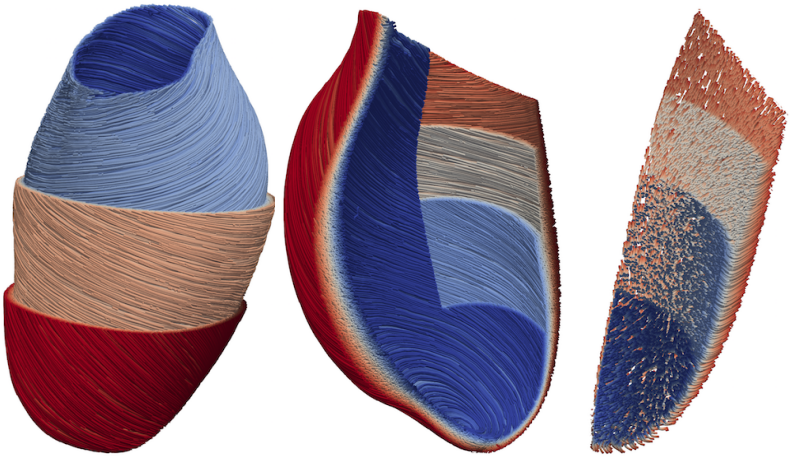

(a) (b) (c)

Figure 3.9: (a)-(b) layer-wise visualisation of the transmural change in fibre direction $\boldsymbol{f}$ in the left ventricle. (c) layer-wise visualisation of the transmural change in sheet direction $\boldsymbol{s}$ in the left ventricle. Reprinted with permission from [170]. Copyright © 2022 ASME.

In Fig. 3.10, single fits for the apical and basal subregions based on the data in [86] are shown. It can be observed that the error e_α is slightly smaller in the basal region due to the almost linear fibre distribution in [86]. In Fig. 3.11, single fits of Eq. (3.48) for the apical and basal subregions based on the data in [86] are shown. It can be observed that the error e_β is slightly smaller in the basal regions (3 out of 4 regions). Due to the higher complexity in the measured sheet distribution compared to the fibre distribution, the error e_β exceeds e_α in all eight subregions. In Fig. 3.12, the simultaneous fits (●) of Eq. (3.47) and Eq. (3.48) over all eight subregions are shown. Comparing the original 2-parameter rules for the fibre and sheet angle e.g. in [166] with the proposed functions in Eq. (3.47) and Eq. (3.48), a distinct improvement in the fits for all eight subregions as well as for the simultaneous fits can be observed, see e_α / e_α([166]) and e_β / e_β([166]) in Tab. 3.3. All fitted parameters and errors can be found in Tab. 3.3.

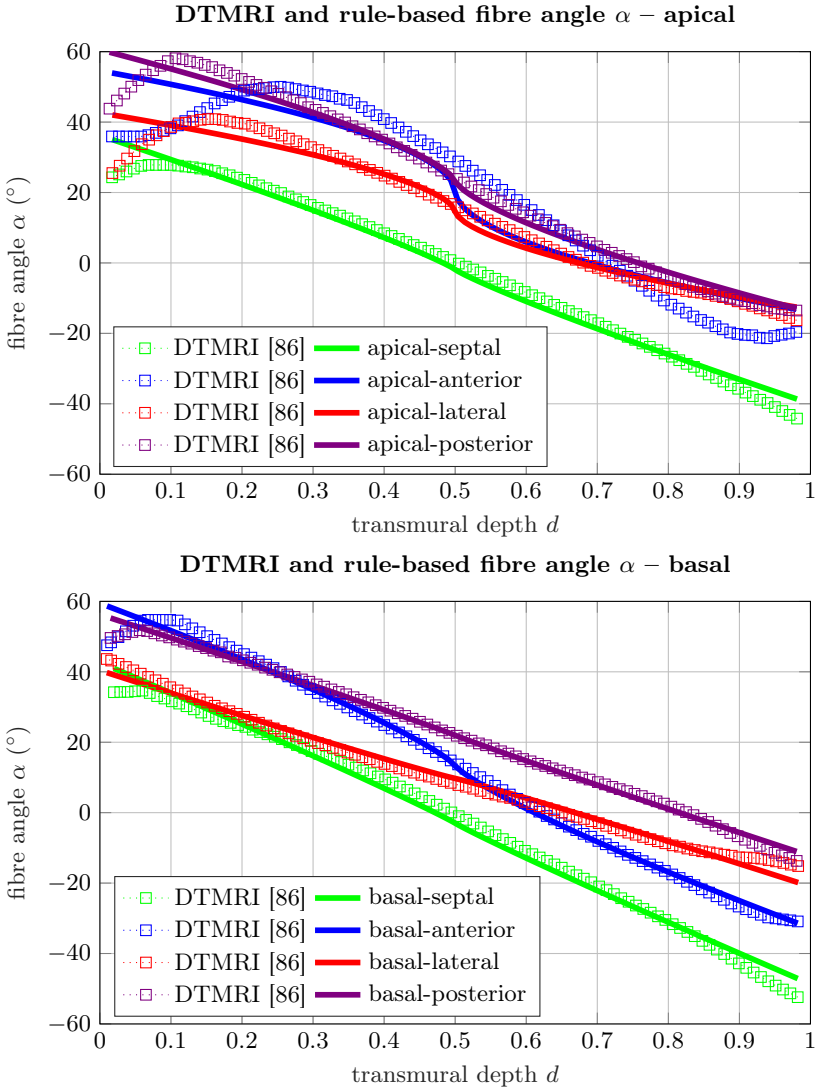

Figure 3.10: Single fits of Eq. (3.47) for the fibre angle α in the apical regions (top). Single fits of Eq. (3.47) for the fibre angle α in the basal regions (bottom). Reprinted with permission from [170]. Copyright © 2022 ASME.

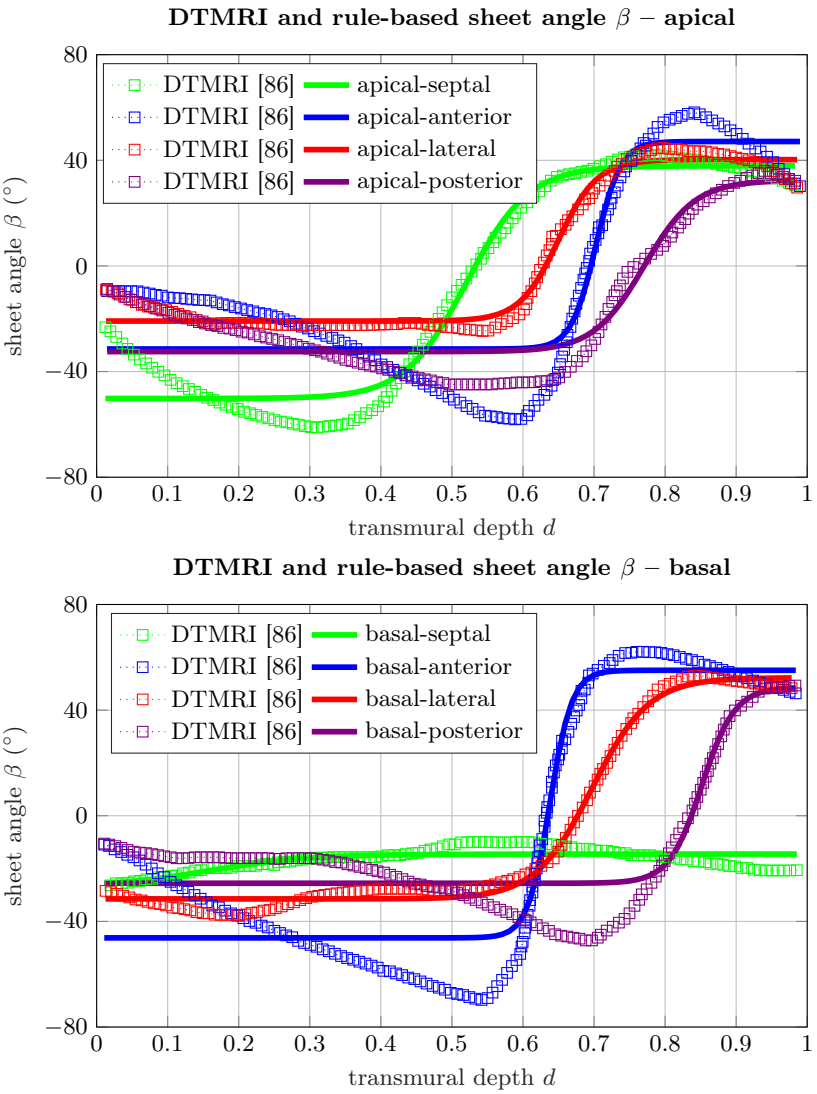

Figure 3.11: Single fits of Eq. (3.48) for the sheet angle β in the apical regions (top). Single fits of Eq. (3.48) for the sheet angle β in the basal regions (bottom). Reprinted with permission from [170]. Copyright © 2022 ASME.

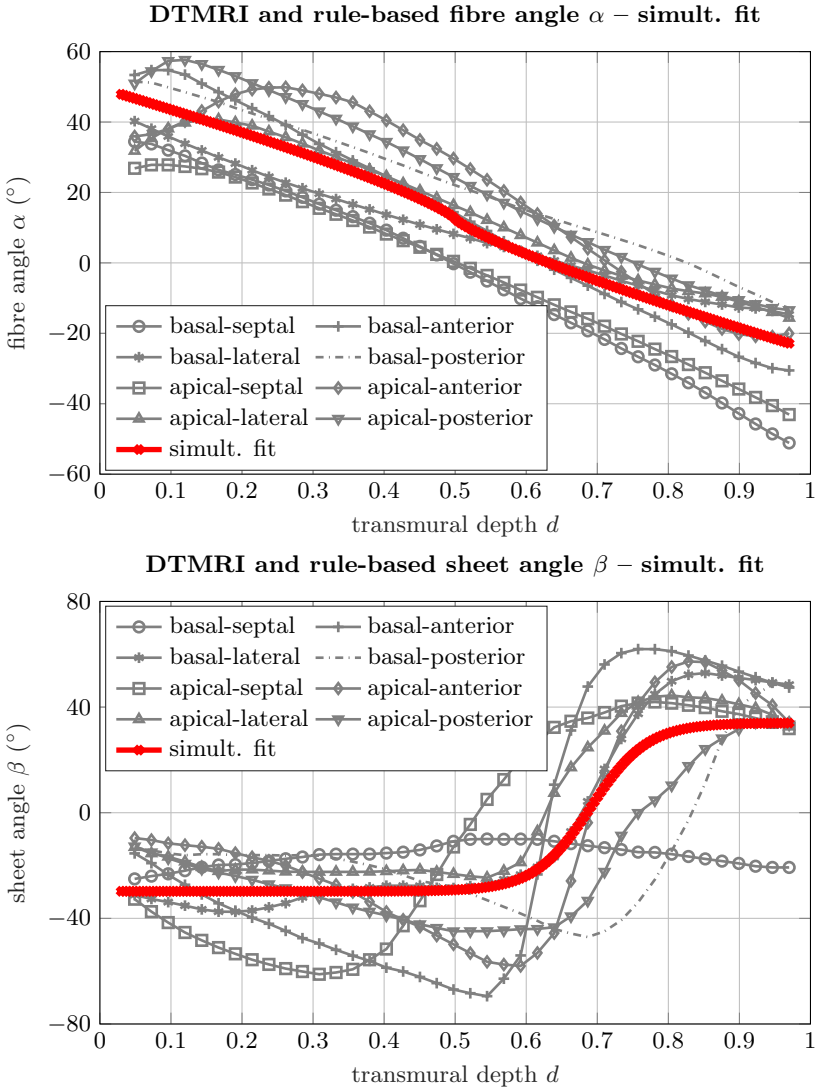

Figure 3.12: Simultaneous fit of Eq. (3.47) for the fibre angle α in the apical and basal regions (top). Simultaneous fit of Eq. (3.48) for the sheet angle β in the apical and basal regions (bottom). Reprinted with permission from [170]. Copyright © 2022 ASME.

Table 3.3: The fibre angle α and sheet angle β were determined for different regions of the heart (basal-apical, basal-anterior, etc.). We used the optimisation problem in Eq. (3.50) to find the global best fit for the LV as well as the distinct fits for each subregion; upper and lower bounds for the optimisation: $\boldsymbol{\mu}_{\alpha,low} = [0, 0, -90]^T$, $\boldsymbol{\mu}_{\alpha,up} = [90, 50, 90]^T$, $\boldsymbol{\mu}_{\beta,low} = [0, 1, -90, -1]^T$, $\boldsymbol{\mu}_{\beta,up} = [90, 50, 90, 1]^T$. Reprinted with permission from [170]. Copyright © 2022 ASME.

Region	R	n	R^*	e_α	e_α([166])	B	K	B^*	T	e_β	e_β([166])
basal – sept.	45.682	0.950	-2.989	2.453	3.846	6.284	7.003	-20.787	0.342	2.811	16.923
basal – ant.	46.110	0.827	13.345	2.238	13.524	50.662	32.183	4.423	-0.138	12.629	35.648
basal – lat.	30.694	1.058	-1.058	1.794	9.876	41.874	12.530	10.392	-0.197	2.811	17.655
basal – post.	34.299	0.967	21.976	1.192	21.891	37.107	21.759	11.554	-0.352	9.636	27.483
apical – sept.	38.084	0.892	-1.863	2.758	3.328	44.057	11.494	-6.138	-0.021	7.368	11.680
apical – ant.	34.242	0.538	20.338	8.651	22.101	39.283	28.809	7.837	-0.203	13.497	31.485
apical – lat.	27.926	0.607	14.703	3.648	15.148	30.563	18.382	9.691	-0.150	3.737	14.857
apical – post.	37.282	0.710	23.287	3.268	23.511	32.438	13.975	-0.005	-0.271	9.299	27.927
simult. fit	37.190	0.816	12.526	10.899	16.604	31.878	12.565	2.120	-0.191	21.029	28.069

3.4 Summary

A new LDRBM is proposed for the computation of the orthotropic tissue structure in cardiac finite element models. To accurately assess the transmural path and depth in unstructured finite element domains, we propose a discontinuous Galerkin-based approach. The accurate transmural depth leads to a correct representation of the transmural fibre and sheet angle rules along complex transmural paths. We illustrate the method through an example of a hollow cylinder and show the difference compared to existing methods ([167, 168]). The finite element-based framework has the essential benefits that the transmural thickness and depth can be instantly computed on the unstructured tetrahedral mesh of the subsequent electromechanical simulation, in other words, it is not limited to structured meshes in the finite difference framework and therefore allows, due to the modularity of the framework, a straightforward integration into existing LDRBMs (e.g. [167, 169]). Setting up the entire framework within the open-source finite element software FEniCS [255, 256] guarantees a user-friendly and straightforward implementation. The framework is not limited to cardiac models and can also readily be used to assess the thickness in a variety of complex geometrical shapes such as the cerebral cortex. Further, the thickness assessment can be also utilised as a post-processing feature for the electromechanically coupled finite element simulation of the cardiac cycle (e.g. at every time step) as the wall thickness plays an important role in clinical interpretation (risk indicator). The proposed rules for the fibre and sheet angle show a distinct improvement compared to existing 2-parameter functions from e.g. [166].
It is important to remark that we need a common convention for all rule-based approaches on how the transmural depth is determined during experimental observation (e.g. DT-MRI) and in computational models. Without a convention, the rule-based modelling of the orthotropic tissue structure can not be consistent with the experimentally derived rules.
For more complex models, such as papillary muscles or trabeculations, the approach can be extended, see [167]. To use the fitted rules of the distinct subregions in Tab. 3.3 for cardiac electromechanical simulations, an interpolation method has to be utilised to ensure a smooth transition zone of adjacent subregions and, consequently, improve the numerical stability.

4 Cardiac muscle model

In the following Chapter, the electromechanical model of the cardiac tissue is described. The balance equations were already introduced in Chapter 2. The constitutive equations for the passive and active mechanics, electrophysiology and mechano-electrical feedback (MEF) are discussed in Section 4.1. In Section 4.2, the geometrical model based on MRI data is presented and information about the MRI device and measurement of the healthy subject-specific LV are provided. The mechanical boundary conditions and Windkessel model are introduced in Section 4.3 and Section 4.4, respectively. In Section 4.5, the different orthotropic tissue structures based on the LDRBMs are visualised. Finally, the weak form of the electromechanical problem, its linearisation and discretisation are presented in Section 4.6.

4.1 Constitutive equations

Mechanical constitutive equations The passive material characteristic of the cardiac tissue is modelled via the well-known orthotropic Holzapfel-Ogden strain energy density function Ψ_{HO}, see [87]. The passive part of the second Piola-Kirchhoff stress tensor $\mathbf{S}^{\mathrm{pas}}$ is defined as the derivative of the strain energy density function Ψ_{pas} w.r.t. the right Cauchy-Green tensor $\mathbf{C}$

$$\mathbf{S}^{\mathrm{pas}} = 2\frac{\partial \Psi_{\mathrm{pas}}}{\partial \mathbf{C}}, \tag{4.1}$$

where the corresponding specific strain-energy function Ψ_{pas} is defined as

$$\Psi_{\mathrm{pas}} = \Psi_{\mathrm{V}}(J) + \Psi_{\mathrm{HO}}(\bar{I}_1, \bar{I}_{4f}, \bar{I}_{4s}, \bar{I}_{8fs}), \tag{4.2}$$

with the volumetric part

$$\Psi_{\mathrm{V}}(J) = \kappa(J-1)^2, \tag{4.3}$$

where κ denotes the bulk modulus of the material. The orthotropic Holzapfel-Ogden strain energy density function Ψ_{HO} is given as

$$\begin{aligned}\Psi_{\mathrm{HO}}(\bar{I}_1, \bar{I}_{4f}, \bar{I}_{4s}, \bar{I}_{8fs}) = &\underbrace{\frac{a}{2b}\exp[b(\bar{I}_1 - 3)]}_{\text{isotropic term}} + \underbrace{\sum_{i=f,s} \frac{a_i}{2b_i}\{\exp[b_i(\bar{I}_{4i}-1)^2] - 1\}}_{\text{transversely isotropic terms}} \\ &+ \underbrace{\frac{a_{fs}}{2b_{fs}}[\exp(b_{fs}\bar{I}_{8fs}^2) - 1]}_{\text{orthotropic term}},\end{aligned} \tag{4.4}$$

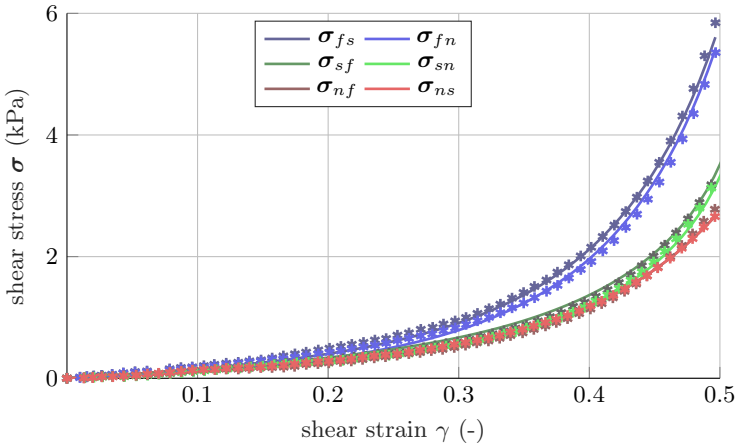

Figure 4.1: Comparison of the stress-strain curves for the six different shear modes based on the Holzapfel-Ogden model (solid lines) and the experimental shear data from [88] (asterisks). Reprinted with permission from [180]. Copyright © 2023 by J. Biomech.

where the isochoric invariants $\bar{I}_1, \bar{I}_{4f}, \bar{I}_{4s}, \bar{I}_{8fs}$ are based on the the isochoric right Cauchy-Green tensor $\mathbf{C}^{\diamond}$. The model consists of an isotropic term representing the matrix material behaviour. Additionally, a transversally isotropic and a coupling term with respect to the fibre and sheet direction $\boldsymbol{f}$ and $\boldsymbol{s}$ are introduced. The invariants I_{4f} and I_{4s} are the stretch-related invariants. I_{8fs} reflects the coupling between the fibre and sheet stretches. In total, eight material parameters $a, b, a_f, a_s, b_f, b_s, a_{fs}, b_{fs}$ in Eq. (4.4) must be identified. The parameters a and b denote the matrix response. The myocardial fibres are represented by the parameters a_f and b_f, while a_s and b_s account for the sheet direction. The coupling between the fibre and sheet direction is described by the parameters a_{fs}, b_{fs}. To obtain a parameter set for healthy human cardiac tissue, the model is fitted to shear experiments from [88]. The fitted curves for the different shear directions can be found in Fig. 4.1.
The active part of the second Piola-Kirchhoff stress tensor $\boldsymbol{S}^{\text{act}}$ is defined as the derivative of the strain energy density function Ψ_{act} w.r.t. the right Cauchy-Green tensor $\mathbf{C}$

$$\mathbf{S}^{\text{act}} = 2\frac{\partial \Psi_{\text{act}}}{\partial \boldsymbol{C}}, \tag{4.5}$$

where the corresponding specific strain-energy function Ψ_{act} is defined as

$$\Psi_{\text{act}} = \frac{1}{2}\nu(I_4^e - 1)^2. \tag{4.6}$$

The parameter ν defines the active modulus and I_4^e is the elastic part of the fourth invariant. More details of the model can be found in [121].
In order to account for the active contraction of the cardiac tissue, the deformation gradient $\mathbf{F}$ is multiplicatively decomposed and reads

$$\mathbf{F} = \mathbf{F}^e\mathbf{F}^a, \tag{4.7}$$

where $\mathbf{F}^a$ represents the active part and $\mathbf{F}^e$ is the elastic part, see also [121]. Based on the experimental observation in [259], active stress along the cross fibre direction $\boldsymbol{n}$ is included (a factor of 0.5 compared to the active stress in fibre direction $\boldsymbol{f}$). The following equations describe the evolution of the active stress depending on the multiplicatively decomposed deformation gradient $\mathbf{F}$

$$\mathbf{S}^{act} = 2\sum_{i\in\{f,n\}}\left[\nu_i(I_{4i}^e - 1)\mathbf{F}^{-a}\tilde{\mathbf{M}}_i^e(\mathbf{F}^a)\mathbf{F}^{-a^T}\right], \tag{4.8}$$

$$\tilde{\mathbf{M}}_i^e(\mathbf{F}^a) = \tilde{\boldsymbol{k}}_0 \otimes \tilde{\boldsymbol{k}}_0,\ \tilde{\boldsymbol{k}}_0 = (\mathbf{F}^a\boldsymbol{k}_0)/||\mathbf{F}^a\boldsymbol{k}_0||, \tag{4.9}$$

$$\mathbf{F}^a(\lambda^a) = \mathbf{I} + \sum_{i\in\{f,n\}}(\lambda^a(g) - 1)\mathbf{M}_i, \tag{4.10}$$

$$\mathbf{M}_f = \boldsymbol{f}_0 \otimes \boldsymbol{f}_0,\ \mathbf{M}_n = \boldsymbol{n}_0 \otimes \boldsymbol{n}_0, \tag{4.11}$$

$$\lambda^a(g) = \frac{\xi\lambda_{max}^a}{1 + g(c)(\xi(g) - 1)}, \tag{4.12}$$

$$g(c(\phi_e)) = \frac{1}{2} + \frac{1}{\pi}\arctan(\beta \ln c(\phi_e)), \tag{4.13}$$

$$\xi = \frac{g(c_0) - 1}{g(c_0) - \lambda_{max}^a}, \tag{4.14}$$

where in Eq. (4.8) I_{4f} and I_{4n} are the fourth invariants in the fibre and sheet-normal directions, respectively [87]. The normalised calcium concentration c depends on the normalised TP ϕ_e and additional parameters k, q, where c_0 represents the initial calcium concentration at $t = t_0$. The parameter λ^a is the active stretch. Equations (4.12)–(4.14) describe the coupling between the electrophysiological quantities and mechanics.

Constitutive equations for electrophysiology and MEF The electrical constitutive equation can be represented as an additive decomposition into an electrical part F_e^Φ and a source term F_m^Φ which accounts for the TP generation arising due to mechanical deformation (mechano-electrical feedback). The nonlinear source term F^Φ reads

$$F^\Phi = F_e^\Phi + F_m^\Phi, \tag{4.15}$$

with F_e^{Φ} being described by the model presented in [110]

$$F_e^{\Phi}(\Phi, r) = \frac{k_\phi}{k_t} f_e^{\phi}(\phi_e, r), \tag{4.16}$$

$$f_e^{\phi}(\phi_e, r) = c\phi_e(\phi_e - \alpha_e)(1 - \phi_e) - r\phi_e, \tag{4.17}$$

where k_ϕ and k_t are conversion parameters, α_e and c are material parameters, and r is the recovery variable that guarantees a return to resting potential. The conversion of the TP Φ and time t reads as

$$\Phi = k_{\phi_e}\phi_e - \delta_{\phi_e}, \qquad t = k_t\bar{t}, \tag{4.18}$$

with the potential difference δ_{ϕ_e} and $\bar{t}$ representing the dimensionless time. The evolution of the recovery variable r is governed by the local ordinary differential equation

$$\dot{r} = \left[\gamma + \frac{\mu_1 r}{\mu_2 + \Phi}\right][-r - c\Phi(\Phi - \beta_e - 1)], \tag{4.19}$$

where the variables μ_1, μ_2, β_e and γ are additional material parameters. The action potential duration and the effective refractory period are controlled by β_e [148, 134]. For the mechanically induced electrical source term F_m^{Φ}, we utilise the model presented in [116, 128]

$$F_m^{\Phi}(\mathbf{C}, \Phi) = \frac{k_{\phi_e}}{k_t} f_m^{\phi}(\mathbf{C}, \phi_e), \tag{4.20}$$

$$f_m^{\phi}(\mathbf{C}, \phi_e) = \vartheta G_s\,(\lambda - 1)\,(\phi_s - \phi_e)\,, \tag{4.21}$$

with the parameter G_s describing the maximum conductance. The potential ϕ_s determines the potential level at which no deformation can cause any current generation. The variable ϑ controls the activation of the MEF. For fibres under tension ($\lambda = \sqrt{\bar{I}_{4f}} > 1$) $\vartheta = 1$, while for fibres under compression or in the initial configuration ($\lambda = \sqrt{\bar{I}_{4f}} \leq 1$) $\vartheta = 0$ [116, 128].

4.2 Geometrical model via MRI

MRI was performed on one 24-year-old healthy female volunteer after an ethically verified informed consent form was signed (internal study approval ID number 3818, Pediatric Cardiology, Friedrich-Alexander-Universität Erlangen-Nürnberg). Electrocardiogram (ECG) triggered 3D whole heart balanced SSFP imaging with fat suppression is carried out on a 3T MR scanner (MAGNETOM Vida Siemens Healthineers, Erlangen, Germany) in end-systolic and end-diastolic phases, while acquisition is realised in the transverse plane. The following parameters are set for the measurement: TR/TE 3.8 ms/1.4 ms; flip angle 60°; number of cardiac phases 1; temporal resolution 60–100 ms;

number of signal averages 1; voxel size 0.5 mm x 0,5 mm x 0.5 mm; number of slices in anteroposterior direction 120. The end-diastolic geometry is defined by the frame with the largest LV cavity, while the end-systolic geometry is defined by the frame with the smallest LV cavity. Threshold-based segmentation with 3D Slicer (free open source software application for medical image computing, see [260]) is utilised to generate the 3D-.stl-file (geometry) of the LV in end-systolic and end-diastolic phase.
From the MRI-based derived end-diastolic (ED) and end-systolic (ES) geometry of the LV, we measured the geometrical properties shown in Fig. 4.2 (a) (long axis view; measurement points ●). Each data point (x_j^i, z_j^i), is created by

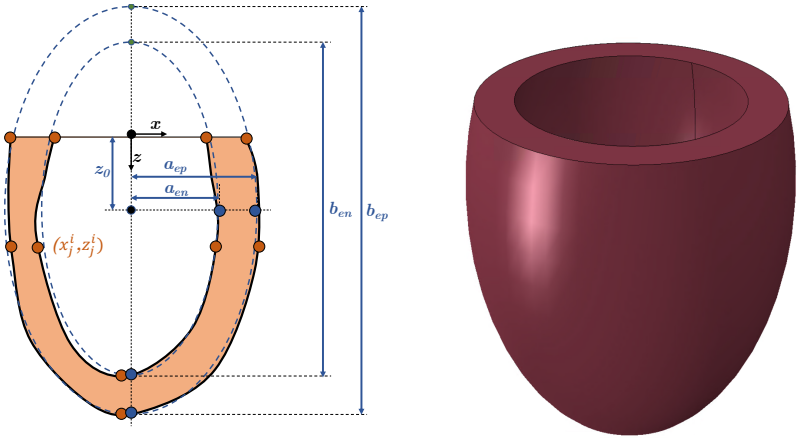

(a) Measurement points. (b) Fitted Geometry.

Figure 4.2: (a) visualisation of the measurement points and fitted parameters of the ellipses. (b) fitted stress-free geometry. Reprinted with permission from [180]. Copyright © 2023 by J. Biomech.

averaging eight measurement points in the short axis plane (approx. every 45° around the z-axis) from the MRI-derived geometry. We assume an axis-symmetric geometry with respect to the longitudinal z-axis. Thus, the averaged measured points (x_j^i, z_j^i), $i \in \{1, .., 5\}$, $j \in \{en, ep\}$ from the MRI on the endo- and epicardial surfaces (five in total; apex (1x), middle (2x) and base (2x) region) are utilised to fit an ellipse centred at $(0, z_0)$. To obtain the fitted ellipsoidal geometries for the ES and ED state, the following optimisation is performed

$$\min_{\boldsymbol{\mu}} \sum_{i=1}^{5} \frac{{x_j^i}^2}{a_j^2} + \frac{(z_j^i - z_0)^2}{b_j^2} - 1, \tag{4.22}$$

where $\boldsymbol{\mu} = (a_{en}, b_{en}, a_{ep}, b_{ep}, z_0)$. The variables a_j, b_j are representing the short and long axis of the fitted ellipses for the endo- and epicardium, respectively. Finally, by truncating the geometry at $z = 0$, the resulting geometrical models in ED and ES state are obtained.
A stress-free state (no residual stresses, see [261]) localised between the end-systolic and end-diastolic states [262, 263], an end-diastolic pressure (EDP) of 7.50 mmHg, and a constant compressibility with $\kappa = 110$ kPa to ensure the measured myocardial volume reduction during the systolic phase is assumed. We use the fitted ED and ES geometry from Eq. (4.22) and linearly scale the parameters $(a_{en}, b_{en}, a_{ep}, b_{ep}, z_0)$ between ED and ES state to fit the end-diastolic volume (EDV) under an acting end-diastolic pressure of 7.50 mmHg. The best fit is obtained for a ratio of 6:4 between the ED and ES values of $a_{en}, b_{en}, a_{ep}, b_{ep}, z_0$. The schematic workflow to determine the stress-free configuration is depicted in Fig. 4.3. The parameters of the geometrical model can be found in Tab. 5.1, Chapter 5.

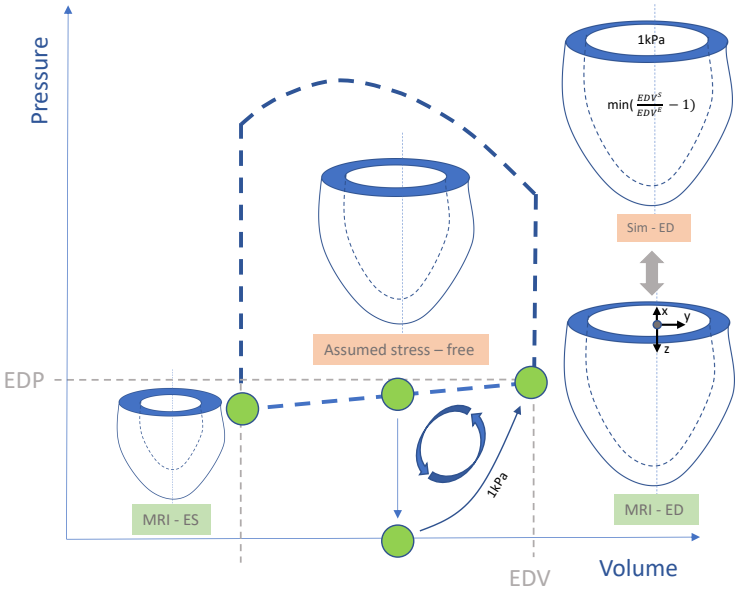

Figure 4.3: Schematic workflow to determine the stress-free configuration for the electromechanical simulation. Reprinted with permission from [180]. Copyright © 2023 by J. Biomech.

4.3 Mechanical boundary condition

For the mechanical boundary condition, the displacement for all nodes on the basal surface is fixed in the longitudinal and circumferential direction (blue surface at the base of the ventricle in Fig. 4.3. This leads to a free movement of the basal surface in the radial direction. Each of the outer edge nodes (a total number of $n_{s/d}$=100 spring/dashpot pairs) on the basal surface (green dots in Fig. 4.4 (b)) is attached to a linear spring/dashpot pair (purple lines in Fig. 4.4 (a)), which allows to control the radial movement during diastole and systole. We fit the spring and dashpot coefficients k_s and k_d as well as the initial spring force F_{init} such that the end-diastolic and end-systolic radial displacement of the measurements can be obtained.

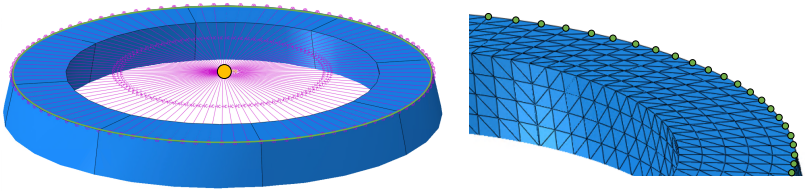

(a) spring/dashpot system base region. (b) detail view nodes.

Figure 4.4: (a) spring/dashpot system on the outer line of the basal plane (green line). A spring/dashpot pair (purple line) is connected to each node (green dot) and fixed to the origin (yellow dot), see also detail view in (b). Reprinted with permission from [180]. Copyright © 2023 by J. Biomech.

4.4 Windkessel model

The haemodynamics in this study is represented by the following five steps:

1. linear pressure increase starting from $p_{lv} = 0$ mmHg to $p_{lv} = 7.50$ mmHg (assumed end-diastolic pressure (EDP); see [264, 265] with 4–10 mmHg),

2. **isovolumetric contraction**: p_{lv} increases from EDP up to 70.00 mmHg kPa,

3. **ejection**: the pressure in the aorta p_a is described by the two-element Windkessel model:

$$\frac{-dV(t)}{dt} = \frac{p_a(t)}{R_p} + C\frac{dp_a(t)}{dt}, \tag{4.23}$$

where $V(t)$ is the current volume of the LV, R_p is the peripheral resistance, and C represents the capacitance/total arterial compliance of the aorta. By adding an additional resistance R_{v1}, imitating the aortic valve, and assuming that the blood flow between the LV and the aorta is proportional to the pressure difference [46], the pressure in the LV reads as

$$p_{lv}(t) = R_{v1}\frac{-dV(t)}{dt} + p_a(t), \tag{4.24}$$

4. **isovolumetric relaxation**, if the condition $p_{lv} < p_a$ is satisfied,

5. early **diastolic filling**, if p_{lv} drops under the EDP. In analogy to Eq. (4.24), the following equation holds

$$p_{lv}(t) = R_{v2}\frac{-dV(t)}{dt} + EDP, \tag{4.25}$$

where R_{v2} represents the atrioventricular valve resistance.

The specific parameters C, R_{v1}, R_{v2} are provided in Tab. 5.1, Chapter 5.

4.5 Orthotropic tissue structure based on LDRBMs

The three LDRBMs, B-RBM, W-RBM and H-RBM, introduced in the previous chapter, are utilised to investigate the influence of the local tissue structure. In Fig. 4.5, the computed fibre orientations for the derived left ventricular geometry based on B-RBM, W-RBM and H-RBM are visualised.

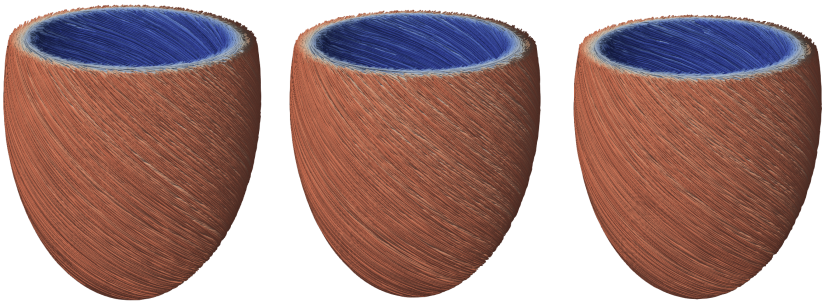

(a) B-RBM (b) W-RBM (c) H-RBM

Figure 4.5: Fibre orientation for the methods B-RBM, W-RBM and H-RBM for the subject-specific left ventricular geometry.

4.6 Finite element formulation

The weak forms have already been introduced in Chapter 2. Assuming a quasi-static problem and adding the pressure boundary condition on the endocardial surface $\boldsymbol{p}_{LV} = p_{lv}\boldsymbol{n}$, where $\boldsymbol{n}$ is the unit normal to the endocardial surface of the domain $\mathcal{B}_t$. Consequently, the weak forms read

$$r^{\varphi} = \int_{\mathcal{B}_0} \nabla_x(\delta\boldsymbol{\varphi}) : \tau \; dV - \int_{\mathcal{B}_0} \delta\boldsymbol{\varphi} \cdot \boldsymbol{B}_0 \; dV - \int_{\partial_t\mathcal{B}_t} \delta\boldsymbol{\varphi} \cdot \hat{\boldsymbol{t}} \; da - \int_{\partial_p\mathcal{B}_t} \delta\boldsymbol{\varphi} \cdot (-\hat{\boldsymbol{p}}_{LV}) \; da = 0, \tag{4.26}$$

$$r^{\Phi} = \int_{\mathcal{B}_0} \delta\Phi\dot{\Phi} \; dV + \int_{\mathcal{B}_0} \nabla_x(\delta\Phi) \cdot \boldsymbol{q} \; dV - \int_{\mathcal{B}_0} \delta\Phi F^{\Phi} \; dV - \int_{\partial_q\mathcal{B}_t} \delta\Phi\hat{q} \; da = 0. \tag{4.27}$$

Linearisation Assuming conservative forces, i.e. the forces caused by the external traction $\hat{\boldsymbol{t}}$ and body force $\boldsymbol{B}_0$ remain unchanged during deformation, the linearisation of Eq. (4.26) follows as

$$\begin{aligned}\Delta r^{\varphi} = &\int_{\mathcal{B}_0} \nabla_x(\delta\boldsymbol{\varphi}) : \nabla_x(\Delta\boldsymbol{\varphi})\boldsymbol{\tau} \; dV + \int_{\mathcal{B}_0} \nabla_x(\delta\boldsymbol{\varphi}) : \mathbb{C}^{\varphi\varphi} : (\boldsymbol{g}\nabla_x(\Delta\boldsymbol{\varphi})) \; dV \\ &+ \int_{\mathcal{B}_0} \nabla_x(\delta\boldsymbol{\varphi}) : \mathbf{C}^{\varphi\Phi}\Delta\Phi \; dV + \int_{\partial_p\mathcal{B}_t} \delta\boldsymbol{\varphi} \cdot \boldsymbol{n} \; \Delta p_{lv} \; da \\ &+ \int_{\partial_p\mathcal{B}_t} \delta\boldsymbol{\varphi} \cdot p_{lv} \; \Delta\boldsymbol{n} \; da,\end{aligned} \tag{4.28}$$

where Δp_{LV} and $\Delta\boldsymbol{n}$ represent the incremental form of the pressure and normal vector, respectively. Analogously, linearisation of the internal and external part of the weak form in Eq. (4.27) leads to

$$\Delta r^{\Phi} = \int_{\mathcal{B}_0} \delta\Phi\frac{\Delta\Phi}{\Delta t} \; dV + \int_{\mathcal{B}_0} \nabla_x(\delta\Phi) \cdot \mathbf{D}^{\Phi\Phi} \cdot \nabla_x(\Delta\Phi) \; dV + \int_{\mathcal{B}_0} \nabla_x(\delta\Phi) \cdot \mathbb{C}^{\Phi\varphi} : (\boldsymbol{g}\nabla_x(\Delta\boldsymbol{\varphi})) \; dV \tag{4.29}$$

$$- \int_{\mathcal{B}_0} \delta\Phi(\mathbf{H} : (\boldsymbol{g}\nabla_x(\Delta\boldsymbol{\varphi}))) + \delta\Phi H\Delta\Phi \; dV. \tag{4.30}$$

More details about the linearisation can be found in [121, 266].

Discretisation With the spatial discretisation of the domain introduced in Eq. (2.31), the element-wise approximations via shape functions N read

$$\boldsymbol{\varphi}_e^h = \sum_{j=1}^{n_{en}} N_j \boldsymbol{\varphi}_j^e, \qquad \nabla_x(\boldsymbol{\varphi}_e^h) = \sum_{j=1}^{n_{en}} \boldsymbol{\varphi}_j^e \otimes \nabla_x N_j, \tag{4.31}$$

$$\delta\boldsymbol{\varphi}_e^h = \sum_{i=1}^{n_{en}} N_i \delta\boldsymbol{\varphi}_i^e, \qquad \nabla_x(\delta\boldsymbol{\varphi}_e^h) = \sum_{i=1}^{n_{en}} \delta\boldsymbol{\varphi}_i^e \otimes \nabla_x N_i, \tag{4.32}$$

$$\Phi_e^h = \sum_{l=1}^{n_{en}} N_l \Phi_l^e, \qquad \nabla_x(\Phi_e^h) = \sum_{l=1}^{n_{en}} \Phi_l^e \nabla_x N_l, \tag{4.33}$$

$$\delta\Phi_e^h = \sum_{k=1}^{n_{en}} N_k \delta\Phi_k^e, \qquad \nabla_x(\delta\Phi_e^h) = \sum_{k=1}^{n_{en}} \delta\Phi_k^e \nabla_x N_k, \tag{4.34}$$

$$\nabla_x(\Delta\boldsymbol{\varphi}_e^h) = \sum_{j=1}^{n_{en}} \Delta\boldsymbol{\varphi}_j^e \otimes \nabla_x N_j, \qquad \nabla_x(\Delta\Phi_e^h) = \sum_{l=1}^{n_{en}} \Delta\Phi_l^e \nabla_x N_l. \tag{4.35}$$

Omitting the sum signs in the previous Eq. (4.31) – (4.35) for the sake of clarity and assuming summation over indices i, j, k and l, the discretised weak forms follow as

$$\begin{aligned}
\mathop{\mathsf{A}}_{e=1}^{n_{el}} \Bigg[& \int_{\mathcal{B}_{0,e}^h} [\delta\boldsymbol{\varphi}_i^e \otimes \nabla_x N_i] : \boldsymbol{\tau}\ dV \ - \int_{\mathcal{B}_{0,e}^h} N_i \delta\boldsymbol{\varphi}_i^e \cdot \boldsymbol{B}_0\ dV - \int_{\partial_t \mathcal{B}_{t,e}^h} N_i \delta\boldsymbol{\varphi}_i^e \cdot \hat{\boldsymbol{t}}\ da \Bigg] \\
& + \mathop{\mathsf{A}}_{e=1}^{n_{el,en}} \left[\int_{\partial_p \mathcal{B}_{t,e}^h} N_i \delta\boldsymbol{\varphi}_i^e \cdot \boldsymbol{p}_{LV}\ da \right] = \mathbf{0},
\end{aligned} \tag{4.36}$$

$$\begin{aligned}
\mathop{\mathsf{A}}_{e=1}^{n_{el}} \Bigg[& \int_{\mathcal{B}_{0,e}^h} N_k \delta\Phi_k^e \dot{\Phi}\ dV + \int_{\mathcal{B}_{0,e}^h} [\delta\Phi_k^e \nabla_x N_k] \cdot \boldsymbol{q}\ dV \\
& - \int_{\mathcal{B}_{0,e}^h} N_k \delta\Phi_k^e F^{\Phi}\ dV - \int_{\partial_q \mathcal{B}_{t,e}^h} N_k \delta\Phi_k^e \bar{q}\ da \Bigg] = \mathbf{0},
\end{aligned} \tag{4.37}$$

where A represents the assembly operator. Equations (4.36) and (4.37) have to hold for arbitrary variations, leading to the discrete global residual vector

$$\boldsymbol{r}_I^{\varphi} = \mathop{\mathsf{A}}_{e=1}^{n_{el}} \left[\int_{\mathcal{B}_{0,e}^h} \nabla_x N_i \cdot \boldsymbol{\tau} \; dV \; - \int_{\mathcal{B}_{0,e}^h} N_i \boldsymbol{B}_0 \; dV - \int_{\partial_t \mathcal{B}_{t,e}^h} N_i \hat{\boldsymbol{t}} \; da \right] + \mathop{\mathsf{A}}_{e=1}^{n_{el,en}} \left[\int_{\partial_p \mathcal{B}_{t,e}^h} N_i \boldsymbol{p}_{LV} \; da \right] = \boldsymbol{0}, \tag{4.38}$$

$$\boldsymbol{r}_K^{\Phi} = \mathop{\mathsf{A}}_{e=1}^{n_{el}} \left[\int_{\mathcal{B}_{0,e}^h} N_k \dot{\Phi} \; dV + \int_{\mathcal{B}_{0,e}^h} \nabla_x N_k \cdot \boldsymbol{q} \; dV - \int_{\mathcal{B}_{0,e}^h} N_k F^{\Phi} \; dV - \int_{\partial_q \mathcal{B}_{t,e}^h} N_k \hat{q} \; da \right] = \boldsymbol{0}. \tag{4.39}$$

The discrete forms of the linearised weak forms in Eq. (4.28) and (4.30) read

$$\begin{aligned} \Delta r_{\mathrm{d}}^{\varphi} = \mathop{\mathsf{A}}_{e=1}^{n_{el}} \Bigg[& \int_{\mathcal{B}_{0,e}^h} [\delta \boldsymbol{\varphi}_i^e \otimes \nabla_x N_i] : \mathbb{C}^{\varphi\varphi} : [\Delta \boldsymbol{\varphi}_j^e \otimes \nabla_x N_j] \; dV \\ & + \int_{\mathcal{B}_{0,e}^h} [\delta \boldsymbol{\varphi}_i^e \otimes \nabla_x N_i] : ([\Delta \boldsymbol{\varphi}_j^e \otimes \nabla_x N_j] \boldsymbol{\tau}) \; dV \\ & + \int_{\mathcal{B}_{0,e}^h} ([\delta \boldsymbol{\varphi}_i^e \otimes \nabla_x N_i] : \mathbf{C}^{\varphi\phi}) N_l \Delta \Phi_l^e \; dV \Bigg] \\ & + \mathop{\mathsf{A}}_{e=1}^{n_{el,en}} \left[\int_{\partial_p \mathcal{B}_{t,e}^h} N_i \delta \boldsymbol{\varphi}_i^e \cdot p_{lv} \; \Delta \boldsymbol{n}_d \; da \right] \\ & + \mathop{\mathsf{A}}_{e=1}^{n_{el,en}} \left[\int_{\partial_p \mathcal{B}_{t,e}^h} N_i \delta \boldsymbol{\varphi}_i^e \cdot \boldsymbol{n} \; \Delta p_{lv,d} \; da \right], \end{aligned} \tag{4.40}$$

$$\begin{aligned}\Delta r_{\mathrm{d}}^{\Phi} = \mathop{\mathsf{A}}_{e=1}^{n_{el}} \Bigg[& \int_{\mathcal{B}_{0,e}^h} (N_k \delta \Phi_k^e) \frac{1}{\Delta t} (N_l \Delta \Phi_l^e) \; dV \\ & + \int_{\mathcal{B}_{0,e}^h} (\delta \Phi_k^e \nabla_x N_k) \cdot \mathbf{D}^{\Phi\Phi} \cdot [\Delta \Phi_l^e \nabla_x N_l] \; dV \\ & + \int_{\mathcal{B}_{0,e}^h} (\delta \Phi_k^e \nabla_x N_k) \cdot \mathbb{C}_3^{\Phi\varphi} \cdot (\Delta \boldsymbol{\varphi}_j^e \otimes \nabla_x N_j) \; dV \\ & - \int_{\mathcal{B}_{0,e}^h} (N_k \delta \Phi_k^e) \mathbf{H} : [\Delta \boldsymbol{\varphi}_j^e \otimes \nabla_x N_j] \; dV - \int_{\mathcal{B}_{0,e}^h} (N_k \delta \Phi_k^e) H (N_l \Delta \Phi_l^e) \; dV \Bigg] . \end{aligned} \tag{4.41}$$

Analogously to Eq. (4.36) and (4.37), Eq. (4.40) and (4.42) have to hold for arbitrary variations. Finally, the cardiac model can be described by the following system of equations

$$\begin{bmatrix} \mathbf{K}_{IJ}^{\varphi\varphi} & \mathbf{K}_{IL}^{\varphi\Phi} \\ \mathbf{K}_{KJ}^{\Phi\varphi} & \mathbf{K}_{KL}^{\Phi\Phi} \end{bmatrix} \cdot \begin{bmatrix} \Delta \boldsymbol{\varphi}_J \\ \Delta \Phi_L \end{bmatrix} = \begin{bmatrix} -\boldsymbol{r}_I^{\varphi} \\ -\boldsymbol{r}_K^{\Phi} \end{bmatrix} , \tag{4.42}$$

where the stiffness matrix $\mathbf{K}_{IJ}^{\varphi\varphi} = \tilde{\mathbf{K}}_{IJ}^{\varphi\varphi} + \hat{\mathbf{K}}_{IJ}^{\varphi\varphi} + \bar{\mathbf{K}}_{IJ}^{\varphi\varphi}$ with

$$\begin{aligned} \tilde{\mathbf{K}}_{IJ}^{\varphi\varphi} \cdot \Delta \boldsymbol{\varphi}_J = \mathop{\mathsf{A}}_{e=1}^{n_{el}} \Bigg[& \int_{\mathcal{B}_{0,e}^h} \nabla_x N_i \cdot \mathbb{C}^{\varphi\varphi} \cdot \nabla_x N_j \\ & + \int_{\mathcal{B}_{0,e}^h} (\nabla_x N_i \cdot \boldsymbol{\tau} \cdot \nabla_x N_j) \boldsymbol{g} \; dV \Bigg] \cdot \Delta \boldsymbol{\varphi}_J , \end{aligned}$$

$$\hat{\mathbf{K}}_{IJ}^{\varphi\varphi} \cdot \Delta \boldsymbol{\varphi}_J = \mathop{\mathsf{A}}_{e=1}^{n_{el,en}} \left[\int_{\partial_p \mathcal{B}_{t,e}^h} N_i p_{LV} \; \Delta \bar{\boldsymbol{n}}_d \; da \right] \cdot \Delta \boldsymbol{\varphi}_J ,$$

$$\bar{\mathbf{K}}_{IJ}^{\varphi\varphi} \cdot \Delta \boldsymbol{\varphi}_J = \mathop{\mathsf{A}}_{e=1}^{n_{el,en}} \left[\int_{\partial_p \mathcal{B}_{t,e}^h} N_i \boldsymbol{n} \; \Delta \bar{p}_{lv,d} \; da \right] \cdot \Delta \boldsymbol{\varphi}_J ,$$

and

$$\mathbf{K}_{IL}^{\varphi\Phi} \cdot \Delta\Phi_L = \mathop{\mathsf{A}}_{e=1}^{n_{el}} \left[\int_{\mathcal{B}_{0,e}^h} (\nabla_x N_i \cdot \mathbf{C}^{\varphi\Phi}) N_l \; dV \right] \cdot \Delta\Phi_L,$$

$$\mathbf{K}_{KJ}^{\Phi\varphi} \cdot \Delta\boldsymbol{\varphi}_J = \mathop{\mathsf{A}}_{e=1}^{n_{el}} \left[\int_{\mathcal{B}_{0,e}^h} \nabla_x N_k \cdot \mathbb{C}^{\Phi\varphi} \cdot \nabla_x N_j \; dV \right.$$

$$\left. - \int_{\mathcal{B}_{0,e}^h} (N_k \mathbf{H} \cdot \nabla_x N_j) \boldsymbol{g} \; dV \right] \cdot \Delta\boldsymbol{\varphi}_J,$$

$$\mathbf{K}_{KL}^{\Phi\Phi} \cdot \Delta\Phi_L = \mathop{\mathsf{A}}_{e=1}^{n_{el}} \left[\int_{\mathcal{B}_{0,e}^h} N_k \frac{1}{\Delta t} N_l + \nabla_x N_k \cdot \mathbf{D}^{\Phi\Phi} \cdot \nabla_x N_l \; dV \right.$$

$$\left. - \int_{\mathcal{B}_{0,e}^h} N_k H N_l \; dV \right] \cdot \Delta\Phi_L. \tag{4.43}$$

5 Influence of orthotropic tissue structure on cardiac function

In this chapter, we explore the extent to which LDRBM-based orthotropic tissue structures influence the electromechanical characteristics of the cardiac tissue model. In detail, we are utilising the three Laplace-Dirichlet-Rule-Based-Methods B-RBM, W-RBM and H-RBM from Chapter 3 and compare the local myofibre orientation, global characteristics (i.e., ejection fraction, peak pressure, apex shortening, myocardial volume reduction, fractional wall thickening, pressure-volume loop) as well as local (active fibre stress, fibre strain) characteristics. Note that this Chapter is to a great extent based on [180].

5.1 Materials & Methods

5.1.1 Fully-coupled electromechanical heart model

The comparison is based on the electromechanical model introduced in the previous Chapter 4. We perform three simulations with the local material orientation obtained by the methods B-RBM, W-RBM and H-RBM. All simulation parameters of the electromechanical model can be found in Tab. 5.1.

5.1.2 Characteristics for comparison

The quantitative comparison of the methods B-RBM, H-RBM and W-RBM is based on the local orthotropic tissue orientation as well as on defined global and local cardiac characteristics.

Local tissue orientation To visualise the differences in the local tissue orientation for B-RBM, H-RBM and W-RBM, we compare the local fibre direction $\boldsymbol{f}$ of the MRI-based LV. The local difference in angle $\Delta\alpha_i^j$ is computed by

$$\Delta\alpha_i^j = \cos^{-1}\left(\left|\frac{\boldsymbol{f}_i^j(\boldsymbol{x})\cdot\boldsymbol{f}_i^{B-RBM}(\boldsymbol{x})}{\parallel \boldsymbol{f}_i^j(\boldsymbol{x}) \parallel\parallel \boldsymbol{f}_i^{B-RBM}(\boldsymbol{x}) \parallel}\right|\right), \tag{5.1}$$

where $\boldsymbol{f}_i^j$ represents the fibre vector for the methods j at the i-th integration point, $j \in \{\text{H-RBM, W-RBM}\}$, $i = 1, ..., N_p$ and N_p is the total number of integration points in the domain. The reference method B-RBM is defined by $\boldsymbol{f}_i^{B-RBM}$. To ensure comparability, the fibre angle is set to $\alpha = \pm 60^\circ$ (+ on endocardium and − on epicardium) and the sheet angle to $\beta = 0^\circ$ for B-RBM, H-RBM and W-RBM (no sheet angle to set for W-RBM).

Global and local cardiac characteristics To quantitatively compare the different approaches w.r.t. the electromechanical behaviour, we specify the following global and local cardiac characteristics (end-diastolic state: $t = 0.0$ ms; end-systolic state: $t = 300.0$ ms):

- global characteristics:
  - ejection fraction EF (%): $\mathrm{EF} = \dfrac{\mathrm{EDV\text{-}ESV}}{\mathrm{EDV}} \cdot 100\%$
  - developed peak pressure p_{max} (mmHg)
  - apical shortening a_s (%): $a_s = \dfrac{a_{\mathrm{ED}} - a_{\mathrm{ES}}}{a_{\mathrm{ED}}} \cdot 100\%$
  - volume reduction V_{red} (%): $V_{red} = \dfrac{\mathrm{MV_{ED}\text{-}MV_{ES}}}{\mathrm{MV_{ED}}} \cdot 100\%$
  - fractional wall thickening t_f (%): $t_f = \dfrac{t_{w,\mathrm{ES}} - t_{w,\mathrm{ED}}}{t_{w,\mathrm{ED}}} \cdot 100\%$
- local characteristics:
  - active fibre stress $\sigma^{act}_{1,1}$ (kPa)
  - fibre strain $\epsilon_{1,1}$ (%)

The local characteristics are computed by averaging the difference w.r.t. the chosen reference method B-RBM at each integration point i in the domain

$$\Delta^j_a = \frac{1}{N_p} \sum_{i=1}^{N_p} \left| \frac{a^j - a_i^{B-RBM}}{a_i^{B-RBM}} \right| \cdot 100\%, \tag{5.2}$$

with $a \in \{\sigma^{act}_{1,1}, \epsilon_{1,1}\}$ being the averaged local characteristics fibre stress and fibre strain, $i = 1, ..., N_p$ with N_p being the total number of integration points in the domain and $j \in \{\text{H-RBM, W-RBM}\}$.
We additionally introduce a sensitivity marker

$$s^j_c = \frac{\Delta^j_c}{M^j}, \tag{5.3}$$

with

$$\Delta^j_c \in \{\Delta^j_{\mathrm{EF}}, \Delta^j_{p_{max}}, \Delta^j_{a_s}, \Delta^j_{V_{red}}, \Delta^j_{t_f}, \Delta^j_{\sigma^{act}_{1,1}}, \Delta^j_{\epsilon_{1,1}}\}, \tag{5.4}$$

$$M^j = \max\{\Delta^j_{\mathrm{EF}}, \Delta^j_{p_{max}}, \Delta^j_{a_s}, \Delta^j_{V_{red}}, \Delta^j_{t_f}, \Delta^j_{\sigma^{act}_{1,1}}, \Delta^j_{\epsilon_{1,1}}\}. \tag{5.5}$$

The index $j \in \{\text{H-RBM, W-RBM}\}$ defines the given methods. The deviations from the reference method B-RBM are given by $\Delta^j_b = \frac{|b^j - b^{\text{B-RBM}}|}{b^{\text{B-RBM}}}$ for the global characteristics $b \in \{\mathrm{EF}, p_{max}, a_s, V_{red}, t_f\}$. In the following, the sensitivity marker s^j_c has the following classification: 0.0-0.25: low (●), 0.25-0.50: moderate (●), 0.50-1.0: high (●).

Table 5.1: Parameters for the electromechanical simulation.

active	$k = 0.20$ [-], $q = 0.2$ [-], $\beta = 5.0$ [-],
	$\nu_f = 0.0075$ [-], $\nu_n = 0.00375$ [-], $\lambda^a_{max} = 0.046$ [-],
passive	$a = 0.987$ kPa, $b = 6.874$ [-], $a_f = 3.890$ kPa,
	$b_f = 17.382$ [-], $a_s = 0.0333$ kPa, $b_s = 67.398$ [-],
	$a_{fs} = 0.392$ kPa, $b_{fs} = 0.054$ [-], $\kappa = 110$ kPa,
conduction	$d_{iso} = 0.15\text{mm}^2\text{ms}^{-1}$, $d_{ani} = 1.5\text{mm}^2\text{ms}^{-1}$,
excitation	$\alpha_e = 0.01$ [-], $\beta_e = 0.3$ [-], $c = 8$ [-], $\gamma = 1 \times 10^{-5}$ [-],
	$\mu_1 = 0.2$ [-], $\mu_2 = 0.3$ [-], $\hat{\Phi} = -60$mV for $t \in$[0,20]ms
MEF	$G_s = 10$ [-], $\phi_s = 0.6$ [-],
conversion	$k_{\phi_e} = 100$mV, $\delta_{\phi_e} = 80$mV, $k_t = 12.9$ms,
Windkessel model	$R_p = 30.0$ kPa ms mL^{-1}, R_{v1} =1.15 kPa ms mL^{-1}
	$C = 8$ mL kPa^{-1} ms^{-1}, R_{v2} =1.70 kPa ms mL^{-1}
spring/dashpot	$k_s = 1.8$mN mm^{-1}, $k_d = 1.0$mN ms mm^{-1}, $F_{init} = 18$mN
orientation tissue structure	W-RBM: see [168]; $\alpha = \pm 60^\circ$,
	B-RBM: $R = 60, R^* = 0, n = 1, B = 0, B^* = 0, K = 1, T = 0,$
	H-RBM: $R = 60, R^* = 0, n = 1, B = 0, B^* = 0, K = 1, T = 0,$
geometrical properties	$a_{en}^{INT} = 48.58$mm, $b_{en}^{INT} = 94.41$mm,
	$a_{ep}^{INT} = 63.63$mm, $b_{ep}^{INT} = 107.26$mm, $z_0^{INT} = 21.18$mm.

5.2 Results

5.2.1 Comparison of the local fibre orientation

A visualisation of the local difference in fibre direction $\boldsymbol{f}$ in terms of $\Delta\alpha_i^j$ based on Eq. (5.1) is depicted in Fig. 5.1 (a) and (b). The colour code shows $\Delta\alpha_i$ at every integration point i in the LV. Fig. 5.1 (a) illustrates $\Delta\alpha_i$ between the methods B-RBM and H-RBM. As observed in [170] for the hollow cylinder, the most significant difference is located close to the middle layers of the myocardium (yellow spots in the base region; $\Delta\alpha_i \geq 10^\circ$), see also Fig. 3.4 in Chapter 3. This result is underlined through Fig. 5.5 (b), where the difference is most significant in the transmural subregion 2 for method H-RBM ($\Delta\alpha$ =5.0°). For the region-specific comparison of the local tissue structure and cardiac characteristics in Fig. 5.5, 3 transmural and 5 apicobasal subregions are defined, see Fig. 5.2 (a) and (b). In Fig. 5.1 (b), it can be observed that for W-RBM, the apex regions as well as the outer and inner base regions show $\Delta\alpha_i \geq 10^\circ$ which can be mainly justified with a globally constant longitudinal axis for W-RBM compared to B-RBM and H-RBM. This observation can be quantified in more detail with Fig. 5.5 (a) W-RBM – apicobasal subregions 1 and 5 (6.8°/13.3°) and Fig. 5.5 (b) W-RBM – transmural subregions 1 and 3 (8.3°/10.1°). It is worth noting that the characteristic transmural behaviour

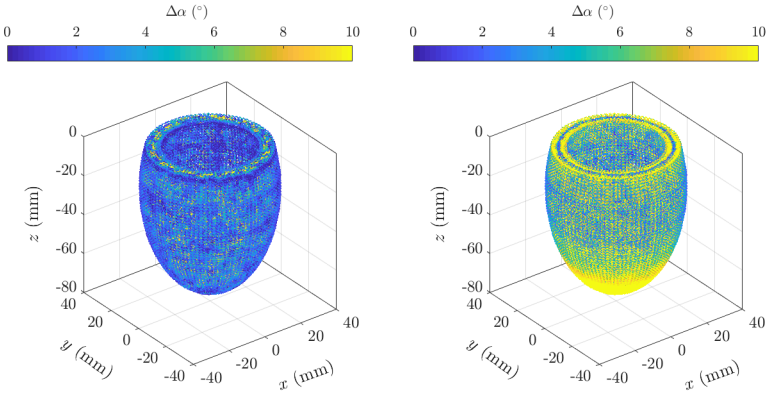

(a) B-RBM vs. H-RBM.

(b) B-RBM vs. W-RBM.

Figure 5.1: (a)-(b) The plots show the direct comparison (difference in fibre angle $\Delta\alpha_i^j$ in (°), see Eq. (5.1)) among the methods B-RBM, H-RBM and W-RBM. The colour bar limits have been set to optimise the visibility of the local differences. Reprinted with permission from [180]. Copyright © 2023 by J. Biomech.

of B-RBM, H-RBM and W-RBM, shown in Fig. 3.4 and discussed in [170], can be also seen in the subject-specific LV. In Fig. 5.5 (a), the highest $\Delta\alpha_i$ between B-RBM and H-RBM is located in the transmural subregion 2 while $\Delta\alpha_i$ between B-RBM and W-RBM is the smallest close to the transmural subregion 2 (blue concentric region at the base close to the middle layer in Fig. 5.1 (b)). In general, it can be stated that even though we limited the study to a small subset of RBMs (namely LDRBMs) and supposedly the same orientation ($\alpha = \pm 60°$, $\beta = \pm 0°$, Laplace equation-based transmural interpolation), one can observe significant differences in specific ventricular subregions w.r.t to the local myofibre orientation.

5.2.2 Comparison of the global and local cardiac characteristics

The electromechanical model with the tissue orientation obtained by B-RBM is utilised to fit the subject-specific global characteristics, see patient experiment (Exp.) in Tab. 5.2. The comparison of the global characteristics based on Tab. 5.2 between the measurement and the simulation B-RBM (Exp./B-RBM; EF (%): 58.10/58.19, p_{max} (mmHg): 110.00/110.00, a_s (%): 19.15/18.14, V_{red} (%): 19.43/21.99, t_f (%): 29.57/27.15) shows that the measured global

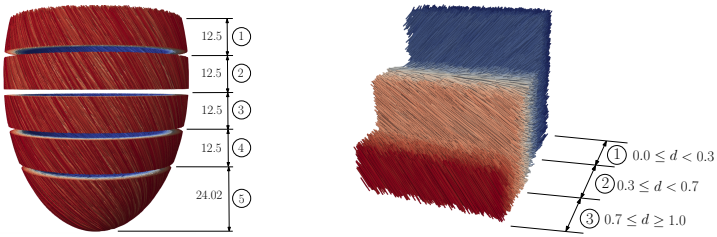

(a) apicobasal subregions. (b) transmural subregions.

Figure 5.2: (a)-(b) For the comparison of the local fibre orientation and the local cardiac characteristics, 3 transmural and 5 apicobasal subregions are defined. Reprinted with permission from [180]. Copyright © 2023 by J. Biomech.

characteristics are predicted with negligible deviations. Furthermore, the measured and simulated end-diastolic as well as end-systolic geometries are visualised and compared in Fig. 5.4 (yellow: simulation B-RBM; blue: measured) and underline the good agreement of the global cardiac characteristics in Tab. 5.2.

Global cardiac characteristics The results for the electromechanical simulation for B-RBM, H-RBM and W-RBM w.r.t. the global cardiac characteristics are summarised in Tab. 5.2. The myocardial volume reduction V_{red} (21.99%; 21.83%; 22.15%; $s_{V_{red}}^{\text{H-RBM}} = 0.16$; $s_{V_{red}}^{\text{W-RBM}} = 0.03$) and developed peak pressure p_{max} (110.00 mmHg; 109.67 mmHg; 104.91 mmHg; $s_{p_{max}}^{\text{H-RBM}} = 0.07$; $s_{p_{max}}^{\text{W-RBM}} = 0.20$) seem to be rather insensitive to a change of the LDRBM. A moderate influence of the LDRBM can be observed for the EF (58.19%; 58.11%; 54.48%; $s_{\text{EF}}^{\text{H-RBM}} = 0.03$; $s_{\text{EF}}^{\text{W-RBM}} = 0.28$). The apex shortening a_s (18.14%; 17.76%; 21.43%; $s_{a_s}^{\text{H-RBM}} = 0.45$; $s_{a_s}^{\text{W-RBM}} = 0.80$) as well as the fractional wall thickening t_f (27.15%; 26.46%; 21.47%; $s_{t_f}^{\text{H-RBM}} = 0.55$; $s_{t_f}^{\text{W-RBM}} = 0.92$) significantly differ when changing the LDRBM. In general, the global characteristics of B-RBM and H-RBM are closer to each other compared to W-RBM (reasonable based on the comparison of the local myofibre orientations), see also Fig. 5.3 (a)-(c) for the PV-loops. Interestingly, by applying the sensitivity marker in Eq. (5.4) to a similar study about the comparison of different LDRBMs and their influence on different mechanical biomarkers in [171], a comparable behaviour of the global characteristics could be observed with the highest sensitivity for the apical shortening a_s and fractional wall thickening t_f, moderate influence on EF and a less sensitive developed peak pressure p_{max}, see Tab. 5.3

Table 5.2: Global cardiac characteristics (EF: ejection fraction; p_{max}: peak pressure; a_s: apical shortening; V_{red}: volume reduction of the myocardium; t_f: fractional wall thickening) of the measured subject (see first column Exp.) as well as for the simulations B-RBM, H-RBM and W-RBM. Deviations of the global characteristics for H-RBM and W-RBM from the reference method B-RBM are defined by Δ^j_{EF}, $\Delta^j_{p_{max}}$, $\Delta^j_{a_s}$, $\Delta^j_{V_{red}}$, $\Delta^j_{t_f}$. The columns $s_c^{\text{H-RBM}}$ and $s_c^{\text{W-RBM}}$ show the level of sensitivity of each global characteristic. In order to improve the readability of the table, the sensitivity marker is coloured as follows: 0.0-0.25: low (●), 0.25-0.50: moderate (●), 0.50-1.0; high (●).

	Exp.	B-RBM	H-RBM	$s_c^{\text{H-RBM}}$	W-RBM	$s_c^{\text{W-RBM}}$
EF (%)	58.10	58.19	58.11	0.03	54.48	0.28
Δ^j_{EF} (%)	-	-	0.14	-	6.38	-
p_{max} (mmHg)	110.00	110.00	109.67	0.07	104.91	0.20
$\Delta^j_{p_{max}}$ (%)	-	-	0.30	-	4.63	-
a_s (%)	19.15	18.14	17.76	0.45	21.43	0.80
$\Delta^j_{a_s}$ (%)	-	-	2.09	-	18.14	-
V_{red} (%)	19.43	21.99	21.83	0.16	22.15	0.03
$\Delta^j_{V_{red}}$ (%)	-	-	0.73	-	0.73	-
t_f (%)	29.57	27.15	26.46	0.55	21.47	0.92
$\Delta^j_{t_f}$ (%)	-	-	2.54	-	20.92	-

Table 5.3: Sensitivity marker $s_c^{\text{H-RBM}}$ and $s_c^{\text{W-RBM}}$ based on Eq. (5.4) with $M^j = \max\{\Delta^j_{\mathrm{EF}}, \Delta^j_{p_{max}}, \Delta^j_{a_s}, \Delta^j_{t_f}\}$ to ensure the comparability with the study in [59]. The sensitivity marker $s_c^{\text{D-RBM}}$ and $s_c^{\text{R-RBM}}$ are computed based on Eq. (5.4) and the data in [59] (Table 7 ($\mathrm{EF_{LV}}$, $\mathrm{P_{LV}}$, LFS, WT)). The B-RBM method in Table 7 ([59]) is chosen as the reference method for $s_c^{\text{D-RBM}}$ and $s_c^{\text{R-RBM}}$. Overall, the sensitivity marker shows similar tendencies with regard to the global characteristics.

	$s_c^{\text{H-RBM}}$	$s_c^{\text{W-RBM}}$	$s_c^{\text{D-RBM}}$	$s_c^{\text{R-RBM}}$
EF (%)	0.06	0.30	0.63	0.33
p_{max} (mmHg)	0.11	0.22	0.16	0.13
a_s (%)	0.82	0.87	1.00	1.00
t_f (%)	1.00	1.00	0.87	0.28

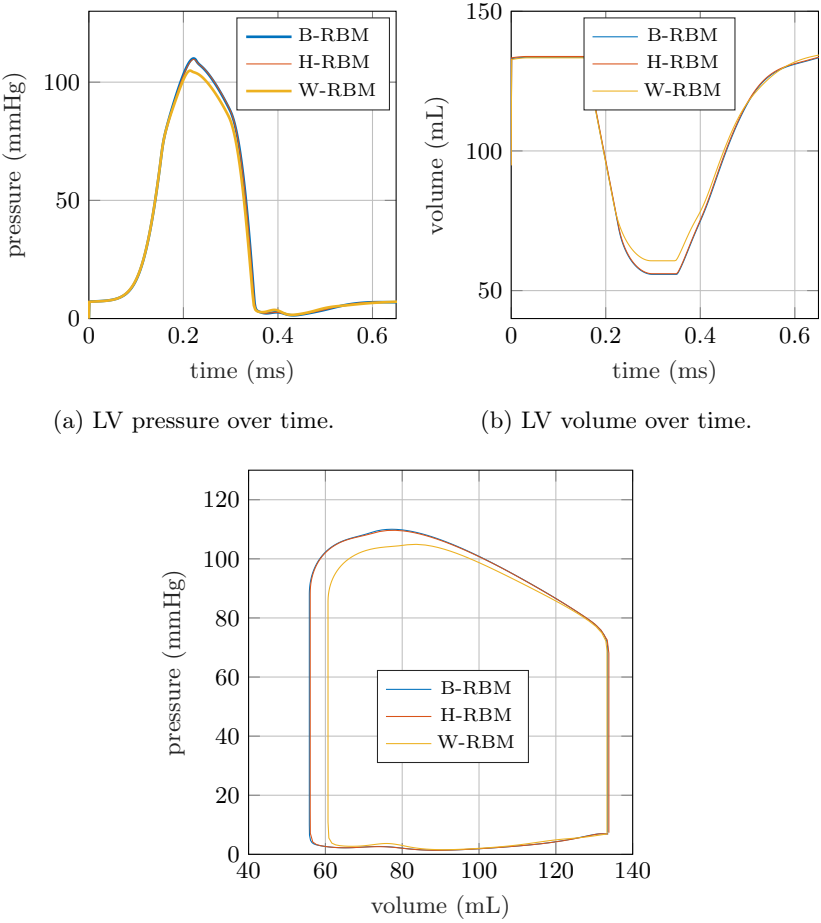

(a) LV pressure over time.

(b) LV volume over time.

(c) LV PV-loop.

Figure 5.3: (a)temporal evolution of the LV pressure (mmHg) over the cardiac cycle for the method B-RBM, H-RBM and W-RBM. (b) temporal evolution of the LV volume (mL) over the cardiac cycle for the method B-RBM, H-RBM and W-RBM. (c) LV pressure-volume loop for the method B-RBM, H-RBM and W-RBM. Reprinted with permission from [180]. Copyright © 2023 by J. Biomech.

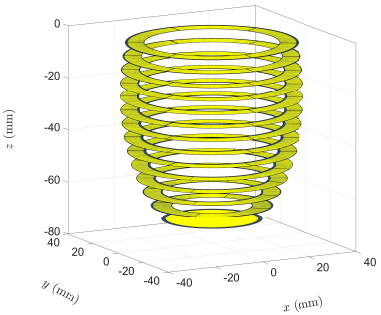

(a) MRI and FEM – ED.

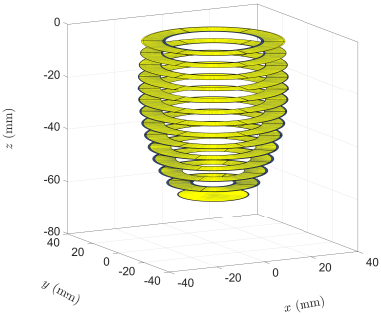

(b) MRI and FEM – ES.

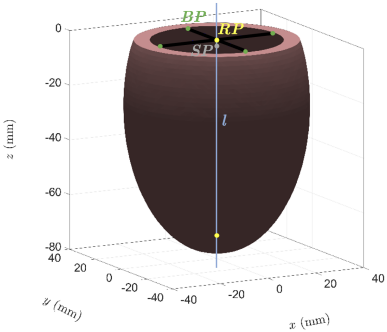

(c) Orientation of geo.

Figure 5.4: (a) Comparison of the MRI- and FEM-based geometry in the end-diastolic state. (b) Comparison of the MRI- and FEM-based geometry in the end-systolic state. (c) Initial orientation of the MRI- and FEM-based LV (yellow: simulation B-RBM; blue: MRI) for the comparison of the geometries (geo.). Points BP (green) at the base are defined in order to set the basic orientation of the ventricle. The reference points RP (yellow) define the longitudinal axis l (blue) while the point SP (grey) defines the position of the first cutting plane perpendicular to the longitudinal axis l. Reprinted with permission from [180]. Copyright © 2023 by J. Biomech.

Local cardiac characteristics In Fig. 5.5 (c)–(f), the results for the local cardiac characteristics (fibre stress $\Delta_{\sigma_{1,1}^{act}}$ and fibre strain $\Delta_{\epsilon_{1,1}}$ based on Eq. (5.2)) are depicted for the different apicobasal and transmural subregions at the time step of 300 ms corresponding to the end-systolic state in the cardiac cycle.
Firstly, it can be observed in Fig. 5.5 (c)–(f) that the local characteristics are significantly influenced by B-RBM, H-RBM and W-RBM. The highest deviations in fibre stress and fibre strain for H-RBM and W-RBM are $\Delta_{\sigma_{1,1}^{act}} = 2.2\%/\Delta_{\sigma_{1,1}^{act}} = 8.5\%$ and $\Delta_{\epsilon_{1,1}} = 4.6\%/\Delta_{\epsilon_{1,1}} = 22.7\%$. In general, B-RBM and H-RBM show more similar characteristics, which correlates with the results for the local fibre orientation.
Secondly, the difference in fibre strain $\Delta_{\epsilon_{1,1}}$, compared to the fibre stress $\Delta_{\sigma_{1,1}^{act}}$, is significantly higher for both methods (see e.g. $s_{\Delta_{\epsilon_{1,1}}}^{\text{W-RBM}} = 1.00$ in apicobasal subregion 1 and $s_{\Delta_{\epsilon_{1,1}}}^{\text{H-RBM}} = 1.00$ in transmural subregion 1). Additionally, the sensitivity markers $s_{\Delta_{\epsilon_{1,1}}}^{\text{W-RBM}} = 1.00$ in apicobasal subregion 1 and $s_{\Delta_{\epsilon_{1,1}}}^{\text{H-RBM}} = 1.00$ in transmural subregion 1 show that the local characteristic $\Delta_{\epsilon_{1,1}}$ is the most sensitive characteristic among all global and local characteristics. Furthermore, it is worth noting that $\Delta_{\epsilon_{1,1}}$ and $\Delta_{\sigma_{1,1}^{act}}$ are still averaged over large subregions and smaller subregions will lead to even larger deviations (e.g. for a small subregion ($N_p = 1000$) of the apicobasal subregion 1, the maximum for $\Delta_{\epsilon_{1,1}}^{\text{W-RBM}} = 80.42\%/\Delta_{\epsilon_{1,1}}^{\text{H-RBM}} = 16.86\%$ and $\Delta_{\sigma_{1,1}^{act}}^{\text{W-RBM}} = 25.01\%/\Delta_{\sigma_{1,1}^{act}}^{\text{H-RBM}} = 5.97\%$).
Thirdly, it is visible in Fig. 5.5 (c) and (e) that the differences for W-RBM in fibre stress $\sigma_{1,1}^{act}$ and fibre strain $\epsilon_{1,1}$ for the apicobasal subregions correlate with the results for the local fibre orientation in Fig. 5.5 (a). W-RBM exhibits a significantly higher $\Delta_{\sigma_{1,1}^{act}}$ of 8.5% and 8.4% and $\Delta_{\epsilon_{1,1}}$ of 22.7% and 14.9% for the apicobasal subregions 1 and 5 (base and apex). In contrast, for the transmural subregions, $\Delta_{\sigma_{1,1}^{act}}$ and $\Delta_{\epsilon_{1,1}}$ exhibit the largest difference in the transmural subregion 2 (see Fig. 5.5 (d) and (f), $\Delta_{\sigma_{1,1}^{act}}$ =8.4% and $\Delta_{\epsilon_{1,1}} = 16.1\%$), showing an opposite behaviour compared to Fig. 5.5 (b), where the difference in fibre orientation is smallest in transmural subregion 2 (4.1%). A possible explanation for this could be the rapid change in fibre angle α in the subregion 2 for W-RBM (see also Fig. 3.4 in Chapter 3). To ensure that the findings are not a time step-specific behaviour, $\Delta_{\sigma_{1,1}^{act}}$ and $\Delta_{\epsilon_{1,1}}$ are additionally plotted for different time frames in the cardiac cycle, see Fig. 5.6. We evaluated the local characteristics for all integration points in the time period of 250 ms to 350 ms. The local difference in the defined local cardiac characteristics of fibre stress $\sigma_{1,1}^{act}$ and fibre strain $\epsilon_{1,1}$ can be observed independently of the chosen time frame.
Interestingly, similar observations have been made by [267] and [268]. In [267], for different transverse or helix angle, they stated that the changes in fibre

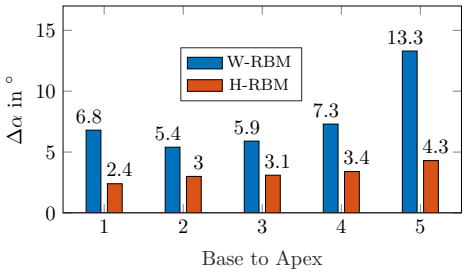

(a) $\Delta\alpha$ in ° – apicobasal

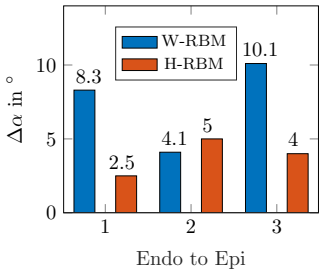

(b) $\Delta\alpha$ in ° – transmural

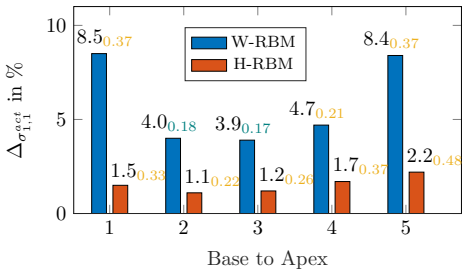

(c) $\Delta_{\sigma_{1,1}^{act}}$ – apicobasal

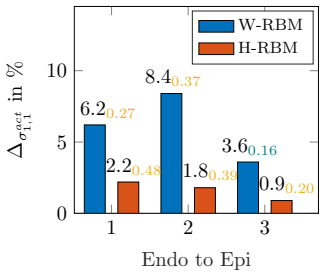

(d) $\Delta_{\sigma_{1,1}^{act}}$ – transmural

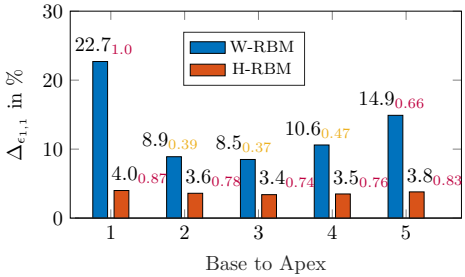

(e) $\Delta_{\epsilon_{1,1}}$ – apicobasal

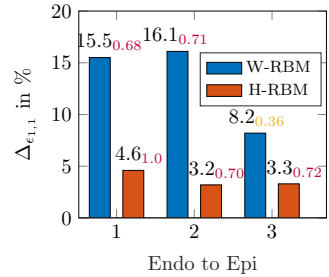

(f) $\Delta_{\epsilon_{1,1}}$ – transmural

Figure 5.5: Comparison of the local fibre orientation, stress and strain for B-RBM, H-RBM and W-RBM. The first and second column represent the apicobasal and transmural subregions defined in Fig. 5.2 (a) and (b), respectively. A single data point for a subregion is computed by averaging the local difference at each integration point in the considered subregion, see Eq. (5.2). The coloured indices are the sensitivity marker for each subregions with: 0.0-0.25: low (●), 0.25-0.50: moderate (●), 0.50-1.0; high (●). Reprinted with permission from [180]. Copyright © 2023 by J. Biomech.

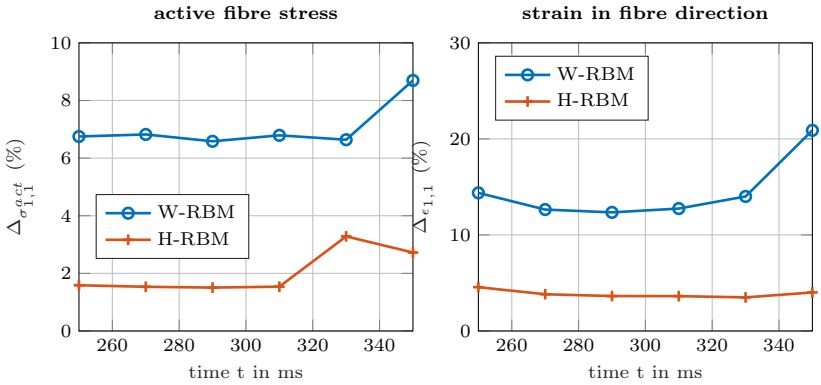

(a) Average of local deviation $\Delta_{\sigma^{act}_{1,1}}$ for the different methods.

(b) Average of local deviation $\Delta_{\epsilon_{1,1}}$ for the different methods.

Figure 5.6: Comparison of the active fibre stress $\sigma^{act}_{1,1}$ and the strain in fibre direction $\epsilon_{1,1}$ for the different approaches B-RBM, H-RBM and W-RBM for $t = 235$ms to $t = 330$ms. In (a) the average of the local difference for the active fibre stress $\Delta_{\sigma^{act}_{1,1}}$ are depicted (w.r.t. the chosen reference method B-RBM), while in (b) the corresponding average of the local deviation for the strain in fibre direction $\Delta_{\epsilon_{1,1}}$ is shown. A single data point in the plots is created by Eq. (5.2). Reprinted with permission from [180]. Copyright © 2023 by J. Biomech.

orientation hardly affect the pressure-volume relation of the ventricle, while the local measures like active muscle fibre stress and sarcomere length significantly vary. [268] concludes in the study about the effect of the fibre orientation that the macroscopic measures like the pressure-volume loop, stroke volume and ejection fraction are relatively insensitive to the varying fibre orientation. Additionally, [268] expect that the fibre direction has a significant impact on local mechanical quantities (e.g. stresses, and strains).

5.3 Summary

In the present study, three Laplace equation-based orthotropic tissue structure models (B-RBM, H-RBM, W-RBM) for human heart simulations are compared. The comparison is based on a subject-specific human LV geometry obtained via MRI and a fully-coupled electromechanical model. We show that for the initial fit of parameters, see Tab. 5.1, the electromechanical model is able to capture

all main characteristics of the measurement. Additionally, the geometrical comparison between the MRI- and FEM-based geometry of the end-systolic and end-diastolic state shows a satisfying agreement, see Fig. 5.4. The focus of this study is on the method-specific local orthotropic tissue structure (fibre orientation) as well as on important global (ejection fraction, peak pressure, apex shortening, myocardial volume reduction, fractional wall thickening) and local (active fibre stress, fibre strain) characteristics. The local fibre orientation significantly differs for all methods, especially in the base and apex regions for W-RBM. Despite the significant difference in the local myofibre orientation, the global cardiac characteristics show a more diverse picture. While the myocardial volume reduction and peak pressure show a rather insensitive behaviour to a change of the LDRBM, the apical shortening as well as the fractional wall thickening sensitively react. The EF shows moderate sensitivity. The local cardiac characteristic, fibre stress and strain, seem to be highly sensitive and in general more than the global characteristics.
The main findings underline the importance of the method-specific orthotropic tissue structure. Even though we limited the study to a small subset of related tissue structure models (LDRBMs) and supposedly the same transmural orientation ($\alpha = \pm 60°$, $\beta = \pm 0°$, Laplace equation-based transmural interpolation), one can observe significant differences w.r.t the local myofibre orientation. Therefore, caution is advised when comparing studies with different orthotropic tissue structure models, even if they supposedly have the same transmural orientation. E.g. for the prediction of the myocardial volume reduction, B-RBM, H-RBM and W-RBM predict similar results (i.e. comparison among studies with different orthotropic tissue structure models B-RBM, H-RBM and W-RBM feasible). For the prediction of e.g. local characteristics like fibre stress or fibre strain, the results seem to be very sensitive w.r.t. the local myofibre orientation (i.e. comparison among studies with different orthotropic tissue structure models B-RBM, H-RBM and W-RBM are not feasible).

6 Background – artificial muscle model

This chapter serves as a theoretical background for the subsequent Chapter 7 on the variational formulation and implementation of the dynamic viscoelastic electromechanical shell model. In Section 6.1, the balance law of linear momentum as well as a reduced set of Maxwell's equations are introduced. The coupling between the mechanical and electrical field is described in Section 6.2. In Section 6.3, local Euler-Lagrange equations are derived via the Lagrange-d'Alembert principle for the two underlying variational principles, namely the variational principle of virtual work and the three-field variational principle of Hu-Washizu. The variational principle of Hu-Washizu is considered in this work since displacement-based shell formulations are prone to e.g. locking, especially shear and membrane locking.

6.1 Governing equations for a dielectric continuum

6.1.1 Balance of linear and angular momentum

Considering an arbitrary domain $\mathcal{B}_0 \in \mathbb{R}^3$, the well-known local balance law of linear momentum reads

$$\nabla_{\boldsymbol{X}} \cdot \mathbf{P}^{\mathrm{m,e,v}} + \boldsymbol{b}_0 = \rho_0 \ddot{\boldsymbol{x}} \qquad \text{in} \qquad \mathcal{B}_0, \tag{6.1}$$

with the Dirichlet and Neumann boundary conditions

$$\boldsymbol{x} = \hat{\boldsymbol{x}} \qquad \text{on} \qquad \partial_u \mathcal{B}_0, \tag{6.2}$$

$$\mathbf{P}^{\mathrm{m,e,v}} \cdot \boldsymbol{N} = \hat{\boldsymbol{T}} \qquad \text{on} \qquad \partial_T \mathcal{B}_0, \tag{6.3}$$

where $\mathbf{P}^{\mathrm{m,e,v}}$ is the first Piola-Kirchhoff stress tensor consisting of mechanical, electrical and viscous parts. The body force vector is denoted by $\boldsymbol{b}_0$, ρ_0 indicates the mass density in the initial configuration and $\boldsymbol{x}$ is the position vector of an arbitrary point in the domain $\mathcal{B}_0$. The prescribed displacement/position vector on $\partial_u \mathcal{B}_0$ and surface traction on $\partial_T \mathcal{B}_0$ is denoted by $\hat{\boldsymbol{x}}$ and $\hat{\boldsymbol{T}}$, respectively. The vector $\boldsymbol{N}$ represents the unit outward normal on $\partial_T \mathcal{B}_0$. The local balance of angular momentum yields

$$\mathbf{F}(\mathbf{P}^{\mathrm{m,e,v}})^T = (\mathbf{P}^{\mathrm{m,e,v}})\mathbf{F}^T. \tag{6.4}$$

6.1.2 Maxwell's equations

Maxwell's equations are a set of coupled PDEs to describe time-dependent electromagnetic phenomena. For the subsequent variational formulation, a reduced set of Maxwell's equations is taken into account by neglecting magnetic effects and free charges, see [198, 222, 269, 270, 271]. Considering the arbitrary domain $\mathcal{B}_0 \in \mathbb{R}^3$, the reduced set of Maxwell's equations reads:

$$\nabla_{\boldsymbol{X}} \times \boldsymbol{E}^e = \boldsymbol{0} \qquad \text{in} \qquad \mathcal{B}_0, \tag{6.5}$$

$$\nabla_{\boldsymbol{X}} \cdot \boldsymbol{D} = 0 \qquad \text{in} \qquad \mathcal{B}_0, \tag{6.6}$$

with Dirichlet and Neumann boundary conditions

$$\phi = \hat{\phi} \qquad \text{on} \qquad \partial_\phi \mathcal{B}_0, \tag{6.7}$$

$$\boldsymbol{D} \cdot \boldsymbol{N} = \hat{Q} \qquad \text{on} \qquad \partial_Q \mathcal{B}_0, \tag{6.8}$$

where $\boldsymbol{E}^e$ and $\boldsymbol{D}$ represent the electrical field and displacement, respectively. The electric potential is described by ϕ. The unit outward normal on $\partial_Q \mathcal{B}_0$ is given by $\boldsymbol{N}$ and $\hat{Q}$ are the charges per unit area on $\partial_Q \mathcal{B}_0$. The definition of the electric field $\boldsymbol{E}^e$ follows as

$$\boldsymbol{E}^e = -\frac{\partial \phi}{\partial \boldsymbol{X}}. \tag{6.9}$$

6.2 Constitutive laws

The coupling between the electrical and mechanical field can be described by a potential energy density functional $\Omega(\mathbf{F}, \boldsymbol{E}^e)$, where $\Omega(\mathbf{F}, \boldsymbol{E}^e)$ is additively split and defined as

$$\Omega(\mathbf{F}, \boldsymbol{E}^e) = \Omega^m(\mathbf{F}) + \Omega^{em}(\mathbf{F}, \boldsymbol{E}^e) + \Omega^e(\boldsymbol{E}^e), \tag{6.10}$$

with $\Omega^m(\mathbf{F})$, $\Omega^{em}(\mathbf{F}, \boldsymbol{E}^e)$ and $\Omega^e(\boldsymbol{E}^e)$ representing the mechanical, coupled and electrical parts, respectively. Concerning Eq. (6.1) and Eq. (6.6), the first Piola-Kirchhoff stress tensor $\mathbf{P}^{\mathrm{m,e}}$ and the electric displacement $\boldsymbol{D}$ are defined as

$$\mathbf{P}^{\mathrm{m,e}} = \frac{\partial \Omega(\mathbf{F}, \boldsymbol{E}^e)}{\partial \mathbf{F}} = \frac{\partial \Omega^m}{\partial \mathbf{F}} + \frac{\partial \Omega^{em}}{\partial \mathbf{F}}, \tag{6.11}$$

$$\boldsymbol{D} = -\frac{\partial \Omega(\mathbf{F}, \boldsymbol{E}^e)}{\partial \boldsymbol{E}^e} = -\frac{\partial \Omega^e}{\partial \boldsymbol{E}^e} - \frac{\partial \Omega^{em}}{\partial \boldsymbol{E}^e}. \tag{6.12}$$

The potential energy density $\Omega(\mathbf{F}, \boldsymbol{E}^{\boldsymbol{e}})$ is a functional of the deformation gradient $\mathbf{F}$ and the electric field $\boldsymbol{E}^{e}$ and reads (e.g., [270, 222, 209]),

$$\Omega(\mathbf{F}, \boldsymbol{E}^{\boldsymbol{e}}) = \underbrace{\frac{\mu}{2}(\boldsymbol{I}_{\mathbf{C}} - 3) - \mu \ln J + \frac{\lambda}{2}(\ln J)^2}_{\text{Neo-Hookean model}} + \underbrace{c_1 \boldsymbol{E}^{\boldsymbol{e}} \cdot \boldsymbol{E}^{\boldsymbol{e}} + c_2 \mathbf{C} : (\boldsymbol{E}^{\boldsymbol{e}} \otimes \boldsymbol{E}^{\boldsymbol{e}})}_{\text{non-linear coupling}} - \underbrace{\frac{1}{2}\epsilon_0 J \mathbf{C}^{-1} : (\boldsymbol{E}^{\boldsymbol{e}} \otimes \boldsymbol{E}^{\boldsymbol{e}})}_{\text{free space term in vacuum}}, \tag{6.13}$$

with μ and λ being the Lamé parameters. The Lamé parameters are related to the bulk modulus κ by $\kappa = \lambda + \frac{2}{3}\mu$. The trace of the right Cauchy-Green tensor $\mathbf{C}$ is given by $\boldsymbol{I}_{\mathbf{C}}$ and the Jacobian J is defined by $J = \det(\mathbf{F})$. The vacuum permittivity is denoted by ϵ_0, while c_1 and c_2 are electrical material parameters, where c_2 affects the coupling between the electrical and mechanical field. The strain energy is decomposed into a purely mechanical elastic part (Neo-Hookean model (see [225]), the non-linear coupling part between $\mathbf{C}$ and $\boldsymbol{E}^{\boldsymbol{e}}$ and the free space term *in vacuum*. The last two terms in Eq. (6.13) express the electromechanical coupling. It is worth noting that the Neo-Hookean material model is, in general, not suitable for representing very high strains of dielectric materials (see [271, 272]). The Yeoh, Mooney-Rivlin and Ogden material models seem to be more appropriate [273, 274, 275, 276, 277, 278]. In this work, the Neo-Hookean material model is used since we stay in the regime of moderate strains for the subsequent numerical examples employed.
To account for viscosity in the dielectric material, viscous stress $\mathbf{P}^{\mathrm{v}}$ is defined as

$$\mathbf{P}^{\mathrm{v}}(\mathbf{F}, \dot{\mathbf{F}}) = \frac{1}{2} J \eta \left(\mathbf{F}^{-T} \cdot \dot{\mathbf{F}}^{T} \cdot \mathbf{F}^{-T} + \dot{\mathbf{F}} \cdot \mathbf{C}^{-1} \right), \tag{6.14}$$

with the damping parameter η, the right Cauchy-Green tensor $\mathbf{C}$ and the time derivative of the deformation gradient $\dot{\mathbf{F}} = \frac{\partial \dot{\mathbf{F}}}{\partial t} = \frac{\partial \dot{\boldsymbol{x}}}{\boldsymbol{X}}$, see e.g. the Kelvin-Voigt model in [279].

6.3 Variational principles for 3D continuum electromechanics

In the following section, the local Euler-Lagrange equations for the 3D continuum electromechanics are derived from the Lagrange-d'Alembert principle. The local Euler-Lagrange equations are derived for the two underlying variational principles, namely the variational principle of virtual work and the three-field principle of Hu-Washizu.

Principle of virtual work The Lagrange-d'Alembert principle reads

$$\delta S + \int_0^T \delta W^{ext} \, dt = 0 \quad \forall \delta \boldsymbol{x}, \tag{6.15}$$

where all variations vanish on the boundary of the space-time domain. The parameter S represents the action, W^{ext} the work of the external non-conservative forces and T the total time interval. The variations at the endpoints $\delta\boldsymbol{x}(0)$ and $\delta\boldsymbol{x}(T)$ are fixed in time. The work W^{ext} of the external non-conservative forces includes the external surface traction, external body forces, external surface charges and viscous stresses *(in the event of viscous material behaviour)*. The action S is defined as the space-time integral over the Lagrangian density $\mathcal{L}$

$$S(\boldsymbol{x}, \phi) = \int_0^T \int_{\mathcal{B}_0} \mathcal{L}(\dot{\boldsymbol{x}}, \mathbf{F}, \boldsymbol{E}^e)\ dV\ dt, \tag{6.16}$$

and describes the dynamic behaviour of the electromechanical system. The Lagrangian density $\mathcal{L}$ reads

$$\mathcal{L}(\dot{\boldsymbol{x}}, \mathbf{F}, \boldsymbol{E}^e) = \mathcal{T}(\dot{\boldsymbol{x}}) - \Omega(\mathbf{F}, \boldsymbol{E}^e), \tag{6.17}$$

with the spatial position vector $\boldsymbol{x}$, its time derivative $\dot{\boldsymbol{x}}$ and the strain energy density functional $\Omega(\mathbf{F}, \boldsymbol{E}^e)$ being a coupled function of the deformation gradient $\mathbf{F}$ and the electric field $\boldsymbol{E}^e$. The kinetic energy density $\mathcal{T}(\dot{\boldsymbol{x}})$ is given by

$$\mathcal{T}(\dot{\boldsymbol{x}}) = \frac{1}{2}\rho_0 \dot{\boldsymbol{x}} \cdot \dot{\boldsymbol{x}}. \tag{6.18}$$

By integrating the kinetic energy density $\mathcal{T}(\dot{\boldsymbol{x}})$ over the domain $\mathcal{B}_0$, the kinetic energy T follows as

$$T = \int_{\mathcal{B}_0} \mathcal{T}(\dot{\boldsymbol{x}})\ dV. \tag{6.19}$$

Similarly, the potential energy Π is obtained by integration of the strain energy density functional $\Omega(\mathbf{F}, \boldsymbol{E}^e)$ over the computational domain $\mathcal{B}_0$

$$\Pi = \int_{\mathcal{B}_0} \Omega(\mathbf{F}, \boldsymbol{E}^e)\ dV. \tag{6.20}$$

Therefore, the variation of the action S is given by the variation of the kinetic energy density $\mathcal{T}(\dot{\boldsymbol{x}})$ and the variation of the strain energy density functional $\Omega(\mathbf{F}, \boldsymbol{E}^e)$

$$\delta S = \int_0^T \int_{\mathcal{B}_0} (\delta\mathcal{T} - \delta\Omega)\ dV\ dt, \tag{6.21}$$

where $\delta\mathcal{T}(\dot{\boldsymbol{x}})$ and $\delta\Omega(\mathbf{F}, \boldsymbol{E}^e)$ read

$$\begin{aligned} \delta\mathcal{T} &= \rho_0 \dot{\boldsymbol{x}} \cdot \delta\dot{\boldsymbol{x}}, \\ \delta\Omega &= \partial_{\mathbf{F}}\Omega\ :\ \delta\mathbf{F} + \partial_{\boldsymbol{E}^e}\Omega \cdot \delta\boldsymbol{E}^e, \end{aligned} \tag{6.22}$$

with $\delta\mathbf{F} = \frac{\partial \delta \boldsymbol{x}}{\partial \boldsymbol{X}}$ and $\delta \boldsymbol{E}^e = -\frac{\partial \delta \phi}{\partial \boldsymbol{X}}$ and $\boldsymbol{X}$ being the position vector in the reference configuration. Applying integration by parts, zero variations at the endpoints and using the divergence theorem lead to the variation of the action

$$\delta S = \int_0^T \left\{ \int_{\mathcal{B}_0} \left[\delta \boldsymbol{x} \cdot (-\rho_0 \ddot{\boldsymbol{x}} + \nabla_{\boldsymbol{X}} \cdot \partial_{\mathbf{F}} \Omega) + \delta\phi(-\nabla_{\boldsymbol{X}} \cdot \partial_{\boldsymbol{E}^e} \Omega) \right] dV \right.$$
$$\left. + \int_{\partial \mathcal{B}_0} \left[\delta \boldsymbol{x} \cdot (-\partial_{\mathbf{F}} \Omega \cdot \boldsymbol{N}) + \delta\phi(\partial_{\boldsymbol{E}^e} \Omega \cdot \boldsymbol{N}) \right] dA \right\} dt, \tag{6.23}$$

where $\delta \boldsymbol{x}$ and $\delta\phi$ represent the variation of the position vector $\boldsymbol{x}$ and the electric potential ϕ, respectively. The external non-conservative work (resulting from body force, surface traction, surface charge, and viscous force) is given by

$$W^{ext} = \int_{\mathcal{B}_0} \boldsymbol{x} \cdot \boldsymbol{b}_0 \, dV + \int_{\partial_T \mathcal{B}_0} \boldsymbol{x} \cdot \hat{\boldsymbol{T}} \, dA - \int_{\partial_Q \mathcal{B}_0} \phi \cdot \hat{Q} \, dA$$
$$- \int_{\mathcal{B}_0} \mathbf{F} \, : \, \mathbf{P}^{\mathrm{v}} \, dV, \tag{6.24}$$

where the body force $\boldsymbol{b}_0$ is acting in the domain $\mathcal{B}_0$ and $\hat{\boldsymbol{T}}$ is the prescribed surface traction on the boundary $\partial_T \mathcal{B}_0$ in the reference configuration. The surface charge is represented by $\hat{Q}$ and $\mathbf{P}^{\mathrm{v}}$ is the viscous stress contribution in terms of the first Piola-Kirchhoff stress tensor. By taking variations of the external non-conservative work (non-conservative quantities are treated fixed during variation), integration by parts, using the divergence and the fundamental lemma of the calculus of variations, the Lagrange-d'Alembert principle yields the local Euler-Lagrange equations

$$\text{balance eq.} \qquad \nabla_{\boldsymbol{X}} \cdot (\mathbf{P}^{\mathrm{m,e}} + \mathbf{P}^{\mathrm{v}}) + \boldsymbol{b}_0 = \rho_0 \ddot{\boldsymbol{x}} \quad \text{in} \quad \mathcal{B}_0, \tag{6.25}$$
$$\text{balance eq.} \qquad \nabla_{\boldsymbol{X}} \cdot \boldsymbol{D} = 0 \quad \text{in} \quad \mathcal{B}_0, \tag{6.26}$$
$$\text{static BC} \qquad (\mathbf{P}^{\mathrm{m,e}} + \mathbf{P}^{\mathrm{v}}) \cdot \boldsymbol{N} = \hat{\boldsymbol{T}} \quad \text{on} \quad \partial_T \mathcal{B}_0, \tag{6.27}$$
$$\text{static BC} \qquad \boldsymbol{D} \cdot \boldsymbol{N} = \hat{Q} \quad \text{on} \quad \partial_Q \mathcal{B}_0. \tag{6.28}$$

In addition, the geometric boundary condition $\boldsymbol{x} = \hat{\boldsymbol{x}}$ on $\partial_u \mathcal{B}_0$ and the electric potential boundary condition $\phi = \hat{\phi}$ on $\partial_\phi \mathcal{B}_0$ have to be fulfilled.

Principle of Hu-Washizu – mechanical For the sake of simplicity, the purely elastodynamic problem is described first. We refer to Eq. (6.21) for the variation of the action

$$\delta S = \int_0^T \int_{\mathcal{B}_0} \delta \mathcal{L} \, dV \, dt = \int_0^T \int_{\mathcal{B}_0} (\delta \mathcal{T} - \delta \Omega) \, dV \, dt. \tag{6.29}$$

Slightly abusing the previous notation of $\Pi, \mathcal{L}$ and Ω, the well-known Hu-Washizu three-field potential energy functional Π is given as (see [280, 281]),

$$\Pi = \int_{\mathcal{B}_0} \Omega(\mathbf{E}) + \mathbf{S} : \left(\mathbf{E}^{\boldsymbol{x}} - \mathbf{E}\right)\, dV, \tag{6.30}$$

where Π is not exclusively a function of the displacement $\boldsymbol{u} = \boldsymbol{x} - \boldsymbol{X}$ or the deformation gradient $\mathbf{F}$, but additionally depends on the assumed stress $\mathbf{S}$ and assumed strain $\mathbf{E}$. The strain energy density functional $\Omega(\mathbf{E})$ is a function of the assumed strain $\mathbf{E}$, while $\mathbf{E}^x = \mathbf{E}(\boldsymbol{x})$ represents the Green-Lagrangian strain based on the displacement field $\boldsymbol{u}$. The assumed strain $\mathbf{E}$ can be defined as $\mathbf{E} = \mathbf{E}^x + \tilde{\mathbf{E}}$, where $\tilde{\mathbf{E}}$ represents the independent assumed strain.
The action S including the three independent fields $\boldsymbol{x}, \mathbf{E}$ and $\mathbf{S}$ becomes

$$\int_{\mathcal{B}_0} \mathcal{L}(\dot{\boldsymbol{x}}, \mathbf{E}, \mathbf{S})\, dV = \int_{\mathcal{B}_0} \mathcal{T}(\dot{\boldsymbol{x}}) - \left[\Omega(\mathbf{E}) + \mathbf{S} : \left(\mathbf{E}^x - \mathbf{E}\right)\right]\, dV. \tag{6.31}$$

The external non-conservative work (resulting from body force, surface traction and viscous force) reads

$$\begin{aligned} W^{ext} = &\int_{\mathcal{B}_0} \boldsymbol{x} \cdot \boldsymbol{b}_0\, dV + \int_{\partial_T \mathcal{B}_0} \boldsymbol{x} \cdot \hat{\boldsymbol{T}}\, dA \\ &- \int_{\mathcal{B}_0} \mathbf{F} \;:\; \mathbf{P}^{\mathrm{v}}\, dV, \end{aligned} \tag{6.32}$$

where the body force is denoted by $\boldsymbol{b}_0$ and acts in the domain $\mathcal{B}_0$. The prescribed traction is represented by $\hat{\boldsymbol{T}}$ on the boundary $\partial_T \mathcal{B}_0$ in the reference configuration. The viscous stress contribution is denoted by $\mathbf{P}^{\mathrm{v}}$.
Hence, the Lagrange-d'Alembert principle from Eq. (6.15) can be written as

$$\begin{aligned} &\delta S + \int_0^T \delta W^{ext}\, dt = \\ &\int_0^T \Bigg\{ \int_{\mathcal{B}_0} \Big(\delta \boldsymbol{x} \cdot (-\rho_0 \ddot{\boldsymbol{x}}) - \underbrace{\frac{\partial \mathbf{E}^x}{\partial \boldsymbol{x}} \cdot \delta \boldsymbol{x}}_{\delta \mathbf{E}(\boldsymbol{x})} : \mathbf{S}\Big)\, dV + \int_{\mathcal{B}_0} \delta \boldsymbol{x} \cdot \boldsymbol{b}_0\, dV \\ &- \int_{\mathcal{B}_0} \delta \mathbf{F} \;:\; \mathbf{P}^{\mathrm{v}}\, dV + \int_{\partial_T \mathcal{B}_0} \delta \boldsymbol{x} \cdot \hat{\boldsymbol{T}}\, dA \\ &- \int_{\mathcal{B}_0} \Big(\delta \mathbf{E} : \big(\frac{\partial \Omega}{\partial \mathbf{E}} - \mathbf{S}\big)\Big)\, dV \\ &- \int_{\mathcal{B}_0} \Big(\delta \mathbf{S} : \left(\mathbf{E}^{\boldsymbol{x}} - \mathbf{E}\right)\Big)\, dV \Bigg\}\, dt = 0 \qquad \forall\ \delta \boldsymbol{x}, \delta \mathbf{E}, \delta \mathbf{S}, \end{aligned} \tag{6.33}$$

where all variations vanish on the boundary of the space-time domain. The variations in Eq. (6.33) can be expressed as $\delta\mathbf{E}(\boldsymbol{x}) \;:\; \mathbf{S} = \delta\mathbf{F}^T \cdot \mathbf{F} \;:\; \mathbf{S} = \mathbf{F}^T \cdot \delta\mathbf{F} \;:\; \mathbf{S} = \delta\mathbf{F} \;:\; \mathbf{F} \cdot \mathbf{S} = \delta\mathbf{F} \;:\; \mathbf{P}$ and $\delta\mathbf{F} = \frac{\partial \delta \boldsymbol{x}}{\partial \boldsymbol{X}}$. Integration by parts, using the divergence theorem and the fundamental lemma of the calculus of variations yields the local Euler-Lagrange equations

$$\text{balance eq.} \qquad \nabla_{\boldsymbol{X}} \cdot (\mathbf{F} \cdot \mathbf{S} + \mathbf{P}^{\mathrm{v}}) + \boldsymbol{b}_0 = \rho_0 \ddot{\boldsymbol{x}} \quad \text{in} \quad \mathcal{B}_0, \tag{6.34}$$

$$\text{compatibility eq.} \qquad \mathbf{E}^x - \mathbf{E} = \mathbf{0} \quad \text{in} \quad \mathcal{B}_0, \tag{6.35}$$

$$\text{constitutive eq.} \qquad \frac{\partial \Omega}{\partial \mathbf{E}} - \mathbf{S} = \mathbf{0} \quad \text{in} \quad \mathcal{B}_0, \tag{6.36}$$

$$\text{static BC} \qquad (\mathbf{F} \cdot \mathbf{S} + \mathbf{P}^{\mathrm{v}}) \cdot \boldsymbol{N} = \hat{\boldsymbol{T}} \quad \text{on} \quad \partial_\sigma \mathcal{B}_0. \tag{6.37}$$

In addition, the geometric boundary condition $\boldsymbol{x} = \hat{\boldsymbol{x}}$ on $\partial_u \mathcal{B}_0$ has to be fulfilled.

Principle of Hu-Washizu – electromechanical In this section, the Hu-Washizu formulation for the mechanical shell is extended by the electric field. Analogous to the mechanical assumed quantities for strain and stress $(\mathbf{E}, \mathbf{S})$, we introduce the assumed quantities for the electrical field and electric displacement as $\bar{\boldsymbol{E}}^{\boldsymbol{e}}$ and $\bar{\boldsymbol{D}}$, respectively. The Hu-Washizu type potential energy functional Π is then given by

$$\Pi = \int_{\mathcal{B}_0} \Omega(\mathbf{E}, \bar{\boldsymbol{E}}^{\boldsymbol{e}}) + \bar{\mathbf{S}}^{\boldsymbol{m},\boldsymbol{e}} : \left(\bar{\mathbf{E}}^{\boldsymbol{m},\boldsymbol{e}} - \mathbf{E}^{\boldsymbol{m},\boldsymbol{e}}\right) \, dV, \tag{6.38}$$

with $\bar{\mathbf{E}}^{\boldsymbol{m},\boldsymbol{e}} = [\mathbf{E}, \bar{\boldsymbol{E}}^{\boldsymbol{e}}]^T$ and $\bar{\mathbf{S}}^{\boldsymbol{m},\boldsymbol{e}} = [\mathbf{S}, -\bar{\boldsymbol{D}}]^T$ being functions of the assumed mechanical and electrical quantities. The electric and electromechanical coupling energy is covered by the potential energy density functional $\Omega(\mathbf{E}, \bar{\boldsymbol{E}}^{\boldsymbol{e}})$, which depends not solely on the assumed strain $\mathbf{E}$ but additionally on the assumed electric field $\bar{\boldsymbol{E}}^{\boldsymbol{e}}$. The action for the four independent fields $\boldsymbol{u}, \mathbf{E}, \mathbf{S}$ and ϕ becomes

$$\int_{\mathcal{B}_0} \mathcal{L}(\dot{\boldsymbol{x}}, \phi, \mathbf{E}, \mathbf{S}, \bar{\boldsymbol{E}}^{\boldsymbol{e}}, \bar{\boldsymbol{D}}) \, dV = \int_{\mathcal{B}_0} \mathcal{T}(\dot{\boldsymbol{x}}) \tag{6.39}$$

$$- \left[\Omega(\mathbf{E}, \bar{\boldsymbol{E}}^{\boldsymbol{e}}) + \bar{\mathbf{S}}^{\boldsymbol{m},\boldsymbol{e}} : \left(\bar{\mathbf{E}}^{\boldsymbol{m},\boldsymbol{e}} - \mathbf{E}^{\boldsymbol{m},\boldsymbol{e}}\right)\right] \, dV. \tag{6.40}$$

Similar to the displacement formulation, the external non-conservative work (resulting from body force, surface traction, surface charge and viscous force; no electric charge density) reads

$$W^{ext} = \int_{\mathcal{B}_0} \boldsymbol{x} \cdot \boldsymbol{b}_0 \, dV + \int_{\partial_T \mathcal{B}_0} \boldsymbol{x} \cdot \hat{\boldsymbol{T}} \, dA - \int_{\partial_Q \mathcal{B}_0} \phi \cdot \hat{Q} \, dA$$

$$- \int_{\mathcal{B}_0} \mathbf{F} \;:\; \mathbf{P}^{\mathrm{v}} \, dV, \tag{6.41}$$

Hence, the Lagrange-d'Alembert principle with the external non-conservative work reads

$$
\begin{aligned}
&\delta S + \int_0^T \delta W^{ext}\, dt = \\
&\int_0^T \Bigg\{ \int_{\mathcal{B}_0} \Big(\delta \boldsymbol{x} \cdot (-\rho_0 \ddot{\boldsymbol{x}}) - \underbrace{\frac{\partial \mathbf{E}^x}{\partial \boldsymbol{x}} \cdot \delta \boldsymbol{x}}_{\delta \mathbf{E}(\boldsymbol{x})} : \mathbf{S} \Big)\, dV + \int_{\mathcal{B}_0} \delta \boldsymbol{x} \cdot \boldsymbol{b}_0\, dV \\
&- \int_{\mathcal{B}_0} \delta \mathbf{F} \;:\; \mathbf{P}^{\mathrm{v}}\, dV + \int_{\partial_T \mathcal{B}_0} \delta \boldsymbol{x} \cdot \hat{\boldsymbol{T}}\, dA \\
&- \int_{\mathcal{B}_0} \Big(\delta \boldsymbol{E}^{\boldsymbol{e}} \cdot \bar{\boldsymbol{D}} \Big)\, dV - \int_{\partial_Q \mathcal{B}_0} \delta \phi \hat{Q}\, dA \\
&- \int_{\mathcal{B}_0} \Big(\delta \mathbf{E} : (\frac{\partial \Omega}{\partial \mathbf{E}} - \mathbf{S}) \Big)\, dV - \int_{\mathcal{B}_0} \Big(\delta \bar{\boldsymbol{E}}^{\boldsymbol{e}} : (\frac{\partial \Omega}{\partial \bar{\boldsymbol{E}}^{\boldsymbol{e}}} + \bar{\boldsymbol{D}}) \Big)\, dV \\
&- \int_{\mathcal{B}_0} \Big(\delta \mathbf{S} : (\mathbf{E}^{\boldsymbol{x}} - \mathbf{E}) \Big)\, dV - \int_{\mathcal{B}_0} \Big(\delta \bar{\boldsymbol{D}} \cdot (\boldsymbol{E}^{\boldsymbol{e}} - \bar{\boldsymbol{E}}^{\boldsymbol{e}}) \Big)\, dV \Bigg\}\, dt = 0 \\
&\quad \forall\ \delta \boldsymbol{x}, \delta \phi, \delta \mathbf{E}, \delta \mathbf{S}, \bar{\boldsymbol{E}}^{\boldsymbol{e}}, \bar{\boldsymbol{D}},
\end{aligned}
\tag{6.42}
$$

where all variations vanish on the boundary of the space-time domain. The additional terms in Eq. (6.42) come from the variation of the electric potential ϕ and incorporation of the surface charges $\hat{Q}$. Integration by parts, using the divergence theorem and the fundamental lemma of the calculus of variations, yields the local Euler-Lagrange equations

$$
\begin{aligned}
\text{balance eq.} \quad & \nabla_{\boldsymbol{X}} \cdot (\mathbf{F} \cdot \mathbf{S} + \mathbf{P}^{\mathrm{v}}) + \boldsymbol{b}_0 = \rho_0 \ddot{\boldsymbol{x}} && \text{in} \quad \mathcal{B}_0, && (6.43)\\
\text{compatibility eq.} \quad & \mathbf{E}^x - \mathbf{E} = \mathbf{0} && \text{in} \quad \mathcal{B}_0, && (6.44)\\
\text{constitutive eq.} \quad & \frac{\partial \Omega}{\partial \mathbf{E}} - \mathbf{S} = \mathbf{0} && \text{in} \quad \mathcal{B}_0, && (6.45)\\
\text{static BC} \quad & (\mathbf{F} \cdot \mathbf{S} + \mathbf{P}^{\mathrm{v}}) \cdot \boldsymbol{N} = \hat{\boldsymbol{T}} && \text{on} \quad \partial_\sigma \mathcal{B}_0, && (6.46)\\
\text{balance eq.} \quad & \nabla_{\boldsymbol{X}} \cdot (\bar{\boldsymbol{D}}) = 0 && \text{in} \quad \mathcal{B}_0, && (6.47)\\
\text{compatibility eq.} \quad & \boldsymbol{E}^{\boldsymbol{e}} - \bar{\boldsymbol{E}}^{\boldsymbol{e}} = \mathbf{0} && \text{in} \quad \mathcal{B}_0, && (6.48)\\
\text{constitutive eq.} \quad & \frac{\partial \Omega}{\partial \bar{\boldsymbol{E}}^{\boldsymbol{e}}} + \bar{\boldsymbol{D}} = \mathbf{0} && \text{in} \quad \mathcal{B}_0, && (6.49)\\
\text{static BC} \quad & \bar{\boldsymbol{D}} \cdot \boldsymbol{N} = -\hat{Q} && \text{on} \quad \partial_D \mathcal{B}_0. && (6.50)
\end{aligned}
$$

In addition, the geometric boundary condition $\boldsymbol{x} = \hat{\boldsymbol{x}}$ on $\partial_u \mathcal{B}_0$ and the electric potential boundary condition $\phi = \hat{\phi}$ on $\partial_\phi \mathcal{B}_0$ have to be fulfilled.

7 Artificial muscle model – dynamic viscoelastic electromechanical shell

In this chapter, the shell formulation is derived in the continuous setting via the Lagrange-d'Alembert principle. In Section 7.1, the formulation for the variational principle of virtual work, presented in Section 6.3 for the 3D continuum case, is introduced. In Section 7.2, important details about the spatial and temporal discretisation are summarised. Numerical examples, including different geometries (rectangular, cylindrical, spherical) and deformation states (contraction, bending), are illustrated and discussed in Section 7.3. The chapter concludes with a brief summary of the implementation, numerical results and prospects in Section 7.4. In the following chapter, the summation convention for repeated indices with Roman numerals and Greek letters is used. Indices based on Roman numerals take on values 1,2,3. Indices based on Greek letters take on values 1,2.

7.1 Variational shell formulation in the continuous setting – virtual work

7.1.1 Mechanical and electrical kinematics

The placement of any material point $\boldsymbol{x}$ in the domain is based on the classical Reissner-Mindlin kinematic assumption [282, 283] with an inextensible director vector. The placement of a material point reads, see e.g. [284, 221],

$$\boldsymbol{x}(\xi^1, \xi^2, \xi, t) = \boldsymbol{\varphi}(\xi^1, \xi^2, t) + \xi \boldsymbol{d}(\xi^1, \xi^2, t), \tag{7.1}$$

with the placement $\boldsymbol{\varphi}(\xi^1, \xi^2, t)$ of the shell mid-surface ζ in the deformed configuration, where the mid-surface is defined as $\zeta := \{(\xi^1, \xi^2, \xi) \in \mathcal{B}_0 \mid \xi = 0\}$. The parameters ξ^1, ξ^2 denote the curvi-linear coordinates of the mid-surface, ξ is the thickness coordinate and $\boldsymbol{d}$ the director pointing in the thickness direction, see Fig. 7.1. The current time is denoted by t. The thickness coordinates along the director $\boldsymbol{d}$ is given by $\xi^3 = \xi \in [-\frac{h}{2}, \frac{h}{2}]$, where h represents the thickness of the shell. The director $\boldsymbol{d}(\xi^1, \xi^2, t = 0)$ in the initial configuration is defined as a unit vector perpendicular to the mid surface. Transverse shearing is accounted for by allowing that the director $\boldsymbol{d}(\xi^1, \xi^2, t)$ in the deformed configuration is not necessarily perpendicular to the mid-surface. The director $\boldsymbol{d}$ is assumed to be inextensible, i.e. $\mid \boldsymbol{d}(\xi^1, \xi^2, t) \mid = 1$ in the complete spatial domain and at all times.

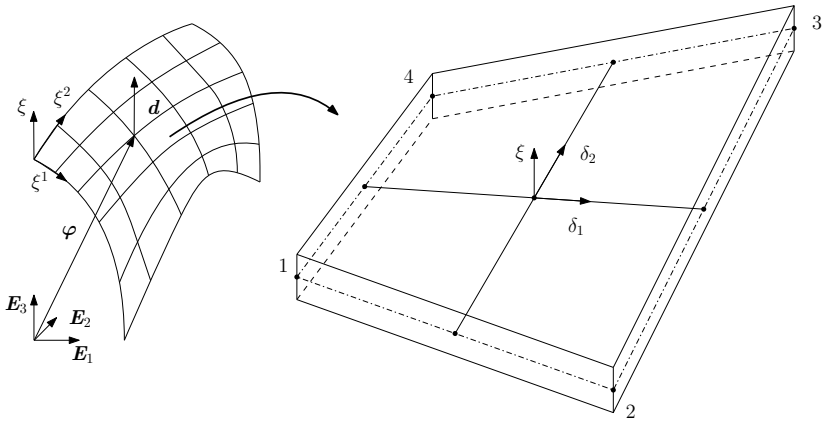

Figure 7.1: Configuration of the spatially discretised shell with curvi-linear coordinates ξ^1, ξ^2 and ξ, the director $\boldsymbol{d}$ and the inertial basis $\boldsymbol{E}_1 = [1 \quad 0 \quad 0]^T$, $\boldsymbol{E}_2 = [0 \quad 1 \quad 0]^T$, $\boldsymbol{E}_3 = [0 \quad 0 \quad 1]^T$ (left). Visualisation of a four-node (1, 2, 3, 4) element with the isoparametric coordinates δ_1, δ_2 (right).

Mechanical kinematics

The membrane strains $\epsilon_{\alpha\beta}$, bending strains $\kappa_{\alpha\beta}$ and transverse shear strains γ_α with $\alpha, \beta = 1, 2$ are defined as follows, see e.g. [284, 220],

$$a_{\alpha\beta} := \boldsymbol{\varphi}_{,\alpha} \cdot \boldsymbol{\varphi}_{,\beta}, \qquad \epsilon_{\alpha\beta} = \frac{1}{2}[a_{\alpha\beta} - a^0_{\alpha\beta}], \tag{7.2}$$

$$b_{\alpha\beta} := \boldsymbol{\varphi}_{,\alpha} \cdot \boldsymbol{d}_{,\beta} + \boldsymbol{\varphi}_{,\beta} \cdot \boldsymbol{d}_{,\alpha}, \qquad \kappa_{\alpha\beta} = \frac{1}{2}[b_{\alpha\beta} - b^0_{\alpha\beta}], \tag{7.3}$$

$$c_\alpha := \boldsymbol{\varphi}_{,\alpha} \cdot \boldsymbol{d}, \qquad \gamma_\alpha = c_\alpha - c^0_\alpha, \tag{7.4}$$

where $(\cdot)$ and $(\cdot)^0$ represent the current and initial configuration, respectively. The notation $(\cdot)_{,\alpha}$ and $(\cdot)_{,\beta}$ denotes the derivative w.r.t. the first and second curvi-linear coordinates, e.g. $\boldsymbol{\varphi}_{,\alpha} = \frac{\partial \boldsymbol{\varphi}}{\partial \xi^\alpha}$.
Following [285], we write the components of the Green-Lagrangian strain tensor $\mathbf{E} = \frac{1}{2}(\mathbf{C} - \mathbf{1})$ in vector notation as $\boldsymbol{E} = [E_{11}, E_{22}, E_{33}, 2E_{12}, 2E_{13}, 2E_{23}]$. The relation between the Green-Lagrangian strain tensor $\boldsymbol{E}$ and the independent shell strains $\boldsymbol{\epsilon} = [\epsilon_{11}, \epsilon_{22}, 2\epsilon_{12}, \kappa_{11}, \kappa_{22}, 2\kappa_{12}, \gamma_1, \gamma_2]$ is given by

$$\boldsymbol{E} = \mathbf{A} \cdot \boldsymbol{\epsilon}, \tag{7.5}$$

with

$$\mathbf{A} = \begin{bmatrix} 1 & 0 & 0 & \xi^3 & 0 & 0 & 0 & 0 \\ 0 & 1 & 0 & 0 & \xi^3 & 0 & 0 & 0 \\ 0 & 0 & 0 & 0 & 0 & 0 & 0 & 0 \\ 0 & 0 & 1 & 0 & 0 & \xi^3 & 0 & 0 \\ 0 & 0 & 0 & 0 & 0 & 0 & 1 & 0 \\ 0 & 0 & 0 & 0 & 0 & 0 & 0 & 1 \end{bmatrix}. \tag{7.6}$$

Electrical kinematics

The electric potential ϕ is introduced as an additional degree of freedom (DoF) at any material point inside the domain

$$\phi(\xi^1, \xi^2, \xi^3) = \phi_m(\xi^1, \xi^2) + \xi\alpha(\xi^1, \xi^2), \tag{7.7}$$

where $\phi_m(\xi^1, \xi^2)$ denotes the electric potential on the mid-surface and $\alpha(\xi^1, \xi^2)$ is the incremental parameter of the electric potential in thickness direction $\boldsymbol{d}$. It is worth noting that Eq. (7.7) assumes a linear change of the electric potential along ξ. A similar approach has been used for an electromechanically coupled beam formulation, see [222]. The electric field $\boldsymbol{E}^e$ is the gradient of the electric potential ϕ defined in Eq. (7.7) and follows as

$$\begin{aligned} \boldsymbol{E}^e &= -\frac{\partial \phi}{\partial \xi^I} \boldsymbol{E}^I \\ &= \Big(\frac{\partial \phi_m}{\partial \xi^1} + \xi^3 \frac{\partial \alpha}{\partial \xi^1}\Big) \boldsymbol{E}^1 + \Big(\frac{\partial \phi_m}{\partial \xi^2} + \xi^3 \frac{\partial \alpha}{\partial \xi^2}\Big) \boldsymbol{E}^2 + \alpha(\xi^1, \xi^2) \boldsymbol{E}^3, \end{aligned} \tag{7.8}$$

with the reciprocal basis $\boldsymbol{E}^I = \boldsymbol{E}_I$, where the superscript and subscript indices refer to the covariant and contravariant vectors, respectively.

7.1.2 Lagrange-d'Alembert principle for the shell

In the following, the variational formulation in a continuous setting in terms of the defined mechanical and electrical quantities is derived via the Lagrange-d'Alembert principle. Finally, the governing equations in terms of the shell quantities are given.
The variation of action δS repeated from Eq. (6.23) is given as

$$\begin{aligned} \delta S = \int_0^T \Bigg\{ & \int_{\mathcal{B}_0} \Big[\delta \boldsymbol{x} \cdot (-\rho_0 \ddot{\boldsymbol{x}} + \nabla_{\boldsymbol{X}} \cdot \partial_{\mathbf{F}} \Omega) + \delta\phi(-\nabla_{\boldsymbol{X}} \cdot \partial_{\boldsymbol{E}} \Omega)\Big] \, dV \\ & + \int_{\partial \mathcal{B}_0} \Big[\delta \boldsymbol{x} \cdot (-\partial_{\mathbf{F}} \Omega \cdot \boldsymbol{N}) + \delta\phi(\partial_{\boldsymbol{E}} \Omega \cdot \boldsymbol{N})\Big] \, dA \Bigg\} \, dt. \end{aligned}$$

To express Eq. (6.23) in terms of the shell quantities defined in Section 7.1.1, the volume integral in Eq. (6.23) is split into the surface integral over the mid surface ζ and the line integral over the shell thickness h. Similar to [284] for the purely mechanical shell formulation, the variation of the action for the electromechanically coupled shell reads

$$\delta S = \int_0^T \left\{ \int_\zeta \int_{-\frac{h}{2}}^{\frac{h}{2}} \left[\delta \boldsymbol{x} \cdot (-\rho_0 \ddot{\boldsymbol{x}} + \nabla_{\boldsymbol{X}} \cdot \mathbf{P}) + \delta\phi(-\nabla_{\boldsymbol{X}} \cdot \boldsymbol{D}) \right] d\xi \; dA \right.$$
$$\left. + \int_\zeta \left[(\delta \boldsymbol{x} \cdot (-\mathbf{P} \cdot \boldsymbol{N})) \,|_{\xi=-\frac{h}{2}}^{\xi=\frac{h}{2}} + (\delta\phi(\boldsymbol{D} \cdot \boldsymbol{N})) \,|_{\xi=-\frac{h}{2}}^{\xi=\frac{h}{2}} \right] dA \right\} dt, \tag{7.9}$$

where the quantities $\delta \boldsymbol{x}$, $\ddot{\boldsymbol{x}}, \nabla_{\boldsymbol{X}} \cdot \mathbf{P}$ and $\nabla_{\boldsymbol{X}} \cdot \mathbf{D}$ are expressed in terms of the shell kinematics. The variation and time derivatives of the position field $\boldsymbol{x}$, $\dot{\boldsymbol{x}}$ and $\ddot{\boldsymbol{x}}$ are given by

$$\boldsymbol{x} = \boldsymbol{\varphi} + \boldsymbol{r} \tag{7.10}$$
$$\delta \boldsymbol{x} = \delta \boldsymbol{\varphi} + \delta \boldsymbol{\eta} \times \boldsymbol{r} \tag{7.11}$$
$$\dot{\boldsymbol{x}} = \dot{\boldsymbol{\varphi}} + \boldsymbol{\omega} \times \boldsymbol{r} \tag{7.12}$$
$$\ddot{\boldsymbol{x}} = \ddot{\boldsymbol{\varphi}} + \dot{\boldsymbol{\omega}} \times \boldsymbol{r} + \boldsymbol{\omega} \times (\boldsymbol{\omega} \times \boldsymbol{r}) \tag{7.13}$$

with the position vector $\boldsymbol{r} = \boldsymbol{x} - \boldsymbol{\varphi} = \xi \boldsymbol{d}$ along the thickness direction, $\boldsymbol{\omega}$ being the spatial angular velocity and $\delta\boldsymbol{\eta}$ representing a virtual rotation. Defining a traction $\boldsymbol{t} = [\boldsymbol{t}_1, \boldsymbol{t}_2, \boldsymbol{t}]$, we can write the forces $\boldsymbol{f}^k$ and torques $\boldsymbol{m}^k$

$$\boldsymbol{f}^k = \int_{-\frac{h}{2}}^{\frac{h}{2}} \boldsymbol{t}_k \; d\xi, \qquad \boldsymbol{m}^k = \int_{-\frac{h}{2}}^{\frac{h}{2}} \boldsymbol{r} \times \boldsymbol{t}_k \; d\xi. \tag{7.14}$$

Thus, the divergence terms in Eq. (7.9) can be formulated as follows

$$\int_{-\frac{h}{2}}^{\frac{h}{2}} \nabla_{\boldsymbol{X}} \cdot \mathbf{P} \; d\xi = \int_{-\frac{h}{2}}^{\frac{h}{2}} \frac{\partial \boldsymbol{t}_1}{\partial \xi^1} + \frac{\partial \boldsymbol{t}_2}{\partial \xi^2} + \frac{\partial \boldsymbol{t}}{\partial \xi} \; d\xi$$
$$= \underbrace{\frac{\partial \boldsymbol{f}^1}{\partial \xi^1} + \frac{\partial \boldsymbol{f}^2}{\partial \xi^2}}_{\boldsymbol{f}^k_{,k}} + \underbrace{\int_{-\frac{h}{2}}^{\frac{h}{2}} \frac{\partial \boldsymbol{t}}{\partial \xi} \; d\xi}_{\boldsymbol{f}^n}, \tag{7.15}$$

$$\int_{-\frac{h}{2}}^{\frac{h}{2}} \boldsymbol{r} \times \nabla_{\boldsymbol{X}} \cdot \mathbf{P} \; d\xi = \underbrace{\frac{\partial \boldsymbol{m}^1}{\partial \xi^1} + \frac{\partial \boldsymbol{m}^2}{\partial \xi^2}}_{\boldsymbol{m}^k_{,k}} + \underbrace{\int_{-\frac{h}{2}}^{\frac{h}{2}} \boldsymbol{r} \times \left(\frac{\partial \boldsymbol{t}}{\partial \xi} \right) \; d\xi}_{\boldsymbol{m}^n}$$
$$+ \underbrace{\frac{\partial \boldsymbol{\varphi}}{\partial \xi^1} \times \boldsymbol{f}^1 + \frac{\partial \boldsymbol{\varphi}}{\partial \xi^2} \times \boldsymbol{f}^2}_{\boldsymbol{\varphi}_{,k} \times \boldsymbol{f}^k}. \tag{7.16}$$

By applying the generalized Stokes' theorem

$$\int_V \nabla_{\boldsymbol{X}} \cdot \mathbf{F} \; d^{(n)}V = \int_S \mathbf{F} \cdot \boldsymbol{v} \; d^{(n-1)}S, \tag{7.17}$$

where $d^{(n)}$ and $d^{(n-1)}$ denote the dimension with the boundary $S = \partial V$ and $\boldsymbol{v}$ being the outer normal, we obtain for $(n = 1)$

$$(\mathbf{P} \cdot \boldsymbol{N}) \; |_{\xi=-\frac{h}{2}}^{\xi=\frac{h}{2}} = \int_S \mathbf{P} \cdot \boldsymbol{N} \; d^{(0)}S = \int_V \nabla_{\boldsymbol{X}} \cdot \mathbf{P} \; d^{(1)}V = \int_{-\frac{h}{2}}^{\frac{h}{2}} \frac{\partial \boldsymbol{t}}{\partial \xi} \; d\xi = \boldsymbol{f}^n, \tag{7.18}$$

and

$$\int_S \boldsymbol{r} \times (\mathbf{P} \cdot \boldsymbol{N}) \; d^{(0)}S = \int_V \boldsymbol{r} \times \nabla_{\boldsymbol{X}} \cdot \mathbf{P} \; d^{(1)}V = \int_{-\frac{h}{2}}^{\frac{h}{2}} \boldsymbol{r} \times (\frac{\partial \boldsymbol{t}}{\partial \xi}) \; d\xi = \boldsymbol{m}^n. \tag{7.19}$$

The definition of the electric displacement vector $\boldsymbol{D}$ in terms of the shell kinematics is analogous to the definition to the Piola-Kirchhoff stress tensor. We define the components of the electric displacement

$$d^k = \int_{-\frac{h}{2}}^{\frac{h}{2}} D_k \; d\xi, \qquad\qquad d = \int_{-\frac{h}{2}}^{\frac{h}{2}} D \; d\xi, \tag{7.20}$$

with $D = [D_1, D_2, D]$ and $\boldsymbol{d}^e = [d^1, d^2, d]$. The divergence of the electric displacement $\boldsymbol{D}$ is expressed in terms of the shell quantities as

$$\int_{-\frac{h}{2}}^{\frac{h}{2}} \nabla_{\boldsymbol{X}} \cdot \boldsymbol{D} \; d\xi = \int_{-\frac{h}{2}}^{\frac{h}{2}} \frac{\partial D_1}{\partial \xi^1} + \frac{\partial D_2}{\partial \xi^2} + \frac{\partial D}{\partial \xi} \; d\xi \tag{7.21}$$

$$= \underbrace{\frac{\partial d^1}{\partial \xi^1} + \frac{\partial d^2}{\partial \xi^2}}_{\boldsymbol{d}^k_{,k}} + \underbrace{\int_{-\frac{h}{2}}^{\frac{h}{2}} \frac{\partial d}{\partial \xi} \; d\xi}_{d^n}, \tag{7.22}$$

with

$$\int_S \boldsymbol{D} \cdot \boldsymbol{N} \; d^{(0)}S = \int_V \nabla_{\boldsymbol{X}} \cdot \boldsymbol{D} \; d^{(1)}V = \int_{-\frac{h}{2}}^{\frac{h}{2}} \frac{\partial d}{\partial \xi} \; d\xi = d^n. \tag{7.23}$$

Using Eq. (7.10)–(7.23), the variation of the action in Eq. (7.9) reads

$$\begin{aligned}\delta S = \int_0^T \Bigg\{ \int_\zeta \Big[\delta\boldsymbol{\varphi} \cdot \Big(- A_\rho \ddot{\boldsymbol{\varphi}} + \boldsymbol{f}^k_{,k} + \boldsymbol{f}^n \Big) \\ + \delta\boldsymbol{\eta} \cdot \Big(- \boldsymbol{I}_\rho \dot{\boldsymbol{w}} + \boldsymbol{m}^k_{,k} + \boldsymbol{m}^n + \boldsymbol{\varphi}_{,k} \times \boldsymbol{f}^k \Big) + \delta\phi \Big(- d^n - \boldsymbol{d}^k_{,k} \Big) \Big] \, dA \Bigg\} \, dt \\ + \int_0^T \Bigg\{ \int_\zeta \Big[\delta\boldsymbol{\varphi} \cdot \Big(- \boldsymbol{f}^n \Big) + \delta\boldsymbol{\eta} \cdot \Big(- \boldsymbol{m}^n \Big) + \delta\phi \Big(d^n \Big) \Big] dA \Bigg\} \, dt, \end{aligned} \tag{7.24}$$

with A_ρ being the constant nominal surface density and I_ρ the constant nominal rotational inertia of the shell, see e.g. [286]. It is worth noting that the forces $\boldsymbol{f}^n$ and torques $\boldsymbol{m}^n$ in the first surface integral of Eq. (7.24) come from the divergence term of the action in Eq. (7.9). Due to opposite signs of $\boldsymbol{f}^n$ and $\boldsymbol{m}^n$ in the second surface integral of Eq. (7.24), the terms $\boldsymbol{f}^n$ and $\boldsymbol{m}^n$ vanish. By considering the Neumann boundary conditions in Eq. (6.3) and Eq. (6.8) and the body force in Eq. (6.1), the external work W^{ext} in terms of the shell can be expressed as

$$\begin{aligned}\delta W^{\text{ext}} &= \int_{\mathcal{B}_0} \delta\boldsymbol{x} \cdot \rho_0 \boldsymbol{b} \, dV + \int_{\partial\mathcal{B}_0} \delta\boldsymbol{x} \cdot \hat{\boldsymbol{T}} \, dA + \int_{\partial\mathcal{B}_0} \delta\phi \cdot \hat{Q} \, dA \\ &= \int_\zeta \delta\boldsymbol{\varphi} \cdot \hat{\boldsymbol{f}} \, dA + \int_\zeta \delta\boldsymbol{\varphi} \cdot \hat{\boldsymbol{t}} \, dA + \int_\zeta \delta\boldsymbol{\eta} \cdot \hat{\boldsymbol{m}} \, dA \qquad (7.25) \\ &\quad + \int_\zeta \delta\boldsymbol{\eta} \cdot \hat{\boldsymbol{\tau}} \, dA + \int_\zeta \delta\phi \cdot \hat{q} \, dA, \qquad (7.26)\end{aligned}$$

where the prescribed body force, traction, torque, and electric charge are given by

$$\begin{aligned} \hat{\boldsymbol{f}} &= \int_{-\frac{h}{2}}^{\frac{h}{2}} \rho_0 \boldsymbol{b} \, d\xi, & \hat{\boldsymbol{t}} &= \hat{\boldsymbol{T}} \, |_{\xi=-\frac{h}{2}}^{\xi=\frac{h}{2}}, \\ \hat{\boldsymbol{m}} &= \int_{-\frac{h}{2}}^{\frac{h}{2}} \boldsymbol{r} \times \rho_0 \boldsymbol{b} \, d\xi, & \hat{\boldsymbol{\tau}} &= \boldsymbol{r} \times \Big[\hat{\boldsymbol{T}} \, |_{\xi=-\frac{h}{2}}^{\xi=\frac{h}{2}} \Big], \\ \hat{q} &= \hat{Q} \, |_{\xi=-\frac{h}{2}}^{\xi=\frac{h}{2}} \, . \end{aligned} \tag{7.27}$$

Inserting Eq. (7.24) and Eq. (7.25) in Eq. (6.15) finally leads to the Lagrange-d'Alembert principle for the shell

$$\begin{aligned}\delta S + \int_0^T \delta W^{ext} dt = \\ \int_0^T \Bigg\{ \int_\zeta \delta\boldsymbol{\varphi} \cdot \Big(- A_\rho \ddot{\boldsymbol{\varphi}} + \boldsymbol{f}^k_{,k} + \hat{\boldsymbol{f}} + \hat{\boldsymbol{t}} \Big) \\ + \delta\boldsymbol{\eta} \cdot \Big(- \boldsymbol{I}_\rho \dot{\boldsymbol{w}} + \boldsymbol{m}^k_{,k} + \boldsymbol{\varphi}_{,k} \times \boldsymbol{f}^k + \hat{\boldsymbol{m}} + \hat{\boldsymbol{\tau}} \Big) \\ + \delta\phi \Big(- \boldsymbol{d}^k_{,k} + \hat{q} \Big) \, dA \Bigg\} \, dt = 0 \qquad \forall \, \delta\boldsymbol{\varphi}, \delta\boldsymbol{\eta}, \delta\phi, \end{aligned} \tag{7.28}$$

where all variations vanish on the boundary of the space-time domain. The requirement of stationarity in Eq. (7.28) leads to

$$\boldsymbol{f}^k_{,k} + \hat{\boldsymbol{f}} + \hat{\boldsymbol{t}} = A_\rho \ddot{\boldsymbol{\varphi}}, \tag{7.29}$$

$$\boldsymbol{m}^k_{,k} + \boldsymbol{\varphi}_{,k} \times \boldsymbol{f}^k + \hat{\boldsymbol{m}} + \hat{\boldsymbol{\tau}} = \boldsymbol{I}_\rho \dot{\boldsymbol{w}}, \tag{7.30}$$

$$\boldsymbol{d}^k_{,k} - \hat{q} = 0, \tag{7.31}$$

where Eq. (7.29)–(7.31) represent the balance of linear momentum, the balance of angular momentum and Maxwell's equation for the shell, respectively.

7.2 Spatial and temporal discretisation

In the following, the space and time discretisation of the shell formulation based on Section 7.1 are introduced.

7.2.1 Finite element discretisation

The shell mid-surface ζ is spatially discretised into quadrilateral finite elements with $e = 1, ..., n_{el}$ and n_{el} representing the total number of elements in the domain, see Fig. 7.1. Based on the isoparametric concept, the coordinates $\boldsymbol{\varphi}^e_i$, director $\boldsymbol{d}^e_i$ and the electric potential ϕ^e_i of the i-th node in the element e are interpolated via bi-linear shape functions $N_i(\delta_1, \delta_2)$

$$\boldsymbol{\varphi}^e(\delta_1, \delta_2, t) = \sum_{i=1}^{4} N_i(\delta_1, \delta_2) \boldsymbol{\varphi}^e_i(t), \tag{7.32}$$

$$\boldsymbol{d}^e(\delta_1, \delta_2, t) = \sum_{i=1}^{4} N_i(\delta_1, \delta_2) \boldsymbol{d}^e_i(t), \tag{7.33}$$

$$\phi^e(\delta_1, \delta_2, t) = \sum_{i=1}^{4} N_i(\delta_1, \delta_2) \phi^e_i(t). \tag{7.34}$$

The bi-linear shape functions N_i are given by

$$N_i(\xi^1, \xi^2) = \frac{1}{4}(1 + \Psi_{1,i}\delta_1)(1 + \Psi_{2,i}\delta_2), \tag{7.35}$$

with $\delta_1, \delta_2 \in [0,1]$, $\Psi_{1,i} \in \{-1,1,1,-1\}$ and $\Psi_{2,i} \in \{-1,-1,1,1\}$, see e.g. [287]. The derivatives of the shape functions N_i w.r.t. the isoparametric coordinates δ_1 and δ_2 are defined as

$$N_{i,\delta_\alpha} = \left[\frac{\partial N_i}{\partial \delta_\alpha}\right]^{\mathrm{T}} = \begin{bmatrix} \frac{\partial N_1}{\partial \delta_1} & \frac{\partial N_2}{\partial \delta_1} & \frac{\partial N_3}{\partial \delta_1} & \frac{\partial N_2}{\partial \delta_1} \\ \frac{\partial N_1}{\partial \delta_2} & \frac{\partial N_2}{\partial \delta_2} & \frac{\partial N_3}{\partial \delta_2} & \frac{\partial N_4}{\partial \delta_2} \end{bmatrix}. \tag{7.36}$$

Thus, the derivatives of the nodal coordinates $\boldsymbol{\varphi}_i$, the director $\boldsymbol{d}_i$ and the electric potential ϕ_i w.r.t. the isoparametric coordinates δ_1 and δ_2 read

$$\boldsymbol{\varphi}^e_{,\delta_\alpha} = \sum_{i=1}^{4} N_{i,\delta_\alpha} \boldsymbol{\varphi}^e_i, \qquad \boldsymbol{d}^e_{,\delta_\alpha} = \sum_{i=1}^{4} N_{i,\delta_\alpha} \boldsymbol{d}^e_i, \qquad \phi^e_{,\delta_\alpha} = \sum_{i=1}^{4} N_{i,\delta_\alpha} \phi^e_i. \tag{7.37}$$

The Jacobian $\boldsymbol{J}$ and the derivative of the shape functions with respect to the curvi-linear coordinates ξ_1 and ξ_2 are given as

$$\boldsymbol{J} = \begin{bmatrix} \frac{\partial \xi_1}{\partial \delta_1} & \frac{\partial \xi_2}{\partial \delta_1} \\ \frac{\partial \xi_1}{\partial \delta_2} & \frac{\partial \xi_2}{\partial \delta_2} \end{bmatrix}, \qquad \begin{bmatrix} N_{i,\xi_1} \\ N_{i,\xi_2} \end{bmatrix} = \boldsymbol{J}^{-1} \begin{bmatrix} N_{i,\delta_1} \\ N_{i,\delta_2} \end{bmatrix}. \tag{7.38}$$

Consequently, the derivatives of the nodal coordinates $\boldsymbol{\varphi}_i$, the director $\boldsymbol{d}_i$ and the electric potential ϕ_i w.r.t. curvi-linear coordinates ξ_1 and ξ_2 follow as

$$\boldsymbol{\varphi}^e_{,\xi_\alpha} = \sum_{i=1}^{4} N_{i,\xi_\alpha} \boldsymbol{\varphi}^e_i, \qquad \boldsymbol{d}^e_{,\xi_\alpha} = \sum_{i=1}^{4} N_{i,\xi_\alpha} \boldsymbol{d}^e_i, \qquad \phi^e_{,\xi_\alpha} = \sum_{i=1}^{4} N_{i,\xi_\alpha} \phi^e_i. \tag{7.39}$$

For all geometries (rectangular, cylindrical, spherical) in the subsequent numerical examples in Section 7.3, a curvi-linear coordinate system is defined. In the case of the rectangular geometry, the Cartesian coordinates just coincide with the curvi-linear coordinates ξ_1 and ξ_2. For the cylindrical and spherical geometry, a polar and spherical coordinate system is chosen, respectively. The

approximated element shell strains defined in Eq. (7.2)–(7.4) are given by

$$\boldsymbol{\epsilon}^e = \begin{bmatrix} \epsilon^e_{11} \\ \epsilon^e_{22} \\ 2\epsilon^e_{12} \\ \kappa^e_{11} \\ \kappa^e_{22} \\ 2\kappa^e_{12} \\ \gamma^e_1 \\ \gamma^e_2 \end{bmatrix} = \begin{bmatrix} \frac{1}{2}[\boldsymbol{\varphi}^e_{,\xi_1} \cdot \boldsymbol{\varphi}^e_{,\xi_1} - \boldsymbol{\varphi}^{e,0}_{,\xi_1} \cdot \boldsymbol{\varphi}^{e,0}_{,\xi_1}] \\ \frac{1}{2}[\boldsymbol{\varphi}^e_{,\xi_2} \cdot \boldsymbol{\varphi}^e_{,\xi_2} - \boldsymbol{\varphi}^{e,0}_{,\xi_2} \cdot \boldsymbol{\varphi}^{e,0}_{,\xi_2}] \\ \boldsymbol{\varphi}^e_{,\xi_1} \cdot \boldsymbol{\varphi}^e_{,\xi_2} - \boldsymbol{\varphi}^{e,0}_{,\xi_1} \cdot \boldsymbol{\varphi}^{e,0}_{,\xi_2} \\ \boldsymbol{\varphi}^e_{,\xi_1} \cdot \boldsymbol{d}^e_{,\xi_1} - \boldsymbol{\varphi}^{e,0}_{,\xi_1} \cdot \boldsymbol{d}^{e,0}_{,\xi_1} \\ \boldsymbol{\varphi}^e_{,\xi_2} \cdot \boldsymbol{d}^e_{,\xi_2} - \boldsymbol{\varphi}^{e,0}_{,\xi_2} \cdot \boldsymbol{d}^{e,0}_{,\xi_2} \\ \boldsymbol{\varphi}^e_{,\xi_1} \cdot \boldsymbol{d}^e_{,\xi_2} + \boldsymbol{\varphi}^e_{,\xi_2} \cdot \boldsymbol{d}^e_{,\xi_1} - \boldsymbol{\varphi}^{e,0}_{,\xi_1} \cdot \boldsymbol{d}^{e,0}_{,\xi_2} - \boldsymbol{\varphi}^{e,0}_{,\xi_2} \cdot \boldsymbol{d}^{e,0}_{,\xi_1} \\ \boldsymbol{\varphi}^e_{,\xi_1} \cdot \boldsymbol{d} - \boldsymbol{\varphi}^{e,0}_{,\xi_1} \cdot \boldsymbol{d} \\ \boldsymbol{\varphi}^e_{,\xi_2} \cdot \boldsymbol{d} - \boldsymbol{\varphi}^{e,0}_{,\xi_2} \cdot \boldsymbol{d} \end{bmatrix}. \tag{7.40}$$

7.2.2 Variational time integration

By modelling the dynamic, viscoelastic electromechanical problem based on Lagrangian mechanics, the structure-preserving time integration can be used to ensure a good long-term energy behaviour and avoid numerical damping or artificial energy gain (e.g. [288, 289, 290].)
For a constrained non-conservative system, the Lagrange-d'Alembert principle is given as, see also [288],

$$\delta \int_0^T [L(\boldsymbol{q}, \dot{\boldsymbol{q}}) - \boldsymbol{g}^T(\boldsymbol{q}) \cdot \boldsymbol{\lambda}] \, dt + \int_0^T \boldsymbol{f}^{ext}(t) \cdot \delta \boldsymbol{q} \, dt = 0, \tag{7.41}$$

where $\boldsymbol{q}(t)$ contains all spatially discrete configuration variables at time t and $\dot{\boldsymbol{q}}(t)$ are the corresponding time derivatives. The last term in Eq. (7.41) represents the variation of the work of non-conservative contributions $\delta W^{\text{ext}}(t)$ with $\delta W^{\text{ext}}(t) = \boldsymbol{f}^{ext}(t) \cdot \delta \boldsymbol{q}$, also known as non-conservative virtual work. The vector $\boldsymbol{f}^{ext}(t)$ contains the non-conservative generalised forces that are treated fixed during variation. In the case of the electromechanical shell, the discrete configuration variable $\boldsymbol{q}_i(t) = [\boldsymbol{\varphi}_i, \boldsymbol{d}_i, \boldsymbol{\phi}_i]^T$ with $\boldsymbol{\phi}_i = [\phi_{m,i}, \alpha_i]$, $i = 1, ..., n_p$ and n_p is the total number of discrete points. Thus, the configuration vector $\boldsymbol{q}(t) \in \mathbb{R}^{n_q}$ with $n_q = 8n_p$ reads

$$\boldsymbol{q}(t) = \begin{bmatrix} \boldsymbol{q}_1(t) \\ \boldsymbol{q}_2(t) \\ \cdot \\ \cdot \\ \boldsymbol{q}_{n_p-1}(t) \\ \boldsymbol{q}_{n_p}(t) \end{bmatrix}. \tag{7.42}$$

$L(\boldsymbol{q}, \dot{\boldsymbol{q}})$ represents the Lagrangian and the argument in the first integral is referred to as augmented Lagrangian $\tilde{L}(\boldsymbol{q}, \dot{\boldsymbol{q}}, \boldsymbol{\lambda}) = L(\boldsymbol{q}, \dot{\boldsymbol{q}}) - \boldsymbol{g}(\boldsymbol{q}) \cdot \boldsymbol{\lambda}$, $\boldsymbol{g}$ represents holonomic constraints, $\boldsymbol{\lambda} \in \mathbb{R}^{n_c}$ is the Lagrangian multiplier, where n_c is the total number of constraints. The Lagrange multiplier $\boldsymbol{\lambda}$ specifies the forces required to enforce the holonomic constraints defined in Eq. (7.43). Thus, the remaining number of degrees of freedom are given by $n_{dof} = n_q - n_c$. The holonomic constraints are defined as, see also [291],

$$\boldsymbol{g}(\boldsymbol{q}) = \left[\tfrac{1}{2}(\boldsymbol{d}^T \cdot \boldsymbol{d} - 1)\right] = \boldsymbol{0}, \tag{7.43}$$

which represents the kinematic assumption of an inextensible director $\boldsymbol{d}$. The continuous Lagrangian $L(\boldsymbol{q}, \dot{\boldsymbol{q}})$ in terms of the configuration $\boldsymbol{q}$ is defined as the difference between the kinetic energy $T(\dot{\boldsymbol{q}})$ and the internal potential energy $\Pi(\boldsymbol{q})$

$$L(\boldsymbol{q}, \dot{\boldsymbol{q}}) = T(\dot{\boldsymbol{q}}) - \Pi(\boldsymbol{q}). \tag{7.44}$$

The kinetic energy for the shell is defined as (see [220, 292]),

$$T(\dot{\boldsymbol{q}}) = \frac{1}{2} \int_{\zeta} [A_{\rho_0} |\dot{\boldsymbol{\varphi}}|^2 + I_{\rho_0} |\dot{\boldsymbol{d}}|^2] \, dA, \tag{7.45}$$

Following [220], the consistent mass matrix for the mechanical part is given by

$$\mathbf{M}^{ij} = \begin{bmatrix} \mathrm{M}_{\varphi}^{ij} \mathbf{I} & \mathbf{0} \\ \mathbf{0} & \mathrm{M}_{d}^{ij} \mathbf{I} \end{bmatrix}, \tag{7.46}$$

where $\mathbf{I}$ is the 3×3 identity matrix, $\mathbf{0}$ is a 3×3 zero matrix and

$$\mathrm{M}_{\varphi}^{ij} = \int_{\zeta} A_{\rho_0} N_i N_j \, dA, \tag{7.47}$$

$$\mathrm{M}_{d}^{ij} = \int_{\zeta} I_{\rho_0} N_i N_j \, dA. \tag{7.48}$$

For the electromechanical case, the matrix $\mathbf{M}^{ij}$ is extended by two additional DoFs w.r.t. the electrical field

$$\mathbf{M}^{ij} = \begin{bmatrix} \mathrm{M}_{\varphi}^{ij} \mathbf{I} & \mathbf{0} & \mathbf{0}_{3x2} \\ \mathbf{0} & \mathrm{M}_{d}^{ij} \mathbf{I} & \mathbf{0}_{3x2} \\ \mathbf{0}_{2x3} & \mathbf{0}_{2x3} & \mathbf{0}_{2x2} \end{bmatrix}. \tag{7.49}$$

Since the kinetic energy in Eq. (7.45) is assumed to be independent of the electric field, the defined mass matrix in Eq. (7.49) is singular. For the energy evaluation (Hamiltonian energy H_d needs the inverse of the mass matrix) and system initialisation, a non-singular reduced mass matrix is needed. More details about consistent initial conditions ($\boldsymbol{q}_{n-1}$ does not exist at $t = 0$) and consistent energy evaluation can be found e.g. in [271, 222].

Conservative problems The action integral is discretised with equidistant time nodes t_n within the time interval $[0, T]$ with $n = 0, 1, ..., n_t$ and n_t representing the total number of time points. The time discrete action integral reads

$$S(\boldsymbol{q}) = \sum_{n=0}^{n_t-1} \int_{t_n}^{t_{n+1}} L(\boldsymbol{q}, \dot{\boldsymbol{q}})\ dt. \tag{7.50}$$

The configuration $\boldsymbol{q}$ and velocity $\dot{\boldsymbol{q}}$ are approximated via finite differences and the midpoint rule, respectively,

$$\dot{\boldsymbol{q}} \approx \frac{\boldsymbol{q}_{n+1} - \boldsymbol{q}_n}{\Delta t}, \qquad \boldsymbol{q} \approx \frac{\boldsymbol{q}_{n+1} + \boldsymbol{q}_n}{2}, \tag{7.51}$$

with $\Delta t = t_{n+1} - t_n$. Thus, the discrete Lagrangian L_d reads

$$\int_{t_n}^{t_{n+1}} L(\boldsymbol{q}, \dot{\boldsymbol{q}})\ dt \approx L_d(\boldsymbol{q}_n, \boldsymbol{q}_{n+1}) = \Delta t\ L\Big(\frac{\boldsymbol{q}_{n+1} + \boldsymbol{q}_n}{2}, \frac{\boldsymbol{q}_{n+1} - \boldsymbol{q}_n}{\Delta t}\Big). \tag{7.52}$$

The variation of the discrete action is given by

$$\begin{aligned} \delta S_d &= \sum_{n=1}^{n_t-1} \delta L_d(\boldsymbol{q}_n, \boldsymbol{q}_{n+1}) \\ &= \sum_{n=1}^{n_t-1} \int_{t_n}^{t_{n+1}} \left[\frac{\partial L_d(\boldsymbol{q}_n, \boldsymbol{q}_{n+1})}{\partial \boldsymbol{q}_n} + \frac{\partial L_d(\boldsymbol{q}_{n-1}, \boldsymbol{q}_n)}{\partial \boldsymbol{q}_n}\right] \delta \boldsymbol{q}_n = 0 \qquad \forall\ \delta \boldsymbol{q}_{\boldsymbol{n}}, \end{aligned} \tag{7.53}$$

with the variation of the configuration $\boldsymbol{q}$ equals zero at the time boundaries, i.e. $\delta \boldsymbol{q}_0 = \delta \boldsymbol{q}_{n_t} = 0$. The well-known discrete Euler-Lagrange equations can be obtained by considering the fundamental lemma of the calculus of variations (term in Eq. (7.53) has to be zero for arbitrary variations)

$$\frac{\partial L_d(\boldsymbol{q}_n, \boldsymbol{q}_{n+1})}{\partial \boldsymbol{q}_n} + \frac{\partial L_d(\boldsymbol{q}_{n-1}, \boldsymbol{q}_n)}{\partial \boldsymbol{q}_n} = \boldsymbol{0}, \tag{7.54}$$

for $n = 1, ..., n_t - 1$. The discrete Legendre transform is applied to initialise the system at t_0. In Eq. (7.54), the unknown configuration of $\boldsymbol{q}_{n-1}$ needs to be known to compute $\boldsymbol{q}_1$. To circumvent the computation of $\boldsymbol{q}_{n-1}$, the discrete momentum obtained from the Legendre transform is initialised with an initial momentum $\boldsymbol{p}(0) = \boldsymbol{p}_0$ which leads to

$$\boldsymbol{p}_0 = -\frac{\partial L_d(\boldsymbol{q}_0, \boldsymbol{q}_1)}{\partial \boldsymbol{q}_0}. \tag{7.55}$$

Consequently, with given $\boldsymbol{q}_0$ and $\boldsymbol{p}_0$, the configuration $\boldsymbol{q}_1$ can be computed.

Constrained problems Including the constraints in the action integral S leads to

$$S(\boldsymbol{q},\boldsymbol{\lambda}) = \sum_{n=1}^{n_t-1} \int_{t_n}^{t_{n+1}} \tilde{L}(\boldsymbol{q},\dot{\boldsymbol{q}},\boldsymbol{\lambda})\ dt = \sum_{n=1}^{n_t-1} \int_{t_n}^{t_{n+1}} L(\boldsymbol{q},\dot{\boldsymbol{q}}) - \boldsymbol{g}(\boldsymbol{q})\cdot\boldsymbol{\lambda}\ dt. \tag{7.56}$$

The Lagrange multiplier term in Eq. (7.56) can be formulated in the discrete setting as (see [271]),

$$\int_{t_n}^{t_{n+1}} \boldsymbol{g}(\boldsymbol{q})\cdot\boldsymbol{\lambda}\ dt \approx \gamma_g(\boldsymbol{q}_n,\boldsymbol{q}_{n+1},\boldsymbol{\lambda}_n,\boldsymbol{\lambda}_{n+1}) \tag{7.57}$$

$$= \Delta t\ \Big(\beta\ \boldsymbol{g}(\boldsymbol{q}_n)\cdot\boldsymbol{\lambda}_n + (1-\beta)\ \boldsymbol{g}(\boldsymbol{q}_{n+1})\cdot\boldsymbol{\lambda}_{n+1}\Big), \tag{7.58}$$

which forms an affine combination with $\beta \in [0,1]$ and $\boldsymbol{\lambda}_n$ being the time discrete Lagrange multiplier at t_n, approximating $\boldsymbol{\lambda}(t_n)$. The variation of the discrete action is given as

$$\delta S_d = \sum_{n=1}^{n_t-1} \Big(\delta L_d(\boldsymbol{q}_n,\boldsymbol{q}_{n+1}) - \delta\gamma_g(\boldsymbol{q}_n,\boldsymbol{q}_{n+1},\boldsymbol{\lambda}_n,\boldsymbol{\lambda}_{n+1})\Big) = 0 \qquad \forall\ \delta\boldsymbol{q_n},\delta\boldsymbol{\lambda_n}, \tag{7.59}$$

with the variation of the configuration $\boldsymbol{q}$ and Lagrange multiplier $\boldsymbol{\lambda}$ equals to zero at the time boundaries, i.e. $\delta\boldsymbol{q}_0 = \delta\boldsymbol{q}_{n_t} = 0$, $\delta\boldsymbol{\lambda}_0 = \delta\boldsymbol{\lambda}_{n_t} = 0$. The well-known constrained discrete Euler-Lagrange equations can be obtained by considering the fundamental lemma of the calculus of variations (term in Eq. (7.59) has to be zero for arbitrary variations),

$$\frac{\partial L_d(\boldsymbol{q}_n,\boldsymbol{q}_{n+1})}{\partial \boldsymbol{q}_n} + \frac{\partial L_d(\boldsymbol{q}_{n-1},\boldsymbol{q}_n)}{\partial \boldsymbol{q}_n} - \mathbf{G}_d^T(\boldsymbol{q}_n)\cdot\boldsymbol{\lambda}_n = \mathbf{0}, \tag{7.60}$$

$$\boldsymbol{g}(\boldsymbol{q}_{n+1}) = \mathbf{0}, \tag{7.61}$$

where $\mathbf{G}_d(\boldsymbol{q}_n) = \Delta t\ {}^{\partial \boldsymbol{g}(\boldsymbol{q}_n)}/_{\partial \boldsymbol{q}_n}$ is the discrete constraint Jacobian.

Constrained and non-conservative problems Non-conservative contributions, e.g. viscoelastic effects, friction and external loads in the dynamic system, are considered as a change of energy in the system due to work by external forces and can be taken into account via the Lagrange-d'Alembert principle from Eq. (7.41). The variation of the non-conservative contributions W^{ext} reads

$$\delta W^{\text{ext}}(\boldsymbol{q},\boldsymbol{f}^{\text{ext}}) = \sum_{n=1}^{n_t-1} \int_{t_n}^{t_{n+1}} \boldsymbol{f}^{\text{ext}}(t)\cdot\delta\boldsymbol{q}\ dt, \tag{7.62}$$

and contains non-conservative generalised forces $\boldsymbol{f}^{\text{ext}}(t)$ which are treated as fixed during variation. The discrete non-conservative contribution δW_d^{ext} is given as (midpoint quadrature rule)

$$\begin{aligned}\delta W_d^{\text{ext}}(\boldsymbol{q}_n, \boldsymbol{q}_{n+1}, \boldsymbol{f}_n^{\text{ext}}, \boldsymbol{f}_{n+1}^{\text{ext}}) &= \Delta t \ \frac{\boldsymbol{f}_n^{\text{ext}} + \boldsymbol{f}_{n+1}^{\text{ext}}}{2} \frac{\delta \boldsymbol{q}_n + \delta \boldsymbol{q}_{n+1}}{2} \\ &\approx \int_{t_n}^{t_{n+1}} \boldsymbol{f}^{\text{ext}}(t) \cdot \delta \boldsymbol{q} \ dt,\end{aligned} \tag{7.63}$$

and $\boldsymbol{f}_n^{\text{ext}}$ being the time discrete generalised external force at t_n, approximating $\boldsymbol{f}^{\text{ext}}(t_n)$.
The discrete Lagrange-d'Alembert principle for constrained systems with non-conservative contributions follows as

$$\begin{aligned}&\sum_{n=1}^{n_t} \Big(\delta L_d(\boldsymbol{q}_n, \boldsymbol{q}_{n+1}) - \delta \gamma_g(\boldsymbol{q}_n, \boldsymbol{q}_{n+1}, \boldsymbol{\lambda}_n, \boldsymbol{\lambda}_{n+1}) \\ &+ \delta W_d^{\text{ext}}(\boldsymbol{q}_n, \boldsymbol{q}_{n+1}, \boldsymbol{f}_n^{\text{ext}}, \boldsymbol{f}_{n+1}^{\text{ext}}) \Big) = 0 \qquad \forall \ \delta \boldsymbol{q_n}, \delta \boldsymbol{\lambda_n},\end{aligned} \tag{7.64}$$

with the variation of the configuration $\boldsymbol{q}$ and Lagrange multiplier $\boldsymbol{\lambda}$ equals to zero at the time boundaries, i.e. $\delta \boldsymbol{q}_0 = \delta \boldsymbol{q}_{n_t} = 0$, $\delta \boldsymbol{\lambda}_0 = \delta \boldsymbol{\lambda}_{n_t} = 0$. With

$$\boldsymbol{f}_n^{\text{ext}-} = \frac{\Delta t}{2} \ \frac{\boldsymbol{f}_n^{\text{ext}} + \boldsymbol{f}_{n+1}^{\text{ext}}}{2}, \qquad \boldsymbol{f}_n^{\text{ext}+} = \frac{\Delta t}{2} \ \frac{\boldsymbol{f}_{n-1}^{\text{ext}} + \boldsymbol{f}_n^{\text{ext}}}{2}, \tag{7.65}$$

the constrained discrete Euler-Lagrange equations can be written as

$$\frac{\partial L_d(\boldsymbol{q}_n, \boldsymbol{q}_{n+1})}{\partial \boldsymbol{q}_n} + \frac{\partial L_d(\boldsymbol{q}_{n-1}, \boldsymbol{q}_n)}{\partial \boldsymbol{q}_n} - \mathbf{G}_d^T(\boldsymbol{q}_n) \cdot \boldsymbol{\lambda}_n + \boldsymbol{f}_n^{\text{ext}-} + \boldsymbol{f}_n^{\text{ext}+} = \mathbf{0}, \tag{7.66}$$

$$\boldsymbol{g}(\boldsymbol{q}_{n+1}) = \mathbf{0}. \tag{7.67}$$

In case of a dependency of $\boldsymbol{f}^{\text{ext}}$ on the configuration $\boldsymbol{q}$ and its time derivative $\dot{\boldsymbol{q}}$, which is the case e.g. for the viscoelastic contribution given in Eq. (6.14),

$$W^{\text{v}} = \int_{\mathcal{B}_0} \mathbf{P}^{\text{v}} : \mathbf{F} \ dV. \tag{7.68}$$

$$\boldsymbol{f}^{\text{v}} = \frac{\partial W^{\text{v}}}{\partial \boldsymbol{q}} = \int_{\mathcal{B}_0} \frac{\partial W^{\text{v}}}{\partial \mathbf{F}} : \frac{\partial \mathbf{F}}{\partial \boldsymbol{q}} \ dV = \int_{\zeta} \int_{-\frac{h}{2}}^{\frac{h}{2}} \mathbf{P}^{\text{v}} : \frac{\partial \mathbf{F}}{\partial \boldsymbol{q}} \ d\xi \ dA, \tag{7.69}$$

the external force $\boldsymbol{f}^{\text{ext}}$ is approximated by

$$\boldsymbol{f}_n^{\text{ext}-} = \frac{\Delta t}{2} \ \boldsymbol{f}^{\text{ext}} \left(\frac{\boldsymbol{q}_n + \boldsymbol{q}_{n+1}}{2}, \frac{\boldsymbol{q}_{n+1} - \boldsymbol{q}_n}{\Delta t} \right), \tag{7.70}$$

$$\boldsymbol{f}_n^{\text{ext}+} = \frac{\Delta t}{2} \ \boldsymbol{f}^{\text{ext}} \left(\frac{\boldsymbol{q}_{n-1} + \boldsymbol{q}_n}{2}, \frac{\boldsymbol{q}_n - \boldsymbol{q}_{n-1}}{\Delta t} \right). \tag{7.71}$$

The tangent matrix w.r.t. the unknown configuration $\boldsymbol{q}_{n+1} \in \mathbb{R}^{n_q}$ and unknown Lagrange multipliers $\boldsymbol{\lambda}_n \in \mathbb{R}^{n_c}$ reads

$$\mathbf{K} = \begin{bmatrix} \dfrac{\partial \mathbf{R}^{EL,1}(\boldsymbol{q}_{n-1}, \boldsymbol{q}_n, \boldsymbol{q}_{n+1}, \boldsymbol{\lambda}_n)}{\partial \boldsymbol{q}_{n+1}} & \dfrac{\partial \mathbf{R}^{EL,1}(\boldsymbol{q}_{n-1}, \boldsymbol{q}_n, \boldsymbol{q}_{n+1}, \boldsymbol{\lambda}_n)}{\partial \boldsymbol{\lambda}_n} \\ \dfrac{\partial \mathbf{R}^{EL,2}(\boldsymbol{q}_{n-1}, \boldsymbol{q}_n, \boldsymbol{q}_{n+1}, \boldsymbol{\lambda}_n)}{\partial \boldsymbol{q}_{n+1}} & \dfrac{\partial \mathbf{R}^{EL,2}(\boldsymbol{q}_{n-1}, \boldsymbol{q}_n, \boldsymbol{q}_{n+1}, \boldsymbol{\lambda}_n)}{\partial \boldsymbol{\lambda}_n} \end{bmatrix}, \quad (7.72)$$

where $\mathbf{R}^{EL,1}$ and $\mathbf{R}^{EL,2}$ represent the residual vectors of the Euler-Lagrange equations defined in Eq. (7.66) and Eq. (7.67), respectively. In this work, the residual vectors $\mathbf{R}^{EL,1}$, $\mathbf{R}^{EL,2}$ and the tangent matrix $\mathbf{K}$ are derived by using the automatic differentiation tool CasADi, see [293]. The nonlinear system of equations, with given configurations $\boldsymbol{q}_{n-1}$ and $\boldsymbol{q}_n$, is solved for $\boldsymbol{q}_{n+1}$ via the Newton-Raphson scheme.

7.3 Numerical examples

The numerical examples presented in this work illustrate the capabilities of the dynamic viscoelastic electromechanical shell model. The structure-preserving time integration ensures good long-term energy behaviour and thus prevents both numerical dissipation and artificial energy gain. The numerical examples comprise different geometries (rectangular, cylindrical, spherical) and deformation states (contraction, bending). The parameters for the dielectric material model from Eq. (6.13) are shown in Tab. 7.1 and originate from the work of [270].

Table 7.1: Parameter set for the dielectric material model from Eq. (6.13). The parameter λ is computed via $\lambda = \kappa - 2\mu/3$, where the bulk modulus κ is set to 10 MPa.

parameter	ρ	λ	μ	ϵ_0	c_1	c_2
unit	$\mathrm{g/mm^3}$	MPa	MPa	C/Vm	$\mathrm{N/V^2}$	$\mathrm{N/V^2}$
value	1	6.66	5.0	8.85410^{-12}	10	6

7.3.1 Contraction

Rectangular geometry

In the following, we consider a rectangular geometry with the dimension 1.0 mm x 1.0 mm and thickness $h = 0.04$ mm lying in the (x, y)-plane. For any node with $x = 0$ mm, all mechanical DoFs are fixed and the electric potential ϕ_m is set to 0 V. For all nodes with $x = 1.0$ mm, an electric potential $\phi_m > 0$ V is applied. The difference in the electric potential ϕ_m for the nodes with $x = 1.0$ mm compared to the nodes with $x = 0$ mm is denoted as $\Delta\phi$. The second electric DoF α (defined in Eq. (7.7)) is set to 0 V/mm in the whole computational domain. The electric potential ϕ is therefore constant along the thickness direction. The total simulation time is 10 ms with a time step $\Delta t = 2 \cdot 10^{-2}$ ms. Initially, the viscous damping parameter is $\eta = 0.003$.
In Fig. 7.2 (a), the contraction for $\Delta\phi = 0.8$ V is visualised at $t = 10$ ms (steady-state due to viscous damping) with approximately 30% shortening in the x-direction. In Fig. 7.2 (b), the convergence of the x-displacement u_x of a corner node (initially at $x = 1.0$ mm, $y = 0$ mm) with respect to the mesh refinement is depicted. Whilst keeping the viscous damping parameter at $\eta = 0.003$, the spatial discretisation is varied between two and ten elements per side length. After $t = 10$ ms of simulation time, we compare the displacement u_x for the different spatial discretisations. By refining the mesh, the x-displacement of the corner node converges to approximately 0.708 mm. Based on the results shown in Fig. 7.2 (b), the discretisation is set to 4^2 elements for the subsequent investigations of the rectangular geometry.

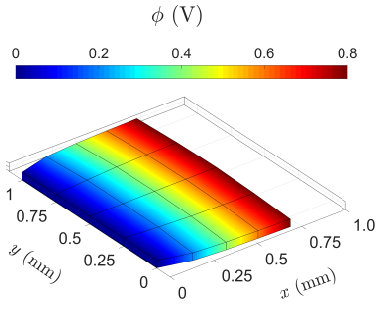

(a) deformed configuration.

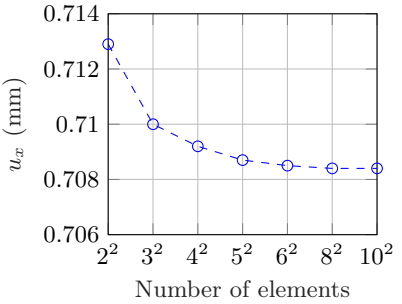

(b) convergence study.

Figure 7.2: In (a), the deformed configuration of the geometry at $t = 10$ ms is depicted with an applied voltage difference $\Delta\phi = 0.8$ V with the viscous damping parameter $\eta = 0.003$. The convergence plot in (b) shows the x-displacement u_x of a corner node (initially at $x = 1$ mm, $y = 0$ mm) on the free end at $t = 10$ ms with the viscous damping parameter $\eta = 0.003$ for different mesh sizes.

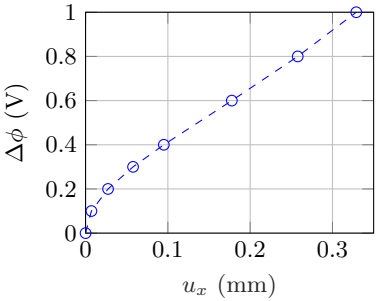

(a) u_x for varying $\Delta\phi$.

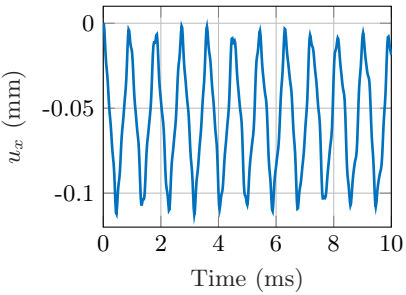

(b) u_x for an undamped oscillation.

Figure 7.3: In (a), the displacement u_x at $t = 10$ ms is shown for a varying electric potential difference $\Delta\phi$ with an additional mechanical Dirichlet boundary condition (displacement $u_y = 0$ mm) for all nodes with $y = 0$ mm and $y = 1.0$ mm. The x-displacement plot in (b) shows the undamped oscillation with $\eta = 0.0$ for $\Delta\phi = 0.3$ V.

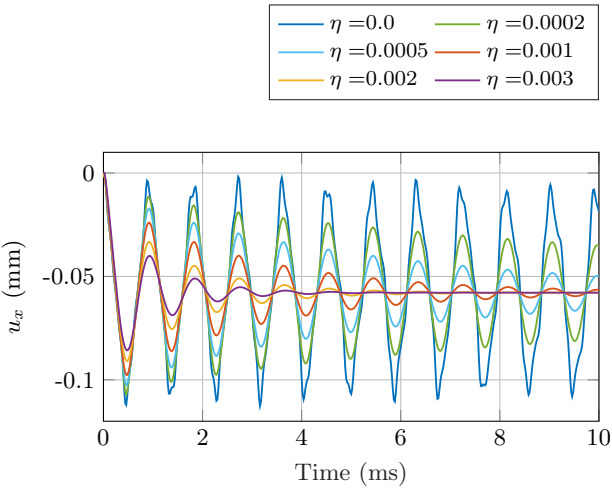

Figure 7.4: The displacement u_x for the edge node ($x = 1.0$ mm, $y = 0$ mm) is shown for varying damping parameters η with an applied electric potential difference of $\Delta\phi = 0.3$ V.

In Fig. 7.3 (a), the displacement u_x for the corner node ($x = 1.0$ mm, $y = 0$ mm) is shown for a varying potential difference $\Delta\phi \in \{0.1, 0.2, 0.3, 0.4, 0.6, 0.8, 1.0\}$V. An additional mechanical boundary condition (displacement $u_y = 0$ mm) for all nodes with $y = 0$ mm and $y = 1.0$ mm is applied. The displacement u_x is measured at $t = 10$ ms with a viscous damping parameter of $\eta = 0.003$. The characteristics of the curve – nonlinear for small displacements, almost linear for larger displacements – reflect the utilised Neo-Hookean material model in Eq. (6.13). The plot in Fig. 7.3 (b) shows the displacement u_x of the undamped system ($\eta = 0$) for a time period of 10 ms. As expected for the undamped system, oscillation can be observed. Neither numerical damping nor artificial energy gain is present (no trend in the amplitude of u_x), which shows the good energy behaviour of the structure-preserving time integration.
In Fig. 7.4, the influence of the viscous material behaviour is shown. The simulation setup from Fig. 7.3 with an applied voltage difference $\Delta\phi = 0.3$ V is utilised. The plot visualises the displacement u_x over a time period of $t = 10$ ms with a time step of $\Delta t = 2 \cdot 10^{-2}$ ms. The viscous damping parameter is varied with $\eta \in \{0.0, 0.0002, 0.0005, 0.001, 0.002, 0.003\}$. For zero damping, i.e. $\eta = 0$, Fig. 7.3 (b) is recovered. With an increasing parameter η, the amplitude of the oscillation starts to decrease. For a damping parameter $\eta = 0.003$, the steady state is reached after approximately 4 ms.

Cylindrical geometry

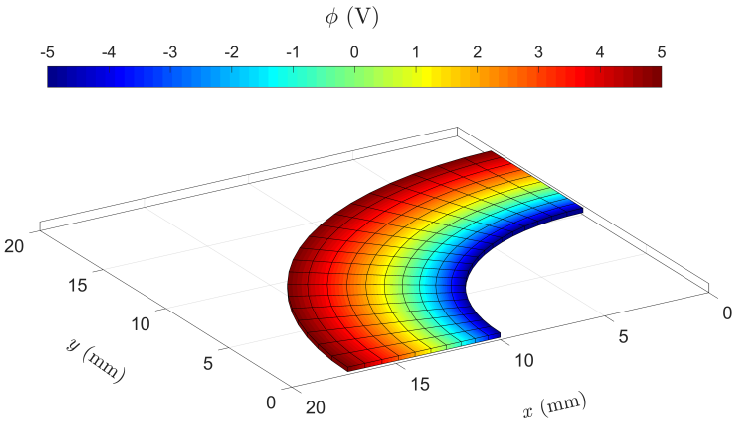

Figure 7.5: Deformed configuration of the cylindrical geometry (inner radius r_i=10 mm, outer radius r_a=20 mm, thickness $h = 0.2$ mm) is depicted with an applied voltage difference $\Delta\phi = 10$ V after $t = 20$ ms.

In this section, the contraction of a cylindrical shape (inner radius r_i=10 mm, outer radius r_a=20 mm, thickness shell $h = 0.2$ mm) is compared with data from the literature, see [270] and Fig. 7.5. Due to the symmetry properties of the geometry (rotationally symmetric with respect to the z-axis), it is sufficient to consider one-quarter of the geometry as the computational domain. Following [270], the geometry is discretised into 200 quadrilateral elements – 10 elements in the radial and 20 elements in the circumferential direction, respectively. The total simulation time is 20 ms with a time increment of $\Delta t = 2 \cdot 10^{-1}$ ms. The viscous damping parameter is $\eta = 10$. The mechanical DoFs are fixed for all nodes at the inner boundary. Due to the symmetric property, an additional mechanical Dirichlet boundary condition (displacement $u_x = 0$ mm) for all nodes with coordinate $x = 0$ mm is applied. Similarly, the displacement is set to $u_y = 0$ mm for all nodes with coordinate $y = 0$ mm. The electrical boundary condition consists of an electric potential difference $\Delta\phi = 10$ V with $\phi_m = -5$ V on the inner radius and $\phi_m = 5$ V on the outer radius, see Fig. 7.5. The second electric DoF α is set to 0 V/mm in the whole computational domain and thus the electric potential ϕ is constant along the thickness direction. The material model in Eq. (6.13) as well as the material parameters in Tab. 7.1 coincide with [270].

In Fig. 7.6, the temporal evolution of the radial displacement r is depicted for all nodes with $x = 0$ mm (11 nodes). In other words, the radial displacement r is shown for all nodes along the radial direction from the inner radius $r_i = 10$ mm to the outer radius $r_a = 20$ mm. Due to the viscoelastic effect, the system

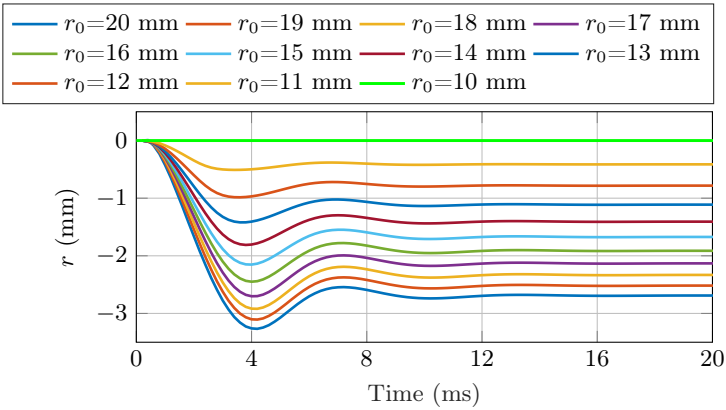

Figure 7.6: The displacement plot shows the temporal evolution of the nodal displacement r in a radial direction along the boundary ($x = 0$) for different initial radii $r_0 \in [r_i, r_a]$.

reaches the steady state after approximately 12 ms. It is worth noting that the radial displacement r is not uniformly increasing along the radial direction (the larger the initial radius r_0 (here r_0 denotes the radial position of a node in the undeformed configuration), the smaller the distance between the lines). This is plausible, as the electric potential distribution along the radial direction is nonlinear (see Fig. 7.5 and Fig. 7.7 (b)). The nonlinear electric potential distribution originates from the difference in the cross-sectional area between the inner and outer radius. Consequently, the nonlinear electric potential distribution leads to a non-homogeneous gradient field of the electric potential ϕ and thus to a non-uniform contraction along the radial direction (higher gradient and electric field $\boldsymbol{E}^e$ for smaller r_0 and thus larger contraction).
In Fig. 7.7 (a) and (b), the results are compared with the study in [270], wherein the same geometry and material model is considered (without dynamics). In Fig. 7.7 (a), the radial displacement r is plotted over the initial radius r_0 for all nodes (△) along the radial direction with the coordinate $x = 0$ mm at $t = 20$ ms (endpoints in Fig. 7.6). The graph (–) is extracted from "Figure 2. Displacement under electric potential loading $\Delta\phi = 10$ V." in [270]. The nodal r-displacements (△) show a good agreement with the results in [270]. In Fig. 7.7 (b), the electric potential ϕ is plotted over the initial radius r_0

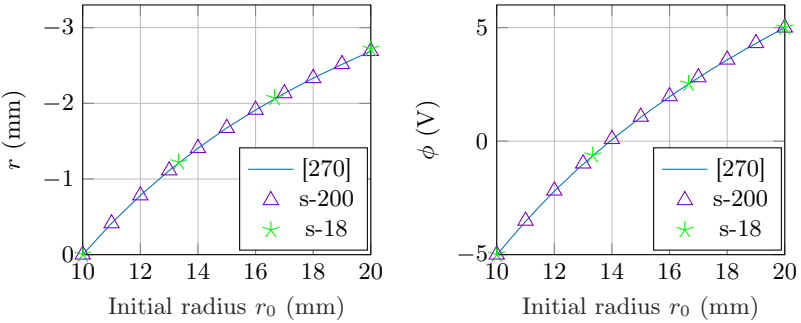

(a) r over initial radius r_0.

(b) ϕ over initial radius r_0.

Figure 7.7: In (a), the r-displacement is shown over the initial radius r_0 for all nodes (△) along the radial direction with $x = 0$ at $t = 20$ ms. The results are compared with literature data [270] and show a very good agreement. In (b), the nonlinear electric potential distribution over the initial radius r_0 is presented. Even with a reduction to 3 elements in the radial direction and 6 elements in the circumferential direction, see (⋆), the results for (a) and (b) still agree well with the literature data.

for all nodes (△) along the radial direction with the coordinate $x = 0$ mm at $t = 20$ ms. The graph (–) is extracted from "Figure 3. Electric potential distribution under electric potential loading $\Delta\phi = 10$ V." in [270]. The nodal electric potentials (△) show a good agreement with the results in [270]. It is noteworthy that the results in Fig. 7.7 still agree well even when the spatial discretisation is significantly coarsened (3 elements in radial direction and 6 elements in circumferential direction), see (⋆ s-18).

Cylindrical geometry – mimicking the inflation of a hemisphere

When coupling the support system (dielectric hemisphere) with the cardiovascular system (myocardial muscle), due to the inflation of the hemisphere, the pressure acting on the pericardium of the heart can be controlled via the applied electric potential ϕ. Thus the systolic and diastolic phases of the cardiac cycle can be supported. In order to mimic a support system for the cardiovascular system based on an artificial muscle/dielectric material, a simplified geometry in the form of a thin-walled hemisphere is considered. The geometry of the 3D thin-walled hemisphere is further simplified by a 2D cross-sectional representation and making use of the symmetry, reducing to the

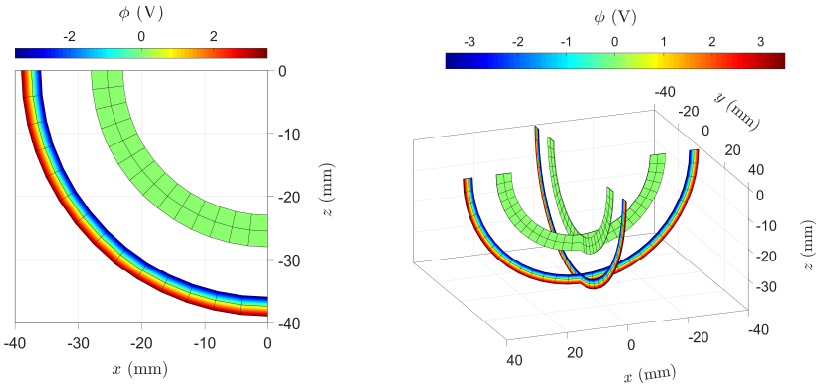

(a) undeformed and deformed configuration.

(b) 3D visualisation.

Figure 7.8: In (a), the undeformed and deformed configurations are depicted for the cylindrical geometry mimicking a cross-section of an inflated hemisphere. In (b), the undeformed and deformed configurations from (a) are visualised in 3D via multiple cross-sections.

well-known cylindrical geometry from the previous section (see Fig. 7.8). Such an artificial muscle-based support system is capable of supporting the cardiovascular system during systole and diastole (positive and negative pressure on the pericardium; see [184] and also Fig. 7.9 (b)). The inner radius of the cylindrical geometry is given by r_i=23 mm, the outer radius r_a=28 mm, and the thickness $h = 0.2$mm. The geometry is discretised with 28 quadrilateral elements with 2 elements in the radial and 14 elements in the circumferential direction, respectively. The damping parameter is set to $\eta = 30$, the time increment is $\Delta t = 2 \cdot 10^{-1}$ ms and the total simulation time is 200 ms. Due to the symmetric property, a mechanical Dirichlet boundary condition (displacement $u_x = 0$ mm) for all nodes with coordinate $x = 0$ mm is applied. Similarly, the displacement is set to $u_z = 0$ mm for all nodes with coordinate $z = 0$ mm. The electrical boundary condition consists of an electric potential difference $\Delta\phi = 7$ V with $\phi_m = -3.5$ V on the inner radius and $\phi_m = 3.5$ V on the outer radius, see Fig. 7.8. The second electric DoF α is set to 0 V/mm in the whole computational domain and thus the electric potential ϕ is constant along the thickness direction. The bulk modulus $\kappa = 70$ MPa is utilised in order to increase the incompressibility of the material. In Fig. 7.8 (a) and (b), the undeformed and deformed configurations of the cylindrical geometry are presented at a time $t = 200$ ms. In Fig. 7.8 (a), concentric inflation can be ob-

served with the initial inner radius r_i increasing from 23 mm to 35.93 mm. The initial wall thickness $t_w = r_a - r_i = 5$ mm reduces to approximately 3.09 mm. In Fig. 7.8 (b) and in Fig. 7.9 (a), the 3D representation of the hemisphere is visualised by plotting multiple cross-sections around the z-axis. In Fig. 7.10, the radius of the inflated hemisphere, as well as the volume, are presented for increasing electric potential difference $\Delta\phi \in \{1.0, 2.0, 3.0, 4.0, 5.0, 6.0, 7.0\}$ V. The characteristic change of the radius w.r.t. the increase of electric potential (nonlinear for small $\Delta\phi$, almost linear for larger $\Delta\phi$), reflects the utilised Neo-Hookean material model in Eq. (6.13). The volume of the hemisphere is given by $V_{he} = \frac{2}{3} \cdot \pi \cdot r_i^3$ and thus a cubic relation between the volume V_{he} and the radius r_i holds. The volume V_{he} increases from 25.48 ml up to 97.39 ml.

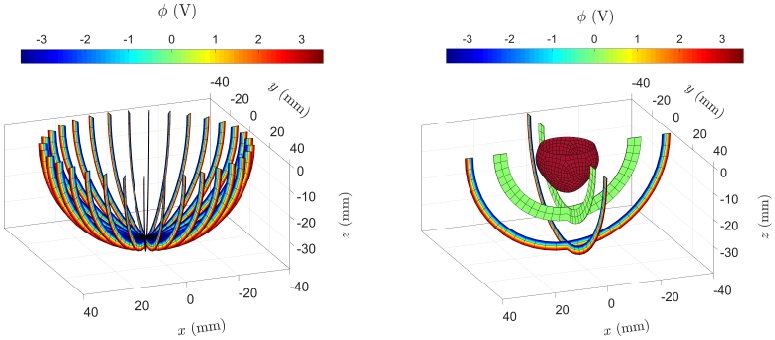

(a) visualisation of layers. (b) support system.

Figure 7.9: In (a), the deformed cross-section is plotted multiple times by a rotation around the z-axis to provide a 3D impression of the hemisphere. In (b), the deformed and undeformed configurations, including a dummy heart, are depicted.

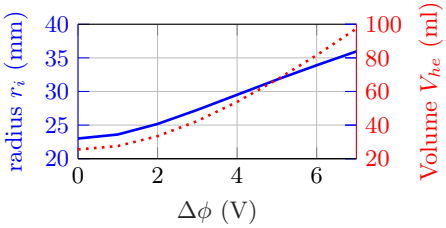

Figure 7.10: Radius r_i as well as the volume V_{he} of the inflated hemisphere over the electric potential difference $\Delta\phi$.

Spherical geometry – hemisphere with 18° hole

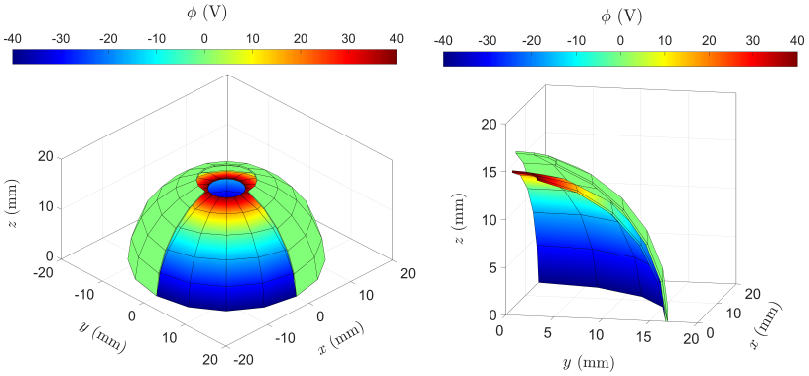

(a) undeformed and deformed configuration

(b) computational domain.

Figure 7.11: In (a), the undeformed and deformed configuration for the hemisphere with an 18° hole are shown. Due to the symmetry of the problem, the computational domain can be reduced to one-quarter of the hemisphere, see (b).

In this section, the geometry of a hemisphere with an 18° hole (measured with respect to the z-axis) is considered, which is a standard test in linear and non-linear shell analysis (pinched hemisphere; e.g., [294, 295, 296]). Due to the symmetry properties of the hemisphere, only one-quarter of the geometry is considered as the computational domain, see 7.11 (b). The radius of the hemisphere is r=16.77 mm with a thickness of $h = 0.2$mm. All translational DoFs are fixed for nodes with coordinate z=0 mm. Due to the symmetric property, a mechanical Dirichlet boundary condition (displacement $u_x = 0$ mm) for all nodes with coordinate $x = 0$ mm is applied. Similarly, the displacement is set to $u_y = 0$ mm for all nodes with coordinate $y = 0$ mm. The electrical boundary condition consists of an electric potential difference $\Delta\phi = 80$ V with $\phi_m = -40.0$ V for nodes with coordinate z=0 mm and $\phi_m = 40.0$ V at the boundary of the 18° hole, see Fig. 7.11. The second electric DoF α is set to 0 V/mm in the whole computational domain and thus the electric potential ϕ is constant along the thickness direction. This 3D geometry imitates the dynamic viscoelastic dielectric thin-walled support system. The geometry is discretised with 20 quadrilateral elements with 4 elements in the azimuthal direction and 5 elements in the polar direction, respectively. The simulation time is 500 ms with a time increment $\Delta t = 8 \cdot 10^{-1}$ ms. The damping parameter is $\eta = 30$.

In Fig. 7.11 (a) and (b), the deformed and undeformed configurations after a time period of 500 ms are visualised. A shortening in z-direction can be observed. In terms of the support system, this would cause a positive pressure acting on the pericardium of the heart. In Fig. 7.12 (b), the z-displacement u_z of the six nodes in the polar direction (all nodes with coordinate $x = 0$) is shown. Additionally, the plot shows the damping due to the viscous material behaviour and thus a steady state is reached after approximately 250 ms. In Fig. 7.12 (a), the nonlinear electric potential distribution along the polar direction is depicted together with a reference solution (meshed with a 4-node quadrilateral shell element, namely DS4) from a commercial CAE software (Abaqus). The potential distribution, based on the six nodes in the polar direction (△), shows a good agreement with the reference solution (–).

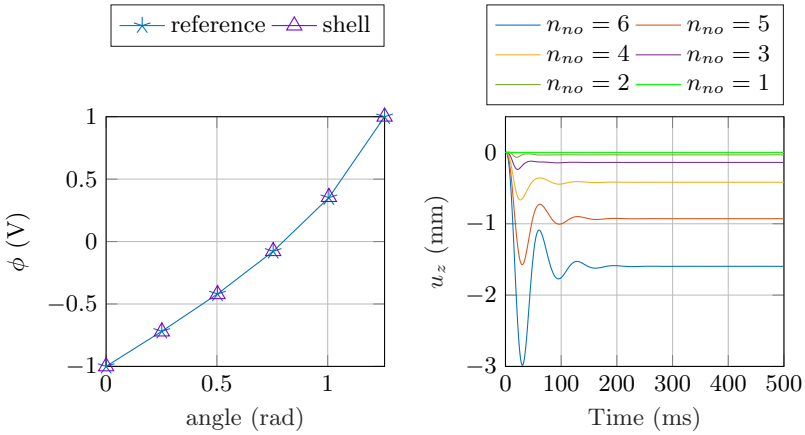

(a) electric potential distribution.

(b) z-displacement.

Figure 7.12: In (a), the nonlinear electric potential distribution along the polar direction is visualised. In (b), the z-displacement of the six nodes in the polar direction (all nodes with coordinate $x = 0$) is shown for a viscous damping parameter $\eta = 30$.

7.3.2 Bending

In this section, the deformation state of bending is induced by a proper choice of electrical boundary conditions. For this purpose, a rectangular geometry with the dimension 4.0 mm x 0.2 mm and a thickness of $h = 0.02$ mm is utilised (see Fig. 7.13. At x=0 mm, all mechanical DoFs are fixed). Additionally, for all nodes with y=0 mm and y=0.2 mm, the translational DoF in y-direction is constrained to zero. The geometry is discretised with 320 quadrilateral elements with 4 elements in y-direction and 80 elements in x-direction, respectively. Assuming the node labeling in Fig. 7.14, for all nodes with index $i = 2, 4, ..., 78, 80$ and $j = 1, 2, 3, 4, 5$, the electrical potential ϕ_m on the mid surface is set to $\phi_m = 30$ V. The second electrical DoF α, which controls the transmural electric potential change, is set to $\alpha = 400$ V/mm. For all nodes with index $i = 1, 3, ..., 79, 81$ and $j = 1, 2, 3, 4, 5$, the electrical potential ϕ_m on the mid surface is set to $\phi_m = 0$ V. The second electrical DoF α is set to $\alpha = 0$ V/mm. See also Tab. 7.2 for a brief summary of the electrical boundary conditions. Due to the coupling between the shear and bending deformation via the material model in Eq. (6.13), pure bending can not be achieved. Thus, a simplified material model is proposed

$$\Omega(\boldsymbol{\epsilon}, \phi) = \underbrace{\frac{100}{2} \boldsymbol{\epsilon}^T \, \mathbf{I}_{8x8} \, \boldsymbol{\epsilon}}_{W_{\text{mech}}} + \underbrace{\frac{\partial \phi_m}{\partial \xi^1} \cdot \epsilon_{11} + \frac{\partial \alpha}{\partial \xi^1} \cdot \kappa_{11}}_{W_{\text{ele}}} . \tag{7.73}$$

The total simulation time is set to 20 ms with a time increment $\Delta t = 2 \cdot 10^{-2}$ ms. The viscous damping parameter is $\eta = 3$.
In Fig. 7.13, the deformed configuration is presented at different time points $t \in \{0, 1, 4, 6, 20\}$ ms. In Fig. 7.15 (a) and (b), the displacement in z-direction over the x-coordinate, as well as the displacement of the tip node (x=4.0 mm, y=0 mm) in z-direction over time, are depicted. The total displacement of the tip node in the z-direction of -0.45 mm is reached after approximately 10 ms when the system has reached the steady state.

Table 7.2: Electrical boundary conditions for bending deformation.

	node index	ϕ_m (V)	α (V/mm)
nodes in x-direction; activated	$i = 2, 4, \ldots, 78, 80$	30	400
nodes in x-direction; non-activated	$i = 1, 3, \ldots, 79, 81$	0	0

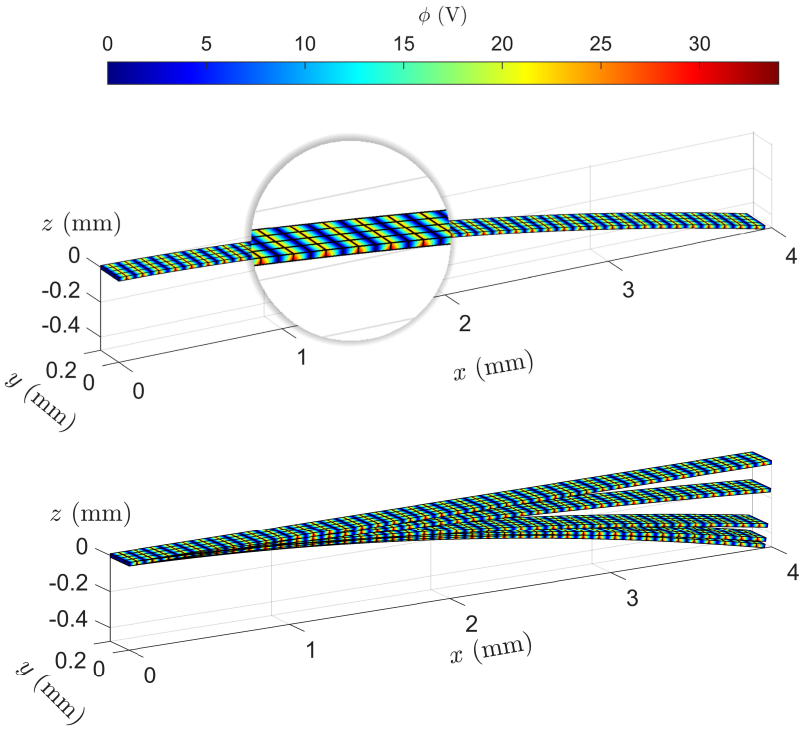

Figure 7.13: Deformed configuration of the bent shell at different time nodes $t \in \{0, 1, 4, 6, 20\}$ ms. The top plot shows the spatial configuration at $t = 20$ ms.

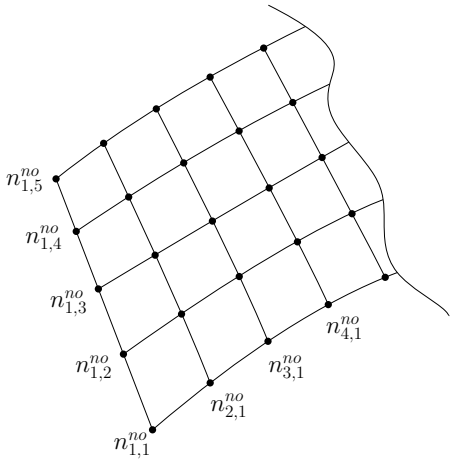

Figure 7.14: Node labeling for the electrical boundary conditions.

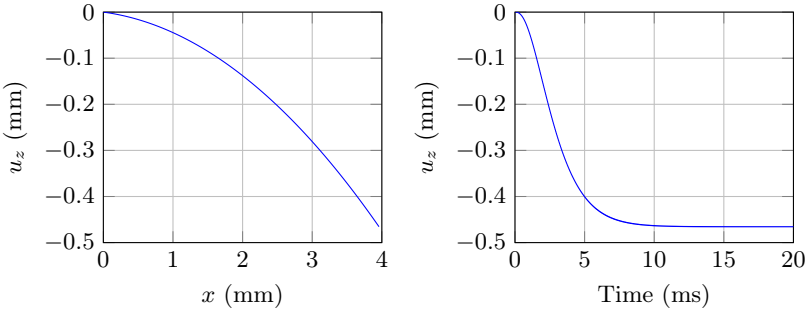

(a) displacement u_z along x-direction. (b) displacement u_z of the tip node over time.

Figure 7.15: In (a), the displacement u_z in the z-direction over the x-coordinate is visualised. In (b), the displacement of the tip node ($x = 4.0$ mm, $y = 0$ mm) over the simulation time of 20 ms is depicted.

7.4 Summary

The local Euler-Lagrange equations are derived for the underlying variational principle of virtual work. The variational formulation of the dynamic viscoelastic electromechanical shell is derived based on the Lagrange-d'Alembert principle. Numerical examples including different geometries (rectangular, cylindrical, spherical) as well as deformation states (contraction, bending) are presented. For the simple benchmark problems like the contraction of the cylindrical geometry, the results show a good agreement with data from the literature. The variational time integration derived in the Lagrangian setting ensures good long-term energy behaviour. We have shown that the implemented shell formulation is generally suitable to simulate a heart support system consisting of a thin dielectric material. However, the implementation of the variational principle of Hu-Washizu could be a promising next step to resolve well-known issues for pure displacement-based shell formulations e.g. locking (especially shear and membrane locking) and to include important features when considering dielectric elastomeric materials (thickness strains).

8 Conclusions

Findings This work contributes to the field of modelling and simulation of both cardiac and artificial muscles. A new robust, efficient and more accurate Laplace-Dirichlet-Rule-Base-Method (LDRBM) for computing the orthotropic cardiac tissue structure on complex unstructured finite element meshes has been developed (objective I.I.). The proposed method is based on the development of a discontinuous Galerkin framework which shows the capability of accurately computing the transmural path (objective I.I.A.) and wall thickness (objective I.I.B.). The finite element-based framework has the essential benefits that the transmural thickness and depth can be instantly computed on the unstructured tetrahedral mesh of the subsequent electromechanical simulation, in other words, it is not limited to structured meshes in the finite difference framework and therefore allows, due to the modularity of the framework, a straightforward integration into existing LDRBMs (e.g. [167, 169]). Additionally, the proposed regional transmural fibre and sheet rules based on diffusion tensor magnetic resonance imaging (DT-MRI) measurements of the left ventricle show a significantly improved fit to DT-MRI data compared to e.g. existing 2-parameter functions [166] and can readily be used in established rule-based methods (RBMs) (objective I.I.C.). Moreover, the comparison with existing LDRBMs shows a significant method-dependent transmural tissue orientation with improved accuracy for the proposed LDRBM (objective I.I.D.). The study about the influence of the orthotropic tissue orientation on the overall cardiac function (based on defined important cardiac characteristics, including local myofibre orientation and global characteristics as well as local characteristics) show that the local fibre orientation in the patient-specific left ventricle differs significantly for all methods. Despite the significant difference in the local myofibre orientation, a more diverse picture is observed in terms of the global cardiac characteristics. While the myocardial volume reduction and peak pressure exhibit a rather insensitive behaviour to a change in the LDRBM, the apical shortening, as well as the fractional wall thickening, react sensitively to a change in myofibre orientation. The ejection fraction shows a moderate sensitivity. The local cardiac characteristics, fibre stress and strain, seem to be highly sensitive, and in general more than the global characteristics (objective I.II.).

The variational formulation of the dynamic, viscoelastic, electromechanical shell is derived from the Lagrange-d'Alembert principle including structure-preserving time integration (objectives II.I.A.-D.). Numerical examples including different geometries (rectangular, cylindrical, spherical), as well as deformation states (contraction, bending), are presented (objective II.II.).

The variational time integration derived in the Lagrangian setting ensures good long-term energy behaviour. As a potential next step, the integration of additional thickness strains, the formulation can be extended to the variational principle of Hu-Washizu. Overall, the initial results of the proposed shell formulation show that it is a promising choice to simulate the dynamic, viscoelastic, electromechanical characteristics of a DEA-based CaAD.

Relevance The proposed LDRBM has a wide field of application and is not limited to cardiac modelling. Possible applications include studying fibre-reinforced materials or other muscular biological tissue. Moreover, such a robust, efficient and accurate method to determine the transmural path/arc length can find application wherever an accurate assessment of the wall thickness in complex 3D domains is necessary (e.g. cortical thickness). Additionally, by considering the significance of transmural thickness as a crucial cardiac risk indicator in the clinical setting, the 3D thickness assessment within the LDRBM framework can be readily applied to patient imaging data in the clinic or during the electromechanically coupled finite element simulation. This is made possible by the user-friendly implementation facilitated by FEniCS and thus opens new opportunities in clinical application or post-processing. In other words, this allows for the instant 3D thickness assessment in the whole cardiac domain and the tedious and time-consuming task of measuring the wall thickness at single regions of interest is eliminated. As previously mentioned, a major advantage of the new LDRBM framework is the modularity of the method allowing for simple integration of the thickness assessment as well as the novel fibre and sheet rules into established LDRBMs. It is worth noting that, for all rule-based approaches, a common convention is needed, on how the transmural depth is defined during experimental observation (e.g., DT-MRI) and in computational models. Without such a convention, the fibre and sheet rules based on the transmural depth are not consistent between measurement and modelling. The electromechanical simulations underline the influence of the orthotropic tissue structure models on cardiac function. Even though we limited the study to a small subset of related tissue structure models (LDRBMs) and supposedly the same transmural orientation ($\alpha = \pm 60°$, $\beta = 0°$, Laplace equation-based transmural interpolation), one can observe significant differences w.r.t. the local myofibre orientation. Therefore, caution is advised when comparing studies with different orthotropic tissue structure models, even if they supposedly have the same transmural orientation (e.g., for the prediction of the myocardial volume reduction), the three LDRBMs, B-RBM, H-RBM and W-RBM, predict similar results (i.e., a comparison among studies with different orthotropic tissue structure models B-RBM, H-RBM and W-RBM is feasible). For the prediction of local characteristics such as fibre stress or fibre strain, the results seem to be very sensitive w.r.t. the local myofibre

orientation (i.e., a comparison among studies with different orthotropic tissue structure models B-RBM, H-RBM and W-RBM is not feasible).
The developed shell formulation is the first dynamic, viscoelastic, electromechanical formulation including structure-preserving time integration. Due to the well-known reduced computational complexity of shell formulations compared to complex 3D finite element models, the formulation can be efficiently applied in time-demanding model predictions for thin-walled dielectric actuators. Moreover, the formulation could be a valuable supplement in a wide field of applications including artificial muscles, energy harvesting, biomedical devices etc. Further, the proposed formulation can be easily integrated into multibody systems or optimal control problems.

Prospects The proposed LDRBM is currently limited to individual ventricular geometries. The approach can be extended to more complex geometrical models (e.g. whole heart or biventricular geometries, complex endocardial structures like papillary muscles or trabeculations, see e.g. [167]). For the determined regional fibre and sheet angle rules, a smoothing algorithm across the interface of different subregions is needed to avoid non-smooth orientations, which can cause numerical issues during electromechanical simulation. The formulation of the shell model based on the variational principle of Hu-Washizu is a promising next step to resolve well-known issues for pure displacement-based shell formulations (e.g. locking, and especially shear and membrane locking) and allow for thickness strains when considering dielectric elastomeric materials with large in-plane expansion and thickness compression (e.g., [285]). Another important step is the validation of the dielectric elastomer shell model via experiments. In the future, the coupling of the DEA-based shell model with the cardiac tissue model is an interesting next step to better understand their interaction. This can be further advanced by extending the model with optimal control to optimally support the heart during systole and diastole, depending on the degree of severity of the pathology, physical activity of the patient, etc. In the long run, the model can be utilised to establish a clinical workflow, coupling patient-specific data (e.g. CT data) with the model and thus to develop and manufacture patient-specific assist devices.

Bibliography

[1] A. Timmis, P. Vardas, N. Townsend, et al. European Society of Cardiology: cardiovascular disease statistics 2021. *European Heart Journal*, 43(8):716–799, 01 2022.

[2] N. A. Trayanova and K. C. Chang. How computer simulations of the human heart can improve anti-arrhythmia therapy. *The Journal of physiology*, 594(9):2483–2502, 2016.

[3] O. J. Abilez, E. Tzatzalos, H. Yang, et al. Passive stretch induces structural and functional maturation of engineered heart muscle as predicted by computational modeling. *Stem cells*, 36(2):265–277, 2018.

[4] F. S. Costabal, K. Matsuno, J. Yao, et al. Machine learning in drug development: Characterizing the effect of 30 drugs on the qt interval using gaussian process regression, sensitivity analysis, and uncertainty quantification. *Computer Methods in Applied Mechanics and Engineering*, 348:313–333, 2019.

[5] P. M. Boyle, T. Zghaib, S. Zahid, et al. Computationally guided personalized targeted ablation of persistent atrial fibrillation. *Nature biomedical engineering*, 3(11):870–879, 2019.

[6] H. J. Arevalo, F. Vadakkumpadan, E. Guallar, et al. Arrhythmia risk stratification of patients after myocardial infarction using personalized heart models. *Nature communications*, 7(1):11437, 2016.

[7] M. Peirlinck, F. S. Costabal, J. Yao, et al. Precision medicine in human heart modeling: Perspectives, challenges, and opportunities. *Biomechanics and modeling in mechanobiology*, 20:803–831, 2021.

[8] M. Genet, L. C. Lee, B. Baillargeon, et al. Modeling pathologies of diastolic and systolic heart failure. *Annals of biomedical engineering*, 44:112–127, 2016.

[9] G. S. Karanasiou, M. I. Papafaklis, C. Conway, et al. Stents: biomechanics, biomaterials, and insights from computational modeling. *Annals of biomedical engineering*, 45:853–872, 2017.

[10] J. Wong, S. Göktepe, and E. Kuhl. Computational modeling of chemo-electro-mechanical coupling: a novel implicit monolithic finite element approach. *International journal for numerical methods in biomedical engineering*, 29(10):1104–1133, 2013.

[11] A. Ruhparwar, P. Piontek, M. Ungerer, et al. Electrically contractile polymers augment right ventricular output in the heart. *Artificial organs*, 38(12):1034–1039, 2014.

[12] J. A. J.-M. Chavanne. Cylindrical dielectric elastomer actuator for cardiac assist device. Technical report, EPFL, 2019.

[13] W. Wu, S. Zhang, Z. Wu, et al. On the understanding of dielectric elastomer and its application for all-soft artificial heart. *Science bulletin*, 66(10):981–990, 2021.

[14] T. Martinez, J. Chavanne, A. Walter, et al. Design and modelling of a tubular dielectric elastomer actuator with constrained radial displacement as a cardiac assist device. *Smart Materials and Structures*, 30(10):105024, 2021.

[15] M. Almanza, F. Clavica, J. Chavanne, et al. Feasibility of a dielectric elastomer augmented aorta. *Advanced science*, 8(6):2001974, 2021.

[16] M. Hirschvogel, L. Jagschies, A. Maier, et al. An in silico twin for epicardial augmentation of the failing heart. *International journal for numerical methods in biomedical engineering*, 35(10):e3233, 2019.

[17] M. Hirschvogel, M. Bassilious, L. Jagschies, et al. A monolithic 3d-0d coupled closed-loop model of the heart and the vascular system: experiment-based parameter estimation for patient-specific cardiac mechanics. *International journal for numerical methods in biomedical engineering*, 33(8):e2842, 2017.

[18] E. T. Roche, R. Wohlfarth, J. T. Overvelde, et al. A bioinspired soft actuated material. *Advanced Materials*, 26(8):1200–1206, 2014.

[19] E. T. Roche, M. A. Horvath, I. Wamala, et al. Soft robotic sleeve supports heart function. *Science translational medicine*, 9(373):eaaf3925, 2017.

[20] R. Wohlfarth. *A mixed-dimensional multi-physics model of a novel cardiac assist device coupled to patient-specific cardiovascular systems*. PhD thesis, Technische Universität München, 2021.

[21] D. B. Skinner, G. L. Anstadt, and T. F. Camp Jr. Applications of mechanical ventricular assistance. *Annals of Surgery*, 166(3):500, 1967.

[22] J. E. Lowe, M. P. Anstadt, P. Van Trigt, et al. First successful bridge to cardiac transplantation using direct mechanical ventricular actuation. *The Annals of thoracic surgery*, 52(6):1237–1245, 1991.

[23] G. Olivetti, G. Giordano, D. Corradi, et al. Gender differences and aging: effects on the human heart. *Journal of the American College of Cardiology*, 26(4):1068–1079, 1995.

[24] D. K. Molina and V. J. DiMaio. Normal organ weights in men: part i – the heart. *The American journal of forensic medicine and pathology*, 33(4):362–367, 2012.

[25] D. K. Molina and V. J. DiMaio. Normal organ weights in women: part i – the heart. *The American journal of forensic medicine and pathology*, 36(3):176–181, 2015.

[26] D. Noble. Cardiac action and pacemaker potentials based on the hodgkin-huxley equations. *Nature*, 188(4749):495–497, 1960.

[27] D. Noble. A modification of the hodgkin–huxley equations applicable to purkinje fibre action and pacemaker potentials. *The Journal of physiology*, 160(2):317, 1962.

[28] A. L. Hodgkin and A. F. Huxley. Currents carried by sodium and potassium ions through the membrane of the giant axon of loligo. *The Journal of physiology*, 116(4):449, 1952.

[29] W. Hanna. A simulation of human heart function. *Biophysical Journal*, 13(7):603–621, 1973.

[30] I. Mirsky. Ventricular and arterial wall stresses based on large deformation analyses. *Biophysical Journal*, 13(11):1141–1159, 1973.

[31] W. P. Hood Jr, W. J. Thomson, C. E. RACKLEY, and E. L. ROLETT. Comparison of calculations of left ventricular wall stress in man from thin-walled and thick-walled ellipsoidal models. *Circulation research*, 24(4):575–582, 1969.

[32] I. Mirsky. Left ventricular stresses in the intact human heart. *Biophysical journal*, 9(2):189–208, 1969.

[33] D. D. Streeter Jr, H. M. Spotnitz, D. P. Patel, et al. Fiber orientation in the canine left ventricle during diastole and systole. *Circulation research*, 24(3):339–347, 1969.

[34] T. Arts, R. S. Reneman, and P. C. Veenstra. A model of the mechanics of the left ventricle. *Annals of biomedical engineering*, 7:299–318, 1979.

[35] D. D. Streeter, R. N. Vaishnav, D. J. Patel, et al. Stress distribution in the canine left ventricle during diastole and systole. *Biophysical Journal*, 10(4):345–363, 1970.

[36] R. F. Janz and A. F. Grimm. Finite-element model for the mechanical behavior of the left ventricle: prediction of deformation in the potassium-arrested rat heart. *Circulation research*, 30(2):244–252, 1972.

[37] Y. Pao, E. L. Ritman, and E. Wood. Finite-element analysis of left ventricular myocardial stresses. *Journal of biomechanics*, 7(6):469–477, 1974.

[38] P. J. Hunter and B. H. Smaill. The analysis of cardiac function: a continuum approach. *Progress in biophysics and molecular biology*, 52(2):101–164, 1988.

[39] J. M. Guccione and A. D. McCulloch. Finite element modeling of ventricular mechanics. *Theory of Heart: biomechanics, biophysics, and nonlinear dynamics of cardiac function*, pages 121–144, 1991.

[40] J. M. Huyghe, T. Arts, D. H. Van Campen, and R. S. Reneman. Porous medium finite element model of the beating left ventricle. *American Journal of Physiology-Heart and Circulatory Physiology*, 262(4):H1256–H1267, 1992.

[41] P. Bovendeerd, T. Arts, J. Huyghe, et al. Dependence of local left ventricular wall mechanics on myocardial fiber orientation: a model study. *Journal of biomechanics*, 25(10):1129–1140, 1992.

[42] J. M. Guccione, K. D. Costa, and A. D. McCulloch. Finite element stress analysis of left ventricular mechanics in the beating dog heart. *Journal of biomechanics*, 28(10):1167–1177, 1995.

[43] F. J. Vetter and A. D. McCulloch. Three-dimensional analysis of regional cardiac function: a model of rabbit ventricular anatomy. *Progress in biophysics and molecular biology*, 69(2-3):157–183, 1998.

[44] M. P. Nash and P. J. Hunter. Computational mechanics of the heart. *Journal of elasticity and the physical science of solids*, 61:113–141, 2000.

[45] N. A. Trayanova. Whole-heart modeling: applications to cardiac electrophysiology and electromechanics. *Circulation research*, 108(1):113–128, 2011.

[46] B. Baillargeon, N. Rebelo, D. D. Fox, et al. The Living Heart Project: A robust and integrative simulator for human heart function. *Eur J Mech A Solids*, 48:38–47, November 2014.

[47] A. Quarteroni, T. Lassila, S. Rossi, and R. Ruiz-Baier. Integrated heart – coupling multiscale and multiphysics models for the simulation of the cardiac function. *Computer Methods in Applied Mechanics and Engineering*, 314:345–407, 2017.

[48] M. Fedele, R. Piersanti, F. Regazzoni, et al. A comprehensive and biophysically detailed computational model of the whole human heart electromechanics. *Computer Methods in Applied Mechanics and Engineering*, 410:115983, 2023.

[49] T. Gerach, S. Schuler, J. Fröhlich, et al. Electro-mechanical whole-heart digital twins: a fully coupled multi-physics approach. *Mathematics*, 9(11):1247, 2021.

[50] M. Strocchi, M. A. Gsell, C. M. Augustin, et al. Simulating ventricular systolic motion in a four-chamber heart model with spatially varying robin boundary conditions to model the effect of the pericardium. *Journal of biomechanics*, 101:109645, 2020.

[51] C. Dowling, A. M. Bavo, N. El Faquir, et al. Patient-specific computer simulation of transcatheter aortic valve replacement in bicuspid aortic valve morphology. *Circulation: Cardiovascular Imaging*, 12(10):e009178, 2019.

[52] P. de Jaegere, G. De Santis, R. Rodriguez-Olivares, et al. Patient-specific computer modeling to predict aortic regurgitation after transcatheter aortic valve replacement. *JACC: Cardiovascular Interventions*, 9(5):508–512, 2016.

[53] F. Sahli Costabal, J. Yao, and E. Kuhl. Predicting drug-induced arrhythmias by multiscale modeling. *International journal for numerical methods in biomedical engineering*, 34(5):e2964, 2018.

[54] A. Prakosa, H. J. Arevalo, D. Deng, et al. Personalized virtual-heart technology for guiding the ablation of infarct-related ventricular tachycardia. *Nature biomedical engineering*, 2(10):732–740, 2018.

[55] E. Garcia-Blanco, R. Ortigosa, A. J. Gil, and J. Bonet. Towards an efficient computational strategy for electro-activation in cardiac mechanics. *Computer Methods in Applied Mechanics and Engineering*, 356:220–260, 2019.

[56] F. Levrero-Florencio, F. Margara, E. Zacur, et al. Sensitivity analysis of a strongly-coupled human-based electromechanical cardiac model: Effect of mechanical parameters on physiologically relevant biomarkers. *Computer methods in applied mechanics and engineering*, 361:112762, 2020.

[57] M. R. Pfaller, M. Cruz Varona, J. Lang, et al. Using parametric model order reduction for inverse analysis of large nonlinear cardiac simulations. *International journal for numerical methods in biomedical engineering*, 36(4):e3320, 2020.

[58] C. M. Augustin, M. A. Gsell, E. Karabelas, et al. A computationally efficient physiologically comprehensive 3d–0d closed-loop model of the heart and circulation. *Computer methods in applied mechanics and engineering*, 386:114092, 2021.

[59] R. Piersanti, F. Regazzoni, M. Salvador, et al. 3d–0d closed-loop model for the simulation of cardiac biventricular electromechanics. *Computer Methods in Applied Mechanics and Engineering*, 391:114607, 2022.

[60] F. Regazzoni, M. Salvador, P. C. Africa, et al. A cardiac electromechanical model coupled with a lumped-parameter model for closed-loop blood circulation. *Journal of Computational Physics*, 457:111083, 2022.

[61] È. Lluch, O. Camara, R. Doste, et al. Calibration of a fully coupled electromechanical meshless computational model of the heart with experimental data. *Computer Methods in Applied Mechanics and Engineering*, 364:112869, 2020.

[62] K. C. Wong, L. Wang, H. Zhang, et al. Meshfree implementation of individualized active cardiac dynamics. *Computerized Medical Imaging and Graphics*, 34(1):91–103, 2010.

[63] J. Yao, G. Liu, D. A. Narmoneva, et al. Immersed smoothed finite element method for fluid–structure interaction simulation of aortic valves. *Computational Mechanics*, 50:789–804, 2012.

[64] C. Jiang, Z.-Q. Zhang, G. Liu, et al. An edge-based/node-based selective smoothed finite element method using tetrahedrons for cardiovascular tissues. *Engineering Analysis with Boundary Elements*, 59:62–77, 2015.

[65] D. Martonová, D. Holz, M. T. Duong, and S. Leyendecker. Towards the simulation of active cardiac mechanics using a smoothed finite element method. *Journal of Biomechanics*, 115:110153, 2021.

[66] R. A. Gray and P. Pathmanathan. Patient-specific cardiovascular computational modeling: diversity of personalization and challenges. *Journal of cardiovascular translational research*, 11(2):80–88, 2018.

[67] S. A. Niederer, J. Lumens, and N. A. Trayanova. Computational models in cardiology. *Nature Reviews Cardiology*, 16(2):100–111, 2019.

[68] P. Nielsen, I. Le Grice, B. Smaill, and P. Hunter. Mathematical model of geometry and fibrous structure of the heart. *American Journal of Physiology-Heart and Circulatory Physiology*, 260(4):H1365–H1378, 1991.

[69] D. Scollan, A. Holmes, J. Zhang, and R. Winslow. Reconstruction of cardiac ventricular geometry and fiber orientation using magnetic resonance imaging. *Annals of biomedical engineering*, 28:934–944, 2000.

[70] P. A. Helm, H.-J. Tseng, L. Younes, et al. Ex vivo 3d diffusion tensor imaging and quantification of cardiac laminar structure. *Magnetic Resonance in Medicine: An Official Journal of the International Society for Magnetic Resonance in Medicine*, 54(4):850–859, 2005.

[71] V. Y. Wang, H. Lam, D. B. Ennis, et al. Modelling passive diastolic mechanics with quantitative mri of cardiac structure and function. *Medical image analysis*, 13(5):773–784, 2009.

[72] V. Gurev, T. Lee, J. Constantino, et al. Models of cardiac electromechanics based on individual hearts imaging data. *Biomechanics and modeling in mechanobiology*, 10(3):295–306, 2011.

[73] M. J. Bishop, G. Plank, R. A. Burton, et al. Development of an anatomically detailed mri-derived rabbit ventricular model and assessment of its impact on simulations of electrophysiological function. *American Journal of Physiology-Heart and Circulatory Physiology*, 298(2):H699–H718, 2010.

[74] X. Papademetris, A. J. Sinusas, D. P. Dione, and J. S. Duncan. Estimation of 3d left ventricular deformation from echocardiography. *Medical image analysis*, 5(1):17–28, 2001.

[75] O. Ecabert, J. Peters, H. Schramm, et al. Automatic model-based segmentation of the heart in ct images. *IEEE transactions on medical imaging*, 27(9):1189–1201, 2008.

[76] O. Ecabert, J. Peters, M. J. Walker, et al. Segmentation of the heart and great vessels in ct images using a model-based adaptation framework. *Medical image analysis*, 15(6):863–876, 2011.

[77] D. Deng, P. Jiao, X. Ye, and L. Xia. An image-based model of the whole human heart with detailed anatomical structure and fiber orientation. *Computational and Mathematical Methods in Medicine*, 2012, 2012.

[78] O. V. Aslanidi, T. Nikolaidou, J. Zhao, et al. Application of micro-computed tomography with iodine staining to cardiac imaging, segmentation, and computational model development. *IEEE transactions on medical imaging*, 32(1):8–17, 2012.

[79] S. C. Mitchell, J. G. Bosch, B. P. Lelieveldt, et al. 3-d active appearance models: segmentation of cardiac mr and ultrasound images. *IEEE transactions on medical imaging*, 21(9):1167–1178, 2002.

[80] R. Löhner. Progress in grid generation via the advancing front technique. *Engineering with computers*, 12:186–210, 1996.

[81] L. L. Demer and F. Yin. Passive biaxial mechanical properties of isolated canine myocardium. *The Journal of physiology*, 339(1):615–630, 1983.

[82] F. C. Yin, R. K. Strumpf, P. H. Chew, and S. L. Zeger. Quantification of the mechanical properties of noncontracting canine myocardium under simultaneous biaxial loading. *Journal of biomechanics*, 20(6):577–589, 1987.

[83] B. Smaill and P. Hunter. Structure and function of the diastolic heart: material properties of passive myocardium. *Theory of heart: biomechanics, biophysics, and nonlinear dynamics of cardiac function*, pages 1–29, 1991.

[84] V. P. Novak, F. Yin, and J. Humphrey. Regional mechanical properties of passive myocardium. *Journal of biomechanics*, 27(4):403–412, 1994.

[85] I. J. LeGrice, B. Smaill, L. Chai, et al. Laminar structure of the heart: ventricular myocyte arrangement and connective tissue architecture in the dog. *American Journal of Physiology-Heart and Circulatory Physiology*, 269(2):H571–H582, 1995.

[86] D. Rohmer, A. Sitek, and G. T. Gullberg. Reconstruction and visualization of fiber and laminar structure in the normal human heart from ex vivo diffusion tensor magnetic resonance imaging (dtmri) data. *Investigative radiology*, 42(11):777–789, 2007.

[87] G. A. Holzapfel and R. W. Ogden. Constitutive modelling of passive myocardium: A structurally based framework for material characterization. *Philosophical Transactions of the Royal Society A: Mathematical, Physical and Engineering Sciences*, 367(1902):3445–3475, 2009.

[88] G. Sommer, A. J. Schriefl, M. Andrä, et al. Biomechanical properties and microstructure of human ventricular myocardium. *Acta biomaterialia*, 24:172–192, 2015.

[89] S. Dokos, B. H. Smaill, A. A. Young, and I. J. LeGrice. Shear properties of passive ventricular myocardium. *American Journal of Physiology-Heart and Circulatory Physiology*, 283(6):H2650–H2659, 2002.

[90] H. Demiray. Stresses in Ventricular Wall. *Journal of Applied Mechanics*, 43(2):194–197, 06 1976.

[91] J. D. Humphrey and F. C. P. Yin. On Constitutive Relations and Finite Deformations of Passive Cardiac Tissue: I. A Pseudostrain-Energy Function. *Journal of Biomechanical Engineering*, 109(4):298–304, 11 1987.

[92] J. D. Humphrey, R. K. Strumpf, and F. C. P. Yin. Determination of a Constitutive Relation for Passive Myocardium: II. – Parameter Estimation. *Journal of Biomechanical Engineering*, 112(3):340–346, 08 1990.

[93] J. M. Guccione, A. D. McCulloch, and L. K. Waldman. Passive Material Properties of Intact Ventricular Myocardium Determined From a Cylindrical Model. *Journal of Biomechanical Engineering*, 113(1):42–55, 02 1991.

[94] K. D. Costa, P. J. Hunter, J. S. Wayne, et al. A Three-Dimensional Finite Element Method for Large Elastic Deformations of Ventricular Myocardium: II – Prolate Spheroidal Coordinates. *Journal of Biomechanical Engineering*, 118(4):464–472, 11 1996.

[95] P. J. Hunter. Computational electromechanics of the heart. *Computational biology of the heart*, pages 345–407, 1997.

[96] K. D. Costa, J. W. Holmes, and A. D. McCulloch. Modelling cardiac mechanical properties in three dimensions. *Philosophical transactions of the Royal Society of London. Series A: Mathematical, physical and engineering sciences*, 359(1783):1233–1250, 2001.

[97] H. Schmid, M. P. Nash, A. A. Young, and P. J. Hunter. Myocardial Material Parameter Estimation – A Comparative Study for Simple Shear. *Journal of Biomechanical Engineering*, 128(5):742–750, 03 2006.

[98] R. E. McAllister, D. Noble, and R. Tsien. Reconstruction of the electrical activity of cardiac purkinje fibres. *The Journal of physiology*, 251(1):1–59, 1975.

[99] G. W. Beeler and H. Reuter. Reconstruction of the action potential of ventricular myocardial fibres. *The Journal of physiology*, 268(1):177–210, 1977.

[100] D. Di Francesco and D. Noble. A model of cardiac electrical activity incorporating ionic pumps and concentration changes. *Philosophical Transactions of the Royal Society of London. B, Biological Sciences*, 307(1133):353–398, 1985.

[101] C.-h. Luo and Y. Rudy. A model of the ventricular cardiac action potential. depolarization, repolarization, and their interaction. *Circulation research*, 68(6):1501–1526, 1991.

[102] C.-h. Luo and Y. Rudy. A dynamic model of the cardiac ventricular action potential. i. simulations of ionic currents and concentration changes. *Circulation research*, 74(6):1071–1096, 1994.

[103] L. Priebe and D. J. Beuckelmann. Simulation study of cellular electric properties in heart failure. *Circulation research*, 82(11):1206–1223, 1998.

[104] K. H. ten Tusscher, D. Noble, P.-J. Noble, and A. V. Panfilov. A model for human ventricular tissue. *American Journal of Physiology-Heart and Circulatory Physiology*, 2004.

[105] E. Grandi, F. S. Pasqualini, and D. M. Bers. A novel computational model of the human ventricular action potential and ca transient. *Journal of molecular and cellular cardiology*, 48(1):112–121, 2010.

[106] T. O'Hara, L. Virág, A. Varró, and Y. Rudy. Simulation of the undiseased human cardiac ventricular action potential: model formulation and experimental validation. *PLoS computational biology*, 7(5):e1002061, 2011.

[107] R. Frotscher, D. Muanghong, G. Dursun, et al. Sample-specific adaption of an improved electro-mechanical model of in vitro cardiac tissue. *Journal of Biomechanics*, 49(12):2428–2435, 2016.

[108] R. FitzHugh. Impulses and physiological states in theoretical models of nerve membrane. *Biophysical journal*, 1(6):445–466, 1961.

[109] J. Nagumo, S. Arimoto, and S. Yoshizawa. An active pulse transmission line simulating nerve axon. *Proceedings of the IRE*, 50(10):2061–2070, 1962.

[110] R. R. Aliev and A. V. Panfilov. A simple two-variable model of cardiac excitation. *Chaos, Solitons & Fractals*, 7(3):293–301, 1996.

[111] F. Fenton and A. Karma. Vortex dynamics in three-dimensional continuous myocardium with fiber rotation: Filament instability and fibrillation. *Chaos: An Interdisciplinary Journal of Nonlinear Science*, 8(1):20–47, 1998.

[112] J. M. Rogers and A. D. McCulloch. A collocation-galerkin finite element model of cardiac action potential propagation. *IEEE Transactions on Biomedical Engineering*, 41(8):743–757, 1994.

[113] A. Bueno-Orovio, E. M. Cherry, and F. H. Fenton. Minimal model for human ventricular action potentials in tissue. *Journal of theoretical biology*, 253(3):544–560, 2008.

[114] C. Cherubini, S. Filippi, P. Nardinocchi, and L. Teresi. An electromechanical model of cardiac tissue: Constitutive issues and electrophysiological effects. *Progress in biophysics and molecular biology*, 97(2-3):562–573, 2008.

[115] S. Göktepe and E. Kuhl. Electromechanics of the heart: a unified approach to the strongly coupled excitation–contraction problem. *Computational Mechanics*, 45:227–243, 2010.

[116] A. V. Panfilov, R. Keldermann, and M. Nash. Self-organized pacemakers in a coupled reaction-diffusion-mechanics system. *Physical review letters*, 95(25):258104, 2005.

[117] P. Pathmanathan, S. Chapman, D. Gavaghan, and J. Whiteley. Cardiac electromechanics: the effect of contraction model on the mathematical problem and accuracy of the numerical scheme. *The Quarterly Journal of Mechanics & Applied Mathematics*, 63(3):375–399, 2010.

[118] L. A. Taber and R. Perucchio. Modeling heart development. *Journal of elasticity and the physical science of solids*, 61:165–197, 2000.

[119] P. Nardinocchi and L. Teresi. On the active response of soft living tissues. *Journal of Elasticity*, 88:27–39, 2007.

[120] D. Ambrosi, G. Arioli, F. Nobile, and A. Quarteroni. Electromechanical coupling in cardiac dynamics: the active strain approach. *SIAM Journal on Applied Mathematics*, 71(2):605–621, 2011.

[121] S. Göktepe, A. Menzel, and E. Kuhl. The generalized hill model: A kinematic approach towards active muscle contraction. *Journal of the Mechanics and Physics of Solids*, 72:20–39, 2014.

[122] P. Kohl, P. Hunter, and D. Noble. Stretch-induced changes in heart rate and rhythm: clinical observations, experiments and mathematical models. *Progress in biophysics and molecular biology*, 71(1):91–138, 1999.

[123] R. Keldermann, M. Nash, and A. Panfilov. Modeling cardiac mechano-electrical feedback using reaction-diffusion-mechanics systems. *Physica D: Nonlinear Phenomena*, 238(11-12):1000–1007, 2009.

[124] M. R. Franz. Mechano-electrical feedback in ventricular myocardium. *Cardiovascular research*, 32(1):15–24, 1996.

[125] A. Panfilov, R. Keldermann, and M. Nash. Drift and breakup of spiral waves in reaction–diffusion–mechanics systems. *Proceedings of the National Academy of Sciences*, 104(19):7922–7926, 2007.

[126] M. R. Franz, R. Cima, D. Wang, et al. Electrophysiological effects of myocardial stretch and mechanical determinants of stretch-activated arrhythmias. *Circulation*, 86(3):968–978, 1992.

[127] H. Hu and F. Sachs. Stretch-activated ion channels in the heart. *Journal of molecular and cellular cardiology*, 29(6):1511–1523, 1997.

[128] R. H. Keldermann, M. P. Nash, and A. V. Panfilov. Pacemakers in a reaction-diffusion mechanics system. *Journal of Statistical Physics*, 128(1):375–392, 2007.

[129] L. D. Weise and A. V. Panfilov. A discrete electromechanical model for human cardiac tissue: effects of stretch-activated currents and stretch conditions on restitution properties and spiral wave dynamics. *PloS one*, 8(3):e59317, 2013.

[130] J. Sainte-Marie, D. Chapelle, R. Cimrman, and M. Sorine. Modeling and estimation of the cardiac electromechanical activity. *Computers & structures*, 84(28):1743–1759, 2006.

[131] T. P. Usyk, I. J. LeGrice, and A. D. McCulloch. Computational model of three-dimensional cardiac electromechanics. *Computing and visualization in science*, 4:249–257, 2002.

[132] M. P. Nash and A. V. Panfilov. Electromechanical model of excitable tissue to study reentrant cardiac arrhythmias. *Progress in biophysics and molecular biology*, 85(2-3):501–522, 2004.

[133] X. Jie, V. Gurev, and N. Trayanova. Mechanisms of mechanically induced spontaneous arrhythmias in acute regional ischemia. *Circulation research*, 106(1):185–192, 2010.

[134] F. S. Costabal, F. A. Concha, D. E. Hurtado, and E. Kuhl. The importance of mechano-electrical feedback and inertia in cardiac electromechanics. *Computer methods in applied mechanics and engineering*, 320:352–368, 2017.

[135] A. Santiago, J. Aguado-Sierra, M. Zavala-Aké, et al. Fully coupled fluid-electro-mechanical model of the human heart for supercomputers. *International journal for numerical methods in biomedical engineering*, 34(12):e3140, 2018.

[136] M. T. Duong, D. Holz, M. Alkassar, et al. Interaction of the mechano-electrical feedback with passive mechanical models on a 3d rat left ventricle: a computational study. *Frontiers in physiology*, 10:1041, 2019.

[137] S. N. Doost, D. Ghista, B. Su, et al. Heart blood flow simulation: a perspective review. *Biomedical engineering online*, 15:1–28, 2016.

[138] F. Nobile and C. Vergara. An effective fluid-structure interaction formulation for vascular dynamics by generalized robin conditions. *SIAM Journal on Scientific Computing*, 30(2):731–763, 2008.

[139] N. Westerhof, N. Stergiopulos, M. I. Noble, et al. *Snapshots of hemodynamics: an aid for clinical research and graduate education*, volume 7. Springer, 2010.

[140] I. E. Vignon-Clementel, C. A. Figueroa, K. E. Jansen, and C. A. Taylor. Outflow boundary conditions for three-dimensional finite element modeling of blood flow and pressure in arteries. *Computer methods in applied mechanics and engineering*, 195(29-32):3776–3796, 2006.

[141] T. S. Eriksson, A. J. Prassl, G. Plank, and G. A. Holzapfel. Modeling the dispersion in electromechanically coupled myocardium. *International journal for numerical methods in biomedical engineering*, 29(11):1267–1284, 2013.

[142] R. Chabiniok, P. Moireau, P.-F. Lesault, et al. Estimation of tissue contractility from cardiac cine-mri using a biomechanical heart model. *Biomechanics and modeling in mechanobiology*, 11:609–630, 2012.

[143] S. Marchesseau, H. Delingette, M. Sermesant, and N. Ayache. Fast parameter calibration of a cardiac electromechanical model from medical images based on the unscented transform. *Biomechanics and modeling in mechanobiology*, 12(4):815–831, 2013.

[144] M. R. Pfaller, J. M. Hörmann, M. Weigl, et al. The importance of the pericardium for cardiac biomechanics: from physiology to computational modeling. *Biomechanics and modeling in mechanobiology*, 18:503–529, 2019.

[145] C. M. Augustin, A. Neic, M. Liebmann, et al. Anatomically accurate high resolution modeling of human whole heart electromechanics: a strongly scalable algebraic multigrid solver method for nonlinear deformation. *Journal of computational physics*, 305:622–646, 2016.

[146] S. Land and S. A. Niederer. Influence of atrial contraction dynamics on cardiac function. *International journal for numerical methods in biomedical engineering*, 34(3):e2931, 2018.

[147] T. Fritz, C. Wieners, G. Seemann, et al. Simulation of the contraction of the ventricles in a human heart model including atria and pericardium: Finite element analysis of a frictionless contact problem. *Biomechanics and modeling in mechanobiology*, 13:627–641, 2014.

[148] F. S. Costabal, D. E. Hurtado, and E. Kuhl. Generating purkinje networks in the human heart. *Journal of biomechanics*, 49(12):2455–2465, 2016.

[149] D. Martonová, D. Holz, J. Seufert, et al. Comparison of stress and stress–strain approaches for the active contraction in a rat cardiac cycle model. *Journal of Biomechanics*, 134:110980, 2022.

[150] F. Sahli Costabal, Y. Yang, P. Perdikaris, et al. Physics-informed neural networks for cardiac activation mapping. *Frontiers in Physics*, 8:42, 2020.

[151] A. Pollard and R. Barr. Computer simulations of activation in an anatomically based model of the human ventricular conduction system. *IEEE Transactions on Biomedical Engineering*, 38(10):982–996, 1991.

[152] O. Berenfeld and J. Jalife. Purkinje-muscle reentry as a mechanism of polymorphic ventricular arrhythmias in a 3-dimensional model of the ventricles. *Circulation Research*, 82(10):1063–1077, 1998.

[153] K. D. Costa, Y. Takayama, A. D. McCulloch, and J. W. Covell. Laminar fiber architecture and three-dimensional systolic mechanics in canine ventricular myocardium. *American Journal of Physiology-Heart and Circulatory Physiology*, 276(2):H595–H607, 1999.

[154] M. Fernandez-Teran and J. Hurle. Myocardial fiber architecture of the human heart ventricles. *The Anatomical Record*, 204(2):137–147, 1982.

[155] A. A. Holmes, D. Scollan, and R. L. Winslow. Direct histological validation of diffusion tensor mri in formaldehyde-fixed myocardium. *Magnetic Resonance in Medicine: An Official Journal of the International Society for Magnetic Resonance in Medicine*, 44(1):157–161, 2000.

[156] D. F. Scollan, A. Holmes, R. Winslow, and J. Forder. Histological validation of myocardial microstructure obtained from diffusion tensor magnetic resonance imaging. *American Journal of Physiology-Heart and Circulatory Physiology*, 275(6):H2308–H2318, 1998.

[157] N. Toussaint, C. T. Stoeck, T. Schaeffter, et al. In vivo human cardiac fibre architecture estimation using shape-based diffusion tensor processing. *Medical image analysis*, 17(8):1243–1255, 2013.

[158] P. Helm, M. F. Beg, M. I. Miller, and R. L. Winslow. Measuring and mapping cardiac fiber and laminar architecture using diffusion tensor mr imaging. *Annals-New York Academy of Sciences*, 1047:296, 2005.

[159] E. E. Konofagou, J. D'hooge, and J. Ophir. Myocardial elastography – a feasibility study in vivo. *Ultrasound in medicine & biology*, 28(4):475–482, 2002.

[160] C. Papadacci, V. Finel, J. Provost, et al. Imaging the dynamics of cardiac fiber orientation in vivo using 3d ultrasound backscatter tensor imaging. *Scientific reports*, 7(1):1–9, 2017.

[161] A. Gonz.-Tendero, C. Zhang, V. Balicevic, et al. Whole heart detailed and quantitative anatomy, myofibre structure and vasculature from x-ray phase-contrast synchrotron radiation-based micro computed tomography. *European Heart Journal-Cardiovascular Imaging*, 18(7):732–741, 2017.

[162] F. Varray, I. Mirea, M. Langer, et al. Extraction of the 3d local orientation of myocytes in human cardiac tissue using x-ray phase-contrast microtomography and multi-scale analysis. *Medical Image Analysis*, 38:117–132, 2017.

[163] M. J. Bishop, G. Plank, R. A. Burton, et al. Development of an anatomically detailed mri-derived rabbit ventricular model and assessment of its impact on simulations of electrophysiological function. *American Journal of Physiology-Heart and Circulatory Physiology*, 298(2):H699–H718, 2010.

[164] K. L. Sack, E. Aliotta, D. B. Ennis, et al. Construction and validation of subject-specific biventricular finite-element models of healthy and failing swine hearts from high-resolution dt-mri. *Frontiers in Physiology*, 9:539, 2018.

[165] M. Potse, B. Dubé, J. Richer, et al. A comparison of monodomain and bidomain reaction-diffusion models for action potential propagation in the human heart. *IEEE Transactions on Biomedical Engineering*, 53(12):2425–2435, 2006.

[166] V. Carapella, R. Bordas, P. Pathmanathan, et al. Quantitative Study of the Effect of Tissue Microstructure on Contraction in a Computational Model of Rat Left Ventricle. *PLoS ONE*, 9(4):e92792, Apr 2014.

[167] J. D. Bayer, R. C. Blake, G. Plank, and N. A. Trayanova. A novel rule-based algorithm for assigning myocardial fiber orientation to computational heart models. *Annals of biomedical engineering*, 40(10):2243–2254, 2012.

[168] J. Wong and E. Kuhl. Generating fibre orientation maps in human heart models using Poisson interpolation. *Computer Methods in Biomechanics and Biomedical Engineering*, 17(11):1217–1226, Aug 2014.

[169] R. Doste, D. Soto-Iglesias, G. Bernardino, et al. A rule-based method to model myocardial fiber orientation in cardiac biventricular geometries with outflow tracts. *International journal for numerical methods in biomedical engineering*, 35(4):e3185, 2019.

[170] D. Holz, M. T. Duong, D. Martonová, et al. A transmural path model improves the definition of the orthotropic tissue structure in heart simulations. *Journal of Biomechanical Engineering*, 144(3), 2022.

[171] R. Piersanti, P. C. Africa, M. Fedele, et al. Modeling cardiac muscle fibers in ventricular and atrial electrophysiology simulations. *Computer Methods in Applied Mechanics and Engineering*, 373:113468, 2021.

[172] F. Torrent-Guasp, G. D. Buckberg, C. Clemente, et al. The structure and function of the helical heart and its buttress wrapping. i. the normal macroscopic structure of the heart. In *Seminars in thoracic and cardiovascular surgery*, volume 13, pages 301–319. Elsevier, 2001.

[173] H. V. Huikuri, A. Castellanos, and R. J. Myerburg. Sudden death due to cardiac arrhythmias. *New England Journal of Medicine*, 345(20):1473–1482, 2001.

[174] D. A. Hooks, M. L. Trew, B. J. Caldwell, et al. Laminar arrangement of ventricular myocytes influences electrical behavior of the heart. *Circulation Research*, 101(10):e103–e112, 2007.

[175] G. Buckberg, J. I. Hoffman, A. Mahajan, et al. Cardiac mechanics revisited: the relationship of cardiac architecture to ventricular function. *Circulation*, 118(24):2571–2587, 2008.

[176] T. S. Eriksson, A. J. Prassl, G. Plank, and G. A. Holzapfel. Influence of myocardial fiber/sheet orientations on left ventricular mechanical contraction. *Mathematics and Mechanics of Solids*, 18(6):592–606, 2013.

[177] B. Taccardi, E. Macchi, R. L. Lux, et al. Effect of myocardial fiber direction on epicardial potentials. *Circulation*, 90(6):3076–3090, 1994.

[178] B. J. Maron and W. C. Roberts. Quantitative analysis of cardiac muscle cell disorganization in the ventricular septum of patients with hypertrophic cardiomyopathy. *Circulation*, 59(4):689–706, 1979.

[179] G. W. Dec and V. Fuster. Idiopathic dilated cardiomyopathy. *New England Journal of Medicine*, 331(23):1564–1575, 1994.

[180] D. Holz, D. Martonová, E. Schaller, et al. Transmural fibre orientations based on laplace–dirichlet-rule-based-methods and their influence on human heart simulations. *Journal of Biomechanics*, 156:111643, 2023.

[181] L. Miller, E. Birks, M. Guglin, et al. Use of ventricular assist devices and heart transplantation for advanced heart failure. *Circulation research*, 124(11):1658–1678, 2019.

[182] D. Zimpfer, A. E. Fiane, R. Larbalestier, et al. Long-term survival of patients with advanced heart failure receiving an left ventricular assist device intended as a bridge to transplantation: the registry to evaluate the heartware left ventricular assist system. *Circulation: Heart Failure*, 13(3):e006252, 2020.

[183] D. Timms. A review of clinical ventricular assist devices. *Medical engineering & physics*, 33(9):1041–1047, 2011.

[184] D. Martonová, D. Holz, D. Brackenhammer, et al. Support pressure acting on the epicardial surface of a rat left ventricle–a computational study. *Frontiers in Cardiovascular Medicine*, 9, 2022.

[185] B. Long, J. Robertson, A. Koyfman, and W. Brady. Left ventricular assist devices and their complications: a review for emergency clinicians. *The American journal of emergency medicine*, 37(8):1562–1570, 2019.

[186] H. J. Eisen. Left ventricular assist devices (lvads): history, clinical application and complications. *Korean circulation journal*, 49(7):568–585, 2019.

[187] A. Kilic, M. A. Acker, and P. Atluri. Dealing with surgical left ventricular assist device complications. *Journal of thoracic disease*, 7(12):2158, 2015.

[188] R. J. Gordon, B. Quagliarello, and F. D. Lowy. Ventricular assist device-related infections. *The Lancet infectious diseases*, 6(7):426–437, 2006.

[189] Y. Pya, J. Maly, M. Bekbossynova, et al. First human use of a wireless coplanar energy transfer coupled with a continuous-flow left ventricular assist device. *The Journal of Heart and Lung Transplantation*, 38(4):339–343, 2019.

[190] B. H. Waters, A. P. Sample, P. Bonde, and J. R. Smith. Powering a ventricular assist device (vad) with the free-range resonant electrical energy delivery (free-d) system. *Proceedings of the IEEE*, 100(1):138–149, 2011.

[191] J. X. Wang, J. R. Smith, and P. Bonde. Energy transmission and power sources for mechanical circulatory support devices to achieve total implantability. *The Annals of thoracic surgery*, 97(4):1467–1474, 2014.

[192] A. C. Eringen. On the foundations of electroelastostatics. *International Journal of Engineering Science*, 1(1):127–153, 1963.

[193] R. A. Toupin. The elastic dielectric. *Journal of Rational Mechanics and Analysis*, 5(6):849–915, 1956.

[194] R. A. Toupin. Elastic materials with couple-stresses. *Archive for Rational Mechanics and Analysis*, 11(1):385–414, 1962.

[195] A. C. Eringen and G. A. Maugin. *Electrodynamics of Continua I: Foundations and Solid Media*. Springer, 1989.

[196] G. A. Maugin. *Continuum mechanics of electromagnetic solids*. Elsevier, 1988.

[197] A. Dorfmann and R. W. Ogden. Magnetoelastic modelling of elastomers. *European Journal of Mechanics - A/Solids*, 22(4):497–507, 2003.

[198] A. Dorfmann and R. W. Ogden. Nonlinear electroelasticity. *Acta Mech.*, 174:167–183, 2005.

[199] A. Dorfmann and R. W. Ogden. Nonlinear electroelastic deformations. *Journal of Elasticity*, 82(2):99–127, 2006.

[200] A. Dorfmann and R. W. Ogden. Nonlinear electroelastostatics: Incremental equations and stability. *International Journal of Engineering Science*, 48(1):1–14, 2010.

[201] R. M. McMeeking and C. M. Landis. Electrostatic forces and stored energy for deformable dielectric materials. *Journal of Applied Mechanics*, 72(4):581–590, 2005.

[202] R. M. McMeeking, C. M. Landis, and S. M. Jimenez. A principle of virtual work for combined electrostatic and mechanical loading of materials. *International Journal of Non-Linear Mechanics*, 42(6):831–838, 2007.

[203] D. K. Vu and P. Steinmann. Nonlinear electro- and magneto-elastostatics: Material and spatial settings. *International Journal of Solids and Structures*, 44:7891–7905, 2007.

[204] D. K. Vu, P. Steinmann, and G. Possart. Numerical modelling of nonlinear electroelasticity. *International Journal for Numerical Methods in Engineering*, 70(6):685–704, May 2007.

[205] A. Ask, A. Menzel, and M. Ristinmaa. On the modelling of electro-viscoelastic response of electrostrictive polyurethane elastomers. *IOP Conference Series: Materials Science and Engineering*, 10(1), 2010.

[206] A. Ask, A. Menzel, and M. Ristinmaa. Electrostriction in electro-viscoelastic polymers. *Mechanics of Materials*, 50:9–21, 2012.

[207] A. Ask, A. Menzel, and M. Ristinmaa. Phenomenological modeling of viscous electrostrictive polymers. *International Journal of Non-Linear Mechanics*, 47(2):156–165, 2012.

[208] A. Ask, A. Menzel, and M. Ristinmaa. Modelling of viscoelastic dielectric elastomers with deformation dependent electric properties. In *Proceedings of the IUTAM Symposium on Mechanics of Soft Active Materials*, volume 12, pages 134–144, 2015.

[209] T. Schlögl and S. Leyendecker. Electrostatic–viscoelastic finite element model of dielectric actuators. *Computer Methods in Applied Mechanics and Engineering*, 299:421–439, 2016.

[210] T. Schlögl and S. Leyendecker. A polarisation based approach to model the strain dependent permittivity of dielectric elastomers. *Sensors and Actuators A: Physical*, 267:156–163, 2017.

[211] T. Schlögl. *Modelling, Simulation and Optimal Control of Dielectric Elastomer Actuated Systems.* PhD thesis, Chair of Applied Dynamics, Friedrich- Alexander-Universität Erlangen-Nürnberg, 2017.

[212] A. Ask, R. Denzer, A. Menzel, and M. Ristinmaa. Inverse-motion-based form finding for quasi-incompressible finite electroelasticity. *Numerical Methods in Engineering*, 94(6):554–572, 2013.

[213] M. Klassen, B.-X. Xu, and R. Müller. The influence of incompressibility on the microstructure of dielectric elastomers. In *Proceedings of the 84th Annual Meeting of the International Association of Applied Mathematics and Mechanics (GAMM)*, volume 13, 2013.

[214] M. Klassen. *Numerical Modeling for the Static and Dynamic Analysis of Nearly Incompressible Dielectric Elastomers*. PhD thesis, University of Kaiserslautern, 2016.

[215] N. Liu, T. Martinez, A. Walter, et al. Control-oriented modeling and analysis of tubular dielectric elastomer actuators dedicated to cardiac assist devices. *IEEE Robotics and Automation Letters*, 7(2):4361–4367, 2022.

[216] D. Martonová, M. Alkassar, J. Seufert, et al. Passive mechanical properties in healthy and infarcted rat left ventricle characterised via a mixture model. *Journal of the Mechanical Behavior of Biomedical Materials*, 119:104430, 2021.

[217] S. Klinkel, S. Zwecker, and R. Müller. A solid shell finite element formulation for dielectric elastomers. *Journal of Applied Mechanics*, 80(2), 2013.

[218] J. Altenbach, H. Altenbach, and V. A. Eremeyev. On generalized cosserat-type theories of plates and shells: a short review and bibliography. *Archive of Applied Mechanics*, 80(1):73–92, 2010.

[219] M. Bîrsan. On a thermodynamic theory of porous cosserat elastic shells. *Journal of Thermal Stresses*, 29(9):879–899, 2006.

[220] P. Betsch and N. Sänger. On the use of geometrically exact shells in a conserving framework for flexible multibody dynamics. *Comput Methods Appl Mech Eng*, 198(17-20):1609–1630, 2009.

[221] S. Leyendecker, P. Betsch, and P. Steinmann. The discrete null space method for the energy-consistent integration of constrained mechanical systems. part iii: Flexible multibody dynamics. *Multibody System Dynamics*, 19(1):45–72, 2008.

[222] D. Huang and S. Leyendecker. An electromechanically coupled beam model for dielectric elastomer actuators. *Computational Mechanics*, 69(3):805–824, 2022.

[223] D. Huang and S. Leyendecker. Optimal control of dielectric elastomer actuated multibody dynamical systems. *Soft Robotics*, 2023.

[224] M. E. Gurtin. *An introduction to continuum mechanics*. Academic press, 1982.

[225] J. Bonet and R. D. Wood. *Nonlinear continuum mechanics for finite element analysis*. Cambridge university press, 1997.

[226] G. Holzapfel. *NONLINEAR SOLID MECHANICS. A Continuum Approach for Engineering*. (second print Aufl.)John Wiley & Sons, 2001.

[227] O. C. Zienkiewicz, R. L. Taylor, and R. L. Taylor. *The finite element method: solid mechanics*, volume 2. Butterworth-heinemann, 2000.

[228] K.-J. Bathe. *Finite element procedures*. Klaus-Jurgen Bathe, 2006.

[229] P. Wriggers. *Nonlinear finite element methods*. Springer Science & Business Media, 2008.

[230] T. J. Hughes. *The finite element method: linear static and dynamic finite element analysis*. Courier Corporation, 2012.

[231] R. De Borst, M. A. Crisfield, J. J. Remmers, and C. V. Verhoosel. *Nonlinear finite element analysis of solids and structures*. John Wiley & Sons, 2012.

[232] T. Belytschko, W. K. Liu, B. Moran, and K. Elkhodary. *Nonlinear finite elements for continua and structures*. John wiley & sons, 2014.

[233] W. H. Reed and T. R. Hill. Triangular mesh methods for the neutron transport equation. Technical report, Los Alamos Scientific Lab., N. Mex.(USA), 1973.

[234] P. Lesaint and P.-A. Raviart. On a finite element method for solving the neutron transport equation. *Publications mathématiques et informatique de Rennes*, (S4):1–40, 1974.

[235] B. Cockburn, G. E. Karniadakis, and C.-W. Shu. *Discontinuous Galerkin methods: theory, computation and applications*, volume 11. Springer Science & Business Media, 2012.

[236] S. E. Jones, B. R. Buchbinder, and I. Aharon. Three-dimensional mapping of cortical thickness using Laplace's equation. *Human brain mapping*, 11(1):12–32, 2000.

[237] A. J. Yezzi and J. L. Prince. An Eulerian PDE approach for computing tissue thickness. *IEEE transactions on medical imaging*, 22(10):1332–1339, 2003.

[238] Y. Lv and M. Ihme. Discontinuous galerkin method for multicomponent chemically reacting flows and combustion. *Journal of Computational Physics*, 270:105–137, 2014.

[239] F. P. Baaijens. Application of low-order discontinuous galerkin methods to the analysis of viscoelastic flows. *Journal of Non-Newtonian Fluid Mechanics*, 52(1):37–57, 1994.

[240] A. Bahhar, J. Baranger, and D. Sandri. Galerkin discontinuous approximation of the transport equation and viscoelastic fluid flow on quadrilaterals. *Numerical Methods for Partial Differential Equations: An International Journal*, 14(1):97–114, 1998.

[241] G. Engel, K. Garikipati, T. Hughes, et al. Continuous/discontinuous finite element approximations of fourth-order elliptic problems in structural and continuum mechanics with applications to thin beams and plates, and strain gradient elasticity. *Computer Methods in Applied Mechanics and Engineering*, 191(34):3669–3750, 2002.

[242] P. Hansbo and M. G. Larson. Discontinuous galerkin methods for incompressible and nearly incompressible elasticity by nitsche's method. *Computer methods in applied mechanics and engineering*, 191(17-18):1895–1908, 2002.

[243] B. Cockburn and C.-W. Shu. The local discontinuous galerkin method for time-dependent convection-diffusion systems. *SIAM Journal on Numerical Analysis*, 35(6):2440–2463, 1998.

[244] I. Babuška, C. E. Baumann, and J. T. Oden. A discontinuous hp finite element method for diffusion problems: 1-d analysis. *Computers & Mathematics with Applications*, 37(9):103–122, 1999.

[245] C. Johnson and J. Pitkäranta. An analysis of the discontinuous galerkin method for a scalar hyperbolic equation. *Mathematics of computation*, 46(173):1–26, 1986.

[246] F. Brezzi, L. D. Marini, and E. Süli. Discontinuous galerkin methods for first-order hyperbolic problems. *Mathematical models and methods in applied sciences*, 14(12):1893–1903, 2004.

[247] B. Rivière. *Discontinuous Galerkin methods for solving elliptic and parabolic equations: theory and implementation*. SIAM, 2008.

[248] B. Rivière and M. F. Wheeler. A discontinuous galerkin method applied to nonlinear parabolic equations. In *Discontinuous Galerkin methods*, pages 231–244. Springer, 2000.

[249] B. Cockburn and C.-W. Shu. The runge–kutta discontinuous galerkin method for conservation laws v: multidimensional systems. *Journal of Computational Physics*, 141(2):199–224, 1998.

[250] F. Bassi and S. Rebay. High-order accurate discontinuous finite element solution of the 2d euler equations. *Journal of computational physics*, 138(2):251–285, 1997.

[251] B. Cockburn, G. E. Karniadakis, and C.-W. Shu. The development of discontinuous galerkin methods. In *Discontinuous Galerkin Methods*, pages 3–50. Springer, 2000.

[252] V. H. van Hal, D. Zhao, K. Gilbert, et al. Comparison of 2d echocardiography and cardiac cine mri in the assessment of regional left ventricular wall thickness. *International Workshop on Statistical Atlases and Computational Models of the Heart*, pages 52–62, 2019.

[253] Y. Wang, Z. Xiong, A. Nalar, et al. A robust computational framework for estimating 3d bi-atrial chamber wall thickness. *Computers in biology and medicine*, 114:103444, 2019.

[254] B. L. Troy, J. Pombo, and C. E. Rackley. Measurement of left ventricular wall thickness and mass by echocardiography. *Circulation*, 45(3):602–611, 1972.

[255] M. S. Alnæs, J. Blechta, J. Hake, et al. The fenics project version 1.5. *Archive of Numerical Software*, 3(100):9–23, 2015.

[256] A. Logg, K.-A. Mardal, G. N. Wells, et al. *Automated Solution of Differential Equations by the Finite Element Method*. Springer, 2012.

[257] D. N. Arnold, F. Brezzi, B. Cockburn, and L. D. Marini. Unified analysis of discontinuous galerkin methods for elliptic problems. *SIAM journal on numerical analysis*, 39(5):1749–1779, 2002.

[258] C. Geuzaine and J.-F. Remacle. Gmsh: A 3-d finite element mesh generator with built-in pre-and post-processing facilities. *International journal for numerical methods in engineering*, 79(11):1309–1331, 2009.

[259] D. H. S. Lin and F. C. P. Yin. A Multiaxial Constitutive Law for Mammalian Left Ventricular Myocardium in Steady-State Barium Contracture or Tetanus. *Journal of Biomechanical Engineering*, 120(4):504–517, August 1998.

[260] R. Kikinis, S. D. Pieper, and K. G. Vosburgh. *3D Slicer: A Platform for Subject-Specific Image Analysis, Visualization, and Clinical Support*, pages 277–289. Springer New York, 2014.

[261] E. K. Rodriguez, A. Hoger, and A. D. McCulloch. Stress-dependent finite growth in soft elastic tissues. *Journal of biomechanics*, 27(4):455–467, 1994.

[262] J. C. Walker, M. B. Ratcliffe, P. Zhang, et al. Mri-based finite-element analysis of left ventricular aneurysm. *American Journal of Physiology-Heart and Circulatory Physiology*, 289(2):H692–H700, 2005.

[263] M. Sermesant and R. Razavi. Personalized computational models of the heart for cardiac resynchronization therapy. In *Patient-specific modeling of the cardiovascular system*, pages 167–182. Springer, 2010.

[264] J. Parker and R. Case. Normal left ventricular function. *Circulation*, 60(1):4–12, 1979.

[265] J. J. Feher. *Quantitative human physiology: an introduction*. Academic press, 2017.

[266] B. Cansız. *Computational Modelling of Cardiac Electromechanics Towards Predictive Patient Specific Simulations*. PhD thesis, iSD, Institut für Statik und Dynamik der Tragwerke, 2019.

[267] P. Bovendeerd, J. Huyghe, T. Arts, et al. Influence of endocardial-epicardial crossover of muscle fibers on left ventricular wall mechanics. *Journal of biomechanics*, 27(7):941–951, 1994.

[268] L. Azzolin, L. Dede, A. Gerbi, and A. Quarteroni. Effect of fibre orientation and bulk modulus on the electromechanical modelling of human ventricles. *Mathematics in engineering*, 2(4):614–638, 2020.

[269] D. J. Griffiths. *Introduction to electrodynamics*. Addison-Wesley, 2012.

[270] D. K. Vu, P. Steinmann, and G. Possart. Numerical modelling of nonlinear electroelasticity. *International Journal for Numerical Methods in Engineering*, 70(6):685–704, 2006.

[271] T. Schlögl. *Modelling, simulation and optimal control of dielectric elastomer actuated systems*. PhD thesis, Friedrich-Alexander-Universität Erlangen-Nürnberg (FAU), 2018.

[272] M. Kaliske and H. Rothert. On the finite element implementation of rubber-like materials at finite strains. *Engineering Computations*, 14(2):216–232, 1997.

[273] M. Mooney. A theory of large elastic deformation. *Journal of applied physics*, 11(9):582–592, 1940.

[274] R. S. Rivlin. Large elastic deformations of isotropic materials iv. further developments of the general theory. *Philosophical transactions of the royal society of London. Series A, Mathematical and physical sciences*, 241(835):379–397, 1948.

[275] R. W. Ogden. Large deformation isotropic elasticity–on the correlation of theory and experiment for incompressible rubberlike solids. *Proceedings of the Royal Society of London. A. Mathematical and Physical Sciences*, 326(1567):565–584, 1972.

[276] O. H. Yeoh. Some forms of the strain energy function for rubber. *Rubber Chemistry and technology*, 66(5):754–771, 1993.

[277] M. Wissler and E. Mazza. Modeling of a pre-strained circular actuator made of dielectric elastomers. *Sensors and Actuators A: Physical*, 120(1):184–192, 2005.

[278] M. Wissler and E. Mazza. Electromechanical coupling in dielectric elastomer actuators. *Sensors and Actuators A: Physical*, 138(2):384–393, 2007.

[279] P. Wriggers. *Nonlinear Finite Element Methods*. Springer, 2008.

[280] M. Bischoff and E. Ramm. Shear deformable shell elements for large strains and rotations. *International Journal for Numerical Methods in Engineering*, 40(23):4427–4449, 1997.

[281] M. Bischoff. *Theorie und Numerik einer dreidimensionalen Schalenformulierung*. PhD thesis, Universität Stuttgart, 1999.

[282] E. Reissner. The Effect of Transverse Shear Deformation on the Bending of Elastic Plates. *Journal of Applied Mechanics*, 12(2):A69–A77, 2021.

[283] R. D. Mindlin. Influence of Rotatory Inertia and Shear on Flexural Motions of Isotropic, Elastic Plates. *Journal of Applied Mechanics*, 18(1):31–38, 2021.

[284] J. Simo and D. Fox. On a stress resultant geometrically exact shell model. part i: Formulation and optimal parametrization. *Computer Methods in Applied Mechanics and Engineering*, 72(3):267–304, 1989.

[285] S. Klinkel, F. Gruttmann, and W. Wagner. A mixed shell formulation accounting for thickness strains and finite strain 3d material models. *International journal for numerical methods in engineering*, 74(6):945–970, 2008.

[286] C. Sansour, P. Wriggers, and J. Sansour. Nonlinear dynamics of shells: Theory, finite element formulation, and integration schemes. *Nonlinear Dynamics*, 13:279–305, 1997.

[287] O. C. Zienkiewicz, R. L. Taylor, and J. Z. Zhu. *The finite element method: its basis and fundamentals*. Elsevier, 2005.

[288] S. Leyendecker, J. Marsden, and M. Ortiz. Variational integrators for constrained dynamical systems. *Journal of Applied Mathematics and Mechanics (ZAMM)*, 88(9):677–708, 2008.

[289] R. Maas, T. Siebert, and S. Leyendecker. On the relevance of structure preservation to simulations of muscle actuated movements. *Biomechanics and modeling in mechanobiology*, 11(3):543–556, 2012.

[290] J. E. Marsden and M. West. Discrete mechanics and variational integrators. *Acta Numerica*, 10:357–514, 2001.

[291] S. Leyendecker, P. Betsch, and P. Steinmann. The discrete null space method for the energy-consistent integration of constrained mechanical systems. part iii: Flexible multibody dynamics. *Multibody System Dynamics*, 19(1):45–72, 2008.

[292] P. Betsch and A. Janz. An energy–momentum consistent method for transient simulations with mixed finite elements developed in the framework of geometrically exact shells. *International Journal for Numerical Methods in Engineering*, 108(5):423–455, 2016.

[293] J. A. Andersson, J. Gillis, G. Horn, et al. Casadi: a software framework for nonlinear optimization and optimal control. *Mathematical Programming Computation*, 11(1):1–36, 2019.

[294] W. Wagner and F. Gruttmann. A robust non-linear mixed hybrid quadrilateral shell element. *International Journal for Numerical Methods in Engineering*, 64(5):635–666, 2005.

[295] K. Wisniewski and E. Turska. Four-node mixed hu–washizu shell element with drilling rotation. *International journal for numerical methods in engineering*, 90(4):506–536, 2012.

[296] J. C. Simo, D. D. Fox, and M. S. Rifai. On a stress resultant geometrically exact shell model. part iii: Computational aspects of the nonlinear theory. *Computer Methods in Applied Mechanics and Engineering*, 79(1):21–70, 1990.